Swimming water droplet in complex environment, confinement, gravity and collective effects.

Charlotte de Blois de La Calande

PSL
UNIVERSITÉ PARIS

THÈSE DE DOCTORAT
DE L'UNIVERSITÉ PSL

Préparée à ESPCI Paris

Swimming water droplets in complex environments, Confinement, gravity and collective effects.

Gouttes nageuses en environnement complexe, Confinement, gravité et effets collectifs.

Soutenue par
Charlotte de Blois
Le 05/11/19

École doctorale n°564
Physique en Île-de-France

Spécialité
Physique

Composition du jury :

Mme Anke Lindner Professeur, Paris Diderot	*Présidente*
Mme Elise Lorenceau Chargé de recherche, CNRS-Université de Grenoble Alpes	*Rapportrice*
M. Francois Gallaire Associate professor, École polytechnique fédérale de Lausanne	*Rapporteur*
M. Hamid Kellay Professeur, Université de Bordeaux	*Examinateur*
Mme Mathilde Reyssat Maître de conférence, ESPCI Paris	*Examinatrice*
M. Olivier Dauchot Directeur de recherche, CNRS-ESPCI Paris	*Directeur de thèse*

ESPCI PARIS | PSL

Laboratoire Gulliber - UMR CNRS 7083
ESPCI Paris -PSL university
10 rue Vauquelin
75005 Paris

Ecole doctorale 564
Physique en Île-de-France

Acknowledgments

Faire de la recherche, c'est un peu comme naviguer sur un bateau. Il y a la soif de l'inconnu, la quête de l'horizon qui sans cesse recule. Ces voyages là, on ne les fait pas seul, il y a autour de nous un équipage grâce à qui le navire avance. Il y a, dans chaque port, des rencontres qui nous enrichissent. Il y a, au port d'attache, une famille, des amis, vers qui on peut toujours revenir. Ce grand voyage de trois années a été pour moi une source d'étonnement, de découvertes, de joies et d'émerveillement. A Vous qui êtes à l'origine de tout cela,

Merci.

Avant tout, j'aimerais exprimer toute ma reconnaissance à Olivier Dauchot et Mathilde Reyssat, mes deux encadrants, les deux capitaines, pour toute l'énergie, tout le temps et tout l'enthousiasme qu'ils ont investis dans cette thèse.

Olivier a initié le projet "goutte nageuse"; et l'a conduit tel le capitaine d'une flotte, coordonnant les projets, soutenant les idées et donnant l'impulsion qui les fait avancer. Tout ceci en accompagnant le petit apprenti marin (moi) pour qu'il choisisse sa propre voie et se construise à son rythme. Olivier, du fond du cœur, merci.

Mathilde a rejoint le projet à la fin de ma première année; capitaine en second, elle est un soutien indéfectible sur tous les plans (psychologique, pratique) pour l'apprenti marin, mais je le crois aussi, pour tout le labo. Sa bienveillance et son empressement à aider sont deux qualités que j'aimerais prendre en exemple en tant que chercheuse. Mathilde, du fond du cœur, merci.

J'ai beaucoup de gratitude pour les membres de mon jury de thèse ; non seulement pour avoir accepté d'évaluer mon travail, mais aussi pour y avoir montré beaucoup d'intérêt, posant des questions très pertinentes menant à des discussions scientifiques sur le fond de mon sujet. Grâce à eux, ma soutenance a été un bon moment. Merci au Professeur Anke Lindner, présidente du Jury de thèse, à Elise Lorenceau et au professeur Francois Gallaire, rapporteurs, et au professeur Hamid Kellay, examinateur.

Merci aussi à Vincent Demery et Philippe Nghé qui ont formé mon comité de suivi, et veillé à ce que ma thèse se déroule dans les meilleures conditions (scientifiques et humaines) possibles.

Je remercie ceux qui ont fait une contribution directe à ce travail, ils sont citées tout au long du manuscrit.

A mon embarquement, j'ai reçu une formation intense de microfluidique par Marjolein Van Der Linden. Merci!

Naviguer serait bien difficile sans les pilotes et timoniers, qui prédisent (littéralement!) les courants marins (en particulier aux toutes petites échelles). Merci à Sébastien Michelin, qui m'a fait plonger dans la théorie des gouttes, de la nage, et de leurs instabilités. Merci à Pierre Illien pour avoir pris le "train" en marche, et en avoir fait un système théorique robuste. Merci à Vincent Bertin de l'entrain qu'il met à discuter, et surtout à m'expliquer la résolution d'équations complexes!

Merci à Saori Suda, de la flotte japonaise, d'avoir traversé les mers pour réaliser un projet commun. Merci à Sandra Lerouge, pour m'avoir lancée sur les projets de PIV.

Merci aussi aux trois matelots, Hong Pô, Théo Lenavetier et Victor Maquart qui sont venus passer quelques mois sur le bateau "gouttes nageuses" (et pas la galère...). Ils ont fait preuve de beaucoup d'ingéniosité pour résoudre les problèmes scientifiques auxquels ils étaient confrontés. Je leur souhaite pour la suite de belles réussites.

La cohésion de l'équipage fait, je le crois, la qualité du navire. J'aurais été difficilement plus heureuse qu'au laboratoire Gulliver, qui favorise la bienveillance et les échanges.

Merci à l'ensemble des permanents toujours prêts à poser ou à répondre à une question, quelle richesse pour mon travail! En particulier, merci à Michael Schindler qui a répondu à mes questions théoriques naïves avec une grande profondeur et rigueur, et Juliane Klamser pour son éclairage très pédagogique sur les transitions de phase 1D.

Merci aux "bons génies" du laboratoire, qui nous soutiennent constamment, et sans qui nous resterions en rade, Stéphanie Ledoux, pour sa gentillesse, Hyo-Jin Cho, pour sa bonne humeur, Fée Sorrentino pour son dynamisme. Merci à Aurélie Lloret, j'ai eu grand plaisir à maniper, et surtout à discuter avec toi; la prochaine fois que je passerai à Gulliver, c'est toi qui m'apprendras des trucs de microfluidique (je compte sur toi!).

Merci à tous les non-permanents, post-doc, doctorants, stagiaires, ingénieurs, anciens et nouveaux; travailler avec vous, c'était fun! Le monde des sciences est petit, j'espère tous vous recroiser souvent. Merci en particulier à Guillaume Durey, pour le projet lutétium ou les ballades dans Paris, j'ai hâte de voir quel projet fantastique tu nous réserves pour le futur. Un salut tout à fait spécial au bureau G308; de manière fortuite, le bureau des filles; Kunyun He, merci pour ton accueille quand je suis arrivée. Alice Billon, tu es formidable, je souhaiterais que beaucoup de gens aient ta sensibilité et ton intelligence du monde... Et ton gout pour les énigmes (#enigmedulundi). Martyna Goral, tu m'épates, j'admire ta volonté et ton ouverture intellectuelle (oui oui!), women's power! Mengshi Wei you have a great hearth, your "joie de vivre" is a wonderful strength (and also your cat). Et merci à tous les autres pour les chouettes moments passés ensemble, les Olympiades Gulliver, les sorties...

Mes amis, ma famille, empêchent le bateau de couler en lui offrant un port d'attache. Pour avoir été là pour moi, merci.

Merci à mes amis, Chau, Seth, Sophie, qui vous êtes accommodés de mon indisponibilité; et à mes amis de la danse Chantraine, que serais je devenue sans la danse?

Merci, enfin, à ma famille, sans en dire beaucoup, car il y en aurait trop à dire, merci de m'avoir toujours soutenue, dans mes choix, dans mes projets, aussi loufoques et farfelus qu'ils eussent pu vous sembler (des gouttes qui nagent? Non mais sans blague!).

Contents

General introduction

This manuscript is the result of my work as a PhD student in the Gulliver laboratory, at ESPCI Paris, under the supervision of Mathilde Reyssat and Olivier Dauchot. It is structured of two main parts, composed of respectively three and four chapters.

Part I, *Theoretical and experimental context*, presents the general, theoretical and experimental contexts. Its purposes are both to place our work in a broader history, and to provide the general tools used throughout this work.

Chapter (1), *Swimming, a biological and physical challenge*, gives an original introduction on swimming droplets by emphasizing how similar soft matter systems can get to living systems. In particular, the ability to self induce motion has most likely be critical in the early life development, and is the particularity of our swimming droplets system. Moving at micro-scales requires a different physics than the one we are used to, at our macroscopic scale. This is why, micro-swimmers have developed specific strategies to induce motion. A better understanding of these strategies is one of the motivation of the field of microswimmers.

Chapter (2), *General theory*, is a pedagogical introduction to the hydrodynamics of spherical micro-swimmers. It was intended to answer the fundamental questions of *what is swimming at microscales?* And *what might influence the swimming motion?* The potential answers to this second question - the geometry and confinement, other swimmers, and an external force - have been the starting point and the motivation of the present work.

Chapter (3), *Pure water swimming droplets*, presents the experimental model system that is being studied. Using microfluidic, we create, put into various environments and observe a model swimmer: a pure water swimming droplet in an outer oil-micelle solution. Past work on these pure water swimming droplets is presented, as well as the experimental tools that we use recurrently in the following chapters. We use this opportunity to provide details about our experimental methods, as well as several tips for successful experiments.

Part II, *Experimental and theoretical work*, presents my original work. We place our study in the framework of swimming in a realistic environment where external factors

- such as the presence of confinement, of other swimmers, or of an external force – may influence the swimming properties. In each chapter, we conduct experimental realizations to answer an existing question or to explore new problems, and we propose theoretical approaches in order to better capture the physics laying behind the observed phenomena. Each chapter can be read independently from the others.

In chapter (4), *Swimming in 2D*, we first study the effect of one or two walls on the swimming droplet. The presence of one wall breaks the natural axisymmetry of the flow field around the droplet. We investigate this effect using confocal PIV in three dimensions, and propose a simplified analytical formulation taking into account the presence of the wall; and the effect of buoyancy. This model is able to account for the far field hydrodynamics of the droplet close to a wall that differs from the one generated by a droplet far from walls. This chapter has been the object of a published article [1].

In chapter (5), *Swimming in 1D*, we look at more confined geometries using glass capillary microfluidics. The velocity of the droplet is observed to decrease with increasing confinement; but, surprisingly, it saturates at a non-zero value for droplets bigger than the channel height: even very long droplets swim. In more complex geometries, such as stretched capillaries, the droplet elongates while swimming; and, amazingly, may undergo successive spontaneous splitting events for high enough confinement. To understand these phenomena, we use a theoretical approach inspired from the Bretherton model[2] (for the study of long bubbles in tubes), including the effect of the activity of our droplet. A paper presenting the results and analysis of this chapter is in preparation.

In chapter (6), *Swimming together in 1D*, we investigate the collective dynamics of self-propelled droplets, confined in a one-dimensional microfluidic channel. The experimentally observed dynamics exhibits a rich phenomenology: neighbouring droplets align and form large trains of droplets moving in the same direction. A careful examination of the interactions between two "colliding" droplets demonstrates that alignment takes place as a result of the interplay between velocity fluctuations and the absence of Galilean invariance. Taking these observations as the basis for a minimalistic 1D model of active particles and combining analytical arguments and numerical evidence, we show that the system exhibits a transition to collective motion for a large range of values of the control parameters. A paper presenting these results will soon be submitted.

In chapter (7), *Ongoing work: swimming under gravity*, we present an ongoing work: the effect of gravity on the swimming. In 2D, by observing swimming droplets on an inclined plane, we show that gravity strongly orients the droplets motion, and that under strong gravity, the droplets velocity is more than the simple addition of the sedimentation and active velocity in the absence of gravity. Droplets confined in 1D capillaries exhibit a similar behaviour, but are also able to swim against gravity. Surprisingly, long droplets in 1D do not seem to feel gravity.

Writing this manuscript has proven to be extremely fulfilling as it pointed out missing

arguments in the understanding of the explored topics, and gave me the time to analyse in much more depth the physics behind the observed phenomena. I hope the reader will enjoy, as much as I did, the discovery of the amazing behaviour of these swimming droplets.

Part I

Theoretical and experimental context

Chapter 1

Swimming, a biological and physical challenge

1.1 From physico-chemistry to complex living-like behaviour

1.1.1 How to characterize life

One may simply be amazed in front of the diversity and complexity of life. Yet, and maybe even more bewildering, living systems all share common hallmarks [3]: compartmentalization, growth and division, information processing, energy transduction and adaptability (i.e. mobility).

The compartmentalization is the separation between the biological components (chemical milieu and reactions, genetic material...) and the environment. This separation has the double purpose of protecting the inside of the compartment against the environment, and spatially concentrate the biological components. For cells, this compartmentalization is achieved by a lipid bilayer membrane, semi permeable and functional to allow communication between the environment and the cell. Notably, this functionalization allows the cells to create chemical gradients, and to function out of equilibrium.

The growth and division are the fundamental ingredients of self-replication. It requires the ability to grow (taking in "food" from the environment), to deform its boundary, but also eventually to manage spatial organization. For living cells, it is achieved thanks to the complex dynamics of the cell cytoskeleton. Note that in the vision of a prebiotic system, in the absence of compartmentalization, this self replication process could be achieved by a collective autocatalytic sets, where an ensemble of molecules can reproduce each other [4, 5].

The information processing is the ability to generate, vehiculate, translate and store information, at the intracellular level as well as at the extracellular level. In cells it is achieved in multiple ways, including the genetic information processing

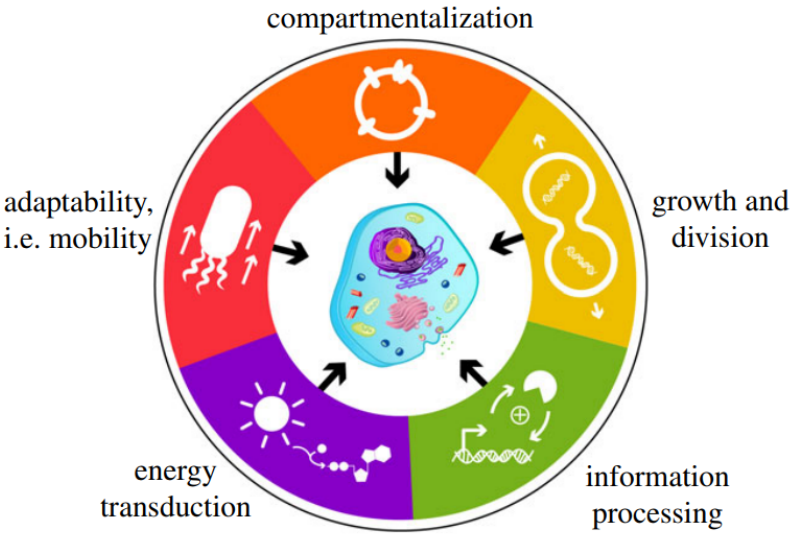

Figure 1.1: **Figure 1 from [3], the hallmarks of life:** a summary of the five characteristics required for systems to live and thrive. In the last decade, developments in bioanalogous and bio-mimetic bottom-up technologies have emulated aspects of each hallmark to inform us about the functional mechanisms behind each process, and about the opportunities to construct integrated artificial cell platforms.

(using DNA and RNA), the membrane activity management (using ions channel) and extracellular communication (using multi-scale signals from small molecules to vesicles). One of the keys for a complex information processing is the presence of a feedback system, which allows two ways communication (sending an information, receiving an answer, which triggers a reaction)

The energy transduction is the harnessing of the energy necessary for the system activity. The energy is taken from the external environment (light, chemical component...); thus the living system is out of equilibrium. The principal cellular energy currencies are ATP and NADH, and also FADH2 and GTP.

The adaptability is the capacity of the living system to adapt to the environment. It plays a crucial role in the competitiveness between different species (exploring environment, sensing the best food spot, protecting against threat). A simple form of adaptability is the motility. Cells developed several strategies in order to generate motion, such as the use of cilia or a bacterial flagellar rotor [6]. One of the stakes of motility is to go toward regions with "food", and thus motility is often combined with signal sensing.

All these characteristics of the living world can be found in simpler non-living chemical or physico-chemical systems [7], although not all together. This ascertainment motivated the scientific world to design proto-cells (physico-chemical systems that would mimic the early stage of life) or artificial cells (artificially made systems reproducing all above characteristics) using bottom-up strategies [8, 9, 10]: starting from a very simple system such as only a compartment (droplet - shell), or a chemical reaction (polymerization), and complexifying it progressively (adding physico-chemical compo-

nents, chemical reaction...), to obtain a system with multiple characteristics capable of mimicking life. For such a purpose, microfluidics [11] has demonstrated to be a very pertinent tool. It allows the highly controlled production and manipulation of fluid and microfluidics objects (droplet, shells...) with scales comparable to the one of the living world.

1.1.2 A droplet to mimic life

Droplets are particularly simple, yet very rich systems [7, 12]: they constitute an inner fluid separated from an outer fluid (environment) by an interface (compartmentalization), eventually stabilized by a surfactant (potential source of activity). Even if it is unlikely that the first lifeforms are derived directly from droplets (vesicles are more likely candidates [13]), all life-like characteristics can be mimicked using droplets:

1. A droplet is trivially compartmentalized.

2. Droplets may grow through droplet fusion (by Ostwald ripening or by externally triggered fusion [14], using geometry or an external field), but also through more "feeding-like" process [15], such as phase separation or the absorption of material from the environment. Both are possible if the final state of the system is energetically favorable (if the molecular interactions win against the entropy gain of mixing). Droplets division can also be externally driven, by geometry or by an external field [14], or comes from a spontaneous instability, that can be chemically driven [16, 17] (generally by the production of surfactant) or hydrodynamically driven [18]. To summarize schematically the spontaneous growth and division process, one can remember that the system {droplet+food} needs to be less stable than the system {grown droplet}, itself less stable than the system {two droplets}.

3. Information processing in droplets can be implemented by adding DNA and RNA molecules inside the droplet, but for more bottom-up perspectives, it can be achieved through complex chemical reactions, involving catalytic and autocatalytic loops, to get computing capacities [19].

4. The energy transduction comes with the implementation of activity in the droplet (growth, deformation division, motility, chemical reactions, etc). The activity exists for out of equilibrium systems. Thus throughout the activity cycles, there is a global loss in the system "energy". For the activity to continue, the system needs to be maintained out of equilibrium by an external input of energy (the "fuel"). The robust transduction of fuel (chemical component - light - heat ...) to activity is probably the most intuitive characteristic of life.

5. Motility might seem to require a very complex machinery, and indeed cells and micro-organisms have developed amazing mechanisms to propel themselves [20]. However, a simple isotropic droplet may also produce motion, through, for instance, an instability mechanism coupling its surface properties (self-induced non-isotropic surface tension) and hydrodynamics (Marangoni flow). This mechanism is also very sensible to the composition of the environment; sensing chemical gradients, it can lead to directed motion toward regions of high food concentration.

The present work focus on this last characteristic of life: the motility, at scales comparable to the ones of the living world.

1.2 Swimming at the microscale

As we go down in scale, the surface phenomena start to win over the volume phenomena. If at our macroscopic scale, we are dominated by inertia and gravity, it's a different story at the microscopic scale, where viscosity and interfacial forces play a much more important role. This has consequences, in particular in the choice of transport in the living world: microorganisms, including cells, need to develop strategies specific to their scale to produce motion. The understanding of such strategies is crucial at the fundamental level to apprehend the behaviour of biological micro-swimmers, but also to achieve artificial locomotion in a surrounding fluid at the micron-scale, in order to perform a multitude of tasks in technical and medical applications (transport, mixing, etc), which has become a central goal of nanosciences.

1.2.1 Scallop theorem

For micro-organisms, or objects of the micro-metric scale (a, the typical size of the object, is typically from 10 μm to 500 μm), the inertial effects are small compared to the viscous effects. This is quantified by the Reynolds number $\mathrm{Re} = \frac{\rho U a}{\eta}$, ρ is the density of the environment, U is the characteristic velocity of the outer flow, and η is the viscosity of the outer fluid. In the microscopic word (small a, generally small U, viscous fluid), $\mathrm{Re} \ll 1$. Then the equation that describes the hydrodynamics for an incompressible Newtonian fluid with uniform properties (ρ and η constant), in the absence of body force, is the Stokes equation (which comes from the simplification of the Navier–Stokes equation when $\mathrm{Re} \to 0$):

$$\rho \frac{\partial u}{\partial t} = -\nabla p + \eta \Delta \mathbf{u}, \tag{1.1}$$

$$\tag{1.2}$$

and the mass conservation, for an incompressible fluid:

$$\frac{\partial \rho}{\partial t} + \nabla \rho \cdot \mathbf{u} = 0. \tag{1.3}$$

$$\tag{1.4}$$

$\mathbf{u}$ being the flow field.

One property of the Stokes equation is that it has no time dependency (instantaneity). Note that the system may still have a time dependency through the boundary conditions. An immediate consequence is that this equation is invariant through time reversion. This affects the swimming of microorganisms [21]: no net motion can emerge from reciprocal motion (time reversible sequence motion). This property is called the scallop theorem (illustration in Fig. 1.2): a scallop swims by taking in water quickly, and then releasing it slowly. At the macroscale, thanks to inertia this cycle leads to net motion (the scallop advances a lot by taking in water, and moves back a little

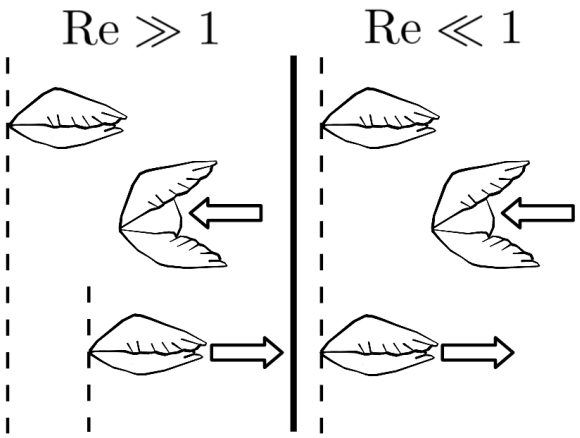

Figure 1.2: **Scallop theorem:** Simple illustration of the scallop theorem through the swimming cycle of a scallop at high Reynolds number (left), which leads to a net displacement, and at low Reynolds number (right), which leads to no net displacement.

when releasing it). At the microscale however, independently of the velocity of the two actions, they both lead to the same displacement, the cycle leads to no net motion.

Therefore, to produce motion at microscales, microorganisms developed non-reversible motion strategies.

1.2.2 Different strategies for different swimmers

One amazing point is the diversity of possible methods to go beyond the scallop theorem. A lot of them have been summarized in [20]. We can pinpoint a few categories of swimmers:

- Some use an external part, such as a flagella [22, 23], with non-reversible motion to mechanically act on the outer fluid. Examples include the rotation of bacteria's helical flagellar bundle [24], or the actuated motion of a sperm flagellum [25]. To mimic such complex and coordinated motion is possible, as illustrated, for instance, by magnetically-powered microswimmers [23, 26], but requires highly specific design of actuated multi-component systems. Two illustration of such swimmers are shown in Fig. 1.3(a) and (b).

- Some change their surface properties, mechanically, like for the synchronized beating of cilia on ciliated protozoa [27, 28], or chemically by inducing phoretic and/or Marangoni flows [29] at the swimmer interface. Two illustrations of such swimmers are shown in Fig. 1.3(c) and (d):

- Some use volume properties, for instance through jet like propulsion, by ejecting small bubbles of gas [30]. An example of such a swimmer is shown in Fig. 1.3(e):

The study of microswimmers, and the design of artificial swimmers is a very active field, at the interface of hydrodynamics, physico-chemical engineering and soft matter [35]. Several theoretical models have been developed in order to understand the swimming of the different swimmers. Among them the Purcell swimmer model [21], describing the swimming of a two arms swimmer by non time-reversible beating; the three-bead

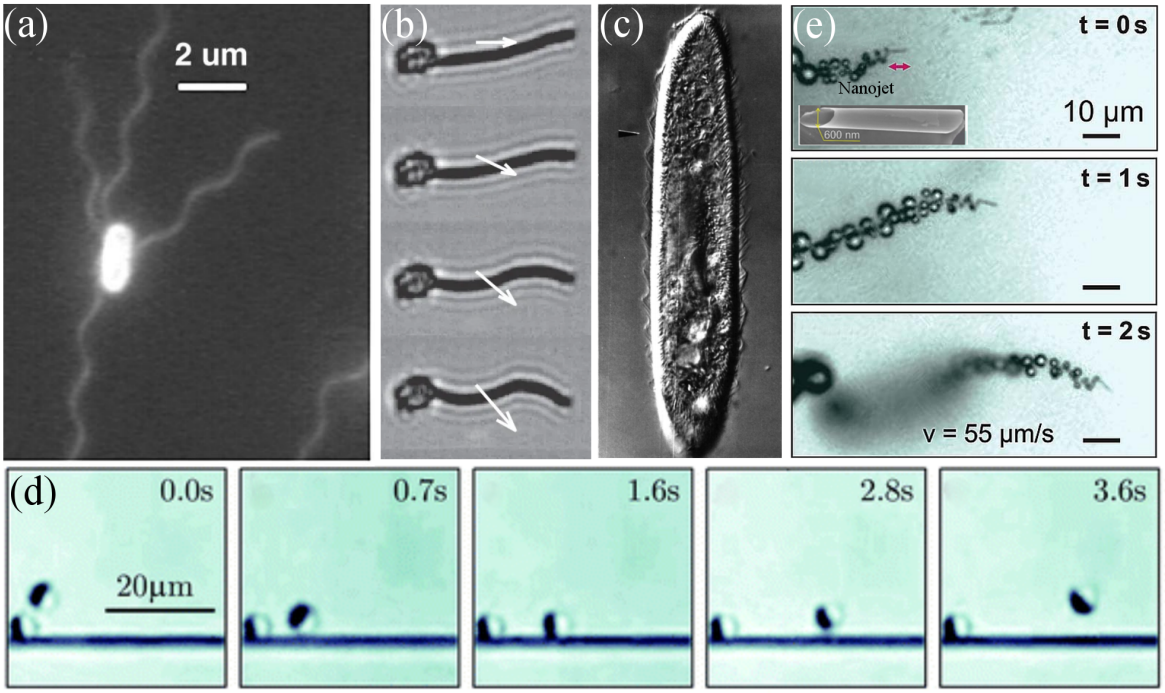

Figure 1.3: **Examples of biological and artificial microswimmers:** (a) Image from [31], imaging of Fluorescent Flagellar Filaments of E. Coli bacteria. (b) Image from [23], beating pattern of the motion of a magnetic flexible filament attached to a red blood cell. (c) Image from [32], imaging of a Paramecia while swimming. Cilia waves appear in profile views (arrowheads). (d) Image from [33], time series of snapshots demonstrating the approach, contact and detachment of a Janus particle at a wall. (e) Image from [34], catalytic nanojet engines: optical sequence of the motion of the nanojet engine (insert: SEM image of the smallest man-made jet engine consisting of 600 nm diameter and about 5 μm length)

swimmer [36], similar to the first one, but that swims by non time-reversible contraction of his arms; and the squirmer model [37, 38], describing the flow field around spherical swimmer imposing a slip velocity or a stress jump at their interface. The squirmer model, a thorough exposition and description of which is given in chapter (2), in section (2.2.1); will be largely used in the present work.

1.2.3 Confinement, external constrain, collective effects

The theoretical approach generally considers, at first, one swimmer alone in an infinite medium. However, be it in a biological environment or in a microfluidic device, there are many cases where the microswimmer evolves (1) close to boundaries [39], (2) in presence of other swimmers, and (3) even under other physical constrains, such as a force (gravity), or an external flow field.

1. Several observations reveal the critical importance of confinement on the swimmer's dynamics. Microswimmers are often attracted by the boundaries [40, 41, 42], which can then be used to capture [43, 33], or steer the swimmer motion [44, 45, 46]. The presence of a boundary has been observed to influence, not only the motion of a single particle [47, 48, 49], but also the collective behaviour

and phase transitions of swarms [50, 51, 52, 53]. Ultimately, the interactions with boundaries can be used to harvest energy from the population of swimmers [54].

2. Interactions between swimmers coupled to their motility may lead to some amazing collective effect [55]. Colonies of bacteria explore their environment by swarming [56], and polar order may emerge from these dense phases [57]. Dense active suspension of Escherichia coli bacteria are observed to exhibit convection patterns [58]. Active particles, such as light-activated colloidal surfers, assemble into living crystals [59]. Such complexity emerges from the various effects at play: the swimmers geometry (through steric interactions), the hydrodynamics (that affects the flow field far from the swimmer) or the physico-chemistry (as some chemically active swimmers leave a chemical trail behind them); and often these effects are coupled.

3. In the biological world, many microorganisms are observed to undergo gravitaxis [60, 61, 62, 63, 64] - a response in motility to a gravitational field. This behaviour fight against sedimentation, and its interest is most likely the possibility to explore a widest part of the environment. On another hand, under sedimentation, some swimming particles are observed to partially align, oriented against the gravitational field [65, 66, 67]. Such phenomena reflect the effect of gravity not only on the swimming, but also on the activity of the swimmer.

We place the current work in the framework of swimming in a realistic and complex environment, in the case where external factors - such as the presence of confinement, of an external force, or of other swimmers – may influence the swimming properties. In the following of this Part I, we present the basic theoretical tools necessary to understand the swimming of a spherical swimmer (chapter 2), and then we present the experimental model swimmer, that we use for all experiments: a pure water swimming droplet (chapter 3).

Chapter 2

General theory

Introduction

Context

In this chapter, we present the general theoretical framework of a spherical microswimmer and introduce the theoretical tools that we shall use in the following chapters.

What we call a microswimmer (or for simplicity a swimmer) in the following is an object able to **self-propel** at a **micrometric scale** in a surrounding fluid by **interacting with this surrounding fluid**:

- **The self-propulsion** implies that the swimmer is able to collect energy from its environment, and convert it into motion. This swimmer is out of equilibrium.
- **The micrometric scale** means that the hydrodynamics follows the Stokes equation (as introduced section (1.2)).
- **The interaction with the surrounding fluid** happens through the boundary conditions at the interface of the swimmer.

In this introduction, we define our notations and the mathematical tools that are used in the following. We present in section (2.1) the solution of the Stokes equation for an axisymmetric flow around a spherical object. We then introduce in section (2.2) the boundary conditions imposed by a swimmer. Finally, in section (2.3), we discuss the effects of breaking the axisymmetry of the system - by changing the boundary conditions, imposing an external force or adding boundaries such as walls.

Object of study and Notations

We consider two kinds of objects. (i) **A spherical solid particle** of radius a, undeformable, impermeable, and that absorbs all stresses. This particle goes at a velocity $\mathbf{U}$ in an external fluid of viscosity η, imposing a slip velocity at its interface v_s, and generating an outer flow $\mathbf{u}$. (ii) **A spherical droplet** of radius a, undeformable, impermeable, and that absorbs radial stress. This droplet, constituted of an inner

fluid of viscosity η_i goes at a velocity $\mathbf{U}$ in an outer fluid of viscosity η, imposing a slip velocity v_s and a tangential stress jump σ_s at its interface, and generating an inner flow $\mathbf{u}_i$ and an outer flow $\mathbf{u}$. Note that the solid particle i is simply a droplet ii in the limit $\eta_i \to \infty$. A priori, the direction of motion $\mathbf{e}_x$ - which is the direction of $\mathbf{U}$ - and the swimming direction $\mathbf{e}$ - which is the direction imposed by the boundary conditions - may not be the same (for instance, because of an external force, or the geometry). We introduce here some notations used throughout this manuscript. Note in particular that, per convention, experimentally measured velocities and flow fields are noted $\mathbf{V}$ and $\mathbf{v}$, while they are noted $\mathbf{U}$ and $\mathbf{u}$ in analytic expressions.

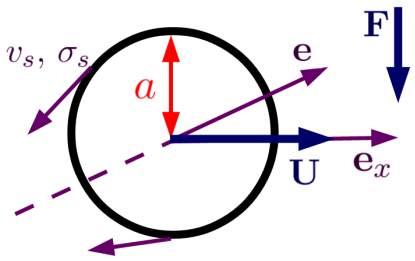

Figure 2.1: Notations: Object of study

Object of study:
a the droplet radius,
$\mathbf{U}$ or $\mathbf{V}$ the velocity of the object,
$\mathbf{e}_x$ the direction of motion,
$\mathbf{F}$ the external force,
v_s the slip velocity at the interface,
σ_s the stress jump at the interface,
$\mathbf{e}$ the swimming direction (direction imposed by the boundary conditions).

hydrodynamics:
$\mathbf{u}$ or $\mathbf{v}$ the flow field of the outer fluid,
η the viscosity of the outer fluid,
p the pressure in the outer fluid,
$\bar{\bar{\sigma}}$ the stress tensor in the outer fluid,
$\mathbf{u}_i$ the flow field of the inner fluid,
η_i the viscosity of the inner fluid,
p_i the pressure in the inner fluid,
$\bar{\bar{\sigma}}_i$ the stress tensor in the inner fluid,

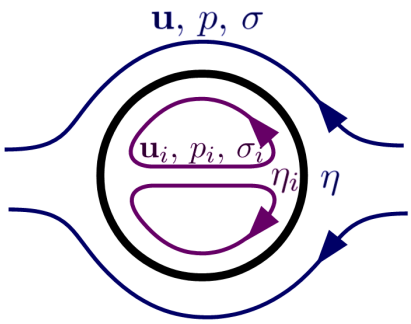

Figure 2.2: Notation - hydrodynamics

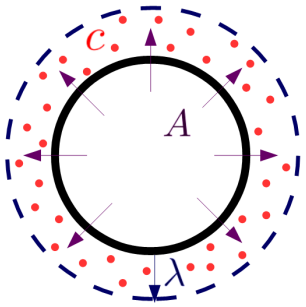

Figure 2.3: Notations: Physico-chemistry

Physico-chemistry:
c the concentration field of solute,
$\mathcal{V}$ the interaction potential between the solute and the interface,
λ the interfacial layer thickness,
A the activity,
K the phoretic constant,
M the Marangoni constant,
$\mathcal{M}$ the motility,
γ the surface tension of the interface,
Γ_c the surface excess of the solute.

Mathematical tools

Basis and coordinates

Depending on the considered geometry, we use different basis and coordinates.

The Cartesian basis ($\mathbf{e}_x$, $\mathbf{e}_y$, $\mathbf{e}_z$) and coordinates (x,y,z) - Fig. 2.4(a): $\mathbf{e}_x$ is defined as the direction of motion (the direction axis of the swimmer $\mathbf{e}$, imposed by the boundary conditions, might not be aligned with this direction of motion). In presence of a wall, if the direction of motion is parallel to the wall, we define $\mathbf{e}_z$ as the direction perpendicular to the wall, and h as the distance between the wall and the center of the droplet.

The spherical basis ($\mathbf{e}_r$, $\mathbf{e}_\theta$, $\mathbf{e}_\varphi$) and coordinates (r,θ,φ) - Fig. 2.4(b): it is the most natural coordinate system to describe an axisymmetric flow around a spherical object. r is the distance to the center of the object. θ is the angle with the direction of the swimmer $\mathbf{e}_x$. φ is the revolution angle. If the flow is axisymmetric, then nothing depends on φ. We also introduce the notation $\mu = \cos\theta$. We call the axisymmetric coordinates (r,μ).

The cylindrical basis ($\mathbf{e}_\rho$, $\mathbf{e}_{\hat{\theta}}$, $\mathbf{e}_z$) and coordinates (ρ,$\hat{\theta}$,z) - Fig. 2.4(c): The presence of a wall breaks the natural axisymmetry of a swimming spherical object. But it does not break the planar symmetry with regard to the plane $y = 0$ (the plane perpendicular to the wall, containing the direction of motion of the droplet). In the case of an object swimming parallel to a wall, it is natural to use the cylindrical coordinates to describe the flow field, where ρ and $\hat{\theta}$ are the polar coordinates in any observation plane parallel to the wall, and the origin of z is taken at the center of the object. We also introduce the notation $\nu = \cos\hat{\theta}$. We call the polar coordinates (ρ,$\hat{\theta}$).

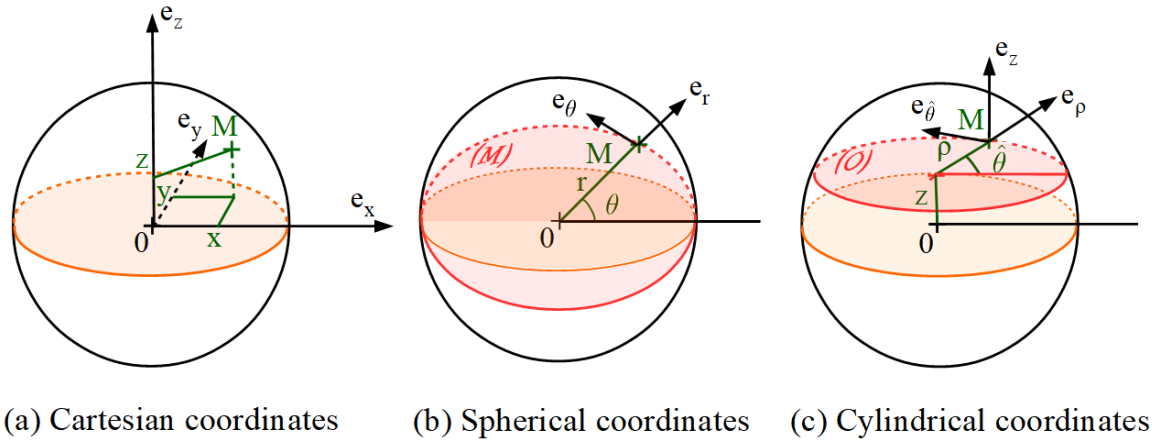

(a) Cartesian coordinates (b) Spherical coordinates (c) Cylindrical coordinates

Figure 2.4: **Basis and coordinates:** (a) Cartesian basis ($\mathbf{e}_x$, $\mathbf{e}_y$, $\mathbf{e}_z$) and coordinates (x,y,z). (b) Isotropic spherical basis ($\mathbf{e}_r$, $\mathbf{e}_\theta$) and coordinates (r,θ), the planes ($\mathcal{M}$) for which φ is a constant are called the median planes. (c) Cylindrical basis ($\mathbf{e}_\rho$, $\mathbf{e}_{\hat{\theta}}$, $\mathbf{e}_z$) and coordinates (ρ,$\hat{\theta}$,z), the planes ($\mathcal{O}$) for which z is a constant are called the observation planes.

Change of basis: Between the Cartesian basis and the spherical basis:

$$\mathbf{e}_r = \sin\varphi\cos\theta\mathbf{e}_x + \sin\varphi\sin\theta\mathbf{e}_y + \cos\varphi\mathbf{e}_z, \qquad x = r\cos\theta, \tag{2.1}$$
$$\mathbf{e}_\varphi = \cos\varphi\cos\theta\mathbf{e}_x + \cos\varphi\sin\theta\mathbf{e}_y - \sin\varphi\mathbf{e}_z, \qquad y = r\sin\theta\cos\varphi, \tag{2.2}$$
$$\mathbf{e}_\theta = -\sin\theta\mathbf{e}_x + \cos\theta\mathbf{e}_y, \qquad z = r\sin\theta\sin\varphi. \tag{2.3}$$

Between the Cartesian basis and the cylindrical basis:

$$\mathbf{e}_\rho = \cos\hat{\theta}\mathbf{e}_x + \sin\hat{\theta}\mathbf{e}_y, \qquad x = \rho\cos\hat{\theta}, \tag{2.4}$$
$$\mathbf{e}_{\hat{\theta}} = -\sin\hat{\theta}\mathbf{e}_x + \cos\hat{\theta}\mathbf{e}_y, \qquad y = \rho\sin\hat{\theta}. \tag{2.5}$$

Between the cylindrical basis and the spherical basis:

$$r\mathbf{e}_r = \rho\mathbf{e}_\rho + z\mathbf{e}_z, \qquad r^2 = \rho^2 + z^2, \tag{2.6}$$
$$\sin\theta\mathbf{e}_\theta = \sin\hat{\theta}\mathbf{e}_{\hat{\theta}} + \left(\frac{\rho}{r} - 1\right)\cos\hat{\theta}\mathbf{e}_r + \frac{\rho z}{r^2}\cos\hat{\theta}\mathbf{e}_z, \qquad r\cos\theta = \rho\cos\hat{\theta}. \tag{2.7}$$

Operators

Axisymmetric spherical coordinates:

$$\nabla^2 = (\frac{\partial^2}{\partial r^2} + \frac{(1-\mu^2)}{r^2}\frac{\partial^2}{\partial\mu^2}) \tag{2.8}$$

Useful relations:

$$\nabla\cdot(\nabla) = \Delta, \tag{2.9}$$
$$\nabla\cdot(\nabla\wedge) = 0, \tag{2.10}$$
$$\nabla\wedge(\nabla) = \mathbf{0}, \tag{2.11}$$
$$\nabla\wedge(\nabla\wedge) = \nabla(\nabla\cdot) - \Delta. \tag{2.12}$$

Legendre polynomials

The Legendre polynomials [68] $L_n(\mu) \equiv L_n^0(\mu)$ and the associated Legendre polynomials of m^{th} kind, $L_n^m(\mu)$ are families of orthogonal polynomials that form a basis of the **azimuthal symmetries**. They are respectively defined as:

$$L_n(\mu) = \frac{1}{2^n n!}\frac{d^n}{d\mu^n}((\mu^2-1)^n), \tag{2.13}$$
$$L_n^m(\mu) = (-1)^m(1-\mu^2)^{\frac{m}{2}}\frac{d^m}{d\mu^m}L_n(\mu). \tag{2.14}$$

They are solutions of the equations:

$$\frac{d}{d\mu}\Big((1-\mu^2)\frac{dL_n(\mu)}{d\mu}\Big)+n(n+1)L_n(\mu)=0, \tag{2.15}$$

$$\frac{d}{d\mu}\Big((1-\mu^2)\frac{dL_n^m(\mu)}{d\mu}\Big)+\Big(n(n+1)-\frac{m^2}{(1-\mu^2)}\Big)L_n^m(\mu)=0. \tag{2.16}$$

The Legendre polynomials of the same kind are orthogonal with each other:

$$\int_{-1}^{1} L_n^m(\mu)L_{n'}^m(\mu)d\mu=\frac{2(n+m)!}{(2n+1)(n-m)!}\delta_{n,n'}, \tag{2.17}$$

and in particular

$$\int_{-1}^{1} L_n^1(\mu)L_{n'}^1(\mu)d\mu=\frac{2n(n+1)}{(2n+1)}\delta_{n,n'}, \tag{2.18}$$

$$\int_{-1}^{1} L_n(\mu)L_{n'}(\mu)d\mu=\frac{2}{(2n+1)}\delta_{n,n'}. \tag{2.19}$$

We explicit a few useful Legendre polynomials, and associated Legendre polynomials of the first kind:

$$L_0(\mu)=1, \qquad L_0^1(\mu)=0, \tag{2.20}$$

$$L_1(\mu)=\mu, \qquad L_1^1=-\sqrt{1-\mu^2}, \tag{2.21}$$

$$L_2(\mu)=\frac{1}{2}(3\mu^2-1), \qquad L_2^1(\mu)=-3\mu\sqrt{1-\mu^2}. \tag{2.22}$$

The Legendre and associated Legendre polynomials are of great interest for the description of isotropic functions in space: all isotropic functions in space can be decomposed into the Legendre polynomials basis (or into any associated Legendre polynomial basis), $L_n(\mu=\cos\theta)$, θ being the angle with the direction of axisymmetry in the spherical coordinates. Similarly, all functions with a symmetry axis in a plane can be decomposed into the Legendre polynomials basis (or into any associated Legendre polynomial basis), $L_n(\nu=\cos\hat{\theta})$, $\hat{\theta}$ being the angle with the symmetry axis in the cylindrical coordinates.

2.1 Axisymmetric flow field around a spherical object

2.1.1 The problem studied

In this section we present the problem of an hydrodynamics flow field around an axisymmetric[i], undeformable[ii] spherical object, without external force applied on the fluid[iii], nor external flux[iv]. This object interacts with the external fluid through the boundary conditions at its interface.

i. The flow field around the object can be considered axisymmetric if such is the problem. This means that the object must have axisymmetric boundary conditions, whose direction $\mathbf{e}$ is aligned with all other directions of the problem (direction of an external force exerted on the object, symmetry of the geometry...). As a consequence, it is also aligned with the direction of motion $\mathbf{e}_x = \mathbf{e}$.

ii. The object is undeformable, if it remains spherical at all times. In that case, the radial velocity must be zero at the boundary $u_r(r = a) = 0$, and the radial stress is absorbed at the interface (free boundary condition for σ_{rr}).

iii. We consider that no external force is applied on the fluid (typically the gravity is neglected), Note that there can still be an external force applied on the object (for instance gravity, if the object does not have the same density as the outer fluid, but it could also be a magnetic force, if the object is magnetic, etc...). Even if, in this second case, the force is applied on the object, it can have an impact on the fluid through the boundary conditions.

iv. No external flow means that the flow field tends to zero far from the object $\mathbf{u}\ (\ r\ \rightarrow\ +\infty\ )\ \rightarrow\ 0$.

The object of study can be a solid spherical particle going at a velocity $U\mathbf{e}_x$, imposing an azimuthal isotropic slip velocity $v_s(r = 1, \mu)$ at its interface. The equations describing the steady motion of such a system are then the Stokes equation and the mass-conservation equation for the outer fluid, and the boundary conditions. In the lab frame:

$$\eta\Delta\mathbf{u} = \nabla p, \tag{2.23}$$
$$\nabla \cdot \mathbf{u} = 0, \tag{2.24}$$
$$\mathbf{u}(r = a) - \mathbf{U} = v_s\mathbf{e}_\theta. \tag{2.25}$$

The object of study can also be a spherical droplet, imposing an azimuthal velocity jump v_s and an azimuthal stress jump σ_s through its interface. The equations describing the steady motion of such a system are then the Stokes equation and the mass conservation equation for the outer fluid and for the inner fluid, and the boundary conditions. In the lab frame:

$$\eta\Delta\mathbf{u} = \nabla p, \tag{2.26}$$
$$\nabla \cdot \mathbf{u} = 0, \tag{2.27}$$
$$\eta\Delta\mathbf{u}^i = \nabla p^i, \tag{2.28}$$
$$\nabla \cdot \mathbf{u}^i = 0, \tag{2.29}$$
$$\mathbf{u}(r = a) - \mathbf{u}^i(r = a) = v_s\mathbf{e}_\theta, \tag{2.30}$$
$$\eta\frac{\partial u_\theta}{\partial r}\Big|_{r=a} - \eta^i\frac{\partial u^i_\theta}{\partial r}\Big|_{r=a} = \sigma_s. \tag{2.31}$$

Having supposed the interface of our object undeformable, the radial velocity is simply related to the object velocity,

$$u_r(r = a) = u^i_r(r = a) = U\mu. \tag{2.32}$$

Finally, in the steady regime, the sum of the forces applied on the object cancels. If the object feels an external force F (e.g. buoyancy), and if the outer fluid exerts a viscous force $F_{o\to i}$ on the object, then $F = -F_{o\to i}$. With $F_{i\to o} = \int_S \Big(-p\mu + \sigma_{rr}\mu - \sigma_{r\theta}\sqrt{1-\mu^2}\Big)_{r=a} dS$:

$$F = \int_S \Big(-p\mu + \sigma_{rr}\mu - \sigma_{r\theta}\sqrt{1-\mu^2}\Big)_{r=a} dS. \tag{2.33}$$

If there is no external force exerted on the object, then $\int_S \Big(-p\mu + \sigma_{rr}\mu - \sigma_{r\theta}\sqrt{1-\mu^2}\Big)_{r=a} dS = 0$.

In the following, we start by solving the stokes equation in spherical coordinates for an axisymmetric problem, then we apply the boundary conditions. In a second time, we present a few examples of characteristic flow fields under various conditions.

2.1.2 Solution to the Stokes equation in spherical coordinates for an axisymmetric problem

The inner and outer hydrodynamics flow fields are described by the Stokes and the mass-conservation equations:

$$\eta \Delta \mathbf{u} = \nabla p, \tag{2.34}$$
$$\nabla \cdot \mathbf{u} = 0. \tag{2.35}$$

For an axisymmetric flow, we use the spherical coordinates, (Fig. 2.4(b)): r, the distance from the center of the object, is made dimensionless using the object radius a; θ is the angle with the direction of axisymmetry, which is also the swimming direction $\mathbf{e} = \mathbf{e}_x$; and ϕ is the revolution angle on which nothing depends in the axisymmetric case. Finally, $u_\varphi = 0$ by symmetry. Then $\mathbf{u} = u_r(r,\mu)\mathbf{e}_r + u_\theta(r,\mu)\mathbf{e}_\theta$, where the dependence in $\mu = \cos\theta$ reflects the parity in θ included in the axisymmetric hypothesis. Physically, the flow field is the same in any plane containing the direction of axisymmetry $\mathbf{e}$, called median planes. For this axisymmetric flow field, we can define the stream-function ψ such that $\mathbf{u} = \nabla \wedge (\psi \mathbf{e})$; then $\mathbf{u}$ directly fulfills equation (2.35). In spherical coordinates:

$$u_r(r,\mu) = \frac{-1}{r^2}\frac{\partial \psi(r,\mu)}{\partial \mu}, \tag{2.36}$$
$$u_\theta(r,\mu) = \frac{1}{r\sqrt{1-\mu^2}}\frac{\partial \psi(r,\mu)}{\partial r}. \tag{2.37}$$

Physically, the stream-function describes the stream lines - the trajectory that would takes a tracer in the fluid - in a steady flow (more precisely, a stream-line corresponds to an iso-ψ). Mathematically, we use it to solve the Stokes equation in spherical coordinates, by injecting it in the Stokes equation (2.34). We get[1]:

$$\nabla^4 \psi(r,\mu) = 0, \tag{2.38}$$

[1] All operators and their useful properties are given in this chapter introduction, equations (2.8) to (2.12) in spherical coordinates.

with:

$$\nabla^4 = \Big(\frac{\partial^2}{\partial r^2} + \frac{1-\mu^2}{r^2}\frac{\partial^2}{\partial \mu^2}\Big)^2. \tag{2.39}$$

One can look for solutions of the particular form:

$$\psi(r,\mu) = \frac{1}{r^m}(1-\mu^2)L_n'(\mu), \tag{2.40}$$

using the Legendre polynomials $L_n(\mu)$. The Legendre polynomials[2] form a system of complete and orthogonal polynomials, which, when applied to $\mu = \cos\theta$, describe the planar azimuthal symmetries[3]. For instance, $L_0(\mu) = 1$ describes the monopolar symmetry (isotropic), $L_1(\mu) = \mu$ the dipolar symmetry, $L_2(\mu) = \frac{1}{2}(3\mu^2-1)$ the quadrupolar symmetry, and so on. Using the property that:

$$\frac{d}{d\mu}\Big((1-\mu^2)\frac{\partial L_n(\mu)}{\partial \mu}\Big) + n(n+1)L_n(\mu) = 0, \tag{2.41}$$

equation (2.38) gives:

$$\Big(m(m-1) - n(n+1)\Big)\Big((m-2)(m-3) - n(n+1)\Big) = 0, \tag{2.42}$$

the solutions of which are $m = n+3$, $m = n+1$, $m = -n+2$ or $m = -n$.

Using the fact that the Stokes equation is linear, we have the additivity property of its solutions, and its general solution [69] can be written as:

$$\psi(r,\theta) = \sum_{n=1}^{\infty} \frac{2n+1}{2n(n+1)}\Big(\frac{\alpha_n}{r^n} - \frac{\tilde{\alpha}_n}{r^{n-2}} + \beta_n r^{n+1} - \tilde{\beta}_n r^{n+3}\Big)(1-\mu^2)L_n'(\mu) \tag{2.43}$$

Where the coefficient α_n, $\tilde{\alpha}_n$, β_n, $\tilde{\beta}_n$ are defined as such by convention, and have the dimension of a velocity. Back to the velocity and pressure, using equations (2.36) and (2.37), one finds:

$$u_r(r,\mu) = \sum_{n=1}^{\infty} \frac{(2n+1)}{2}\Big(\frac{\alpha_n}{r^{n+2}} - \frac{\tilde{\alpha}_n}{r^n} + \beta_n r^{n-1} - \tilde{\beta}_n r^{n+1}\Big)L_n(\mu), \tag{2.44}$$

$$u_\theta(r,\mu) = \sum_{n=1}^{\infty} \frac{2n+1}{2n(n+1)}\Big(-\frac{n\alpha_n}{r^{n+2}} + \frac{(n-2)\tilde{\alpha}_n}{r^n} + (n+1)\beta_n r^{n-1} - (n+3)\tilde{\beta}_n r^{n+1}\Big)L_n^1(\mu), \tag{2.45}$$

$$p(r,\mu) = -\eta\sum_{n=1}^{\infty}(2n+1)\Big(\frac{(2n-1)}{(n+1)}\tilde{\alpha}_n\frac{1}{r^{n+1}} + \frac{(2n+3)}{n}\tilde{\beta}_n\Big)r^n L_n(\mu). \tag{2.46}$$

Where $L_n^1(\mu) = \sqrt{1-\mu^2}\frac{\partial L_n(\mu)}{\partial \mu}$ are called the associate Legendre polynomials of the first kind, and also form an orthogonal basis of the azimuthal symmetries, with different orientations.

[2]There is more information about the Legendre polynomials, the associated Legendre polynomials, and their useful properties in this chapter introduction, equations (2.13) to (2.22).

[3]Here the planes in question are the median planes that contain the direction of axisymmetry $\mathbf{e}$.

In summary: the general solution to the Stokes equation in spherical coordinates can be written as:

$$u_r(r,\mu) = \sum_{n=1}^{\infty} \phi_n^r(r) L_n(\mu), \tag{2.47}$$

$$u_\theta(r,\mu) = \sum_{n=1}^{\infty} \phi_n^\theta(r) L_n^1(\mu). \tag{2.48}$$

The radial dependence of the amplitude of the n$^{\text{th}}$ azimuthal symmetry of respectively the radial velocity and the tangential velocity - $\phi_n^r(r)$ and $\phi_n^\theta(r)$ - are given by projecting the flow field onto the n$^{\text{th}}$ Legendre and associated Legendre polynomials:

$$\phi_n^r(r) = \frac{2n+1}{2} \int_{-1}^{1} u_r(r,\mu) L_n(\mu) d\mu, \tag{2.49}$$

$$= \frac{2n+1}{2} \Big(\frac{\alpha_n}{r^{n+2}} - \frac{\tilde{\alpha}_n}{r^n} + \beta_n r^{n-1} - \tilde{\beta}_n r^{n+1} \Big), \tag{2.50}$$

$$\phi_n^\theta(r) = \frac{2n+1}{2n(n+1)} \int_{-1}^{1} u_\theta(r,\mu) L_n^1(\mu) d\mu, \tag{2.51}$$

$$= \frac{2n+1}{2n(n+1)} \Big(- \frac{n\alpha_n}{r^{n+2}} + \frac{(n-2)\tilde{\alpha}_n}{r^n} + (n+1)\beta_n r^{n-1} - (n+3)\tilde{\beta}_n r^{n+1} \Big). \tag{2.52}$$

Fig. 2.5 gives simple physical flow fields in the median plane of the object, to illustrate the symmetry of these flow fields.

2.1.3 Boundary conditions

A physical flow field cannot diverge, and has boundary conditions at the interface with the swimmer. In the lab frame the outer flow: $\mathbf{u} \underset{r\to+\infty}{\longrightarrow} 0$ (in the case of no external flux), and the inner flow: $\mathbf{u}^i \underset{r\to 0}{\longrightarrow}$ finite value. Then non diverging inner and outer flow fields can be re-written as:

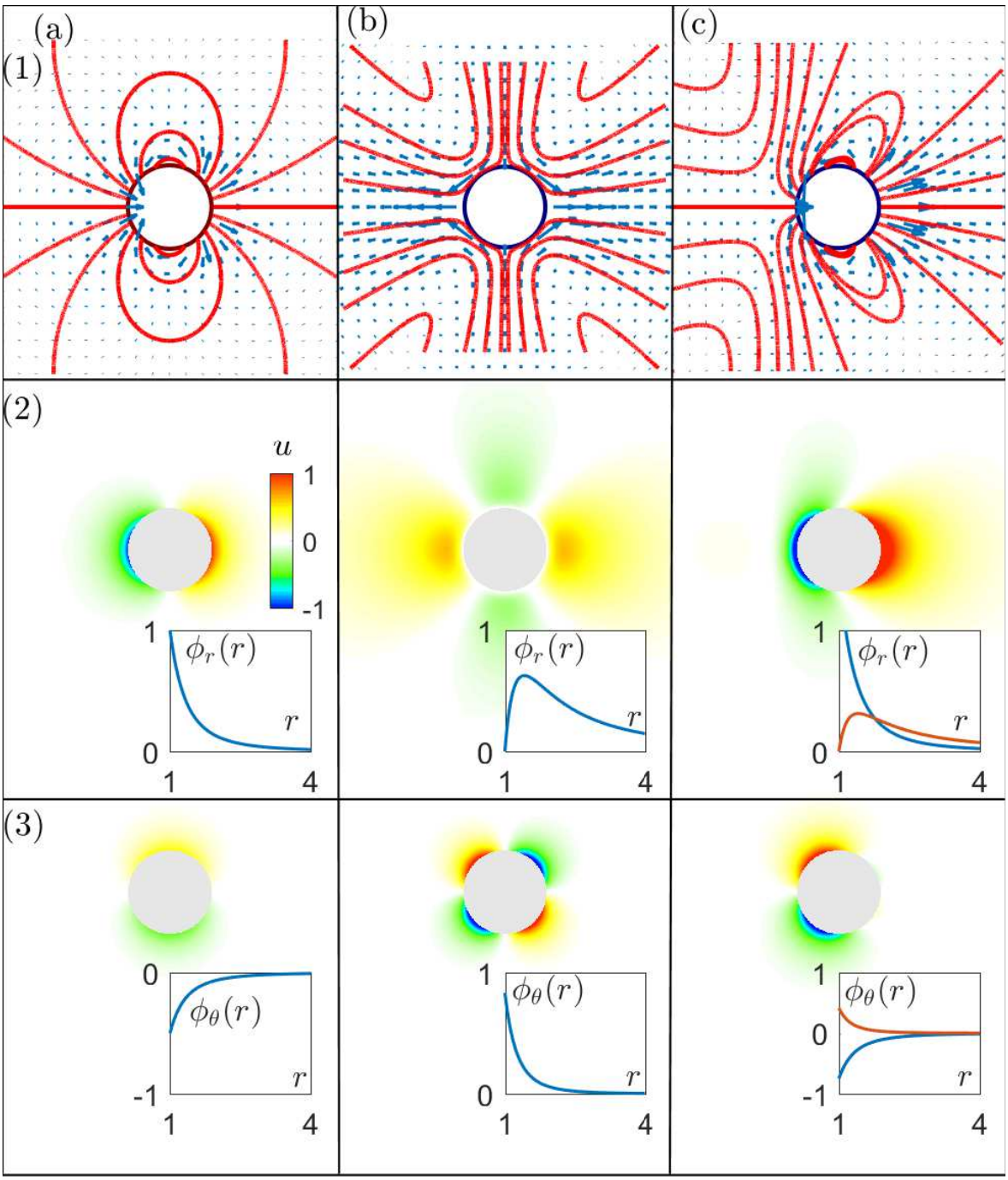

Figure 2.5: **Illustration of physical flow fields around a physical object:** (a) dipolar flow field with a coefficients $\alpha_1 = 1$ and $\tilde{\alpha}_1 = 0$ (no external forces). (b) Quadrupolar flow field with coefficients $\alpha_2 = \tilde{\alpha}_2 = -1$. (c) Flow field around a squirmer, composed of a hydrodynamics dipole with coefficients $\alpha_1 = 1$ and $\tilde{\alpha}_1 = 0$ and a hydrodynamics quadrupole, with coefficients $\alpha_2 = \tilde{\alpha}_2 = -0.5$ (pusher). Different visualizations of the flow field are given. (1) Vector field of the velocities around the object with the streamlines (red). (2) Mapping of the radial component of the velocity u_r, the color-scale being the amplitude. The insert corresponds to the evolution of the amplitude of u_r with r, $\phi_r(r)$. (3) Mapping of the azimuthal component of the velocity u_θ, the color-scale being the amplitude. The insert corresponds to the evolution of the amplitude of u_θ with r, $\phi_\theta(r)$.

$$u_r = \sum_{n=1}^{\infty} \frac{(2n+1)}{2}\Big(\frac{\alpha_n}{r^{n+2}} - \frac{\tilde{\alpha}_n}{r^n}\Big)L_n(\mu), \tag{2.53}$$

$$u_\theta = \sum_{n=1}^{\infty} \frac{2n+1}{2n(n+1)}\Big(-\frac{n\alpha_n}{r^{n+2}} + \frac{(n-2)\tilde{\alpha}_n}{r^n}\Big)L_n^1(\mu), \tag{2.54}$$

$$p = -\frac{\eta}{a}\sum_{n=1}^{\infty} \frac{(2n+1)(2n-1)}{(n+1)}\frac{\tilde{\alpha}_n}{r^{n+1}}L_n(\mu), \tag{2.55}$$

$$u_r^i = \sum_{n=1}^{\infty} \frac{(2n+1)}{2}\Big(\beta_n r^{n-1} - \tilde{\beta}_n r^{n+1}\Big)L_n(\mu), \tag{2.56}$$

$$u_\theta^i = \sum_{n=1}^{\infty} \frac{2n+1}{2n(n+1)}\Big((n+1)\beta_n r^{n-1} - (n+3)\tilde{\beta}_n r^{n+1}\Big)L_n^1(\mu), \tag{2.57}$$

$$p^i = \frac{\eta_i}{a}\sum_{n=1}^{\infty} \frac{(2n+1)(2n+3)}{n}\tilde{\beta}_n r^n L_n(\mu). \tag{2.58}$$

To close the problem of the Stokes equations, one finally needs the right set of boundary conditions, which are the relation of continuity through the interface between the inner and outer fluid, as presented above. We consider an undeformable, normal stress free and impermeable interface (there is no radial flow at the interface). At the interface, we consider that there is an azimuthal velocity jump, and in the case of a liquid-liquid interface, a stress jump.
For a solid particle:

$$u_r(r=1,\mu) = UL_1(\mu), \tag{2.59}$$

$$u_\theta(r=1,\mu) = UL_1^1(\mu) + v_s(\mu). \tag{2.60}$$

For a droplet:

$$u_r(r=1,\mu) = u_r^i(r=1,\mu) = UL_1(\mu), \tag{2.61}$$

$$u_\theta(r=1,\mu) - u_\theta^i(r=1,\mu) = v_s(\mu), \tag{2.62}$$

$$\sigma_{r\theta}(r=1,\mu) - \sigma_{r\theta}(r=1,\mu) = \sigma_s(\mu). \tag{2.63}$$

We also have to add the force balance - the force being aligned with the swimmer direction as we are looking at axisymmetric flow field, $\mathbf{F} = F\mathbf{e}$:

$$F = \int_S \Big(- p\mu + \sigma_{rr}\mu - \sigma_{r\theta}\sqrt{1-\mu^2}\Big)_{r=1} dS, \tag{2.64}$$

with in spherical coordinates:

$$\sigma_{rr}(r,\mu) = 2\frac{\eta}{a}\frac{\partial u_r}{\partial r}, \tag{2.65}$$

$$\sigma_{r\theta}(r,\mu) = \frac{\eta}{a}\Big(r\frac{\partial}{\partial r}(\frac{u_\theta}{r}) - \frac{\sqrt{1-\mu^2}}{r}\frac{\partial u_r}{\partial \mu}\Big). \tag{2.66}$$

If applied on the expression of the radial and orthoradial velocities of the outer (and inner) fluids (equation (2.53), (2.54) and (2.55)), we obtain:

$$\sigma_{rr}(r,\mu) = -\frac{\eta}{a}\sum_{n=1}^{\infty}(2n+1)\Big(\frac{(n+2)\alpha_n}{r^{n+3}} - \frac{n\tilde{\alpha}_n}{r^{n+1}}\Big)L_n(\mu), \tag{2.67}$$

$$\sigma^i_{rr}(r,\mu) = \frac{\eta_i}{a}\sum_{n=1}^{\infty}(2n+1)\Big(\beta_n(n-1)r^{n-2} - (n+1)\tilde{\beta}_n r^n\Big)L_n(\mu), \tag{2.68}$$

$$\sigma_{r\theta}(r,\mu) = \frac{\eta}{a}\sum_{n=1}^{\infty}(2n+1)\Big(\frac{(n+2)}{(n+1)}\frac{\alpha_n}{r^{n+3}} - \frac{(n-1)}{n}\frac{\tilde{\alpha}_n}{r^{n+1}}\Big)L^1_n(\mu), \tag{2.69}$$

$$\sigma^i_{r\theta}(r,\mu) = \frac{\eta_i}{a}\sum_{n=1}^{\infty}(2n+1)\Big(\frac{(n-1)}{n}\beta_n r^{n-2} - \frac{(n+2)}{n+1}\tilde{\beta}_n r^n\Big)L^1_n(\mu) \tag{2.70}$$

The integral over the surface of all Legendre and associated Legendre polynomials of order other than $n = 1$ is zero. Then after simplification, one finds for the force balance:

$$F = 6\pi\eta a\tilde{\alpha}_1. \tag{2.71}$$

From this equation, we find that the coefficient $\tilde{\alpha}_1$ is directly linked with the amplitude of the external force. If there is no external force, then $\tilde{\alpha}_1 = 0$.

2.1.4 Example of flow fields around spherical objects

In the following we decline various problems with different boundary conditions (active versus passive, solid particle versus droplet, external force versus no external force), to go toward presenting the most general case of an active droplet under an external force.

Projecting onto the Legendre and associated Legendre polynomials of the first kind physically consists in taking the n$^{\text{th}}$ moment over the surface of the object. We note this moment $\langle\cdot\rangle_n = \frac{1}{2}\int_{-1}^{1}\cdot L^1_n(\mu)d\mu$. It also corresponds to the projection onto the n$^{\text{th}}$ order symmetry of the flow. For the associated Legendre polynomial of order $n = 1$, it corresponds to the average over the surface $\langle\cdot\rangle$.

2.1.4.1 Passive particle under an external force

A passive particle has no slip velocity at its interface: $\mathbf{u}(\mathbf{r} = 1) = \mathbf{U}$. Projecting this boundary condition, one finds:

$$\alpha_1 - \tilde{\alpha}_1 = \frac{2}{3}U, \tag{2.72}$$

$$-\alpha_1 - \tilde{\alpha}_1 = \frac{4}{3}U, \tag{2.73}$$

and

$$\alpha_n = \tilde{\alpha}_n = 0. \tag{2.74}$$

The external force imposes $\tilde{\alpha}_1 = \frac{F}{6\pi\eta a}$. This leads to the relation:

$$U = -\frac{F}{6\pi\eta a}, \tag{2.75}$$

$$\alpha_1 = \frac{F}{18\pi\eta a}. \tag{2.76}$$

The force balance at the particle interface gives that $-F$ is simply the force exerted by the outer flow on the particle, also called the drag force: equation (2.75) is simply the usual expression of the drag force exerted on a particle moving at a certain velocity U. Equation (2.76) then tells us that the flow field created by such moving particle has a dipolar symmetry (α_1 and $\tilde{\alpha}_1$ are the coefficients of the dipolar symmetry of the flow field). The flow field around a passive particle dragged by an external force is given in Fig. 2.6(a).

2.1.4.2 Active solid particle in the absence of external force

We consider a solid spherical particle in the absence of external force ($\tilde{\alpha}_1 = 0$), then projecting the boundary conditions (2.59) and (2.60) on the Legendre and associated Legendre polynomials, using their orthogonal property, equations (2.18) and (2.19), we get:

$$\alpha_1 = \frac{2U}{3}, \tag{2.77}$$

$$\alpha_{n>1} - \tilde{\alpha}_{n>1} = 0, \tag{2.78}$$

$$-\alpha_1 = \frac{4}{3}U + 2\langle v_s \rangle, \tag{2.79}$$

$$-n\alpha_{n>1} + (n-2)\tilde{\alpha}_{n>1} = 2\langle v_s \rangle_{n>1}, \tag{2.80}$$

and obtain:

$$U = -\langle v_s \rangle, \tag{2.81}$$

$$\alpha_1 = -\frac{2}{3}\langle v_s \rangle, \tag{2.82}$$

$$\alpha_{n>1} = \tilde{\alpha}_{n>1} = -\langle v_s \rangle_{n>1}. \tag{2.83}$$

From these results, one can infer that the swimming ($U \neq 0$) exclusively comes from $\langle v_s \rangle$, which is the dipolar symmetry of the boundary condition at the interface. In other words, to produce a net motion, a solid particle must impose asymmetric boundary conditions between its "front" and its "back". Then higher order symmetries of these boundary conditions $\langle v_s \rangle_{n>1}$ produce a flow field of the same symmetry (the α_n and $\tilde{\alpha}_n$ coefficient are associated with the n^{th} order symmetries of the flow field), but it does not contribute to the net motion of the particle. An example of an active solid particle in the absence of external flow is given in Fig. 2.6(b).

2.1.4.3 Active droplet in the absence of external force: the Lamb formula

The exact same reasoning can be done for the droplet in the absence of external force by projecting the boundary conditions at the interface of the droplet (2.61), (2.62) and (2.63). One then finds relations between the coefficient α_n, $\tilde{\alpha}_n$, β_n and $\tilde{\beta}_n$, the moments of the slip velocity, $\langle v_s \rangle_n$ and of the stress jump, $\langle \sigma_s \rangle_n$, and the velocity of the droplet U. After simplification, one obtains:

$$U = \frac{a\langle \sigma_s \rangle - 3\eta_i \langle v_s \rangle}{2\eta + 3\eta_i}. \tag{2.84}$$

This equation is called the Lamb formula [70]. We have also:

$$\alpha_1 = \frac{2a\langle\sigma_s\rangle - 6\eta_i\langle v_s\rangle}{6\eta + 9\eta_i}, \tag{2.85}$$

$$\beta_1 = \frac{5a\langle\sigma_s\rangle + 6(\eta - \eta_i)\langle v_s\rangle}{6\eta + 9\eta_i}, \tag{2.86}$$

$$\tilde{\beta}_1 = \frac{a\langle\sigma_s\rangle + 2\eta\langle v_s\rangle}{2\eta + 3\eta_i}. \tag{2.87}$$

And for higher order symmetries:

$$\alpha_{n>1} = \tilde{\alpha}_{n>1} = \frac{a\langle\sigma_s\rangle_n - (2n+1)\eta_i\langle v_s\rangle_n}{(2n+1)(\eta + \eta_i)}, \tag{2.88}$$

$$\beta_{n>1} = \tilde{\beta}_{n>1} = \frac{a\langle\sigma_s\rangle_n + (2n+1)\eta\langle v_s\rangle_n}{(2n+1)(\eta + \eta_i)}. \tag{2.89}$$

Once again, we observe that the n^{th} symmetry of the boundary conditions ($\langle v_s\rangle_n$ and $\langle\sigma_s\rangle_n$) gives rise to a flow field of the same symmetry (α_n, $\tilde{\alpha}_n$, β_n and $\tilde{\beta}_n$ are the coefficient of the n^{th}-polar symmetry of the flow field). Only the dipolar symmetry of the boundary conditions gives rise to motion, through the Lamb formula.

2.1.4.4 Active solid particle aligned with an external force

Now we consider the case of an active solid particle aligned with an external force (this means that the direction of the swimmer imposed by the boundary conditions, $\mathbf{e}$ is aligned with the direction of the force). Projecting the boundary conditions (2.59) and (2.60) with an external force ($\tilde{\alpha}_1 \neq 0$), one finds:

$$U = -\langle v_s\rangle - \frac{F}{6\pi\eta a}, \tag{2.90}$$

$$\alpha_1 = \frac{F}{18\pi\eta a} - \frac{2}{3}\langle v_s\rangle. \tag{2.91}$$

We can note that the coefficients $\alpha_{n>1}$ and $\tilde{\alpha}_{n>1}$ are not modified by the presence of an external force, and that adding a $\tilde{\alpha}_1$ for the outer flow only changes the projection of the boundary conditions on the first order Legendre and associated Legendre polynomials. Equation (2.90) shows that the velocity of the solid particle comes from its activity, $\langle v_s\rangle$, and the external force F. For fixed boundary conditions (which is not necessarily the case, as will be discussed in section (2.2)), adding a force accelerates or slows down an active particle according to a simple additivity law of the velocities. One can compute the force F_a needed to stop the active particle, such that $U = 0$:

$$F_a = -6\pi\eta a\langle v_s\rangle. \tag{2.92}$$

In the following we call F_a, the active force, although it is not strictly speaking a force propelling an object, but it is the force needed to stop an active object. The amplitude of the dipolar symmetry of the flow field is also a contribution of both the activity and the external force. All higher symmetries of the flow field are not disturbed by the presence of the external force. Note that even tough the particle is immobile, there is still a flow field around the particle.

The effects of an external force on the flow field around an active solid particle are shown in Fig. 2.6(c), (d), (e) and (f) for different amplitudes of the external force.

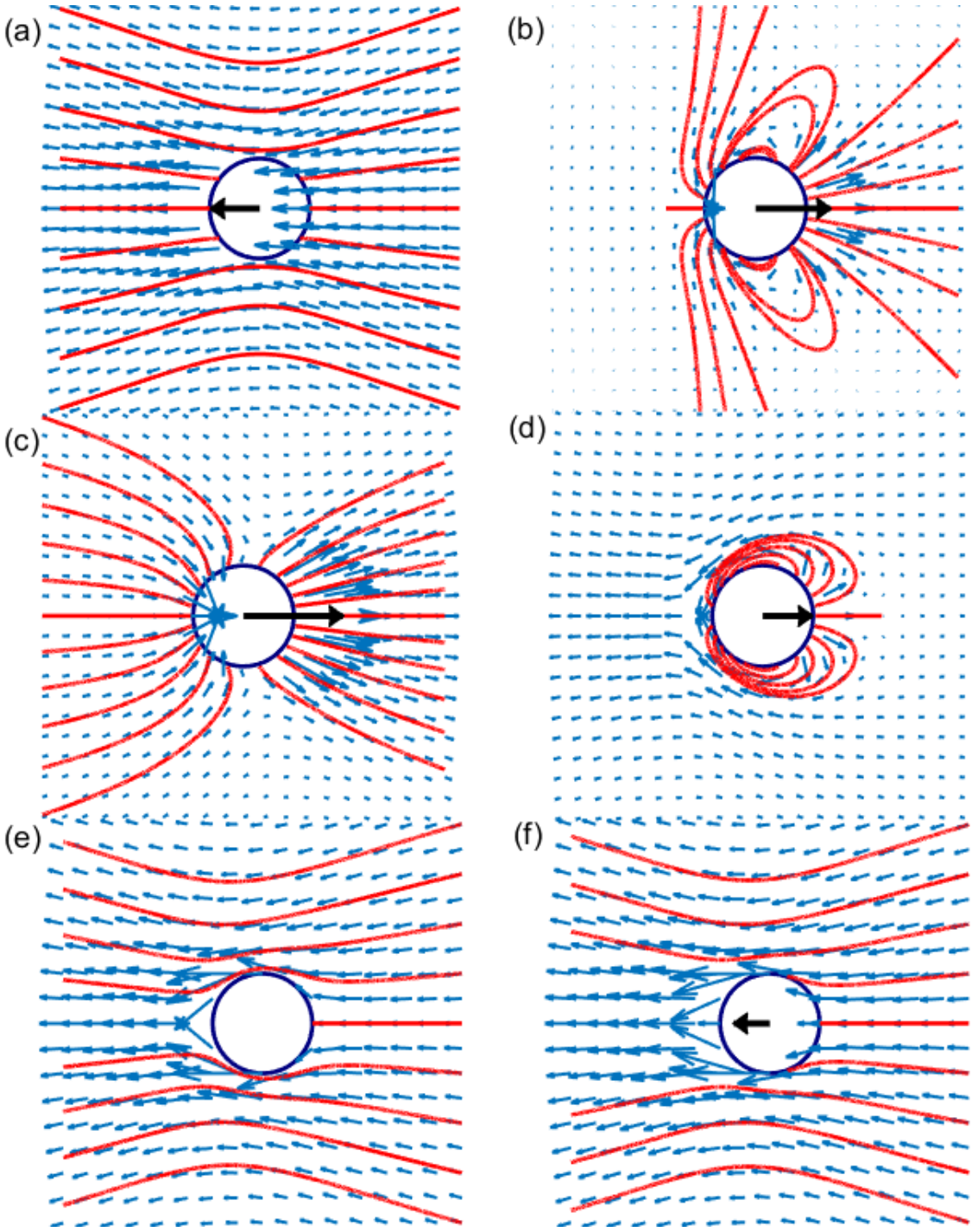

Figure 2.6: **Effect of an external force on the flow field:** (a) passive object under a force - $\langle\sigma_s\rangle = 0$ and $\tilde{\alpha_1} = 1$ (thus $\alpha_1 = \frac{1}{3}$, and $U = -1$). (b) Squirmer under no force - $\langle\sigma_s\rangle = -\frac{3}{2}$ and $\tilde{\alpha_1} = 0$ (thus $\alpha_1 = 1$, and $U = 1.5$). (c) Squirmer going in the same direction than an external force - $\langle\sigma_s\rangle = -\frac{3}{2}$ and $\tilde{\alpha_1} = -0.5$ (thus $\alpha_1 = \frac{5}{6}$, and $U = 2$). (d) Squirmer going in the opposite direction of an external force - $\langle\sigma_s\rangle = -\frac{3}{2}$ and $\tilde{\alpha_1} = 0.5$ (thus $\alpha_1 = \frac{7}{6}$, and $U = 1$). (e) Squirmer stopped by an external force - $\langle\sigma_s\rangle = -\frac{3}{2}$ and $\tilde{\alpha_1} = \frac{3}{2}$ (thus $\alpha_1 = \frac{3}{2}$, and $U = 0$). (f) Squirmer returned by an external force - $\langle\sigma_s\rangle = -\frac{3}{2}$ and $\tilde{\alpha_1} = 2$ (thus $\alpha_1 = \frac{5}{3}$, and $U = -0.5$). The velocity field is given by the blue arrows, the streamlines are in red and the velocity of the droplet is given by the black arrow.

2.1.4.5 Active droplet aligned with an external force

A similar reasoning can be done for the active droplet aligned with an external force. Projecting the boundary conditions (2.61), (2.62) and (2.63), one obtains:

$$U = \frac{a\langle\sigma_s\rangle - 3\eta_i\langle v_s\rangle}{2\eta + 3\eta_i} - \frac{F}{6\pi a}\frac{3(\eta+\eta_i)}{\eta(2\eta+3\eta_i)}, \tag{2.93}$$

$$\alpha_1 = \frac{2}{3}\frac{a\langle\sigma_s\rangle - 3\eta_i\langle v_s\rangle}{2\eta + 3\eta_i} - \frac{F}{6\pi a}\frac{\eta_i}{\eta(2\eta+3\eta_i)}, \tag{2.94}$$

$$\beta_1 = \frac{5a\langle\sigma_s\rangle + 6(\eta-\eta_i)\langle v_s\rangle}{2\eta + 3\eta_i} - \frac{F}{6\pi a}\frac{\eta+2\eta_i}{\eta(2\eta+3\eta_i)}, \tag{2.95}$$

$$\tilde{\beta}_1 = \frac{a\langle\sigma_s\rangle + 2\eta\langle v_s\rangle}{2\eta + 3\eta_i} + \frac{F}{6\pi a}\frac{1}{2\eta+3\eta_i}. \tag{2.96}$$

The velocity and all the hydrodynamics constants associated with the dipolar symmetries of the inner and outer flow fields have two parts, one that is due to the activity of the droplet, and the other that is due to the external force. These are the most general relations for an active droplet aligned with an external force; and all previous results can be derived from this one. One could also consider other problems such as a passive droplet driven by an external force by simply taking $v_s = 0$ and $\sigma_s = 0$. In the particular case where the inner fluid is less viscous than the outer fluid ($\eta_i \ll \eta$), we retrieve a well-known result $F = -4\pi\eta a U$ (for the rise of spherical bubble for instance). In the general case, the force that one needs to apply to stop the droplet is:

$$F_a = 2\pi\eta a \frac{a\langle\sigma_s\rangle - 3\eta_i\langle v_s\rangle}{\eta + \eta_i}. \tag{2.97}$$

2.1.5 Description of the flow field in term of singularities

A flow field can be reinterpreted in term of mathematical objects called singularities. Let's first consider the case of the point force singularity (a punctual force exerted on the fluid). The flow field around this point force $\mathbf{F} = F\mathbf{e}$ (usually called the Stokeslet) is described by the Stokes equation:

$$\eta\Delta\hat{\mathbf{u}} - \nabla p = -\mathbf{F}\delta_{r=0}, \tag{2.98}$$

$$\nabla\cdot\hat{\mathbf{u}} = 0. \tag{2.99}$$

Its solution in spherical coordinates is[4]:

$$\hat{\mathbf{u}} = \frac{F}{8\pi\eta a}\Big(\frac{\mathbf{e}}{r} + \frac{(\mathbf{e}\cdot\mathbf{e}_r)\mathbf{e}_r}{r}\Big). \tag{2.100}$$

In the following, and in order to alleviate later formalism, we define the flow field $\mathbf{u}^f$ produced by a point force, and make it dimensionless dividing $\hat{\mathbf{u}}$ by $-\frac{F}{6\pi\eta a}$:

$$u_r^f = -\frac{3}{2}\frac{1}{r}L_1(\mu), \qquad u_\theta^f = \frac{3}{4}\frac{1}{r}L_1^1(\mu). \tag{2.101}$$

One then notices that the flow field generated by this point force has the same azimuthal symmetry and radial amplitude than the one that is associated with the

[4]With r still being dimensionless

coefficient $\tilde{\alpha}_1$ for the flow field around a spherical object. Remember that this $\tilde{\alpha}_1$ is also directly linked to an external force applied on the object. Thus, the hydrodynamics flow field generated by a point force, and the flow field generated by a spherical object under an external force are the same, away from the object.

Because of the linearity of the Stokes equation, derivatives - taken in the axisymmetric direction[5] $\mathbf{e}$ - of this point force are also solutions to the Stokes equation. We define this way a family of solution called the Stokes singularities (force dipole, force quadrupole, and so on):

$$\mathbf{u}^{fn}(\mathbf{r}) = -\nabla \left[\mathbf{u}^{f(n-1)}(\mathbf{r})\right] \cdot \mathbf{e}. \tag{2.102}$$

Their associated dimensionless flow field is then:

$$u_r^{f,(n-1)} = -\frac{(2n+1)}{2}\frac{1}{r^n}L_n(\mu), \tag{2.103}$$

$$u_\theta^{f,(n-1)} = \frac{2n+1}{2n(n+1)}\frac{(n-2)}{r^n}L_n^1(\mu). \tag{2.104}$$

Example of these singularities and their associated flow fields are illustrated in Fig. 2.7(1). Note that the terms associated with the $\tilde{\alpha}_n$ coefficients of our problem create the same flow field as a (n-1)$^{\text{th}}$ order force singularity (force (n-1)$^{\text{th}}$-pole), with a radial dependency of $\frac{1}{r^n}$.

Similarly, we look at a point source singularity (a punctual source of fluid). The flow field around this point source Q is described by the Stokes equation:

$$\eta\Delta\mathbf{u} - \nabla p = 0, \tag{2.105}$$

$$\nabla \cdot \mathbf{u} = Q\delta_{r=0}. \tag{2.106}$$

Its solution in spherical coordinates is:

$$\hat{\mathbf{u}} = \frac{Q}{4\pi a^2}\frac{\mathbf{e}_r}{r^2}. \tag{2.107}$$

In the same way than before, we define the flow field $\mathbf{u}^s$ produced by a point source, and make it dimensionless dividing $\hat{\mathbf{u}}$ by $\frac{Q}{2\pi a^2}$:

$$u_r^s = \frac{1}{2r^2}, \qquad u_\theta^s = 0. \tag{2.108}$$

Note that the point source singularity corresponds to a creation of flux - which does not happen in our physical problem. This explain why there is no "point source" term in equations (2.53) and (2.54). Still, its derivative in the swimmer direction are also solutions to the Stokes equation. We define this way a family of solutions called the potential singularities (source dipole, source quadrupole, and so on):

$$\mathbf{u}^{sn}(\mathbf{r}) = -\nabla \left[\mathbf{u}^{s(n-1)}(\mathbf{r})\right] \cdot \mathbf{e}. \tag{2.109}$$

[5] Although the derivative of the point force taken in any direction are solutions, only the singularities obtained by derivation in the swimmer direction $\mathbf{e}$ produce an axisymmetric flow.

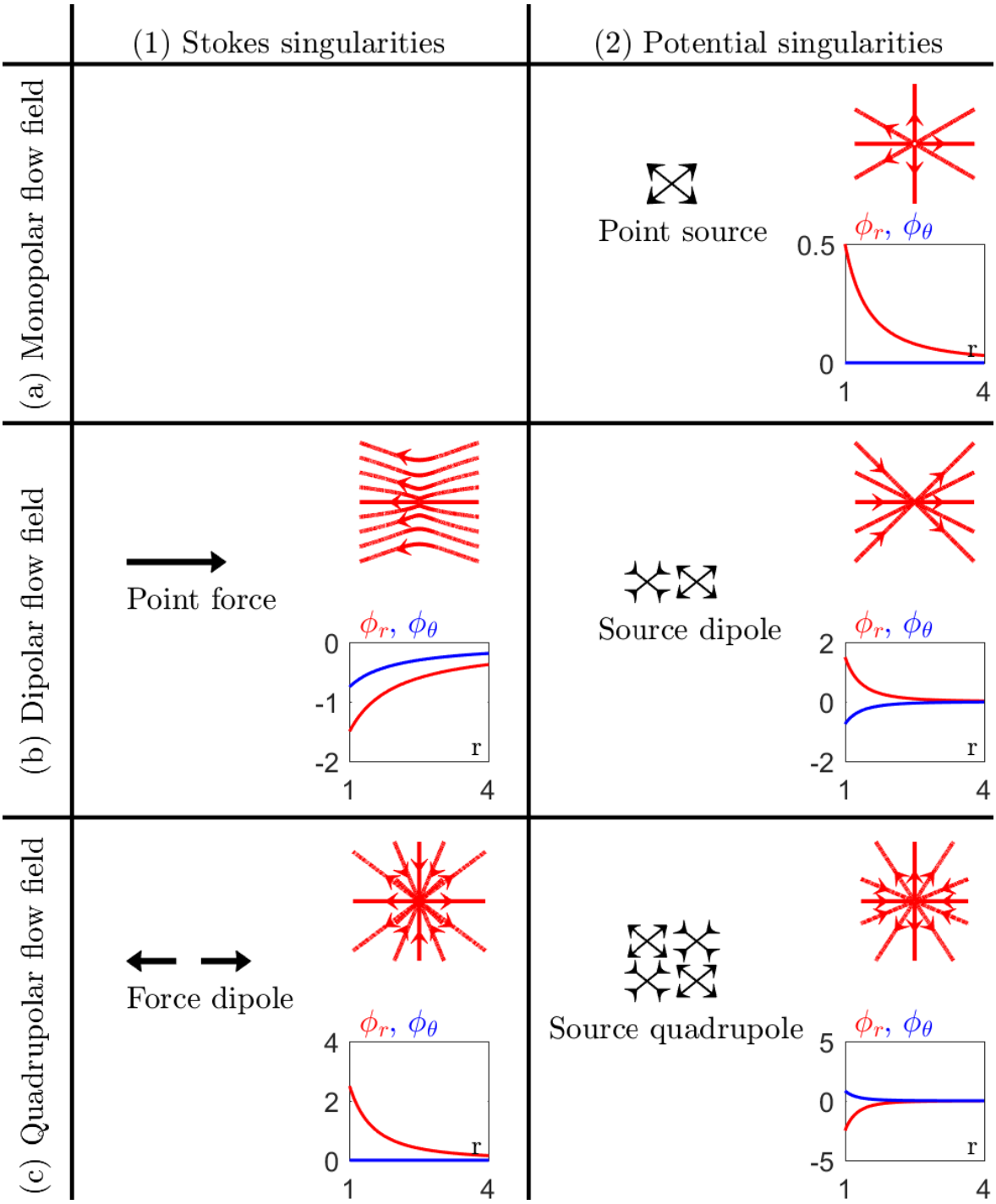

Figure 2.7: **Representation and flow field generated by a few singularities:** (1) Singularities from the family of the Stokes singularities, a point force that produces a flow field of dipolar symmetry (b), and a force dipole that produces a flow field of quadrupolar symmetry (c). No Stokes singularity produces a flow field of monopolar symmetry. (2) Singularities from the family of the potential singularities, a point source that produces a flow field of monopolar (isotropic) symmetry (a), a source dipole that produces a flow field of dipolar symmetry (b), and a source quadrupole that produces a flow field of quadrupolar symmetry (c). In insert are represented the streamlines (red), and the radial dependencies of the amplitudes of the singularities ϕ_r and ϕ_θ.

Their associated flow field is then:

$$u_r^{s,n} = \frac{(2n+1)}{2}\frac{1}{r^{n+2}}L_n(\mu), \tag{2.110}$$

$$u_\theta^{s,n} = -\frac{2n+1}{2n(n+1)}\frac{n}{r^{n+2}}L_n^1(\mu). \tag{2.111}$$

Example of these singularities and their associated flow fields are illustrated in Fig. 2.7(2). Note that the terms associated with the α_n of our problem create the same flow field as a n^{th} order source singularity (source n^{th}-pole), with a radial dependency of $\frac{1}{r^{n+2}}$.

Back to a physical object: The azimuthal symmetry and radial dependency of the force n^{th}-pole are the same than the one associated with the $\tilde{\alpha}_{n+1}$ coefficient of the flow field around a spherical object. Similarly, the azimuthal symmetry and radial dependency of the source n^{th} pole are the same than the one associated with the α_n coefficient of the flow field around a spherical object. Then, one can describe the flow field around a spherical object (equation (2.53) and (2.54)) in term of the dimensionless flow fields generated by singularities (remember that α_n and $\tilde{\alpha}_n$ have the dimension of a velocity, and that $u^{s,n}$ and $u^{f,n}$ are dimensionless):

$$\mathbf{u} = \sum_{n=1}^{\infty} \alpha_n \mathbf{u}^{s,n} + \tilde{\alpha}_n \mathbf{u}^{f,(n-1)} \tag{2.112}$$

2.2 Boundary conditions - how to make a swimmer?

Physical swimmers impose boundary conditions at their interface through various means such as physical actuation [38], local increases of temperature [71] or emission of a chemical [72]... It is then necessary to understand how these interactions with the outer fluid lead to a slip velocity or/and a stress jump, and thus to a net motion. In this section, we describe different strategies used by swimmers.

2.2.1 The squirmer model - Fixed boundary conditions

A first approach is to consider a swimmer that prescribes directly a fixed boundary condition (for instance through physical actuation). In this case, the slip velocity and the stress jump are **fixed** and not modified by an external force, nor the geometry, nor a chemical gradient... Typically, one fixes the slip velocity. This is the so-called squirmer model [37, 38].

Using the result of section (2.1.4.2), for an active solid particle moving in the absence of external force, the complete hydrodynamics flow field of a squirmer moving at velocity U is:

$$u_r = \frac{U}{r^3}L_1(\mu) + \sum_{n=2}^{\infty}\frac{(2n+1)}{2}\langle v_s\rangle_n\Big(-\frac{1}{r^{n+2}} + \frac{1}{r^n}\Big)L_n(\mu), \tag{2.113}$$

$$u_\theta = \frac{U}{2r^3}L_1^1(\mu) + \sum_{n=2}^{\infty}\frac{2n+1}{2n(n+1)}\langle v_s\rangle_n\Big(\frac{n}{r^{n+2}} - \frac{(n-2)}{r^n}\Big)L_n^1(\mu). \tag{2.114}$$

The most commonly used squirmer model consists in taking into account only the three first terms: the swimming term (source dipole ⇒ flow of dipolar symmetry), the term that decays the slowest at long range (force dipole ⇒ flow of quadrupolar symmetry), and the source term with the same symmetry (source quadrupole ⇒ flow of quadrupolar symmetry) to fulfill the impermeability condition:

$$u_r = \frac{U}{r^3}\mu + \frac{5}{2}\alpha_2\Big(\frac{1}{r^4} - \frac{1}{r^2}\Big)L_2(\mu), \tag{2.115}$$

$$u_\theta = -\frac{U}{2r^3}\sqrt{1-\mu^2} - \frac{5}{6}\frac{\alpha_2}{r^4}L_1^2(\mu). \tag{2.116}$$

This simplified squirmer model describes the swimming and the flow field generated at long distance. The flow field at long range has the symmetry of a quadrupole, which allows to infer the long range interacting behaviour of the swimmer depending on the sign of α_2. This is the so called pusher ($\alpha_2 < 0$) / puller ($\alpha_2 > 0$) behaviour. The Fig. 2.8 proceeds to a recap of these interactions: A pusher at long range (a) attracts fluid on its side and repels it on its back and front. This behaviour results in specific long range interactions (b): two pushers meeting face to face will repel each-other, while two pushers arriving side by side will attract each other. Hence the pushers tend to align with each others in raw. In the contrary, a puller at long range (c) attracts fluid on its front and back and repels it on its side and front. This behaviour results in specific long range interactions (d): two pullers meeting face to face will attract each other, while two pullers arriving side by side will repel each other. Hence the pullers tend to align with each-others in columns.

2.2.2 The phoretic particle - Slip velocity and stress jump

The Marangoni effect [73, 74] is the establishment of a flow at a fluid-fluid interface: a tangential gradient of "surface tension[6]" induces a stress jump across the interface. Similarly, the phoretic effect [29] is the establishment of a flow across a fluid-solid[7] interface: a tangential gradient of "a chemical species[8]" induces a slip velocity across the interface. These two effects have been shown to put into motion objects [77, 78] - in agreement with section (2.1.4.2) and (2.1.4.3) that states that an active particle can swim by imposing a slip velocity and/or a stress jump at its interface. One would then want to understand the microscopic phenomenon at the interface that produces these slip velocity and stress jump.

A realistic interface is a volume of a certain thickness λ, called the interfacial layer, where the inner and outer phase coexist and interact (the idea that an interface is diffuse, i.e. has a finite thickness, goes back to Poisson (1831) and Gibbs [79]). In this region, the normal and tangential velocities (u_r and u_θ) as well as the normal and tangential stresses (σ_r and σ_θ) are continuous, and affected by the interactions between the two phases. These interactions may be of various natures that have been developed in the paper by Anderson [29]. Among them, an electric field (the phenomenon is then called electrophoresis), the temperature (thermophoresis), a chemical compound

[6] the surface tension [75] is defined as the energy needed to increases the surface of an interface. It finds its origin in the interactions between the inner and outer fluid.

[7] Altough this effect is a priori also present for a fluid-fluid interface [76], it is generally dominated by the Marangoni effect, and thus is mainly considered for solid-liquid interfaces.

[8] More generally, a gradient of interaction between the inner and outer fluid along the interface.

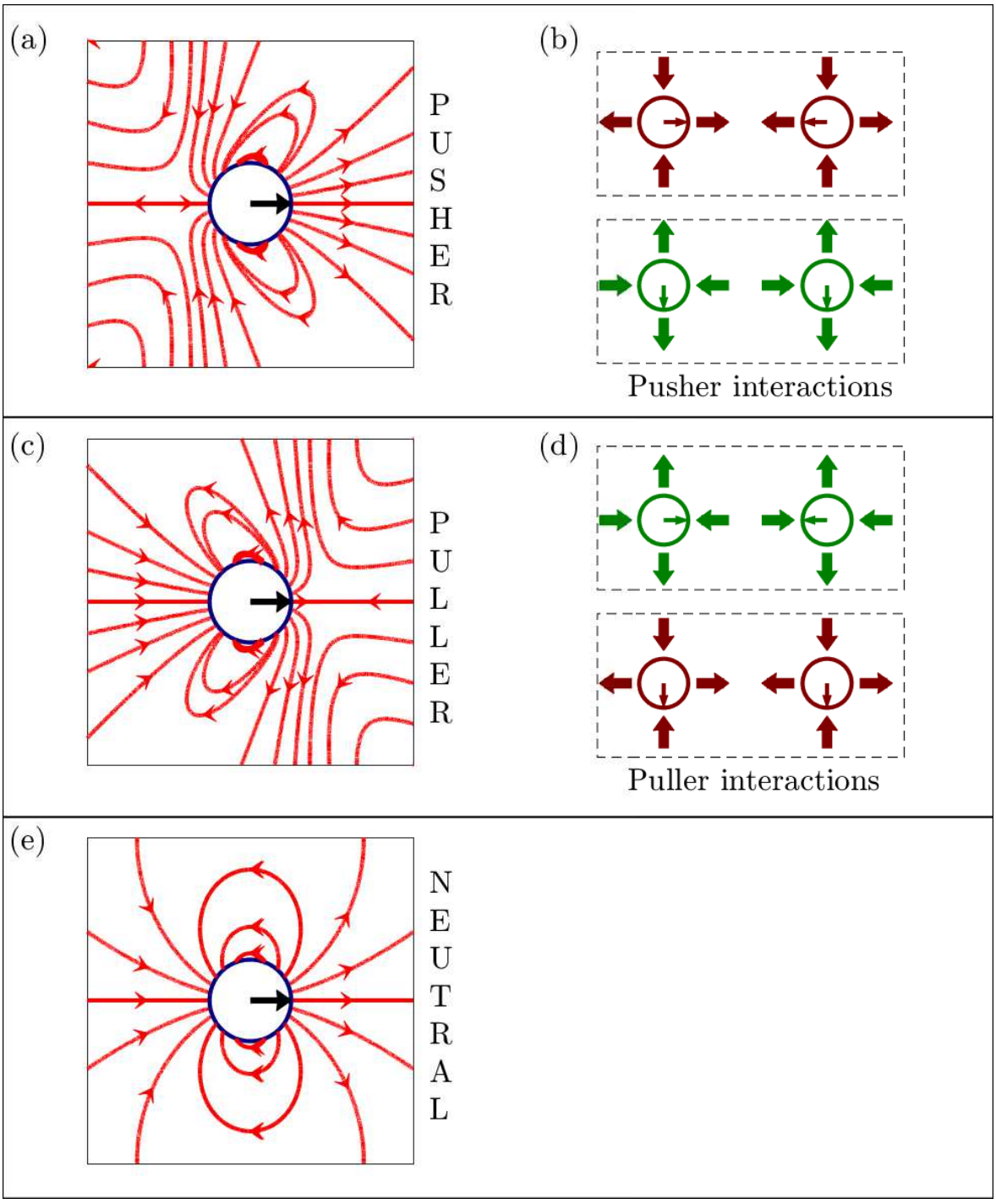

Figure 2.8: **Squirmers - flow fields and interactions:** (a,c,e) flow fields of squirmers that have the same dipolar contributions $\alpha_1 = 1$, without external force $\tilde{\alpha}_1 = 0$, but with different quadrupolar contributions. (a) Flow field generated by a pusher ($\alpha_2 = \tilde{\alpha}_2 = -0.5 < 0$), (c) flow fields generated by a puller ($\alpha_2 = \tilde{\alpha}_2 - 0.5 > 0$) and (e) flow field generated by a neutral squirmer ($\alpha_2 = \tilde{\alpha}_2 = 0$). (b,d) Corresponding long range interactions when two pushers (b) or two pullers (d) arrive face to face or side by side. The colors stand for the resulting interaction: green if the two squirmers attract each other and brown if they repel each other.

(diffusio-phoresis), the surfactant (Marangoni effect)... If the thickness of this interfacial layer is small compared to the object size ($\lambda \ll a$), it is possible to separate the scales of the problem: first solving the problem in the interfacial layer getting the velocity and stress profiles through the boundary, and second solving the problem at the object scale, considering a boundary of zero thickness through which there is a velocity and a stress jump. Here we look inside an interfacial layer at the microscopic origin of these slip velocity v_s and stress jump σ_s in the particular case that we are interested in - the presence of a chemical solute.

The interfacial layer:

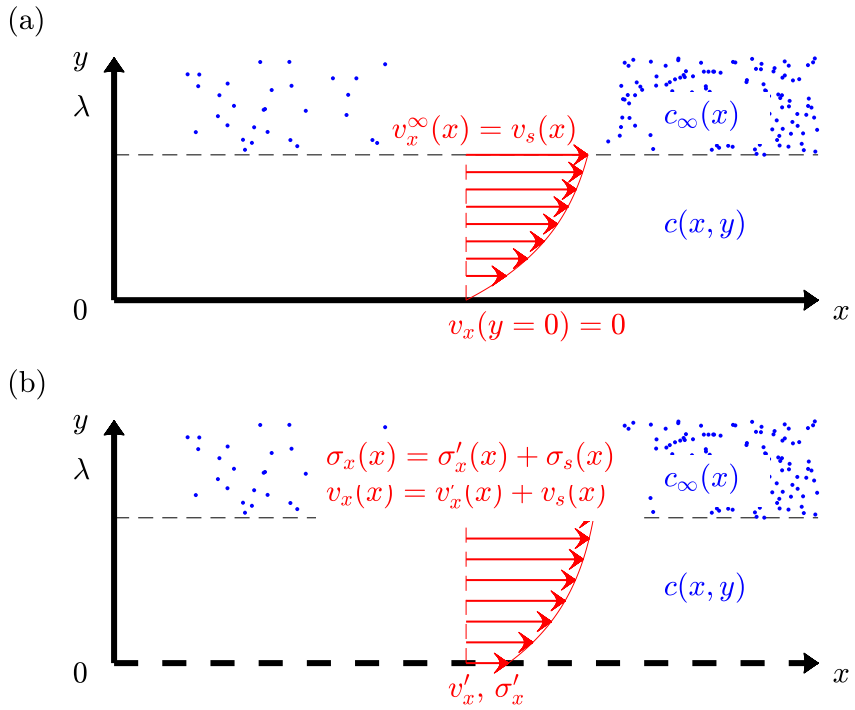

Figure 2.9: **Flow field induced by a concentration gradient in the interfacial layer:** (a) at the interface between a solid and a liquid and (b) at the interface between two liquids. The concentration gradient (in blue) induces a flow (in red), in the interfacial layer of typical thickness λ.

We consider an interfacial layer of thickness λ, where two non-miscible phases[9], the outer phase (viscosity η, velocity $\mathbf{u}$, pressure p) and the inner phase (viscosity η_i, velocity $\mathbf{u}^i$, pressure p^i) are separated by a virtual surface along the axis $\mathbf{e}_x$ and $\mathbf{e}_z$, at $y = 0$ (see Fig. 2.9). If $\mathbf{f}_{i\to o}$ is the force exerted by the interface on the outer phase, then the Stokes equation in the outer phase is:

$$\eta\Delta\mathbf{u} - \nabla p + \mathbf{f}_{i\to o} = \mathbf{0} \tag{2.117}$$

[9]Note that this is already a simplified vision of an interfacial layer which should be strictly speaking a region of continuous viscosity where all species coexist [80]. We use this simplified vision as we are only interested in the interaction of one solute in the outer phase with the inner phase, and this specie is considered to be the only one that induces gradients on the interface.

We are interested in the case of a force produced by a gradient of solute dissolved at a concentration $c(x,y)$, interacting with the interface with a potential $\mathcal{V}(y)$ that depends only on the distance from the interface. $\mathcal{V}(y)$ tends to zero at the outer edge of the interfacial region. In this configuration, the interface exerts a force $\mathbf{f}_{i\to o} = -c(x,y)\frac{d\mathcal{V}(y)}{dy}\mathbf{e}_y$ on the external fluid. Furthermore, the geometry of the problem allows to consider a laminar flow $\mathbf{u} = u_x(x,y)\mathbf{e}_x$ parallel to the interface. The Stokes equation (2.34) re-writes as:

$$\eta\frac{\partial^2 u_x(x,y)}{\partial y^2} - \frac{\partial p(x,y)}{\partial x} = 0, \tag{2.118}$$

$$\frac{\partial p(x,y)}{\partial y} + c(x,y)\frac{d\mathcal{V}(y)}{dy} = 0. \tag{2.119}$$

Through a realistic interface between two phases, the velocity and stress are continuous. Here we consider either an undeformable liquid-liquid interface (absorption of the normal stress) either an undeformable and no slip solid-liquid interface (absorption of the normal and tangential stresses). The boundary conditions at an undeformable liquid-liquid interface are then:

$$u_x(y=0) = u_x^i(y=0), \tag{2.120}$$

$$\eta\Big(\frac{\partial u_x}{\partial y}\Big)_{y=0} = \eta_i\Big(\frac{\partial u_x^i}{\partial y}\Big)_{y=0}. \tag{2.121}$$

For the particular case of a solid-liquid interface ($\eta_i \to +\infty$), only the first one (2.120) is considered.

At the outer edge of the interfacial region, we impose a solute concentration $c_\infty(x)$. The "infinity" is then a few times the typical decaying distance of $\mathcal{V}$. Assuming local equilibrium, we consider that the concentration follows the Boltzmann distribution: $c = c_\infty(x)\exp^{-\frac{\mathcal{V}(y)}{kT}}$. Then, integrating over y equation (2.119), we get the pressure field:

$$p(x,y) - p_\infty = kTc_\infty(x)(1 - \exp^{-\frac{\mathcal{V}(y)}{kT}}). \tag{2.122}$$

After one integration, the equation (2.118) gives the stress σ_∞, and after two integrations, the velocity u_∞:

$$\sigma_\infty = \eta\frac{\partial v_x}{\partial y}\Big|_\infty = \sigma(y=0) + kT\frac{dc_\infty}{dx}\int_0^\infty (1 - \exp^{-\frac{\mathcal{V}(y)}{kT}})dy, \tag{2.123}$$

$$u_\infty = u_x(y=0) - \frac{kT}{\eta}\frac{dc_\infty}{dx}\int_0^\infty y(1 - \exp^{-\frac{\mathcal{V}(y)}{kT}})dy. \tag{2.124}$$

Finally, we define the slip velocity as the difference between the velocity of the inner phase at the interface, and the velocity of the outer phase at the outer edge of the interfacial layer, and respectively for the stress jump (Fig. 2.9(b)):

$$\sigma_s = -\mathrm{K}\frac{dc_\infty}{dx}; \qquad \mathrm{K} = kT\int_0^\infty (\exp^{-\frac{\mathcal{V}(y)}{kT}} - 1)dy, \tag{2.125}$$

$$v_s = \mathrm{M}\frac{dc_\infty}{dx}; \qquad \mathrm{M} = \frac{kT}{\eta}\int_0^\infty y(\exp^{-\frac{\mathcal{V}(y)}{kT}} - 1)dy. \tag{2.126}$$

Where K is called the Marangoni coefficient, and M is called the phoretic coefficient. In the case of a solid interface, we simply have a zero-velocity condition at the wall, and thus a slip velocity at λ (Fig. 2.9(a)):

$$v_s = \mathrm{M}\frac{dc_\infty}{dx}. \tag{2.127}$$

The important point to notice is that both σ_s and v_s are proportional to the concentration gradient $\frac{dc_\infty}{dx}$.

M and K depend on $\mathcal{V}$:

- If $\mathcal{V} < 0$, then $c(x, y = 0) > c_\infty$: the solute accumulates at the interface: it corresponds to an attractive interaction between the solute and the interface. Then $(\exp^{-\frac{\mathcal{V}(y)}{kT}} - 1) > 0$: K and M are positive. The flow induced by the concentration gradient goes toward high concentration area.
- If $\mathcal{V} > 0$, then $c(x, y = 0) < c_\infty$: the solute depletes at the interface: it corresponds to a repulsive interaction between the solute and the interface. Then $(\exp^{-\frac{\mathcal{V}(y)}{kT}} - 1) < 0$: K and M are negative. The flow induced by the concentration gradient goes toward low concentration area.

For instance, if $\mathcal{V}$ is a Heaviside step function that is equal to $\mathcal{V}_0$ up to a distance λ from the interface, and is zero after, then

$$\mathrm{K} = \epsilon kT\lambda, \tag{2.128}$$

$$\mathrm{M} = \epsilon\frac{kT\lambda^2}{2\eta}, \tag{2.129}$$

where $\epsilon = (\exp^{-\frac{\mathcal{V}_0}{kT}} - 1)$ is a constant representing the interaction sign and strength, and would be equal to -1 for a repulsive hard sphere steric interaction ($\mathcal{V}_0 \to +\infty$).

Now, how does this relate to the surface tension? The surface tension is defined as the energy that costs the interfacial layer per unit surface. With the Gibbs adsorption equation, the interfacial tension γ is defined as:

$$d\gamma = -\Gamma_c da_c = -\Gamma_c kT\frac{dc_\infty}{c_\infty}, \tag{2.130}$$

where $a_c = kT\ln c$ is the activity of the solute, and Γ_c is the surface excess of the solute defined as the difference between the actual solute concentration in the interface and the solute concentration if there was no interface [81]: $\Gamma_c = c_\infty\int_0^\infty(\exp^{-\frac{\mathcal{V}(y)}{kT}} - 1)dy$. Then:

$$\frac{d\gamma}{dx} = -\frac{dc_\infty}{dx}kT\int_0^\infty(\exp^{-\frac{\mathcal{V}(y)}{kT}} - 1)dy.$$

Leading for an expression of the stress jump: $\sigma_s = -\frac{d\gamma}{dx}$, or more generally $\sigma_s = -\nabla_\parallel\gamma$ which is the expression generally used for the relation of continuity of the tangential stress at an interface when γ varies along this interface (Marangoni effect).

Motion of a solid particle in a concentration gradient:
Back to the object scale, we can use the expression of the slip velocity and the stress jump at the interface, equations (2.126) and (2.125) injected in the Lamb equation (2.84), to get the expression of the droplet's velocity that rises from such velocity slip and stress jump. The velocity of the droplet can then be expressed as a function of the concentration gradient:

$$U = -\frac{aK + 3\eta_i M}{2\eta + 3\eta_i}\langle \nabla_{\parallel} c \rangle, \tag{2.131}$$

and we can define the motility:

$$\mathcal{M} = \frac{aK + 3\eta_i M}{2\eta + 3\eta_i} = \epsilon k T \lambda \frac{a + 3\lambda\frac{\eta_i}{\eta}}{4\eta + 6\eta_i} \tag{2.132}$$

such that

$$U = -\mathcal{M}\langle \nabla_{\parallel} c \rangle. \tag{2.133}$$

For a simple step function potential (equations (2.128) and (2.129)), M and K have the same sign, that depends directly on the sign of the interactive potential:

- If the solute is attracted by the interface ($\mathcal{V}_0 < 0$), then $\mathcal{M}$ is positive. The velocity of the droplet U goes against the gradient of c: the droplet swims toward low concentration area.
- If the solute is repelled by the interface ($\mathcal{V}_0 > 0$), then $\mathcal{M}$ is negative. The velocity of the droplet U goes with the gradient of c: the droplet swims toward high concentration area.

Equation (2.131) highlights that the velocity of a droplet indeed results from both the Marangoni effect (stress jump τ_s), and the phoretic effect (slip velocity v_s). However, as usually the size of the interfacial layer is very small compared to the droplet size ($\lambda \ll a$), and when the viscosity of the inner fluid is not too high compared to the viscosity of the outer fluid, then the phoretic contribution is small compared to the Marangoni effect contribution. Still, the two effects rise from the *same* microscopic phenomena: the gradient of concentration of a solute that interacts with the interface. Then the case of a droplet moving in a concentration gradient, and the case of a solid particle moving in a concentration gradient are conceptually the same: the induced velocity is proportional to the average of the azimuthal gradient of concentration $\langle \nabla_{\parallel} c \rangle$, the only difference being the value of the motility $\mathcal{M}$.

2.2.3 The autophoretic particle - how to self-induce a concentration gradient

Section (2.2.2) shows that a gradient of concentration induces a slip velocity and a stress jump at an interface, and that the dipolar symmetry of this concentration gradient generates a net motion for a spherical particle (or spherical droplet). More generally, swimming requires a breaking of symmetry either of activity (asymmetric production of solute), or motility (asymmetric interaction with the solute) [82], or a spontaneous

breaking of symmetry [83]. The first two cases arise from an asymmetry in the surface property of the particle (geometrical breaking of symmetry, section (2.2.3.1)), which can be achieved by the design of the swimmer. The third case comes from an instability in the problem (spontaneous breaking of symmetry, section (2.2.3.2)).

In the case of the diffusio-phoretic particle, the solute concentration field around the particle depends on the rate at which it is produced at the interface (called activity, A, with dimension $[L]^{-2}[T]^{-1}$), its advection by the outer flow (through the motility, $\mathcal{M}$, with dimension $[L]^{5}[T]^{-1}$), and its diffusion (with a diffusion coefficient, D, with dimension $[L]^{2}[T]^{-1}$). We can now define a characteristic velocity $U^* = \frac{A\mathcal{M}}{D}$ with the parameters of the problem, and the Peclet number $\mathrm{Pe} = \frac{U^* a}{D} = \frac{aA\mathcal{M}}{D^2}$ that compares the relative influence of the advection to the diffusion. Then the solute concentration follows the dimensionless advection-diffusion equation with the boundary conditions (c, $\mathbf{u}$, x and t are made dimensionless using respectively $\frac{Aa}{D}$, U^*, a and $\frac{a}{U^*}$, but the notation are kept the same for simplicity purpose):

$$\mathrm{Pe}(\frac{\partial c}{\partial t} + \mathbf{u}.\nabla c) = \Delta c, \tag{2.134}$$

$$\frac{\partial c}{\partial r}\Big|_{r=1} = -1. \tag{2.135}$$

If the Peclet number is small, equation (2.134) becomes the linear diffusion equation:

$$\Delta c = 0. \tag{2.136}$$

The Stokes equation and the diffusion equation being linear, they cannot lead to an instability. When the Peclet number is small, the only way to self-induce a gradient of solute is a geometrical breaking of symmetry. However, when the Peclet number is high, the Stokes equation and the advection-diffusion are coupled, and, the latter being non-linear, it might lead to an instability, and thus a spontaneous breaking of symmetry.

2.2.3.1 $\mathrm{Pe} \ll 1$: geometrical breaking of symmetry

The geometrical breaking of symmetry might be achieved by designing a spherical object with asymmetric surface properties: a Janus particle (for instance [84, 85]). There are many different kinds of Janus particles, spherical particles, rod particles, or even Janus droplets. The underlying common principle is that half of the particle changes locally the interaction between the interface and the outer fluid, while the other half remains neutral (or eventually changes it, but in a different way) so that there is, in fine, a gradient of interaction between the two halves.

In the case of a diffusioporetic Janus particle [72], the Janus particle produces solute only on one side which induces a concentration gradient, hence a slip velocity, and thus a net motion. The complete calculation for the hydrodynamics flow field has been done in [86], and won't be further detailed here. We are just going to underline a few important properties that will help the reader understands the swimming behaviour of such phoretic particles.

Janus particle and trail: The Janus particle modifies its environment: it leaves behind a trail of solute. The Janus particle may then interact with the solute gradient

in its own trail. Such a phenomena is called auto-chemotaxie. Note that diffusion might make this trail disappear with time.

Janus particles and the Squirmer model: For Janus particles, the slip velocity is not fixed but depends on the concentration field around the swimmer, which can be modified by external factors such as the geometry (presence of a wall), or an external flow. In particular, the concentration might depend on time (formation of a trail behind the droplet) and/or the position (approach to a wall). As a result (i) there is little chance that the flow field remains axisymmetric, and (ii) even if it does, the coefficients $\alpha_n(\mathbf{x}, t)$ and $\tilde{\alpha}_n(\mathbf{x}, t)$ defined in equation (2.53) and (2.54) are not constant. In principle, real autophoretic Janus particles are already more complex than the Squirmer model.

If the Janus reaches a stationary regime, then it is possible to compute constant coefficients α_n and $\tilde{\alpha}_n$ and to use the properties of the squirmer model for the Janus particles. Note however that the description of the interactions using the squirmer model neglects in essence the mutual influence of the particles and the solute concentration field.

2.2.3.2 Pe $\gg 1$ - spontaneous symmetry breaking

We consider here an *isotropic* object that emits a solute. For small Pe, the equations are linear and the unique solution is that of an isotropic concentration field leading to no motion. For high Pe, the system follows the two sets of equations, the Stokes equation (2.34) and (2.35) for the flow field and the advection-diffusion equation (2.134) for the concentration field, which is non-linear and coupled to the Stokes equation through the advection term $\mathbf{u}.\nabla c$.

A motionless object emitting a solute that diffuses isotropically around the droplet is still solution of these equations. However, because of the non-linearity of the equations, this solution might be unstable, and the system may undergo a spontaneous symmetry breaking, producing a gradient of solute and thus a net motion of the object.

Sébastien Michelin et al. studied the stability of the trivial isotropic solution for a solid particle [83], and for a droplet [87] and the existence of other solutions. He showed that, if the motility $\mathcal{M}$ is positive, then the trivial solution $\mathbf{u} = \mathbf{0}$ is unstable for $\mathrm{Pe} > \mathrm{Pe}_c \simeq 5$, and the problem has a stable solution, where the object reaches a steady velocity U, that depends on the Peclet number. The bifurcation diagram that was computed in the case of a droplet is shown in Fig. 2.10(a). When the Peclet number is high enough, it has been shown that $\frac{U}{U^*}$ decreases very slowly and is of the order of 0.1. The Fig. 2.10(b) recapitulates the physical phenomenon that leads to the net motion of the particle:

1. If the diffusion of the solute is fast compared to the advection ($\mathrm{Pe} < \mathrm{Pe}_c$), then the concentration field homogenizes itself before any advection happens. The particle remains immobile.

2. If the diffusion of the solute is slow enough ($\mathrm{Pe} > \mathrm{Pe}_c$), the instability takes place, a gradient of concentration is established at the droplet interface, leading to a phoretic and Marangoni flow: a slip velocity and a tangential stress develop at the interface, and the droplet responds to the concentration gradient by moving.

(a)

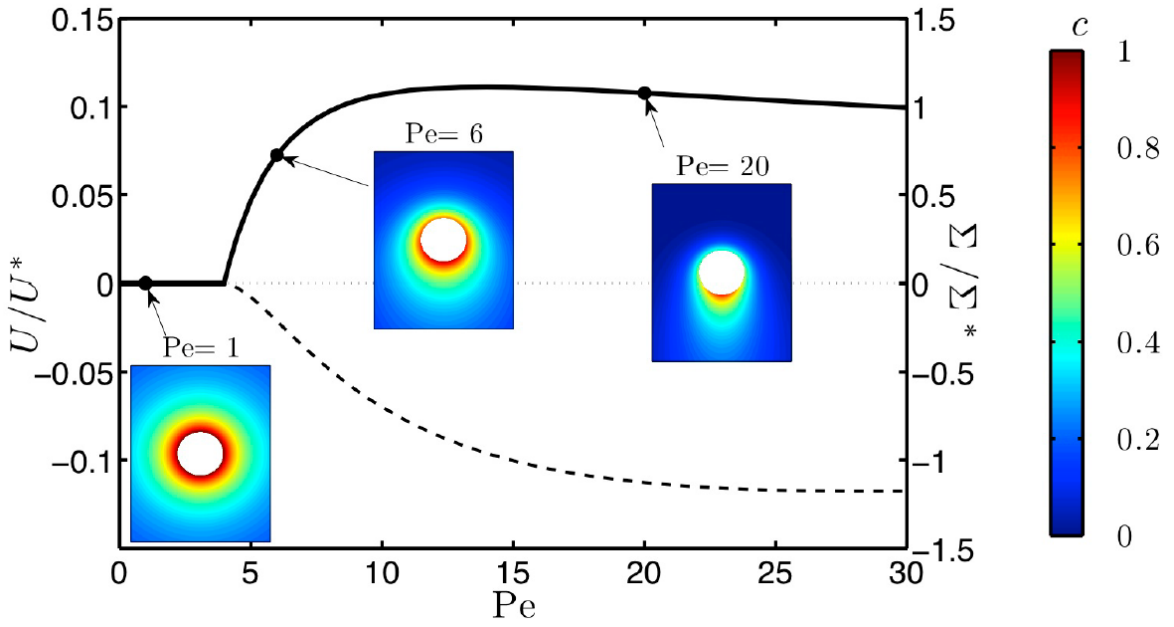

(b)

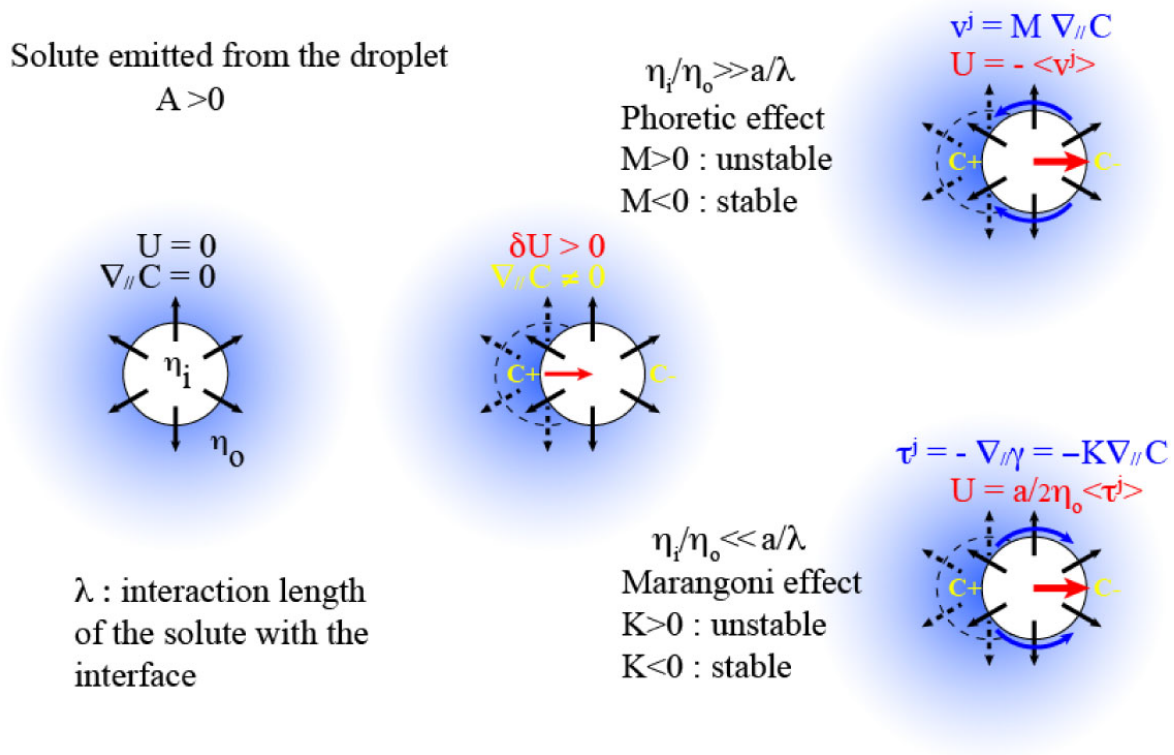

Figure 2.10: Figures taken from [87], and supplementary: (a) Evolution with Pe of the non-dimensional droplet velocity $\frac{U}{U^*}$ (black continuous line). The non-dimensional relative concentration is also shown for selected Pe, showing the symmetry breaking in the solute distribution associated with self-propulsion, despite the isotropy of the solute flux at the droplet boundary. (b) Swimming mechanism behind the spontaneous autophoretic and Marangoni-driven motion of an isotropic droplet.

(a) If the presence of the solute decreases the interaction between the inner and outer fluid (*i.e.* for a droplet, decreases the surface tension, $\mathcal{M} < 0$), the particle moves toward high concentration region, meaning where it was before the perturbation. The particle remains at its equilibrium position: the equilibrium is stable. The particle does not acquire persistent motion.

(b) On the contrary, if the presence of the solute increases the interaction between the inner and outer fluid ($\mathcal{M} > 0$), the particle moves toward low concentration region, meaning away from where it was before the perturbation. The particle goes further from its equilibrium position: the equilibrium is unstable. The particle starts swimming.

In the exact same way than for the Janus particles, the flow field generated by the isotropic self-propelled particle - solid or droplet - depends on the concentration field, and thus on the geometry, on external constrains, or on external concentration gradients such as the trail of the particle. Only in a stationary state the flow field might be considered as fixed, and it is then possible to compare the flow field with the squirmer model. For instance, the computation conducted in [87] in a stationary state far from any wall, showed that the amplitude of the quadrupolar symmetry is negative ($\alpha_2 < 0$): this means that the particle behaves like a pusher at long distance. However, the calculation is only valid as long as the particle does not interact with anything.

Furthermore, in the present case, in the presence of a wall, of an external force, or of another swimmer, the concentration field will be affected not only because of the modification of the boundary conditions for the concentration field, but also because of the advection by the modified flow field (which in turn depends on the concentration field...).

In particular, in the presence of an external force, using the equation (2.97), one finds that the relation between the droplet velocity, the concentration field and the external force is:

$$U = -\frac{K + 3\eta_i M}{2\eta + 3\eta_i}\langle \nabla_{\parallel} c(r = a, U)\rangle - \frac{1}{2\pi a}\frac{\eta + \eta_i}{\eta(2\eta + 3\eta_i)}F, \tag{2.137}$$

where the concentration field c strongly depends on the velocity of the droplet U. To stop such a droplet, one needs to apply a force $F_a = -2\pi a\eta\frac{K+3\eta_i M}{\eta+\eta_i}\langle \nabla_{\parallel} c(r = a, U)\rangle$. However, because when it is applied the droplet slow down, the force needed to stop the droplet changes, and more precisely decreases. Then to stop a droplet, one needs to apply a force that progressively decreases, until it reaches zero and the droplet is immobile. Note that this equilibrium state $F = 0$ and $U = 0$ is unstable, as seen before, thus the droplet is likely to undergo an instability and start swimming again in a random direction. In practice, it is not possible to permanently stop this kind of swimmer by applying an external force, as the state reached is unstable.

2.3 Breaking axisymmetry

2.3.1 Non axisymmetric swimmer

The axisymmetry of the problem can be broken for two reasons:

1. The swimmer is intrinsically non axisymmetric - For instance the geometry of the swimmer is not axisymmetric (not a sphere nor an ellipsoid) or the boundary conditions at the swimmer interface are not axisymmetric.

2. External factors break the axisymmerty - for instance if there is a force non-aligned with the swimmer direction, or a boundary such as a wall.

Note that if the boundary condition (or the shape) depends on the external flow field, then the second case might lead to the first case: an external source of asymmetry can break the swimmer axisymmetry.

Some non-axisymmetric problems have been investigated in the literature. For instance [88, 89] studied ciliary propulsion (a swimming mechanism consisting in generating surface waves along the swimmer interface). The shape of the swimmer is then time dependent, but almost spherical, and the non-axisymmetry is treated using a spherical envelope approach, which consists in adding small perturbation of the interface shape to the axisymmetric problem. Another example is the case of a spherical swimmer with non-axisymmertic boundary conditions [90], far from any boundary: the solution can then be expressed using a combination of the Legendre polynomial of any kind of μ, and a dependence in the revolution angle ϕ: $r^l e^{-im\phi} L_m^l(\mu)$.

Along the present work, we are going to meet two forms of external breaking of axisymmetry: (i) the problem of an external force not aligned with the swimming direction. This is treated in the following in the format of a short exercise, much like was done in section (2.1.4), and will be used in chapters (4) and (7) and (ii) the presence of a wall which is the main focus of the chapter (4), and will be briefly introduced here.

2.3.2 External force not aligned with the swimmer direction

If the swimmer is not aligned with the external force, then the axisymmetry of the problem is broken. The flow field $\mathbf{u}$ obeys the Stokes equation (2.34) and (2.35), with the boundary conditions at the swimmer interface (2.61), (2.62) and (2.63) for a droplet, and (2.59) and (2.60) for a solid particle. All equations, and relations between the different variables being linear, and provided that the boundary conditions at the droplet interface are not altered by the presence of the external force (for a squirmer for instance) it is possible to separate the problem in two different ones by defining $\mathbf{u} = \mathbf{u}_\parallel + \mathbf{u}_\perp$, $\mathbf{u}_\parallel$ being the solution of the problem of an active object aligned with an external force $F_\parallel$, and $\mathbf{u}_\perp$ being the solution of the problem of a passive object under a force $F_\perp$. $F_\parallel$ is the projection of the force on the swimmer direction, and $F_\perp$ is the projection on the normal to the swimmer direction $\mathbf{e}_\perp$ with $\mathbf{F} = F_\parallel \mathbf{e} + F_\perp \mathbf{e}_\perp$. In this case, $\mathbf{u}$ is indeed solution to the Stokes equations, and follows the right boundary conditions.

Then, using the solutions of these two problems, equation (2.75) and (2.90), one finds, for a passive particle under an external force $F_\perp$ in the direction $\mathbf{e}_\perp$:

$$F_\perp = -6\pi\eta a U_\perp, \tag{2.138}$$

$$\alpha_1^\perp = \frac{F_\perp}{18\pi\eta a}. \tag{2.139}$$

And for an active particle aligned with an external force in the direction $\mathbf{e}$:

$$\alpha_1^\parallel = \frac{F_\parallel}{18\pi\eta a} - \frac{2}{3}\langle v_s \rangle, \tag{2.140}$$

$$U_\parallel = -\langle v_s \rangle - \frac{F_\parallel}{6\pi\eta a} \tag{2.141}$$

with all higher order $\alpha_{n>1}$ and $\tilde{\alpha}_{n>1}$ still undisturbed by the presence of the external force, and given by equation (2.83).

Then the total flow field is the sum of an axisymmetric flow field in the swimmer direction, and a dipolar flow field perpendicular to the swimmer direction (dipolar flow field that can be described in term of a point force singularity and a responsive source dipole singularity), that tends to zero at the interface. The velocity of the solid particle is the sum of the previous ones:

$$\mathbf{U} = U_\parallel \mathbf{e} + U_\perp \mathbf{e}_\perp \tag{2.142}$$

$$= -\langle v_s \rangle \mathbf{e} - \frac{\mathbf{F}}{6\pi\eta a} \tag{2.143}$$

A similar calculation can be done for the swimming droplet, still assuming that the boundary conditions are fixed. The flow field is then similarly the superposition of an axisymmetric flow field, and a perpendicular dipolar flow, that tends to zero at the droplet interface. The velocity is:

$$U = \frac{a\langle \sigma_s \rangle - 3\eta_i \langle v_s \rangle}{2\eta + 3\eta_i}\mathbf{e} - \frac{\mathbf{F}}{6\pi a}\frac{3(\eta + \eta_i)}{\eta(2\eta + 3\eta_i)} \tag{2.144}$$

In both cases, because of this perpendicular dipolar flow field caused by the external force, the flow field is non-axisymmetric.

2.3.3 Microswimmers in real environments

Be it in a biological environment or in a microfluidic device, there are many cases where the microswimmers does not evolve in a 3D infinite and unbounded medium [39]. Several observations indeed reveal the critical importance of confinement on the swimmer's dynamics. Some microswimmers are attracted by the boundaries [40, 41, 42], which can then be used to capture [43, 33], or steer the swimmer motion [44, 45, 46]. The presence of a boundary has been observed to influence not only the motion of a single particle [47, 48, 49] but also the collective behaviour and phase transitions of swarms [50, 51, 52, 53]. Ultimately, the interactions with boundaries can be used to

harvest energy from the population of swimmers [54]. Obtaining a reliable description of the interaction of a swimmer with a wall is thus of significant importance. It is also a first step towards a better understanding of the interactions among swimmers and thereby the emergence of collective behaviour [55, 91].

2.3.3.1 The method of images: A Squirmer close to a wall

The method of images [92] has been used to look at a simplified problem of a squirmer close to a wall. The presence of a no-slip infinite plane wall imposes a vanishing flow velocity $\mathbf{u} = \mathbf{0}$ at the wall. One way out to compute an approximation of the flow field generated by an object close to such a wall consists in taking the "mirror image" through the wall of the hydrodynamics flow field produced by the object far from walls such that the sum of the two flow field is zero at the wall.

A squirmer - whose boundary conditions are fixed - can be described as a linear combination of fundamental solutions to the Stokes equations, the singularities (see section (2.1.5)). Then the image of each of these singularities can be computed to construct the mirror image of the object, and then the flow field of the object close to a wall. Such a strategy has been applied recently to the case of an axisymmetric swimmer [93]. The hydrodynamics image system differs from the simple mirror image of the original object, as this is the case in other fields such as diffusion or electrostatics, where the field satisfies Laplace's equation. Although the problem of the wall is treated exactly (no slip wall), the boundary conditions at the object interface are not exactly fulfilled, because of the image object flow field. [93] focused on characterizing the accuracy of the far-field approximation, and showed that this simplified description can be very useful, and quantitatively predictive, for describing the behaviour of a selection of swimmers close to a wall.

More specifically, the lower order singularities - the point force and point source - have been computed [38] using Fourier transform, to fulfill the no slip condition at the wall.

The geometry of the problem is illustrated in Fig. 2.11. We use a set of axes centered on the sphere's center. $\mathbf{e}_z$ is a unit vector along the vertical axis and h is the distance between the center of the swimmer and the wall. Image singularities are thus positioned at a point $\mathbf{X} = -h\mathbf{e}_z$ below the wall, and we note $\mathbf{r}$ the position of the observation point (where the flow is evaluated) with respect to the sphere's center and $\mathbf{R} = \mathbf{r} + 2h\mathbf{e}_z$ the position of the same point with respect to the position of the image system. For each singularity, which leads to a velocity field $\mathbf{u}_i$[10] in unbounded flow, we denote by $\mathbf{u}_i^*$ the corresponding flow field near a wall (i.e. including both the original singularity and the effect of its image system). The singularities and their images are illustrated in Fig. 2.11.

The image of a point source computed by [38] is a sink, plus a symmetric force dipole perpendicular to the wall and a source dipole perpendicular to the wall. The corre-

[10] i stands for the singularity - s is for a point source, sd for a source dipole, f for a point force, fd for a force dipole, and so on)

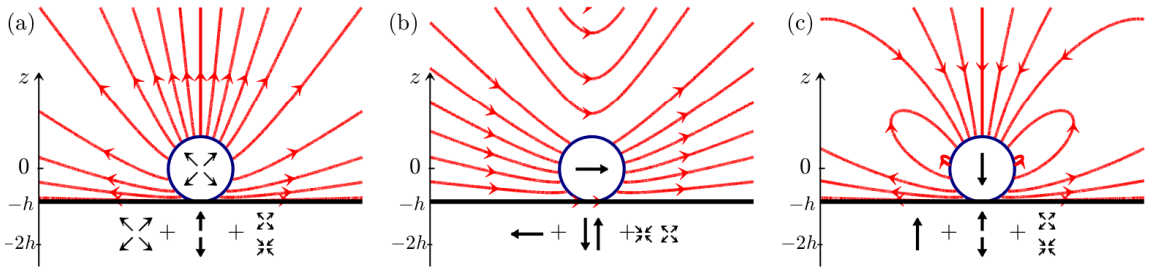

Figure 2.11: **Flow fields in presence of a no slip wall:** Flow field produced by singularities (at $z = 0$) and their images (placed at $z = -2h$ through a no slip wall (black line, at $z = -5$), in a median plane perpendicular to the wall $\{\mathbf{e}_x, \mathbf{e}_z\}$. (a) A point source and its images, a point source, a force dipole and a source dipole. (b) A point force parallel to the wall and its images, a point force, a force dipole and a source dipole. (c) A point force perpendicular to the wall and its images, a point force, a force dipole and a source dipole.

sponding flow field is:

$$\mathbf{u}_s^*(\mathbf{r}) = \overbrace{\frac{\mathbf{r}}{r^3}}^{\text{Original source}} + \overbrace{\frac{\mathbf{R}}{R^3}}^{\text{Image source}} \overbrace{- 2\left(\frac{\mathbf{R}}{R^3} - \frac{3\mathbf{R}(\mathbf{R}\cdot\mathbf{e}_z)^2}{R^5}\right)}^{\text{force dipole}} + \overbrace{2h\left(\frac{\mathbf{e}_z}{R^3} - \frac{3(\mathbf{R}\cdot\mathbf{e}_z)\mathbf{R}}{R^5}\right)}^{\text{source dipole}}. \tag{2.145}$$

Similarly, the image of a point force computed by [38] is a point force of opposite direction, an asymmetric force dipole and a source dipole parallel to the wall, and the corresponding flow field is:

$$\begin{aligned}\mathbf{u}_f^*(\mathbf{r}) = &\overbrace{\frac{\mathbf{e}}{r} + \frac{(\mathbf{e}\cdot\mathbf{r})\mathbf{r}}{r^3}}^{\text{Original force}} - \overbrace{\frac{\mathbf{e}}{R} - \frac{(\mathbf{e}\cdot\mathbf{R})\mathbf{R}}{R^3}}^{\text{Image force}} + \overbrace{\frac{2h^2\mathbf{e}}{R^3} - \frac{6h^2(\mathbf{e}\cdot\mathbf{R})\mathbf{R}}{R^5}}^{\text{source dipole}} \\ &+ \overbrace{\frac{2h(\mathbf{e}\cdot\mathbf{R})\mathbf{e}_z}{R^3} + \frac{6h(\mathbf{R}\cdot\mathbf{e}_z)(\mathbf{e}\cdot\mathbf{R})\mathbf{R}}{R^5} - \frac{2h(\mathbf{e}_z\cdot\mathbf{R})\mathbf{e}}{R^3}}^{\text{force dipole}}.\end{aligned} \tag{2.146}$$

Then, the higher order singularities are obtained by taking the successive gradients of these flow field (with a similar reasoning than in section (2.1.5):

$$\mathbf{u}_{fn}^*(\mathbf{r}) = -\nabla\left[\mathbf{u}_{f(n-1)}^*(\mathbf{r})\right]\cdot\mathbf{e}_z, \tag{2.147}$$

$$\mathbf{u}_{sn}^*(\mathbf{r}) = -\nabla\left[\mathbf{u}_{s(n-1)}^*(\mathbf{r})\right]\cdot\mathbf{e}_z; \tag{2.148}$$

the gradient being taken in the same direction than the singularity (for instance if we consider an axisymmetric swimmer, it is taken in the swimming direction).

The flow field in the presence of the wall then simply reads:

$$\mathbf{u}^* = \sum_{n=1}^{\infty} \alpha_n^* \mathbf{u}_{f,(n-1)}^* + \tilde{\alpha}_n^* \mathbf{u}_{s,n}^* \tag{2.149}$$

The complete expression of the flow field generated by a force dipole, a source dipole and a source quadrupole for any angle with the wall and at any distance are given in [93].

2.3.3.2 Effect of a no-slip wall on the activity

For swimmers driven by mechanical surface distortions, it is reasonable to assume that hydrodynamics mechanisms are the dominant contributor to the motion. If the mechanical surface distortions at the origin of self-propulsion are not modified by the proximity of the wall, a squirmer description could be used with a prescribed and unaltered slip velocity. Even in this simplified context, solving for the exact flow around a squirmer in the presence of a wall is in general not possible. Currently, the only exact solution is that of the flow field resulting from the motion of an axisymmetric squirmer approaching a wall, along the wall normal direction [94].

Things becomes even more complicated, when the object is not a squirmer - i. e. when the boundary conditions themselves can be modified by the presence of the wall. Considering for instance the case of phoretic or Marangoni swimmers, the self-generated external field, responsible for the swimming motion, is likely to be distorted by the presence of the wall, which alters the diffusion of the physico-chemical field. This was first illustrated in [95], before it was indeed demonstrated that in the presence of boundaries the behaviour of chemically active colloids is qualitatively different, even in the far field, from the one that could have been expected for fixed boundary conditions [96].

At low Peclet number, the hydrodynamics problem and the concentration problem can be treated separately, first solving the concentration field close to a wall that gives boundary conditions at the object interface, second solving the hydrodynamics problem in presence of a wall using these boundary conditions. Focusing on the near-wall motion, general analytical solutions for the concentration field, velocity and rotation of the locomotor, as a function of distance and orientation of the active cap with the surface, were obtained in the form of infinite series expansions [97]. These solutions were then used to compute general trajectories and categorize the swimming regimes. Yet, for such expansions, the correspondence between each term (i.e. angular mode) to a precise set of hydrodynamics singularities of increasing order is lost, in stark contrast with the classical decomposition of the flow field generated by a spherical swimmer in unbounded flow [90].

At high Peclet number, the flow field and the concentration field are non-linearly coupled. The concentration field is modified by the presence of the wall *and* advected by the flow field, and the flow field boundary conditions depends on the wall *and* the concentration field at its interface. Considering the flow field around such a swimmer is part of the present work, and will be addressed in chapter (4).

Key messages

Here is a condensed summary of the key notions explored in this chapter.

In the case of an unbounded axisymetric problem, the flow field around a spherical object is the superposition of contributions of an infinite number of azimutal symmetries (monopolar, dipolar, quadrupolar symmetries, and so on). The amplitudes of theses symmetries are determined by the boundary conditions of the same symmetries at the object interface. Only the dipolar symmetry of the hydrodynamic flow field, and thus the dipolar symmetry of the boundary conditions (asymmetry front-back) leads to a net motion of the spherical object.

The boundary conditions at the interface of a spherical, undeformable object, in the most general case of a droplet, are a slip velocity and a stress jump of the flow field across the interface (equation (2.61), (2.62) and (2.63)), and the balance of force for the droplet (equations (2.33)). The velocity of the droplet is then given by a combination of the average of the slip velocity and of the stress jump over the droplet interface, and of the external force, through the lamb formula (equation (2.84)).

The most commonly used model for swimmer is the squirmer model, whose boundary conditions are fixed. This model is also often limited to two hydrodynamic symmetries: the dipolar symmetry, responsible for the swimming, and the quadrupolar symmetry, decaying the slowest at long range.

The slip velocity and stress jump may comes from physical actuation (for instance through the use of flagella), or from a physico-chemical origin, through the interaction between the inner and outer fluid at the microscopic scale. This interaction take place in an interfactial layer of finite thickness, in which, for instance, a concentration gradient of a solute in the outer fluid interacting with the inner fluid puts fluid into motion (Marangoni and phoretic effects).

A swimmer is an object that self induces these boundary conditions to produce a net motion. The swimmer then needs to break the isotropy around itself (the swimmer needs to impose a front-back asymmetry). This breaking of isotropy may be geometrical - which is the case for Janus particles, or might come from a spontaneous symmetry breaking resulting from an instability - which is the case for swimming droplets. Note that in this last case, the boundary conditions are coupled to the hydrodynamics.

An external breaking of the axisymmetry, because of a wall for instance, or the presence of an external force not aligned with the swimmer direction, modifies the flow field. In the case of a swimming droplet, because of the coupling between the hydrodynamics and the boundary conditions, an external breaking of axisymmetry is likely to modify the boundary conditions of the swimmer itself.

Chapter 3

Pure water swimming droplets

Historical context

In opposition with Brownian motion, a gradient may generate directed swimming - swimming with a certain persistence length. Spontaneous swimming - meaning swimming not induced by an external gradient - needs the swimmer to interact with his environment and change it locally. As droplets are isotropic objects, local gradients must arise from a spontaneous breaking of symmetry around the droplet. Historically, the first self-propelled droplets were sessile droplets chemically reacting with a surface [98, 99, 100, 101, 102, 103, 104], locally changing the wetting angle (and thus the interfacial forces) between the droplet and the surface (an example is given in Fig. 3.1(a) and (b)). In these cases, the surface tension between the surface and the droplet being higher after the chemical reaction, areas already visited by the droplet become repulsive. One should also mention other swimming mechanism using an external source of energy - for instance UV-light inducing a isomerization of the interface [105], or a laser beam locally heating the droplet [71] - which produces an internal convection inside the droplet. By continuity, this internal convection induces external convection, which leads to a net motion of the droplet. The first self-propelled swimming droplet [106] (moving through the bulk with an inner source of energy) was observed for an oil in water droplet producing giant vesicles at its interface (in Fig. 3.1(c) and (d)). The vesicles were formed at the droplet's interface through a reaction between a surfactant in the water phase, and a reactive in the oil phase. Several other kinds of swimming droplets of oil in water [107, 108, 109, 110, 51] or water in oil [111, 112, 87] have been developed since then, the common underlying principle being a "reaction[1]" at the interface that increases locally the "surface tension[2]", which induces a phoretic and Marangoni flow that drives the droplet away from its previous position (see section (2.2.3)).

One system worth mentioning, as it was the first water in oil self propelled swimming droplet, is the system developed by Thutupalli et al (in Fig. 3.1(e) and (f)) [111]: a

[1]By "reaction" we mean chemical reaction but also physical transformation such as the solubilization of a compound from one phase to another, or transfer of one compound (from the surface to the bulk for instance)

[2]By "surface tension", we mean the enlarged definition of the surface tension as seen in section 2.2.2, which is the energy that costs the finite boundary between the droplet and the bulk. This energy is the result of the interactions of all components in this boundary layer, including - but not exhaustively - the two phases, the surfactant and the solutes.

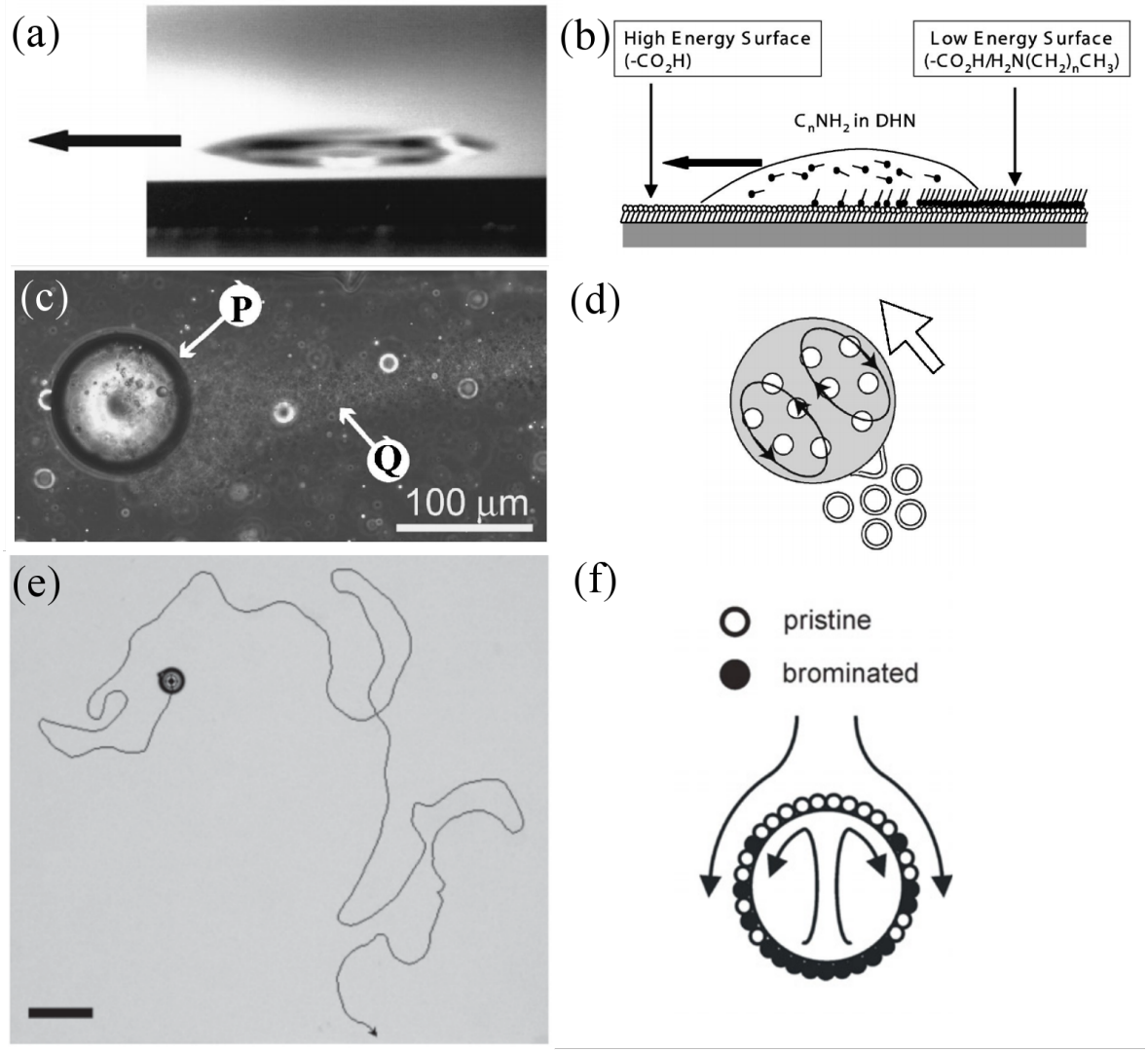

Figure 3.1: **Illustration of some historical swimming droplets.** (a) and (b), figures from [100]: (a) side view of a moving drop on a substrate. (b) Schematic illustration of the surface energy change induced by adsorption of an n-alkylamine onto a CO_2H surface, which produces the swimming. (c) and (d), figures from [106]: (c) Phase-contrast microscopic images on self-propelled motion of an oil emulsion droplet (site P) with a trail of giant vesicles (site Q). (d) Illustration of the schematic dynamics behind the propelling of (c): the production of giant vesicles induces convection inside the droplet. (e) and (f), figures from [111]: (e) path of a single self-propelled water droplet. (f) Schematic representation of the swimming mechanism of (e): bromination increases the tension of the droplet surface. The convective flow pattern is accompanied by a gradient in the bromination density. The corresponding Marangoni stress propels the droplet.

B-Z droplet[3] is made in an oil phase of squalane with a surfactant, the mono-olein (rac-glycerol-1-mono-oleate). One of the byproduct of the BZ reaction is the bromine which reacts at the interface between the water and oil phases with the mono-olein. This reaction produces a brominated mono-olein which is a weaker surfactant than the mono-olein. Then the droplet produces isotropically a "solute" that increases locally the surface tension between the droplet and the bulk. As seen in section (2.2.3), such a system is unstable for a high enough Peclet number, and thus the droplet starts to swim. During his PhD, Ziane Izri [114] studied this system of swimming B-Z droplets, and for comparison a similar system of pure water droplets in oil plus mono-olein, with the intention of making passive droplets. To his surprise, this second kind of droplets was also swimming, even in the absence of chemical reaction. He provided the first description of this system, and proposed a swimming mechanism [87]. This system of swimming pure water droplet in an oil+surfactant solution is what we are going to describe and characterize in this chapter, as it is the central object of study of the present work.

3.1 Pure water swimming droplet

The system we study is constituted of pure water droplet of typical radius $a = 50 - 100$ μm, in a solution of 25mM mono-olein in oil[4].

3.1.1 Swimming mechanism

3.1.1.1 The origin of the swimming motion

Such droplets are observed to swim at a typical velocity of $V = 20\mu$m/s for around two hours (see typical trajectory, velocity and radius in Fig. 3.2(a), (b) and (c). While investigating the origin of the droplets motion, Ziane Izri [114] made several measurements and observations:

- The radius of the droplets decreases with time (Fig. 3.2(c)) at a typical rate of 5 nm/s. After several hours, in system with a few droplets in oil, the droplets disappear completely, while in system with a lot of droplets in oil, the droplets stop moving.
- There is no swimming if the oil solution of squalane + mono-olein have been saturated with water beforehand.
- The velocity of the droplets depends on the surfactant (mono-olein) concentration : below the critical micellar concentration (CMC): the droplets do not swim. Above the CMC, the velocity increases with the mono-olein concentration.
- Dynamic light scattering experiments were performed to measure the evolution of the typical micelle size in a solution of 221mM mono-olein in tetradecane, in

[3] A B-Z droplet is an aqueous phase droplet inside which a Belouzov-Zhabotinsky reaction [113] takes place.

[4] The droplets have been observed to swim in many different oils, and Ziane Izri study focused on two different oils, squalane and tetradecane. In the present work, we use mainly squalane oil.

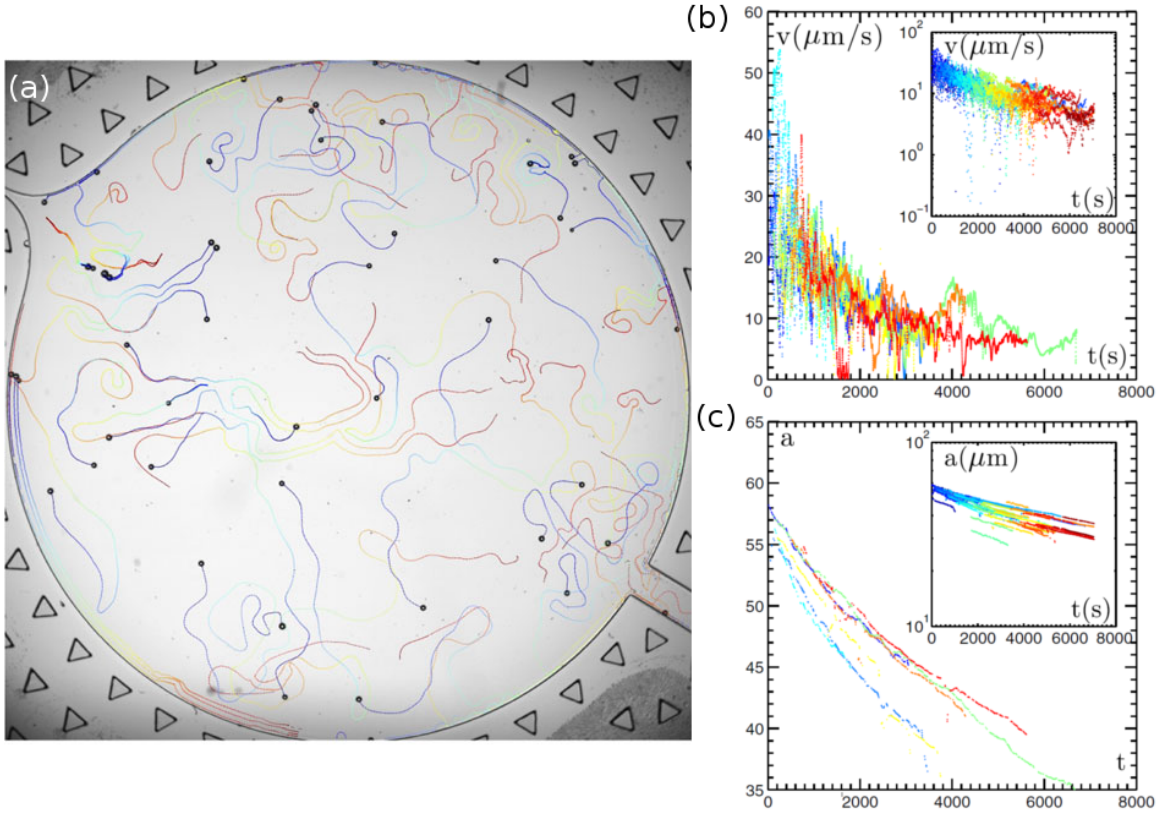

Figure 3.2: **Figures from [87] Pure water droplet motion:** (a) trajectories of ~ 50 water droplets in the observation room (diameter 1 cm) filled with Sq–25 mM MO, recorded during 500 s. The droplet trajectory is color coded with the time preceding its present location. (b) Velocity and (c) diameter versus time for a selection of eight trajectories. Insets: Linear-log plot for a selection of 35 trajectory parts.

contact with water[5]. The radius of the micelles has been found to increase with time, from $\delta = 3$nm to a typical size $\delta = 10$nm.

These observations provide the following arguments : (i) water is sent "somewhere" in the oil solution and this process is linked to the motion, (ii) being above the CMC is necessary for the swimming to occur, (iii) objects of the order of the nm are growing in the oil phase. This allowed to make the hypothesis that water from the droplet is sent inside the micelles in the bulk, forming swollen micelles - or nano-droplets - of typical size 10 nm. The exact mechanism of how the water is sent in the micelles is not known. Stephan Herminghaus [115] proposed two mechanisms:

- The micellear pathway : The micelles swell at the interface of the droplet pumping water and surfactant directly at the droplet interface (see Fig. 3.3(a)). In this case, the depletion flux of water is directly linked to the empty micelles concentration at the interface. The boundary layer, in which the transfer occurs is typically the layer of surfactant plus the size of a micelle.

- The molecular pathway : Water is partially soluble in the oil phase, thus the droplet slowly dissolves with time. The surfactant in the bulk (free surfactants or

[5]More precisely oil sample were taken from a water in oil emulsion at 0.5% volume fraction of water, kept into rotation.

surfactant in micelles) absorbs the solubilized water to form the swollen micelles (see Fig. 3.3(b)). In this case, the depletion flux of water is linked to the solubility equilibrium of the water between the droplet and the bulk phase, this equilibrium being affected by the concentration of surfactant that consumes water in the bulk. The boundary layer, in which the transfer of water occurs, is typically the distance at which the water concentration in the oil phase tends to zero - which is also the distance at which there is still empty micelles.

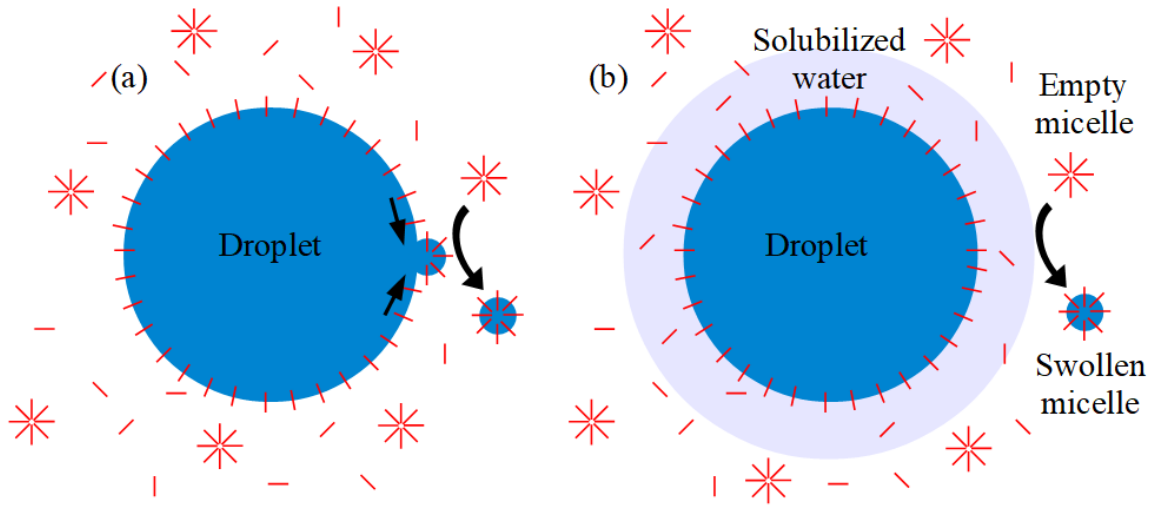

Figure 3.3: **The two imagined pathways for the formation of micelles:** (a) micellar pathway, the empty micelles take water directly from the interface and swell. (b) Molecular pathway, water from the droplet solubilizes in the oil. Empty micelles swell when meeting solubilized water.

These are two model mechanisms of the transfer of water from the droplet to the micelles in the bulk, which explain the apparition of swollen micelles. Although the size of the boundary layer is expected to be different, at the outer edge of this boundary layer, we may simply consider that there is an exchange of water between the droplet and the micelles in solution. These two mechanisms are quite similar in this aspect. However, the dynamic of these two transfer mechanisms are different, leading to different dependency of the flux of water: in the case of the micellar pathway, the flux depends on the concentration of empty micelles at the interface, while in the case of the molecular pathway, the flux depends on the equilibrium of the solubility of the water in oil.

Motility can rise from a gradient of interaction between the droplet and the bulk. In the boundary layer, the component potentially interacting with the interface are the solubilized water and the surfactant in four different states: at the interface, free in the bulk, in empty micelles or in swollen micelles. In reality all these components participate to the interaction between the bulk and the interface, leading at the level of the hydrodynamics to both a phoretic and Marangoni effects (see section (2.2.2)). In his study, S. Hermingaus considered a pure Marangoni effect (a stress jump at the

interface) coming from the concentration of surfactant at the interface[6]. More generally, one should consider the interaction of all compounds inside the boundary layer, which give rise to an interaction that depends on all compounds concentrations. As there is conservation of the water and surfactant, all concentrations ultimately depend on the concentration of swollen micelles produced. One can then have a simplified vision of the boundary layer as an area where swollen micelles are produced and interact with the interface (this interaction then includes the depletion of surfactant at the interface, the consumption of empty micelles, free surfactant and solubilized water, and the direct interaction between the interface and the swollen micelles). This simplified vision of the physico-chemistry in the boundary layer is schematized in Fig. 3.3.

3.1.1.2 Mechanism robustness

The robustness of this swimming mechanism has been tested by changing the different components of the system:

Oil phase: the droplets are observed to swim in squalane, decane and tetradecane. The swimming behaviour differs depending on the oil, for instance the droplets swim quicker in tetradecane than in squalane. This has been intensively studied in Ziane Izri's thesis [114].

Aqueous phase: the droplets are observed to swim whether the inner phase is pure water, acid or basic water (with pH between 3 and 12), salted water (even at a salt concentration above the salt solubility), a solution of water + ethanol [116] and even glycerol. One interesting point to notice is that the presence of salt increases the osmotic pressure inside the droplet, and thus slows down the flux of water from inside to outside: in 2D, the droplet goes slower, and also swims longer. In 1D channel, however, the presence of salt is observed to accelerate the droplet. This effect is not well understood, but might come from a repulsive effect between the channel and the salt, which increases the lubrication layer between the droplet and the channel, and thus decreases the viscous dissipation.

Surfactant: A few different surfactants have been tried, the only one which works is the mono-olein. The reason for that could be that the mono-olein has an especially high solubility in oil, or that the shape of the mono-olein (presence of a double bond) makes the equilibrium size of micelles particularly large, favoring their swelling.

We decided to choose this unique experimental system during this work: a water droplet (pure water or a solution of 15% wt NaCl in water depending on the experiments) in a solution of 25mM mono-olein in Squalane.

[6]He also showed that in this case, only the molecular pathway for the creation of swollen micelles could possibly give rise to a net motion of the droplet.

3.1.2 Swimming behaviour

3.1.2.1 Characteristic and dimensionless numbers

Physico-chemical properties:

We briefly present the two main chemical compounds used in our system: the squalane - the oil constituting the outer phase - and the mono-olein, the surfactant solubilized in the oil phase.

Squalane: 2,6,10,15,19,23-Hexamethyltetracosane,
density $d_{squalane}(T = 298K) = 0.810$,
viscosity $\eta = 36$ mPa.s [117],
water solubility $s = 3.710^{-6}$ mg/mL (ALOGPS).

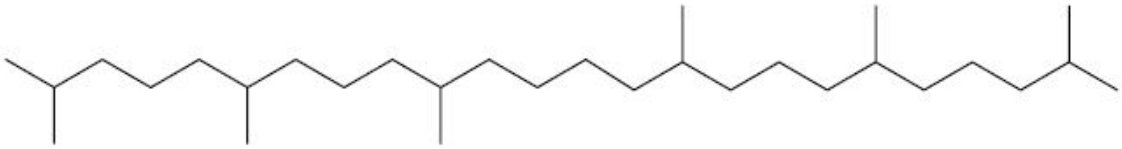

Figure 3.4: Linear representation of the squalane molecule

Mono-oelein: 1-Oleoyl-rac-glycerol,
CMC in Squalane: $CMC \simeq 3$ mmol/L.

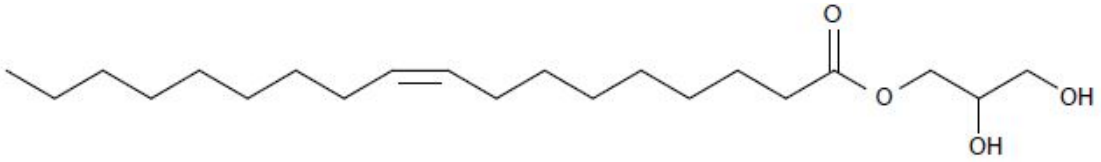

Figure 3.5: Linear representation of the mono-olein molecule

Interfacial tensions:
between Squalane and water: $\gamma_{ow} = 46$ mN/m,
between Squalane + mono-olein (above CMC) and water: $\gamma_{omw} = 1.7$ mN/m.

The system:

We typically study the swimming behaviour of a water droplet of radius $a = 50 - 100$ μm, eventually with salt at a concentration of $c_{NaCl} = 15\%$wt, in a solution of $c_{MO} = 25$ mM $> CMC$. The droplet shrinks with time (it sends water into empty micelles), and the evolution of its radius can be evaluated as $\kappa = \frac{da}{dt} = 4.5 \cdot 10^{-2}$ μm/s. The typical swollen micelle radius has been measured to be $\delta = 10$ nm. The droplet's typical velocity in 2D is $V = 50$ μm/s.

Swimming mechanism:

According to the section 2.2.3, the swimming of our droplets comes from a competition between the advection and the diffusion of the solute. From this problem emerges a dimensionless velocity $U^* = \frac{A\mathcal{M}}{D}$, where A, $\mathcal{M}$ and D are defined as follow [87].

- The activity, A is the surface emission rate of the swollen micelles (number of swollen micelles produced at the droplet interface per unit of surface and per unit of time). It can be linked to the evolution of the droplet size κ through the conservation of volume of water from the droplet to the micelles: $A = \frac{4\pi a^2 \kappa}{\frac{4}{3}\pi\delta^3}\frac{1}{4\pi a^2} = \frac{3}{4\pi}\frac{\kappa}{\delta^3}$. Given all parameters, $A \simeq 10^4$ swollen micelles/μm^2.s.

- The motility defined by the equation 2.132 describes how much the droplet moves as a response to a gradient of solute: $\mathcal{M} = \epsilon k T \lambda \frac{a+3\lambda\frac{\eta_i}{\eta}}{4\eta+6\eta_i}$. In the case of a water droplet in oil, $\eta_i \ll \eta$, and thus the phoretic contribution on the motility can be neglected compared to the Marangoni one: $\mathcal{M} = \frac{kT\epsilon\delta a}{4\eta}$. As a first approximation for the numerical application, we consider only the sterical interaction between the swollen micelles and the droplet: $\epsilon\lambda = \delta$, then $\mathcal{M} = 2.5 \cdot 10^{-2}$ μm^5/s.

- The diffusion of the swollen micelles of radius δ in the oil of viscosity η writes as $D = \frac{kT}{6\pi\eta\delta}$. This can be evaluated as $D = 5 \cdot 10^{-1}$ μm^2/s.

Then $U^* = \frac{9}{4}\frac{a\kappa\epsilon\lambda}{\delta^2} = 4.5 \cdot 10^2 \mu$m/s.

Dimensionless numbers:

A certain number of dimensionless numbers allows us to describe our system, and compare the relative effects of the different phenomena at play on the outer fluid (inertia, viscosity), on the solute concentration (advection, diffusion), or on the object shape (interfacial tension, gravity).

Outer fluid - the Reynold number Re:
the Stokes equation describes a flow field for which the effect of inertia are negligible compared to the viscous effect. This is quantified by the Reynold number:

$$\mathrm{Re} = \frac{\rho U^* a}{\eta} \tag{3.1}$$

$$= 10^{-6} \ll 1. \tag{3.2}$$

Thus we are indeed in the microfluidic realm, where a fluid is described by the Stokes equation.

Solute concentration - the Peclet number Pe:
for the instability to occur, a gradient of concentration needs to exist, which can only happen if the diffusion of swollen micelles (which tends to homogenize the concentration

field) is not too fast compared to the advection. This is quantified by the Peclet number Pe which compare convection effects to diffusive ones:

$$\mathrm{Pe} = \frac{U^* a}{D} \tag{3.3}$$

$$= \frac{aA\mathcal{M}}{D^2} \tag{3.4}$$

$$= 10^5 \gg 1. \tag{3.5}$$

Some numerical application:
we saw in section (2.2.2) that the critical Peclet number for the instability to occur was $\mathrm{Pe}_c = 5$. Then $\mathrm{Pe} \gg \mathrm{Pe}_c$, we are indeed in the regime where the droplet swims. For very large Peclet, using the same numerical method than in [83], for the same system but for high Peclet, one can find that $\frac{V}{U^*}$ saturates toward a constant value $\frac{V}{U^*} \to 0.1$. Then the typical velocity of our system should be $V = 45$ μm/s, which is of the same order as the measured velocities. Note that $V = 0.1\ U^* = 0.2\frac{\epsilon\lambda}{\delta^2} a\kappa \propto \kappa a$. Measuring experimentally [87] the dependency of the velocity with the droplet radius and shrinking rate, Ziane Izri et al. check this relation, Fig. 3.6. Note that the slope of these curves gives an experimental measurement of $\frac{\epsilon\lambda}{\delta^2}$. Here we measure the slop for the three systems used by Z. Izri:

- System of pure water droplets in a squalane+mono-olein solution: $\frac{\delta^2}{\epsilon\lambda} = 20$ nm.
- System of pure water droplets in a tetradecane+mono-olein solution: $\frac{\delta^2}{\epsilon\lambda} = 50$ nm.
- System of salted water droplets in a squalane+mono-olein solution: $\frac{\delta^2}{\epsilon\lambda} = 3$ nm.

We see here that the composition of the two phases has an influence on the characteristics of the interfacial layer ϵ, the strength, and λ, the scope of the interactions between the two phases (eventually also the size of the micelles δ). In particular, the presence of salt in the water phase (which we can suppose does not modify the size of the micelles in the oil phase) increases $\epsilon\lambda$ (decreasing the ratio $\frac{\delta^2}{\epsilon\lambda}$), which is surprising.

Object shape - the capillary length:
one more hypothesis we make is that our droplet is spherical, although they are not density matched with the surrounding fluid ($\Delta\rho = 0.2{\cdot}10^3$ kg/m^3). This approximation is only correct if the interfacial forces, that tend to minimize the droplet surface, and thus keep it spherical, dominate gravity. This is quantified by the capillary length l_c:

$$l_c = \sqrt{\frac{\gamma}{\Delta\rho g}} \tag{3.6}$$

In our problem, $\gamma = 1$ mm which is much larger than the droplet size $a \simeq 100$ μm. The droplets are thus spherical.

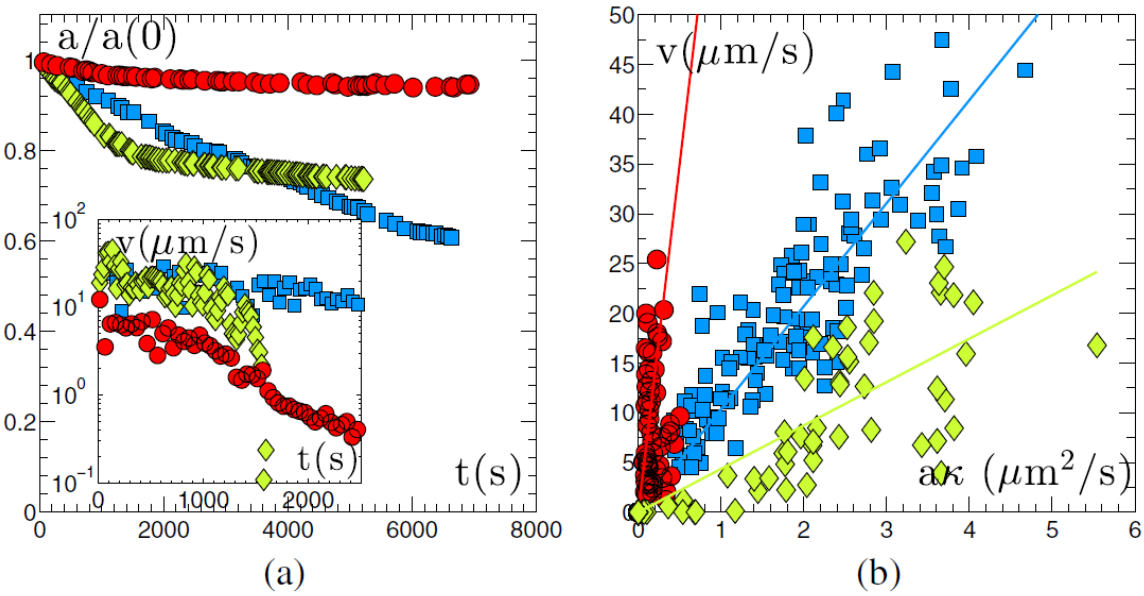

Figure 3.6: figure from [87] Comparison of three different systems. (a) Decay of the relative droplet radius versus time for three droplets under different conditions: water in Sq-MO (blue squares), water in Td-MO (green diamonds), water-26 wt%NaCl in Sq-MO (red circles). Inset: Velocity versus time for the same three droplets. (b) Parametric plot of the velocity versus $a\kappa$ for droplets under the same three different sets of conditions; each point represents a different droplet during a different period of time corresponding to a straight part of its trajectory.

3.1.2.2 Some interesting behaviours

At this point in order to have a more concrete understanding of the behaviour of our swimming droplets, we invite the reader to watch a video of our system:

[Swimming droplets][7]

This video was made by the YouTube channel "The Lutetium Project", intended for the general public and with the purpose of being both educative and entertaining.

Trajectory

Note first that the water phase is denser than all tested oils. Thus the water droplets fall on the bottom wall and swim along this wall.

The behaviour (persistence length, velocity, curvature) of the droplets strongly depends on the system, for instance on the size of the droplets and their composition (pure water vs salted water), but also on the nature of the bottom wall. This will be discussed in chapter (4).

Interactions

[7] https://www.youtube.com/watch?v=2T_C694BOGw

When a droplet meets a vertical wall, it reorients and starts swimming along this wall. This lasts for a while until the droplet eventually leaves the wall. When two droplets come onto contact, their behaviours depend on the orientation of the two swimmers: if they arrive perpendicular to each other (side by side), they align and swim together for a while. If they arrive parallel to each other (face to face), they repeal each other. This kind of behaviour is characteristic of pushers in the squirmer model (section (2.2.1)).

Cargo

It is possible to add something in the droplets (Fig. 3.7), such as colloids, salt crystal (when the salt concentration is above its solubility), but also biological entity (as our system is fully biocompatible) such as bacteria colonies, and to use the droplets as cargo to transport things at the microscopic scale.

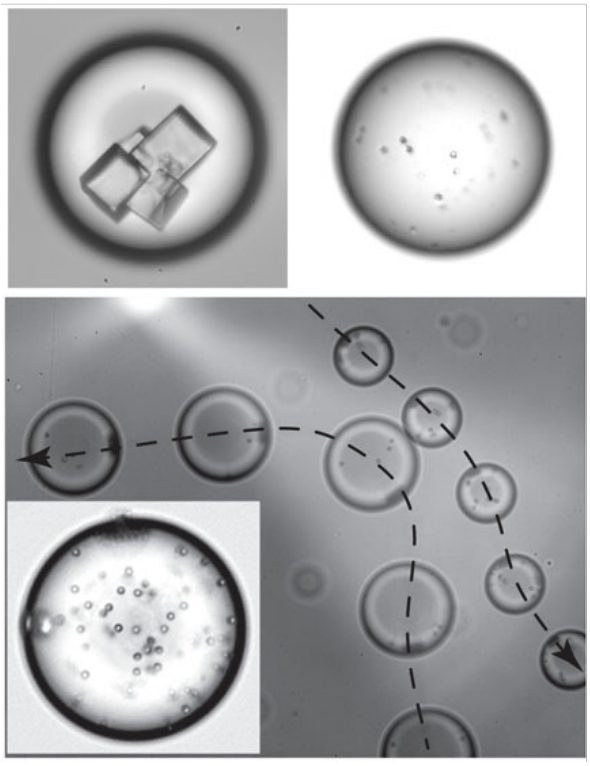

Figure 3.7: Figure from [87] Swimming droplets as microfluidic carriers. Transport of salt crystals (top left), Dami cells [118] (top right), and colloids (bottom).

3.2 Making a swimming droplet

3.2.1 Preparation of the solutions

The continuous phase (outer phase) is a solution of 25 mM mono-olein in Squalane (or eventually if precised, tetradecane), prepared as follow:

(i) A glass vial is weighted with its cap.

(ii) On a precise balance, we weigh the mono-olein (Sigma Aldrich, 1-Oleoyl-rac-glycerol, M7765-1G). The aim is 0.0446 g of mono-olein for 5 mL of final solution.

(iii) We carefully rinse with squalane the tip of a 5 mL micropipette. Then we add 5 mL of Squalane (Sigma Aldrich, Squalane 96%, 234311-500G) to the vial.

(iv) The vial is closed, lightly shaken, and placed 5 min in a 70^{o}C oven, which help with the solubilization of the mono-olein. If all mono-olein hasn't been solubilized after 5 min, one can shake vigorously the solution, and place it in the oven for 5 min more.

(v) After cooling, the vial is weighted to compute the exact amount of squalane added, and to deduce the exact concentration of mono-olein.

(vi) The solution is stored in a syringe from which all air is expelled. Such solution can be kept up to one month in an environment of more than 25^{o}C [8] (for instance an oven, is the room temperature is too low).

The discrete phase (the droplet) is made from milli-Q water, eventually when precised adding salt (Sigma Aldrich, Sodium Chloride, S7653-1KG). To make a solution of 100 mL of 15% wt NaCl in water, we weight 15 g of salt in a 100 mL glass vial, and complete with water so that the whole solution weight 100 mg.

3.2.2 One droplet: Femtojet

In the chapters (4), (5) and (7), we study the behaviour of isolated droplets. One of the drawbacks of microfluidic devices is that it is difficult to make only one droplet at a time. For this, we need another setup which uses an injection needle filled with the water solution, and linked to a pressure controller apparatus, the Femtojet (Eppendorf's electronic micro-injectors Femtojet® 4i with a built-in compressor)

3.2.2.1 Femtojet: Making one droplet ...

The steps necessary to make a water droplet are described in the following, and the setup is illustrated in Fig. 3.8(a) and (b):

(i) The injection needle (1) is made from a 1 mm inner diameter glass cylindrical capillary, using a Needle Pipette Pullers (Kopf® Model 720 Needle Pipette Pullers), and opened using a micro-forge (NARISHIGE MF-900 micro-forge) so that the tip of the needle has an inner diameter of approximatively 10 μm. It is then filled with the water solution using a microloader (Eppendorf's Microloader^{TM}).

(ii) The injection needle connected to the Femtojet (3) through an air tube (2). The Femtojet allows to impose a small pressure[9] (down to 5 hPa above the

[8] The mono-olein crystallize below 25^{o}C . The crystallization disappears if the solution is placed in the 70^{o}C oven for 5 min, but without knowing the effect of such process on the solution, we prefer to avoid this situation.

[9] The Femtojet allows to impose a continuous pressure, but also an injection pressure and injection time if one wants to impose a pulse of pressure, but we do not use these two parameters.

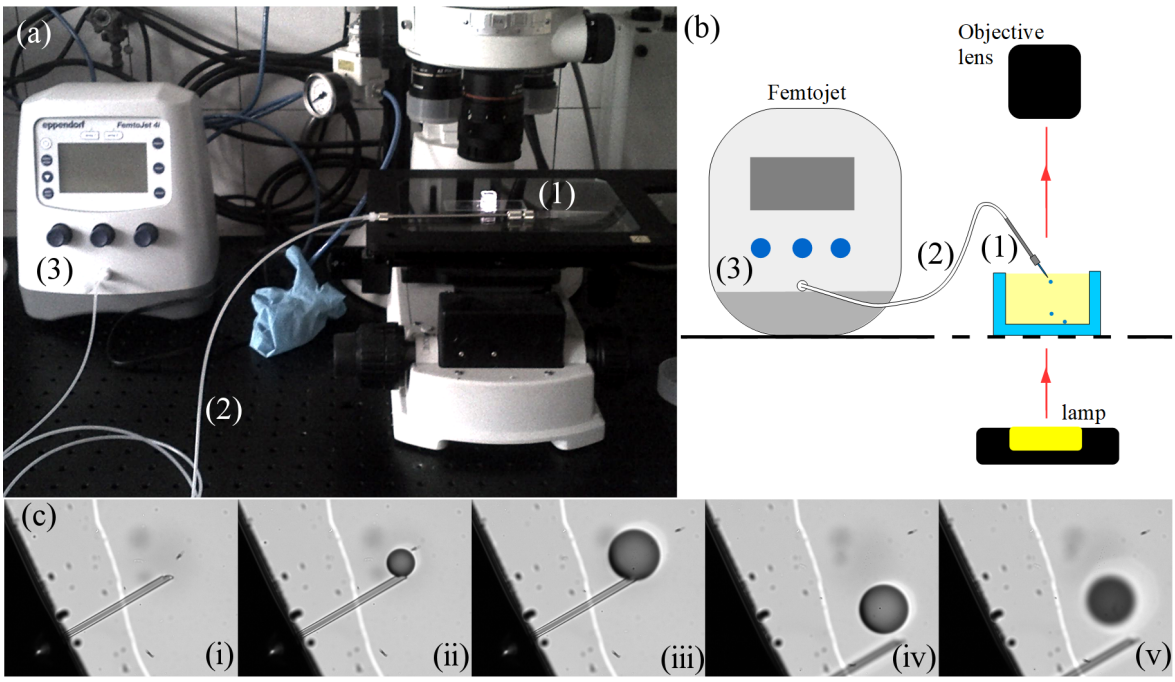

Figure 3.8: **Making an isolated droplet with the femtojet:** (a) image of the femtojet (3) linked with the water filled needle (1) by an air tube (2). (b) Sketch of the same femtojet: by controlling the pressure in the air tube, unique water droplet can be made directly in the observation chamber, and observed through the macroscope. (c) Time sequence of the creation of a water droplet: (i) $t = 0$ s, the needle is immersed in the oil. (ii) $t = 3$ s, the pressure is turned on, a droplet starts forming at the tip of the needle, until it reaches a suitable size at $t = 12$ s (iii). (iv) $t = 13$ s the pressure is cut and the needle removed simultaneously: the droplet detaches from the needle. (v) $t = 15$ s the droplet falls at the bottom of the observation chamber.

ambient pressure) at one end of the injection needle. The injection needle is fixed on a three-axis manipulator (NARISHIGE U-3C, three-dimensional coarse manipulator), and introduced in the oil solution.

(iii) The oil phase enters the injection needle by capillarity. Using the Femtojet, the pressure at the other end of the injection needle is increased to balance the capillarity until the oil-water interface reaches the tip of the injection needle. Then the pressure is increased a little more to form the droplet: the droplet swells slowly enough that it is possible to control its size by eyes, by increasing or decreasing the pressure. Once it reaches the desired size, the pressure is set back to zero, and simultaneously, a little kick is given to the needle to detach the droplet. A time sequence of a droplet production is given in Fig. 3.8(c).

3.2.2.2 ... In all kind of chambers

One advantage of this droplet making setup is that one can use a wide variety of observation chambers, in different materials (NOA, PDMS, glass, silanized glass), and in different geometries (chamber, capillary, complex microfluidic device)... The different observation chambers used through this work are described below.

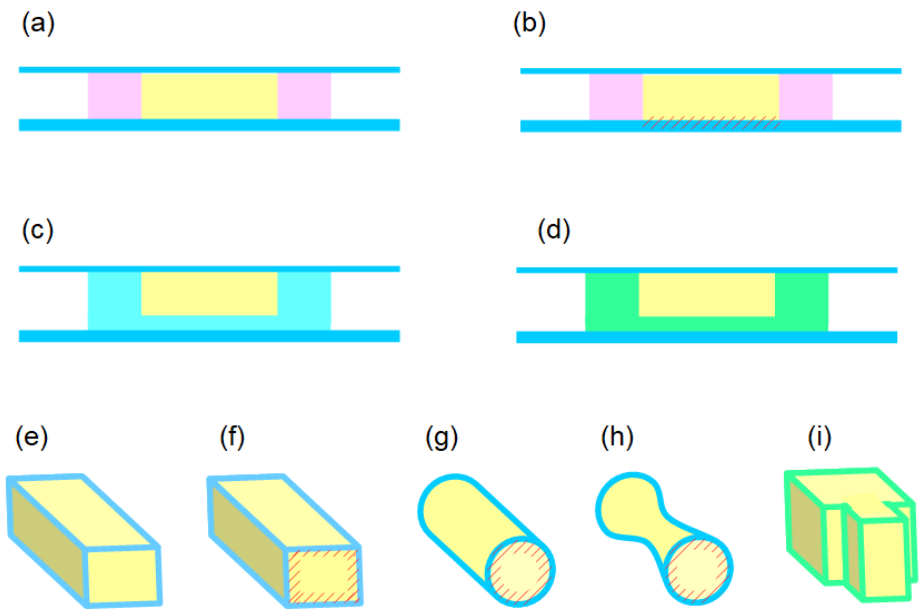

Figure 3.9: **Different types of observation chambers:** Observation chambers used to study isolated droplets. (a) to (d): 2D chambers. (a) Glass chamber (blue) delimited by double face tape walls (pink). (b) Silanized (red hatching) glass chamber (blue) delimited by double face tape walls (pink). (c) PDMS chamber (light blue) between two glass slides. (d) NOA chamber (light green) between two glass slides. (e) to (i): 1D chambers. (e) Square glass capillary. (f) Silanized (red hatching) square glass capillary. (g) Silanized (red hatching) cylindrical capillary. (h) Silanized (red hatching) stretched cylindrical capillary. (i) Square constriction in NOA.

2D chambers: they are constituted of one bottom wall and circular side walls of various natures. The chamber is completely filled with the oil solution, and closed with a glass coverslip after injection of the water droplet.

Fig. 3.9(a) - **Glass chamber:** the bottom wall is a glass slide. The side wall are made using either double face tape (Fimolux, Gudy 800 double face tape cut using a cutting plotter), or PDMS.

Fig. 3.9(b) - **Silanized glass chamber:** the bottom wall is a silanized glass slide. The different silanization processes are described below. The side walls are like for bare glass, double side tape or PDMS.

Fig. 3.9(c) - **PDMS chamber:** the PDMS chamber is made using Sylgard PDMS (Dow, SYLGARD^{TM} 184 Silicone Elastomer Kit). The bottom wall is made of a flat piece of PDMS, put on a glass slide. Side walls of a certain height h are obtained by making a circular hole in another PDM piece.

Fig. 3.9(d) - **NOA chamber:** the NOA chamber is made using NOA81 (Norland Products Inc., Norland Optical Adhesives 81), a liquid adhesive that is cured using a UV lamp. The shape of the chamber is obtained by molding the NOA on a reverse circular PDMS stamp [119].

1D chambers: they are elongated structure, such as capillaries or channels. They are filled with the oil solution, then a droplet is made by inserting the injection needle

inside the capillary or the channel. The two ends of the device are left opened to the air.

Fig. 3.9(e) - **Square glass capillary:** we use square glass capillaries (Hollow Square Capillaries manufactured in Borosilicate Glass, VitroCom's Vitrotubes^{TM}) of length 5 cm, and of four different inner dimensions: $2h = 400$ μm (Product ID 8240), $2h = 200$ μm (Product ID 8320), $2h = 100$ μm (Product ID 8510) and $2h = 80$ μm (Product ID 8508).

Fig. 3.9(f) - **Silanized square glass capillary:** the square glass capillaries $2h = 200$ μm described before are silanized using the silanization method described below.

Fig. 3.9(g) - **Silanized cylindrical glass capillary silanized:** we use cylindrical glass capillaries (Hollow Round Capillaries manufactured in Borosilicate glass, VitroCom's Vitrotubes^{TM}) of length 10 cm, and of two different inner dimensions: $2h = 200$ μm (Product ID CV2033) and $2h = 100$ μm (Product ID CV1017). The silanization method is described below.

Fig. 3.9(h) - **Silanized stretched cylindrical glass capillary:** the $2h = 200$ μm cylindrical capillary described before may be stretched (the method is described in details in section (5)).

Fig. 3.9(i) - **Square NOA constriction:** a square NOA section is designed by pouring and curing NOA on a PDMS mold. The PDMS mold is obtained using the same method than for making a microfluidic device, described in section (3.2.3).

PDMS and NOA are naturally hydrophobic materials. The glass however, is hydrophilic. If the droplet does not move for a long time (for instance if it has "poisoned" itself) it is observed to stick to glass. In order to prevent the sticking, the surface of glass can be silanized.

Liquid phase silanization: All manipulations are done under a fume hood, and we take special care to not introduce water in the system (water neutralize the silane and leave white marks on the glass). We used a home-made method developed by Dae Seok Kim during his Post-Doc at the Gulliver laboratory.

(i) Cleaning the chamber with successively pure ethanol, acetone, water and pure ethanol.

(ii) The chamber is soaked 5 min in a solution of 4 mL hexane (sigma aldritch, 296090, hexane), 1 mL chloroform (sigma aldritch 288306, chloroform), and 20 μL OTS (sigma aldritch 376213, Trimethoxy(octadecyl)silane).

(iii) The chamber is left under the fume hood to dry for 5 min.

(iv) The chamber is soaked 2 min in 5 mL chloroform.

(v) The chamber is dried with a air gun.

(vi) The chamber is dried on a hot plate (in a glass recipient) 2 min at 120^{o}C , and 6 h at 200^{o}C .

(vii) Right before use, the chamber is washed with pure ethanol.

3.2.3 Many droplets: microfluidics

In the chapter (6), we look at collective effects of droplet in 1D. The advantage of using a microfluidic device to make droplets is that it is possible to make many droplets of controlled and mono-disperse size in little time. The setup and method for making swimming droplets in a microfluidic device have been developed successively by Ziane Izri and Marjolein N. van der Linden. This section describes the necessary steps with some useful tips to design the microfluidic device and produce swimming water droplets.

3.2.3.1 Conception: choice of the microfluidic device

Note that we are trying here to make water in oil droplets, while the most usual system in microfluidics is oil in water droplets. There is several ways of making droplets using microfluidics device [120]. The process finally chosen was the step emulsification process [121] for its simplicity and robustness. This process is schematized in Fig. 3.10(I). In this method, the oil and the water are pushed through a quasi 2D channel (of height $h = 10\mu$m, small compared to its thickness $L = 200\mu$m) with certain flow rates, Q_o and Q_w through the inlets (a) and (b). A three phases laminar flow oil-water-oil is formed through a quasi 2D T-junction (A.), and is then pushed into a quasi 2D microchannel that leads to a step change in height (B.). Monodisperse drops are produced at this location and transported through a square channel to the observation chamber (C.). A trash outlet (d) and a oil dilution inlet (c) are added to be able to control what enter the observation chamber, and to decrease the droplet density if necessary. The size of the droplets is controlled by the channel height and the flow rates. The final chip have three inlets (water inlet (a), oil inlet (b) and dilution inlet (c)), whose flow rates are all controlled separately, and two outlets (trash outlet (d) and observation outlet (e)). All inlet and outlet can be opened and closed through external valves.

3.2.3.2 Fabrication: from a mask to a working chip

To reduce as much as possible the response time of the device to external flow, the material to make the microfluidic chip was chosen to be NOA81 [119] (Norland Optical Adhesive), which has a higher elastic modulus than PDMS (typically 1 GPa, versus 1 MPa for PDMS), and thus is less deformable under pressure.

A mask is first drawn using the software ©Adob Illustrator (shown in Fig. 3.10(I)). A positive mold of the device is made on a silicone wafer covered with positive photo-resist SU8 using a soft lithography process [122]. A PDMS negative stamp is made from the mold and silanized [123], and a second positive PDMS stamp is made from the first one. This second stamp will be used for making several NOA chips. A sketch of a side view of the final device is shown in Fig. 3.10(II).

The method for making the NOA device is as follow:

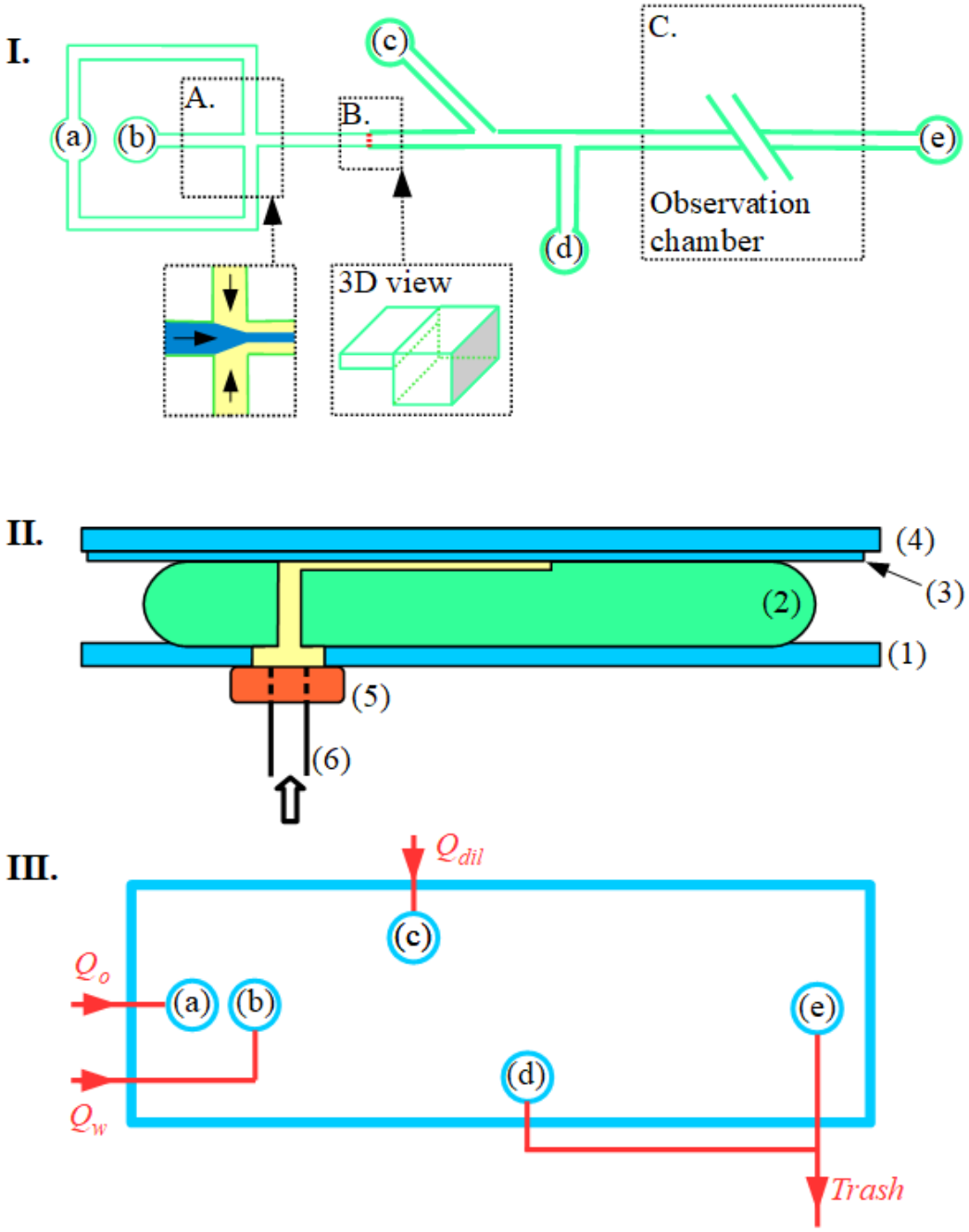

Figure 3.10: **Microfluidic device: I.** Device for making droplet: (a) oil inlet, (b) water inlet, (c) dilution inlet, (d) trash outlet, (e) observation outlet. (A.) 2D T-junction (inlet Sketch of the flows), (B.) step in height (inlet, 3D view), (C.) Observation chamber. **II.** Side view of the microfluidic chip: (1) pierced glass slide, (2) NOA circuit, (3) glass coverslip, (4) glass slide, (5) microfluidic connection, (6) tubing. **III.** Flow circuit, with the same notation as I. More precision on the functioning of this device is given in the text. Q_o, Q_w and Q_{dil} are respectively the flow rates of oil, water and dilution oil.

(i) A microscope slide (1) is pierced using a CO2 laser cutter, making holes that will be the inlet and outlet of the chip.

(ii) The NOA (2) is poured[10] on the PDMS stamp[11]. Then the stamp is applied on the pierced glass slide[12], and the holes are aligned with the chip. A first quick UV exposure is done so that the NOA starts reticulation, while the surface remains active. The stamp is removed, and hole are pierced through the NOA, aligned with the glass holes.

(iii) A glass cover slip (3) is placed on top, and a second long UV exposure is done to complete the reticulation. To reinforce the chip, it is possible to add a glass slide (4) on top of the glass cover slip, attached through a thin layer of NOA.

(iv) The whole chip is cured on a hotplate for 1.5 h at 150 ^{o}C . Then microfluidic connections[13] (5) are glued on the pierced glass slide to connect the holes to the tubing[14] (6).

3.2.3.3 Utilization: making droplets

All inlet and outlets are connected to valves[15]. The whole circuit is schematized in Fig. 3.10(III). The three inlets flow rates are controlled using independent syringe pumps[16], that imposes flow rates (a) Q_o for the oil inlet, (b) Q_w for the water inlet and (c) Q_{dim} for the dilution inlet. The two outlets (d) and (e) are linked to a trash recipient. The typical parameters were found using trials and errors: $Q_w = 1000$ μL/h, $Q_o = 300$ μL/h and $Q_{dil} = 300 \rightarrow 1000$ μL/h. Glass syringes of 1 mL are used to store the liquids.

We describe in the following the method established to make swimming droplets:

(i) Removing bubbles: The external circuit: tubing + valves + connections is washed carefully with ethanol to remove bubbles. The NOA ship is then connected to the external circuit, with all inlets and outlets closed by the valves, except for the trash outlet.

(ii) Turning on the flux: The water inlet is opened, and the water flux turned on[17]. Then the oil inlet is opened, and the oil flux is gradually increased until the water jet destabilizes and droplets are formed. It is then adjusted to control the droplet size. The dilution flux is finally adjusted to obtain the wanted dilution.

[10]It might be helpful to heat the NOA a few minutes at 50 ^{o}C C to decrease it viscosity and facilitate the impregnation.

[11]Be careful to avoid bubbles, a glass pipette might help.

[12]Covering the bottom face of the pierced glass slide helps preventing excess NOA through the holes.

[13]IDEX Health & Science, NanoPort Assembly Headless, 10-32 Coned, for 1/16" OD (N-333).

[14]IDEX Health & Science, FEP Tubing 1/16" OD x .030" ID (1520L), with a connection, : One-Piece Fingertight 10-32 Coned, for 1/16" OD (F120). We use rigid tubing in order to reduce as much as possible the response time of the device.

[15]IDEX Health & Science, 4-Way Flow Valve PEEK (V-100T).

[16]Harvard Apparatus, Standard Infusion Only Pump 11 Elite Syringe Pumps (70-4500)

[17]Once a channel has been in contact with the oil phase, it is very difficult to wash. Thus one should be extremely careful that the oil phase never enters the water channel: the water flux should be always switched on first, and switched off last.

(iii) To the observation chamber: Once the right droplet size and dilution have been achieved, the trash outlet is closed and the observation outlet opened so that the droplets are led to the observation chamber. When the needed droplets have filled the observation chamber, the observation outlet is closed, the trash outlet is opened, and all flow are stopped (gradually, the water flow the last one), and inlets and outlets closed except for the trash outlet in order to relax residual pressure in the circuit.

3.3 Observation tools

3.3.1 Observation of a droplet

To observe the droplet behaviour, we want to track the droplets over distance equal to several times their size, which is typically over distances as large as 1 cm.

3.3.1.1 Large observation area: macroscope

To observe such large area, we use a AZ100 Nikon macroscope, equipped with x1 air objective. The camera is a black and white camera Dalsa Falcon II, with a resolution of 4096 x 3072 pixels, at an acquisition frequency $f_{acq} = 1$ Hz. The macroscope has a continuous zoom between x1 and x8, and thus has a variable resolution, which is measured before each experiment by using a calibration slide. Typically, to visualize a chamber of 1 cm in diameter, we use the x3 zoom, which gives a resolution of 0.3 pix/μm.

3.3.1.2 Tracking

The acquisition can last up to two hours, at a frequency of 1Hz, obtaining up to 7200 8-bit images, namely almost 400 Go of data. We thus want to make the image analysis as efficient as possible to get the interesting data (droplets trajectories, velocity, shape...) as fast as possible. The image processing is done using Matlab® following three basic steps: the background subtraction, the droplet detection and the droplet tracking. For each of these steps, different strategies can be used depending on the system (resolution of the droplets, number of droplets...), which we present below:

- **Background subtraction**:
  - Small moving object in fixed background (most used method): the background is obtained by averaging the images over time (not necessarily all images, it might be a sample). The background is then subtracted to each image and the image inverted, so that the object of interest, the droplet, is white. This step is illustrated in Fig. 3.11a and b.
  - Small fixed object or mobile background: the background is obtained by taking a Gaussian filter of an image. This is especially useful to correct illumination gradient in the image.

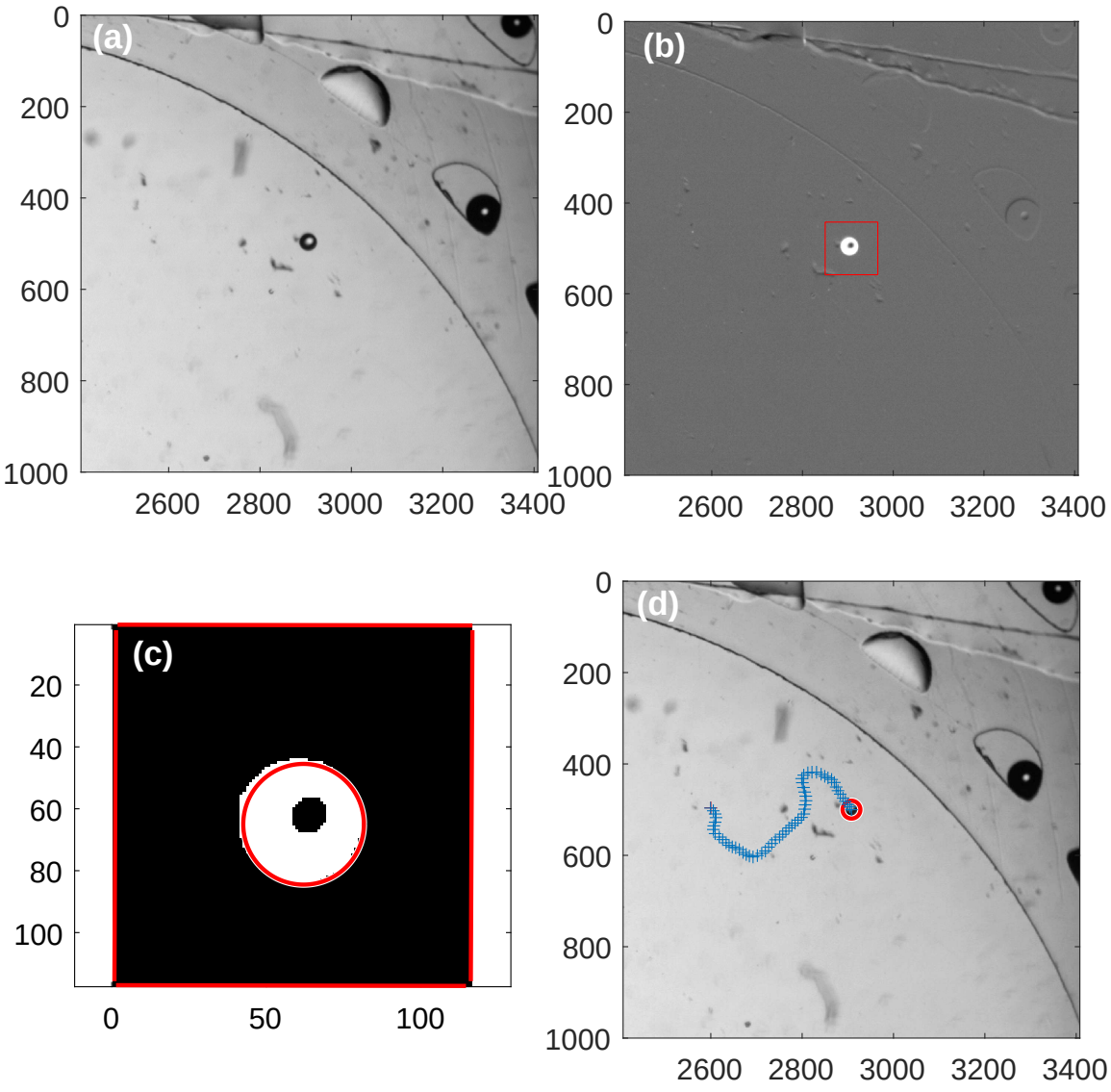

Figure 3.11: Illustration of the complete tracking process (the axis are in pixels). (a) Initial image. (b) Image after subtraction of the background, and windows computed from the previous droplet position, in which the droplet is expected to be. (c) Zoom on the windows computed from the previous droplet position after treatment and binarization, and detection of the droplet. (d) Computed trajectory of the droplet.

  - Big object: When the object is big (of the order of one half of the image), then we usually don't compute a background, as the main signal is already the object.

- **Droplet detection**:

  - Large circular objects ($a > 20$ pixels): the function "imfindcircles" of Matlab detects all circular objects of a certain radius range in an image using the circular Hough transform. Advantages of this method is that it can discriminate two adjacent circular objects, and can be used on grayscale images. A drawback of this method is that it is time consuming (the actual time depends on the radius range). The precision of this method is typically a few pixels. This method is preferentially used when there is a lot of droplets.
  - All objects for binary images: the function "bwconncomp" of Matlab finds connected components in a binary image. Advantages of this method is that it can detect any object shape, and is quick compared to "imfindicicles". A drawback is that it can't discriminate between two adjacent objects. We show an example of the result of this method in Fig. 3.11(C).

  The droplets are detected in each image, but in case there is more than one droplet, we need to be able to recognize the same droplet between successive time steps.

- **Droplet tracking**:

  - One possibility to track the droplet would be to brutally compute the average distance between the droplets in one image to the following one for the $N!$ possible combinations of droplets. This method is very costly in time, and thus an alternative method was chosen.
  - Typically, a droplet of radius $a = 100$ μm swims at a velocity $V = 50$ μm/s, thus between two images, the droplet moves no further than half of its radius. Exploiting this slow swimming of these droplets, we define a moving windows (of size typically 5 times the droplet radius) around the position of the droplet in the previous image, and look for the position of this same droplet in this window. The two advantages of this method are that the droplet detection is done only on a small window, and the tracking is done automatically, at the same time as detection, thus reducing significantly the processing time. This is illustrated in Fig. 3.11(C) and (D).

Choosing between these processes the one that suits the image the most, one obtains the trajectories and the radius of the droplets over time, and can compute some other variables such as the velocity V, the persistence length, the variation of the radius over time κ, etc...

Post processing: some tracking mistakes, or some experimental perturbations (such as the presence of dirt, or poisoning of the droplet) can occur throughout an experiment. For each experiment, a post processing step is used to check the quality, and if needed, to select the "good time" at which the tracking is correct and the droplet behaviour not perturbed by unwanted factors.

3.3.2 Observation of the flow field around the droplet

To visualize a flow, one method is to seed small particles in the outer liquid. This requires a smaller observation area, but a higher resolution, and the possibility to visualize in multiples planes to have a 3D resolution, which is why we use a confocal microscope section. To extract an actual flow field from these particles, we use a technique called micro-PIV.

3.3.2.1 Choice of a tracer:

A good tracer is small enough to not disturb the flow (ideally smaller than 1 μm), but big enough to be visualized. We want to visualize the flow of oil, and thus we need a tracer that can be suspended (meaning they can be dispersed, they don't agglomerate and they don't sediment) in oil, which is unusual as most colloids are made to be suspended in water (in particular they have the same density as water). All these constrains made us spend some time finding the best possible tracer.

1. **Sandra's shell:** a first option was to use specially designed polymeric shell (see figure 3.12) of typically 10 μm of diameter. They were created by Marie-Alice Guedeau-Boudeville and Sandra Lerouge at the Matière et Systèmes Complexes Laboratory of Paris Diderot University. These shells are made of successive layers of polymers. They are transparent, index matched with water, dyed with red fluorescence, and porous. That porosity allows them to be density matched with any liquid they are in, so that they don't sediment.

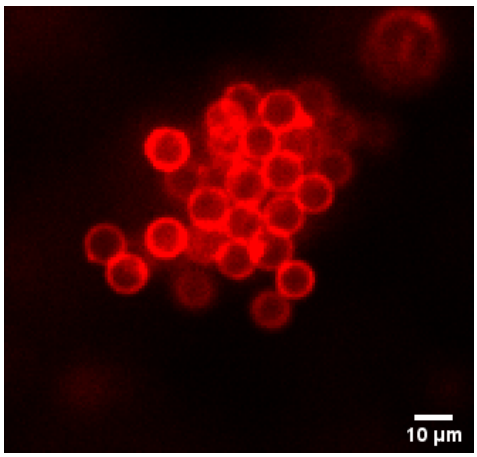

Figure 3.12: Image of the polymeric shells designed by Sandra Lerouge under the confocal microscope, X40 objective, the illumination is done by a laser beam of wavelength 543 nm.

Method:

(i) Sandra's suspension of shells in THF are stored in the fridge, in a quartz tube.

(ii) Prepare the oil solution of 25 mM mono-olein in Squalane.

(iii) Desiccate a few seconds the shell suspension in THF.

(iv) Under fume hood: In a centrifuge tube in quartz, put $80\mu L$ of Sandra's suspension of shells in THF and 60 μ L of the oil solution.

(v) Desiccate a few minutes the solution of THF, oil and shells in the quartz tube closed with parafilm.

(vi) Let the THF evaporate one night by letting the tube open under the fume hood.

(vii) Under microscope, if you observe that the shells are still forming agglomerate, desiccate once more a few minutes.

(viii) Always desiccate a few minutes right before experiment so that the shells are well dispersed.

Precautions:

- As long as there is THF in the solution, be sure to operate under a fume hood, or to close hermetically the vials with parafilm.
- The shells are fragile. Do not heat them, or desiccate them for too long.

The shells don't sediment. Once well dispersed, they still aggregate a little. There is a few limitations to the use of these shells. First, they are long and difficult to make, so our stock are limited. Second, they are a little too big to be considered compared to what we would like.

2. **Small colloids**: another way to avoid sedimentation is to use very small particles so that the sedimentation will be slow enough to be neglected during the experiment time. We used 0.6 μm red fluorescent colloids tracers (Fluoro-Max^{TM}, 0.6 μm Red Fluorescent Polymer Microspheres, Thermo-scientific). Their density is the same as water, so they are slowly sedimenting.

method:

(i) Prepare the oil solution of 25 mM mono-olein in Squalane.

(ii) Put 2 drops of the aqueous colloid suspension in a 1 mL centrifuge tube. Complete with ethanol.

(iii) Centrifuge 5 min at 5000 rcf (Relative Centrifugal Force). Take out the top liquid, and refill with ethanol. Desiccate the tube to disperse the colloids. Repeat this sequence three times.

(iv) Take out the top liquid. Put the tube open for 15 min in a 40 ^{o}C C oven to evaporate all the ethanol.

(v) Add the oil solution in the tube.

(vi) Before each experiment, desiccate the suspension of colloids in oil for 15 min so that the colloids are well dispersed.

(vii) It is possible to reuse the suspended colloids if the oil is too old by centrifuging the tube, take out the old oil and refill with some new oil.

These colloids sediment, but the sedimentation is negligible for experiments shorter than 15 min.

Because colloidal beads are much simpler to handle and use, and because they are smaller, we mainly use them for the PIV in all the following. The seeding is set as around 2.5 10^{-3} colloids/μm ^{3}, which corresponds in an illumination plane to little more than one colloid per μm ^{2}, or one colloid per two pixels.

3.3.2.2 Acquisition

We want to look at the flow field around a droplet of typically 100 μm in radius, while resolving fluorescent particles of around half a micron. For this purpose, we use a confocal microscope with a x10 air objective, which gives a field of view of typically 500 μm, and a resolution of 0.65 μm/pix. This resolution is not enough to actually visualize the tracer (the tracer size is one quarter of a pixel), but it is sufficient to visualize pattern in the tracer concentration. The images are acquired with a CCD camera (Andor Zyla 5.5). The acquisition frequency for the flow field visualization is 10 frames/s and the exposure time is 50 ms. The microscope can be used with white light, or with a laser beam at 540 nm, which is the absorption wavelength of the tracers.

3.3.2.3 Computing the flow field

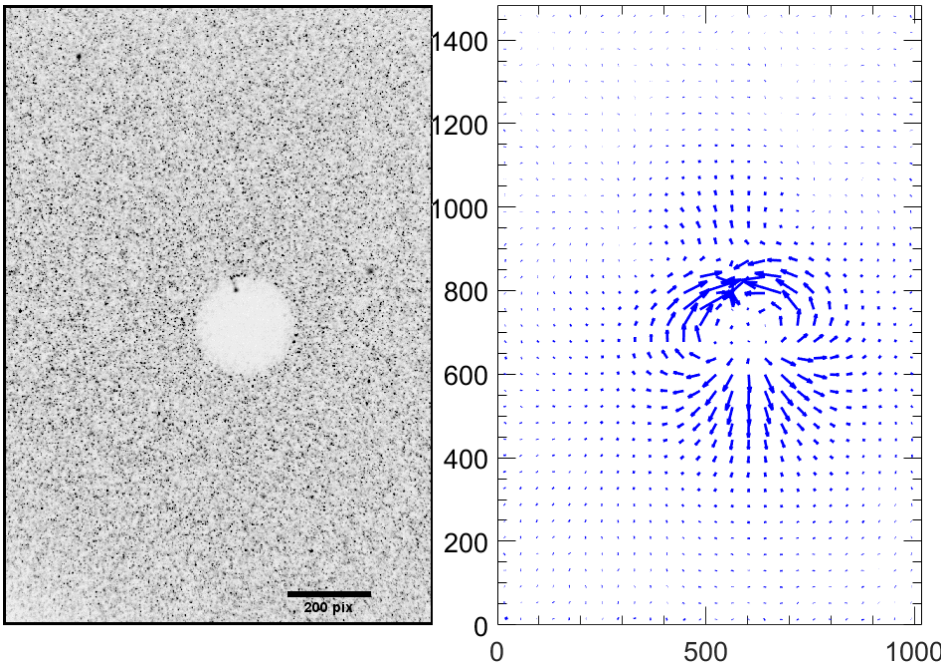

Figure 3.13: (a) Reversed image (for better eyes visualization) of the tracers (in black) around a droplet (in white). (b) Typical flow field computed using "PIV_ lab".

The tracers placed in the outer fluid allow to visualize the flow field. To quantify it, we use the The Particle Image Velocimetry (PIV) method to compute the local flow field [18]. The principle is to use cross correlation between successive images to follow the evolution of patterns in a certain window size (the pattern being in our case the tracers). We use the "PIV_ lab" [124] an open source Matlab code. After

[18]The chapter II of the thesis [124] can be used as a basis to understand the PIV process. A review on the experimental realization of micro-PIV can be found in [125]

pre-processing the images with a Wiener filter (window size of 3 x 3 pixels), we use two successive paths of integration using correlation areas of first 50 x 50 pixels and then 25 x 25 pixels, with a sliding step of 50% of the correlation area. Doing so we obtain the velocity components $V_x(x, y, z, t)$ and $V_y(x, y, z, t)$ with a spatial resolution of 8 μm (around 8% of the droplet radius) for each pair of successive images.

Let us end with stating some limitations of the experimental method. In planes other than the median plane, the quality of the imaging is altered when the incoming light goes through the droplet. As a result, the PIV cannot be performed inside the vertical cylinder tangent to the droplet in the median plane. Also, for distances larger than five droplet radii, the signal to noise ratio is too small to extract reliable velocity fields.

Part II

Experimental and theoretical work

Chapter 4

Swimming in 2D

Motivation

The second section of this chapter is mainly a published article [1], which has both an experimental and a theoretical approaches. Before presenting the results from the paper, in section (4.2), we start by a detailed section on the experimental approach, in section (4.1).

Be it in a biological environment or in a microfluidic device, in many cases, microswimmers do not evolve in a 3D infinite and unbounded medium [39], and several observations indeed reveal the critical importance of confinement on the swimmer's dynamics. Several microswimmers are attracted by the boundaries [40, 41, 42], which can then be used to capture [43, 33], or steer the swimmer motion [44, 45, 46]. The presence of a boundary has been observed to influence not only the motion of a single particle [47, 48, 49] but also the collective behaviour and phase transitions of swarms [50, 51, 52, 53]. Ultimately, the interactions with boundaries can be used to harvest energy from a population of swimmers [54]. Obtaining a reliable description of the interactions of a swimmer with a wall is thus of significant importance. It is also a first step towards a better understanding of the interactions among swimmers and thereby the emergence of collective behaviour [55, 91]

For swimmers driven by mechanical surface distortions, it is reasonable to assume that hydrodynamic mechanisms are the dominant contributor to the motion. If the mechanical surface distortions at the origin of self-propulsion are not modified by the proximity of the wall, a squirmer description can be used with a prescribed and unaltered slip velocity. Even in this simplified context, solving for the exact flow around a squirmer in the presence of a wall is in general not possible. Currently, the only exact solution is that of the flow field resulting from the motion of an axisymmetric squirmer approaching a wall, along the wall normal direction [94]. One way out consists of describing the squirmer as a linear combination of fundamental solutions to the Stokes equations and using the methods of images [92] to compute the flow field in the presence of a wall. Such a strategy has been applied recently to the case of an axisymmetric swimmer [93]. Focusing on characterizing the accuracy of the far-field approximation, the authors show that this simplified description can be very useful, and quantitatively predictive, for describing the behaviour of a selection of swimmers

close to a wall. Such an approach will be used is this chapter, in section (4.2.3).

Considering now the case of phoretic or Marangoni swimmers, the self-generated external field, responsible for the swimming motion, is likely to be distorted by the presence of the wall, which alters the diffusion of the physico-chemical field. This was first illustrated in [95], before it was indeed demonstrated that in the presence of boundaries the behaviour of chemically active colloids is qualitatively different, even in the far field, from the one exhibited by the corresponding "effective squirmer" [96]. Focusing on the near-wall motion, general analytical solutions for the concentration field, velocity and rotation of the swimmer, as a function of distance and orientation of the active cap with the surface, were obtained in the form of infinite series expansions [97]. These solutions were then used to compute general trajectories and categorize the swimming regimes. Yet, for such expansions, the correspondence between each term (i.e. angular mode) to a precise set of hydrodynamic singularities of increasing order is lost, in stark contrast with the classical decomposition of the flow field generated by a spherical swimmer in unbounded flow [90].

Experimental studies of the effect of confinement on phoretic swimmers concentrate on the kinetics of the particle trajectories and very little is known about the actual flow field. On some occasions, it has been measured in the median plane of the swimmer [126, 111, 52, 127], and used for qualitative discussion. Yet, a precise and quantitative description of this flow field is critical, in particular to understand the role of hydrodynamic coupling between swimmers in setting their collective dynamics. To our knowledge, the three-dimensional flow field around a phoretic swimmer remained to be fully characterized experimentally, one obvious reason being that most phoretic swimmers are micron-sized particles, for which such an analysis would require truly high-resolution measurements.

In such a context, we first look in section (4.1) at the kinetics of our droplets trajectories, looking at how the presence and the nature of a wall affect their behaviour. In a second time, in section (4.2) we take advantage of the large size of the droplet – typically 100 μm in radius – to perform PIV measurements in 3D, using confocal microscopy, of the hydrodynamics flow around the swimmer.

4.1 Kinetics in presence of a wall

A first step in understanding the effect of a wall on a swimmer is simply to look at the kinetics of the swimmer close to a wall. For this we design circular chamber of typical diameter 1 cm. A chamber is typically constituted of a bottom wall, a circular side wall and a top wall. The whole chamber is filled with the oil solution so that there is no liquid-air interface. We use three different chambers, varying the nature of the bottom wall (section (3.2.2.2)). (1) A glass bottom wall is made by using a glass slide. (2) A silanized glass bottom wall is made by using a silanized glass slide. For these two chambers, the side walls are made in tape. (3) A NOA bottom wall is made by using a NOA chamber, the side wall are also in NOA. All chambers are closed by a glass cover-slip. The half-height of the chamber is $h = 150$ μm. All chambers have an entry channel on the side, large enough so that we can insert the water filled needle (section (3.2.2)) and produce the droplet directly inside the chamber. One experiment

consists in making one pure water droplet of a certain radius a in the chamber filled with a solution of 25 mM monoolein in squalane.

The water being denser than the surrounding oil medium, the droplet naturally swims at the bottom wall of a micro-fluidic chamber. The swimming droplets basically have a 2D motion. Very small droplets ($a < 50$ μm) may exhibit "3D" motion by "bouncing" out of plane, but remain in the vicinity of the bottom wall. We do not study this effect. The capillary length of our system being 1 mm, our droplet, whose maximum radius is $a = 300$ μm can always be considered spherical (except if some external geometrical constrain prevent them of being so, for instance in the case where they are larger than the chamber height).

The chamber is observed through the macroscope (section 3.3.1.1)), and the image acquisition is made at a typical frequency of 1 fps. We use image analysis tools (section 3.3.1.2)) to track the droplets. We get the evolution of droplet position and size with time.

4.1.1 Typical swimming behaviour

This is a very descriptive section of the behaviours of one droplet swimming alone in the chamber.

The droplet starts swimming upon production. When it attains a constant velocity, we considered that it reached its steady state (this may take a few hundred seconds). A typical experiment is presented in Fig. 4.1.

The droplet normally swims straight ((1) and (3) in Fig. 4.1), with a persistence length (the length over which correlations in the direction of the swimmer are lost) that strongly depends on its size (qualitatively, the larger the droplet, the lower the persistent length). Several events may happen during an experiment, which comes to disturb this steady state: meeting the chamber's wall ((2) and (7) in Fig. 4.1); meeting its trail, and thus a region with swollen micelles, which is repulsive ((5) and (6) in Fig. 4.1); or a sudden turn in the trajectory ((4) in Fig. 4.1), which is not due to any visible cause. All these events have an impact on the droplet velocity: the droplet generally slows down and/or changes direction. After the event, the velocity relaxes once again toward its steady velocity. Note that the droplet radius is as expected observed to decrease with time.

We now focus on the interaction between the droplet and the chamber side walls, in Fig. 4.2. When the droplet collides with a wall, we observe two different behaviours: the first one is when the droplet aligns with the wall ((2), (3) and (6) in Fig. 4.2), and starts swimming along it with a certain velocity lower than when swimming far from the walls. This lasts for a while (the time spent at the wall varies a lot from one case to the other), until the droplet leaves the wall, generally abruptly (sudden change in the droplet direction). Most of the time, there is no obvious reason for the leaving of the droplet. The second behaviour is when the droplet simply bounces on the wall ((4) and (5) in Fig. 4.2). We do not observe any clear reason (such as the meeting angle, or the meeting velocity) that would discriminate one case from the other. The effect of the side wall will be slightly more studied in the section (4.2.4), by looking at the flow field around the droplet using PIV tools.

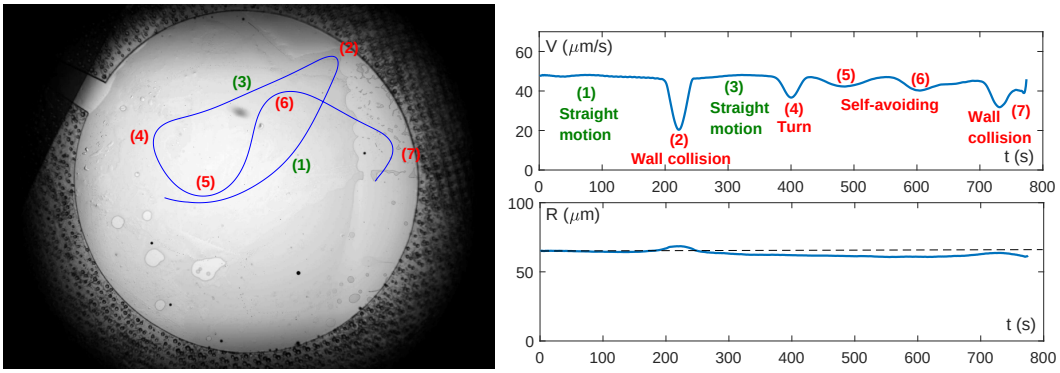

Figure 4.1: **Kinetics of a droplet swimming alone:** trajectory of a droplet ($a = 60$ μm, silanized glass bottom wall) swimming straight (1) and (3), but being disturbed by multiple events: collision with a wall (2) and (7), sudden turns (4), or self-avoiding its trail (5) and (6).

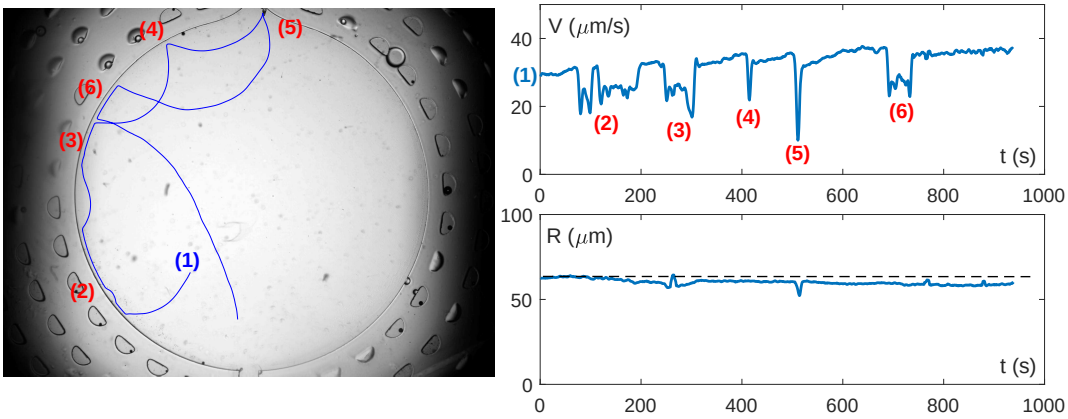

Figure 4.2: **Effect of the bouncing on the chamber side walls on the kinetics:** trajectory of a droplet ($a = 60$ μm, NOA bottom wall) with multiple interactions with the wall. The trajectory starts at (1). When meeting the wall, the droplet either aligns with the wall and follows it (2), (3) and (6), or simply bounces on it (4) and (5).

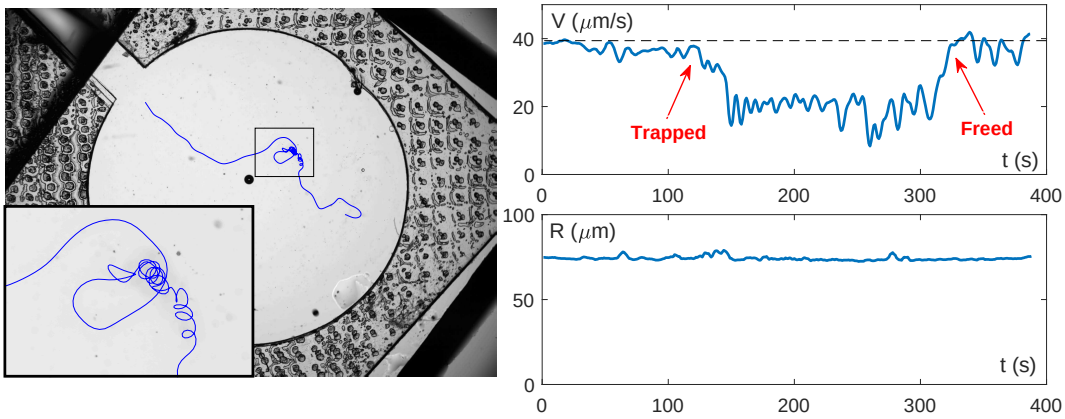

Figure 4.3: **Effect of the self-poisoning of a droplet on the kinetics:** trajectory of a droplet ($a = 75$ μm, glass bottom wall) which becomes trapped in its trail.

The effect of the trail of the droplet on the droplet behaviour is also non-trivial. While swimming, the droplet fills empty micelles from its environment, leaving behind a trail of swollen micelles. This trail is a region of high swollen micelles concentration, and thus is repulsive for the droplet (if one remembers the swimming mechanism of the droplet, the droplet goes away from high swollen micelles concentration region). The swollen micelles still diffuse with time, so the trail disappears, or at least weakens after a certain amount of time. In the experiments, the droplet are observed to avoid their own trail most of the time, but are still able to cross it when the trail is old enough, as it can be observed in Fig. 4.1 and in Fig. 4.2. The droplets may also end up in a situation where they cannot avoid their own fresh trail, such as the case in Fig. 4.3. They are then trapped in a region surrounded by swollen micelles. We observe that after being trapped, the droplet velocity drops considerably, but is not zero: the droplet continues to explore its environment inside the trap. The droplet continues to produce swollen micelles, which diffuse while empty micelles also diffuse close to the droplet: the concentration field inside the trap changes in an unpredictable way, which explains the disordered motion of the droplet. At some point, the droplet finds a breach in its trap, and is able to go out.

In the following, we are exclusively interested in the steady state of the droplet: when they swim at a constant velocity, with a straight trajectory, far from walls and from their own trail.

4.1.2 Effect of the nature of the bottom wall on the kinetics

We make several experiments of one droplet in a chamber made with either a glass, a silanized glass or a NOA[1] bottom wall. The droplet radius varies between $a = 10$ μm and $a = 180$ μm (which is a little larger than the chamber half-height, thus the droplet touches both the bottom and top walls, and is not spherical anymore). A first direct observation on the kinetics is that for a silanized glass bottom wall, the trajectories are always very straight (persistence length of more than the chamber width), and thus only the collision with the walls, or meeting its own trail makes the droplet changes direction. For bare glass bottom wall, the persistence length is smaller, and strongly depends on the droplet size: the bigger the droplet is, the "wavier" is its trajectory. Finally, for NOA bottom wall, the trajectory is "wavy" even for small droplets; and big droplets have erratic motion. We have not quantified this effect.

For each experiment, we measure the average of the velocity $\langle V \rangle$ and the mean square error for when the droplet is in a steady state (in the absence of dynamic events such as meeting wall or poisoning). The results are given in Fig. 4.4(a). Note that because of their erratic motion the big droplets on a NOA wall do not attain a steady velocity[2].

We make several observations:

[1]The NOA bottom wall was tested because previous experiments were done in microfluidics chamber made of NOA.

[2]The erratic motion of big droplets may be due to secondary instabilities, which is currently studied in the team of Masatoshi Ichikawa from the Laboratory of Dissipative and Biological Physics of Kyoto university.

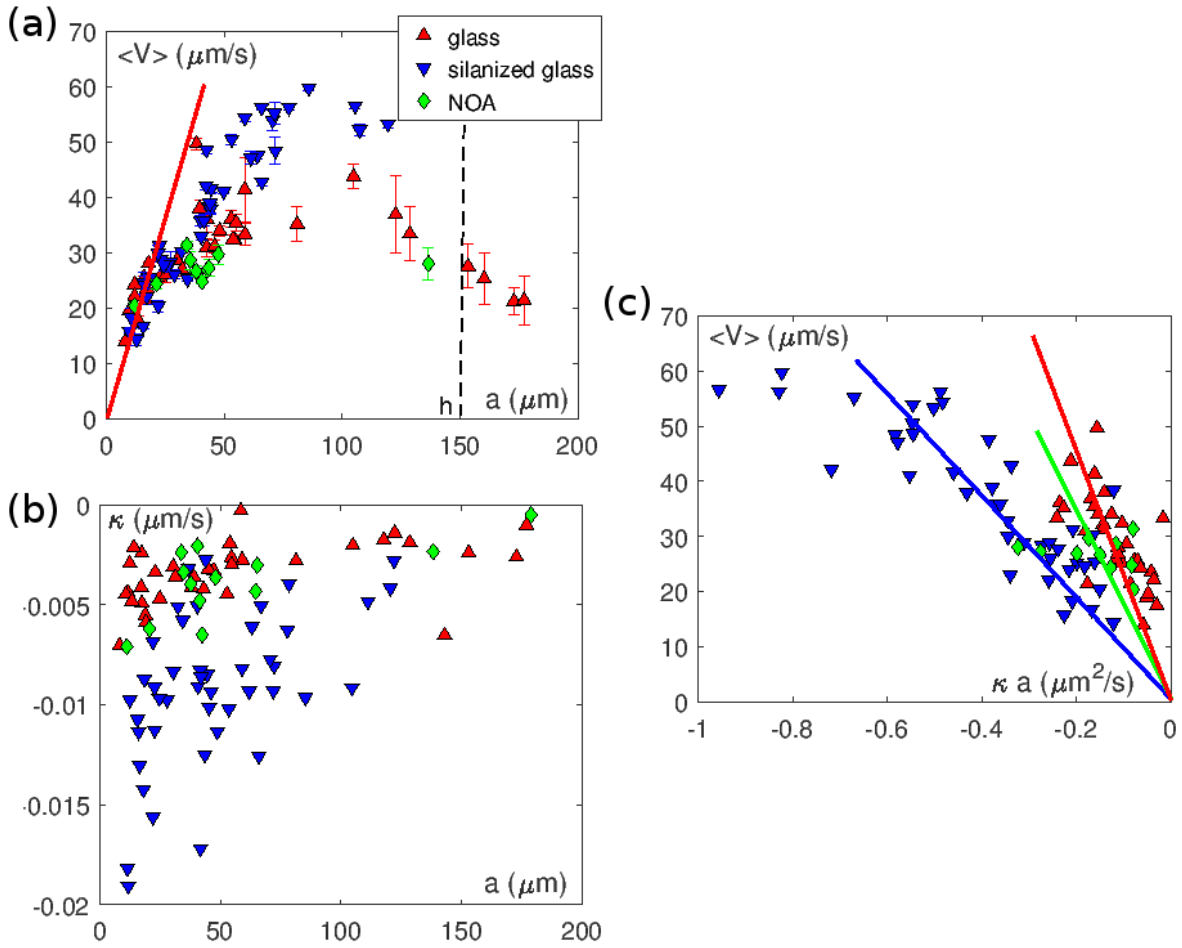

Figure 4.4: **Characteristics of the steady state, for different natures of bottom walls:** red upward triangles stand for a glass bottom wall, blue downward triangles stand for a silanized glass bottom wall and green diamond for a NOA bottom wall. **(a)** Dependency of the steady velocity of the droplet $\langle V \rangle$ on their size a. The red line represents the slop of the curve for small radius. The dashed line represents the half-height of the chamber. **(b)** Dependency of the steady shrinking rate of the droplet κ on their size a. **(c)** Dependency of the steady velocity of the droplet $\langle V \rangle$ on the product $a\kappa$

- For small droplets ($a < 50$ μm), the droplet velocity increases with the droplet size, in a similar way for all bottom walls. Remember that the swimming mechanism predicts that the velocity of the droplet should be proportional to a, assuming that the surface flux of swollen micelles is a constant, thus this result is expected.

- For medium droplets ($50 < a < 100$ μm), the droplet velocity still increases with the droplet size, but also depends on the nature of the bottom glass: the droplet is faster on silanized glass, which is hydrophobic, than on bare glass which is hydrophilic. This shows that the nature of the bottom wall has an influence on the velocity.

- For large droplets ($a > 100$ μm), the velocity starts to decrease when the radius increases. This happens when the droplet size is almost the size of the chamber.

This shows that the confinement has an influence on the velocity.

The effect of the confinement is not surprising: when confined, the droplet has less space to advect the outer fluid. Less trivial is the dependence on the nature of the bottom wall: the droplet is non-wetting, there is always a lubrication layer between the droplet and the bottom wall, thus there is no direct contact between the droplet and the wall. We can think of two possible effects to explain this influence. The first one is the influence of the slip velocity at the wall interface, which has been studied [128] in the case of catalytic colloidal swimmers near a wall. Surface slip depends on liquid surface interaction (between the outer fluid, the oil phase, and the bottom wall in our case). The fluid-surface interactions relate to the wetting properties of the liquid on the surface [129]. However, if qualitatively, our oil solution is observed to wet more glass than NOA, we do not observe a significant difference between glass and silanized glass.

The second possible effect is the influence of the thickness of the lubrication layer between the droplet and the wall, which may depend on the kind of surface. Indeed, these surfaces differ from their roughness, their charge... Which can affect their interaction with a droplet.

We also measured in Fig. 4.4(b) the evolution of the shrinking rate $\kappa = \frac{da}{dt}$ for different droplet sizes. On a glass bottom wall, and on a NOA bottom wall, κ does not depend significantly on the droplet size, and we measure $\kappa_G = -2.8 \cdot 10^{-3} \pm 2 \cdot 10^{-3} \mu$m/s and $\kappa_{NOA} = -3.9 \cdot 10^{-3} \pm 2 \cdot 10^{-3} \mu$m/s. Surprisingly, these values are smaller than the ones measured in [87] which were of the order of $\cdot 10^{-2}$. On silanized glass, the shrinking rate κ is faster, but also depends on the droplet size: the smallest the droplet, the fastest it shrinks.

In a similar way than in [87], we also plot the dependence of $\langle V \rangle$ with κa, and we indeed observe the linear scaling of the droplet velocity with κa, which is consistent with the swimming mechanism.

This first experimental section was about describing the kinetics of our droplet which, because of the density contrast, is swimming on a bottom wall. We presented typical behaviours of a droplet through an experiment, and we highlighted how the droplet size, the nature of the bottom wall and the confinement all played a role in two characteristic values of the droplet steady state, its steady velocity V and its shrinking rate κ. In a second time, we now want to investigate another aspect of the influence of a wall, namely how it affects the swimming mechanism itself through the study of the flow field.

4.2 Visualization of the flow field around the droplet

The study on the effect of a wall on the flow field has been the object of a paper [1], and its contents are exposed in this section.

Here, we take advantage of our large swimming water droplets - typically 100μm in radius - to present first-of-a-kind experimental measurements of the flow field around a swimming water droplet, using confocal PIV in three dimensions (Fig. 4.5).

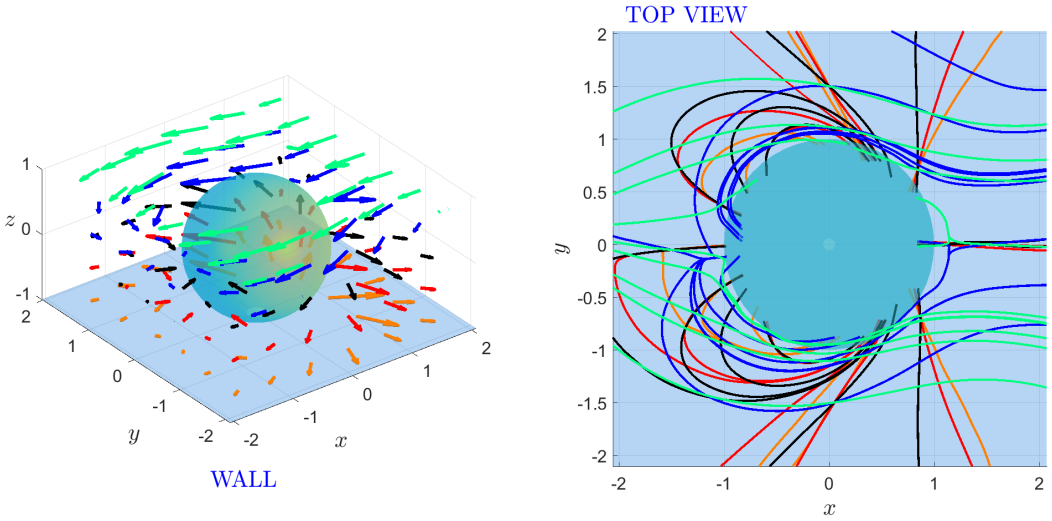

Figure 4.5: **Experimental flow field around a water droplet swimming close and parallel to the bottom wall of a microfluidic chamber:** Left: 3D reconstruction from the PIV analysis in planes parallel to the wall (blue plane). Right: Top view of the streamlines of the flow field. The color code indicates the height of the planes. Only a few planes are presented for clarity.

This section is organized as follow: in subsection (4.2.1), we expose in details the experimental realization and describing the PIV methods and data processing techniques. Subsection (4.2.2) synthesizes our main experimental findings regarding the flow field around a swimming droplet performing steady motion close and parallel to a wall. In section (4.2.3) the experimental flow field is then compared with that of an axisymmetric squirmer performing a steady motion parallel to the wall, as obtained following the methodology introduced in [93]. Finally, we also present in section (4.2.4) and discuss the experimental flow field obtained when the droplet is confined between two parallel walls separated by typically one droplet diameter, a situation of interest in many micro-fluidic devices, for which an analytical treatment remains an open question.

4.2.1 Setting

4.2.1.1 Experimental system

The experimental system consists of 15 %wt NaCl in water droplets, with radius $a \simeq 50$ μm, swimming in a solution of 25 mM mono-oleine in squalane. The droplets are produced using a ©Femtojet apparatus by injecting a single droplet of controlled size in a circular NOA chamber of diameter 1 cm (the design of such chamber is described in section (3.2.2.2)). In the so-called one-wall geometry, the chamber has height $2h \gtrsim 5$ mm $\gg a$ and is closed by a glass coverslip. In this geometry, the droplet swims at the bottom of the chamber, far from the top free surface since the water phase is denser than the oil phase ($d_{Sq} = 0.8$). In the so-called two-wall geometry, the chamber has height $2h \simeq a$ and is closed on its top by a NOA coated glass cover slip. In this geometry, the droplet swims confined between two walls.

The droplet starts swimming immediately and reaches steady motion after a few minutes, with a constant velocity $V_0 \simeq 20$ μm/s, following a trajectory with a typical persistence length of a few droplet diameters. The droplet motion parallel to the wall is tracked in the frame of the laboratory, where (x, y) denote the coordinates parallel to the bottom wall and z the normal coordinate. The origin of the z-axis is located at the center of the droplet. In the following, the droplet radius $a/2$ and velocity V_0 are used as characteristic length and velocity, so that $z_{wall} = -1$ denotes the position of the bottom wall.

4.2.1.2 Methods: PIV measurement and Data representation

The flow field around the droplet is then measured using PIV, such as described in section (3.3.2). The acquisition frequency is 10 frames/s and the exposure time is 50 ms. The spatial resolution parallel to the wall is 0.65 μm/pixel.

For each experiment, 50 images of the droplet and the surrounding flow field are acquired at each z. The PIV analysis, performed using the PIV_lab [124] code on ©Matlab in each z-plane, provides us with the velocity field in cartesian coordinates attached to the lab frame at each time step. Doing so we obtain the velocity components $V_x(x, y, z, t)$ and $V_y(x, y, z, t)$ with a spatial resolution of 8 μm (around 8% of the droplet radius) for each pair of successive images. Note that we don't have access to the z component of the velocity. In principle, this component could be deduced using mass conservation, but the method is highly sensitive to experimental noise and we here choose to restrict ourselves to the analysis of the velocity components parallel to the bottom wall. We focus exclusively on trajectories (i) where the droplet is far from the lateral boundaries of the observation chamber and (ii) during time windows corresponding to steady motion of the droplet along linear trajectory.

The flow fields are dominated by a dipolar symmetry, which is used to extract the position of the droplet center and the direction of its instantaneous displacement and an estimate of it speed V_0. We then apply a translation and a rotation to superimpose all successive flow fields at each z and obtain their temporal average $v_x(x, y, z)$ and $v_y(x, y, z)$, thereby reducing the experimental noise. These velocities are made dimensionless using the droplet velocity V_0.

We are now in position to describe quantitatively the reconstructed flow field in the

one-wall geometry as illustrated on Fig. 4.5. The first step is to adopt a suitable system of coordinates. While spherical coordinates centered on the droplet are natural to describe an axisymmetric swimmer in an unbounded domain, the presence of the wall here calls for a description using cylindrical coordinates (ρ,θ,z)[3] with the z-axis orthogonal to the wall and $\theta = 0$ the swimming direction (as described in section (2)). Recalling that we use the droplet radius as the unit length, $\rho = 1$ describes a cylinder around the droplet, tangent to the median plane ($z = 0$). Additionally, for a steady and linear motion, the flow field conserves a planar symmetry with respect to the vertical plane $\theta = 0$. Exploiting this parity symmetry, the radial and azimuthal components of the dimensionless velocity field in each plane are decomposed onto the basis of Legendre polynomials:

$$v_\rho(\rho, \theta, z) = \sum_{n=0} \phi_\rho^n(\rho, z) L_n(\nu) \tag{4.1}$$

$$v_\theta(\rho, \theta, z) = \sum_{n=1} \phi_\theta^n(\rho, z) L_n^1(\nu), \tag{4.2}$$

where $\nu = \cos\theta$. Note that the flow field is measured in the lab reference frame and the velocities are zero far from the droplet. $L_n(\nu)$ (resp. $L_n^1(\nu) = -\sqrt{1-\nu^2}L_n'(\nu)$) are the Legendre polynomials (resp. associated Legendre polynomials of the first kind), defined in section (2). These Legendre polynomials form an orthogonal basis of hydrodynamic azimuthal symmetries with $\phi_i^n(\rho, z)$ the dimensionless amplitude of the n^{th}-multipolar symmetry for the radial ($i = \rho$) and azimuthal ($i = \theta$) components, which are obtained by the following projections:

$$\phi_\rho^n(\rho, z) = \frac{2n+1}{2} \int_{-1}^{1} v_\rho(\rho, \theta, z) L_n(\nu) d\nu, \tag{4.3}$$

$$\phi_\theta^n(\rho, z) = \frac{2n+1}{2n(n+1)} \int_{-1}^{1} v_\theta(\rho, \theta, z) L_n^1(\nu) d\nu. \tag{4.4}$$

For each z, $\phi_{\rho,\theta}^n(\rho, z)$ describes the radial dependency of the n^{th} azimuthal symmetry of the velocity $u_{\rho,\theta}$. These amplitudes form the output of our experimental measurements and are represented on Fig. 4.6, respectively Fig. 4.11, in the case of a droplet swimming above one wall, respectively between two walls.

4.2.2 Swimming close to a wall

We consider here the one-wall geometry with the water droplet performing a steady linear motion at the bottom of the chamber, parallel to the wall. Our experimental results are summarized on Fig. 4.6.

Let us first concentrate on the flow field in the median plane ($z = 0$). The top panel of Fig. 4.6 displays color coded maps of the radial and azimuthal components of the flow field, together with its decomposition onto the three first hydrodynamic multipolar symmetries (monopolar, dipolar, quadrupolar) and the reconstruction of the flow field from only these three first symmetries. One observes that the reconstructed flow field

[3] In order to alleviate the formalism, we call in this section θ and $\nu = \cos\theta$ what we defined before as $\hat{\theta}$ and $\nu = \cos\hat{\theta}$, the polar angle in any plane parallel to the wall.

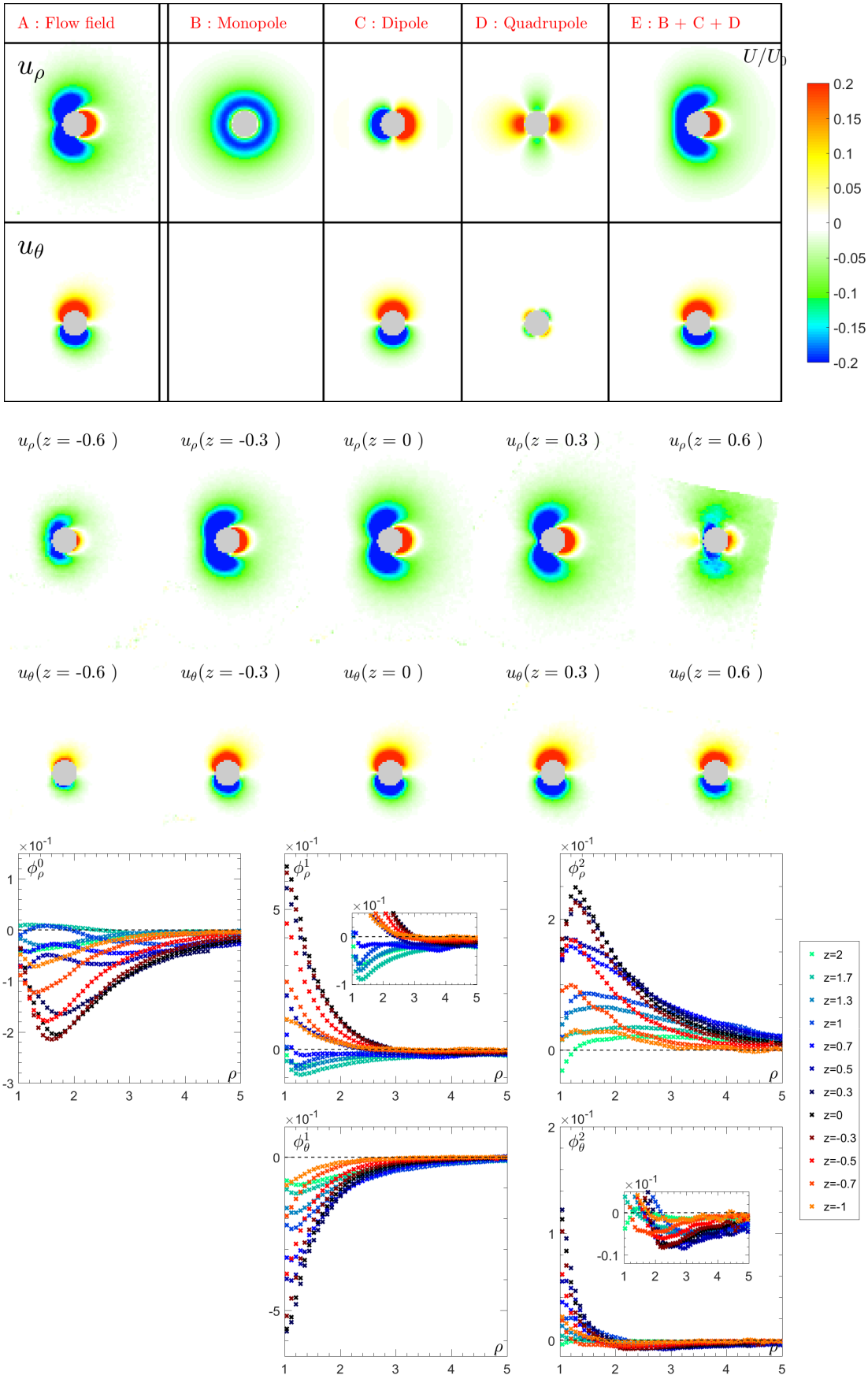

Figure 4.6: **Experimental flow field in the one-wall geometry:** caption in the next page.

Caption from Fig. 4.6: Top: u_ρ and u_θ in the median plane ($z = 0$). The complete experimental flow field (A) is shown as well as its monopolar symmetry (B), its dipolar symmetry (C) and its quadrupolar symmetry (D). The flow reconstruction from the first three symmetries (i.e. the sum of the contributions in B, C and D) is also shown (E). Middle: u_ρ (top) and u_θ (bottom) for $z = -0,6$, $z = -0,3$, $z = 0$; $z = 0,3$; $z = 0,6$ (same color code as above). Bottom: Amplitudes $\phi^n_\rho(\rho, z)$ and $\phi^n_\theta(\rho, z)$, of the first three modes ($n = 0, 1, 2$) as a function of the radial coordinate ρ for different z.

is very similar to the original one. In the following, we shall therefore restrict our analysis to the first three modes ($n = 0, 1, 2$). Second, and most remarkably, the radial component of the flow field exhibits a strong monopolar symmetry, which actually dominates at long range. In the median plane $z = 0$, the cylindrical and spherical coordinates description of the flow field are strictly equivalent, and it is well known that the flow field around an axisymmetric swimmer in an unbounded medium includes no monopolar symmetry contribution: our observations therefore provide a strong indication of the influence of the wall on the flow field.

The influence of the wall is further characterized by considering the flow field components in different planes parallel to the wall (see the middle panel of Fig. 4.6). The flow field appears strongly asymmetric with respect to the median plane, as could already be noticed from Fig. 4.5. This is particularly true for the radial component u_ρ, which has a nearly dipolar symmetry close to the wall and a nearly quadrupolar one when approaching the top of the droplet. The azimuthal component u_θ conserves the same dipolar symmetry across the droplet height, but one still notices a faster decrease of the flow intensity away from the droplet in planes closer to the wall. The complete quantitative description of the flow field is finally provided on the bottom panel of Fig. 4.6, where the amplitudes of the first three azimuthal modes are displayed as a function of the radial distance to the droplet ρ and the distance to the wall z.

4.2.3 Comparison with a squirmer model

Capturing theoretically the complex flow fields reported experimentally is highly non-trivial. A possible strategy would consist in solving exactly, up to numerical truncations, for the hydrodynamics and concentration fields around the droplet in the presence of the wall [97]. This however requires the knowledge of the boundary conditions at the boundary of the swimming body. For a Janus colloid, with an active cap of a prescribed geometry, it is already a strong hypothesis to assume that the phoretic slip velocity is not altered by the wall-modified concentration field. In the present case, we recall that the phoretic slip velocity and Marangoni stresses both result from a linear instability. In other words, in the bifurcated non-linear solution describing the swimming motion, they are functions of both the concentration and hydrodynamic fields. The interaction with the wall thus becomes a highly nonlinear problem, which cannot be solved easily following this strategy.

In the absence of exact treatment, it is still desirable to know how far a simplified model may account for the experimental description. With this goal in mind, we propose here an alternate and approximate model as an axisymmetric squirmer moving parallel to the wall, and computing the associated flow field using the method of images [93], as introduced in section (2.3.3.1). We stress that this description is simplified in the

sense that (i) it overlooks the dynamics of the concentration field and its impact on the hydrodynamic boundary condition at the swimmer's surface; (ii) it is a far-field approximation and therefore overlooks that the droplet radius and distance to the wall are comparable. Whether it would be able to capture the complex structure of the flow field reported experimentally is therefore far from obvious *a priori*.

In the following, we first give in subsection (4.2.3.1) for reference the flow field generated by a squirmer far from wall, in our particular system of cylindrical coordinates, and we see that the flow field is as expected strongly affected by the presence of a wall. We shall see in the subsection (4.2.3.2) that taking into account the presence of the wall by using the method of image to compute the flow field is in fact able to describe surprisingly well the quadrupolar and dipolar symmetries but fails to explain the emergence of a strong monopolar symmetry for the components of the flow field parallel to the wall, which is discussed in subsection (4.2.3.3).

4.2.3.1 Axisymmetric squirmer in an unbounded fluid

In order to fully appreciate the effect of the wall, one shall compare these profiles with those of a model swimmer in an unbounded medium. The flow field around an axisymmetric swimmer can be computed exactly, solving the Stokes equation [38, 37], for any given slip velocity $\mathbf{u}_s$ at the interface (a more detailed description is given in section (2.1)). However, in agreement with our experimental observations, we limit our description to the terms with azimuthal symmetries up to the quadrupolar order. Recalling that a swimmer is force-free (no external force), and source-free (no net flux production at the interface), the swimmer is modeled by a Stokes dipole, responsible for the leading order in $1/r$ of the flow field $\mathbf{u}_{fd}(\mathbf{r}) \sim 1/r^2$, a source dipole $\mathbf{u}_{sd}(\mathbf{r}) \sim 1/r^3$ resulting from the finite size of the swimmer and a source quadrupole, that ensures the absence of normal flux at the interface $\mathbf{u}_{sq}(\mathbf{r}) \sim 1/r^4$. This set of singularities corresponds effectively to the first two modes of the commonly-used squirmer model, which, in an unbounded geometry, generates the flow field:

$$\mathbf{u}(\mathbf{r}) = \lambda \mathbf{u}_{sd}(\mathbf{r}) + \zeta \mathbf{u}_{sq}(\mathbf{r}) + \kappa \mathbf{u}_{fd}(\mathbf{r}), \tag{4.5}$$

where the dimensionless coefficients $\lambda = \frac{1}{2}, \kappa = -3\zeta$ are set by the boundary condition $\mathbf{u}(r=1) = \mathbf{e} + \mathbf{u}_s$, with $\mathbf{e}$ the unit vector pointing in the direction of the swimming motion. The expressions of the singularities $\mathbf{u}_{sd}(\mathbf{r}), \mathbf{u}_{sq}(\mathbf{r})$ and $\mathbf{u}_{fd}(\mathbf{r})$ are obtained from the gradients of the point source $\mathbf{u}_s(\mathbf{r})$ and point force $\mathbf{u}_f(\mathbf{r})$ singularities:

$$\mathbf{u}_s(\mathbf{r}) = \frac{\mathbf{r}}{r^3}, \tag{4.6}$$

$$\mathbf{u}_f(\mathbf{r}) = \left(\frac{\mathbf{e}}{r} + \frac{(\mathbf{e}\cdot\mathbf{r})\mathbf{r}}{r^3} \right), \tag{4.7}$$

$$\mathbf{u}_{sd}(\mathbf{r}) = -\left[\nabla \mathbf{u}_s\right]\cdot\mathbf{e} = \left(\frac{3(\mathbf{r}\cdot\mathbf{e})\mathbf{r}}{r^5} - \frac{\mathbf{e}}{r^3} \right), \tag{4.8}$$

$$\mathbf{u}_{sq}(\mathbf{r}) = -\left[\nabla \mathbf{u}_{sd}\right]\cdot\mathbf{e} = 3\left[\frac{5(\mathbf{r}\cdot\mathbf{e})^2\mathbf{r}}{r^7} - \frac{\mathbf{r}}{r^5} - \frac{2(\mathbf{r}\cdot\mathbf{e})\mathbf{e}}{r^5} \right], \tag{4.9}$$

$$\mathbf{u}_{fd}(\mathbf{r}) = -\left[\nabla \mathbf{u}_f\right]\cdot\mathbf{e} = -\left(\frac{\mathbf{r}}{r^3} - \frac{3(\mathbf{r}\cdot\mathbf{e})^2\mathbf{r}}{r^5} \right). \tag{4.10}$$

We then write the singularities in the cylindrical system of coordinates (ρ, θ, z), using $\mathbf{e} = \nu\mathbf{e}_\rho - \sqrt{1-\nu^2}\mathbf{e}_\theta$, $\mathbf{r} = \rho\mathbf{e}_\rho + z\mathbf{e}_z$ and $\mathbf{r}\cdot\mathbf{e} = \rho\nu$:

$$u_{sd,\rho}(\rho,\nu) = \left(\frac{3\rho^2}{r^5} - \frac{1}{r^3}\right) L_1(\nu), \qquad u_{sd,\theta}(\rho,\nu) = -\frac{1}{r^3} L_1^1(\nu), \tag{4.11}$$

$$u_{sq,\rho}(\rho,\nu) = \left(\frac{10\rho^3}{r^7} - \frac{4\rho}{r^5}\right) L_2(\nu) + 5\left(\frac{\rho^3}{r^7} - \frac{\rho}{r^5}\right) L_0(\nu), \quad u_{sq,\theta}(\rho,\nu) = -\frac{2\rho}{r^5} L_2^1(\nu), \tag{4.12}$$

$$u_{fd,\rho}(\rho,\nu) = \frac{2\rho^3}{r^5} L_2(\nu) - \left(\frac{\rho}{r^3} - \frac{\rho^3}{r^5}\right) L_0(\nu), \qquad u_{fd,\theta}(\rho,\nu) = 0. \tag{4.13}$$

Note that in the median plane, in which the cylindrical and the more usual spherical coordinateS are identical, ($z = 0$ and $r = \rho$), the source quadrupole and the Stokes dipole contribute only to the quadrupolar symmetry of the flow. This is not the case out of the median plane ($z \neq 0$), where they also generate a monopolar symmetry in the radial velocity component $u_\rho(\rho,\nu)$. This is only reflecting the choice of coordinate system as the three-dimensional flow field is inherently the purely dipolar and quadrupolar axi-symmetric squirmer flow field.

Finally, we obtain the amplitude of the monopolar, dipolar and quadrupolar symmetries, projecting onto the Legendre polynomials, Eq. (4.3) and (4.4):

$$\phi_\rho^0(\rho) = 5\zeta\left(\frac{\rho^3}{r^7} - \frac{\rho}{r^5}\right) - \kappa\left(\frac{\rho}{r^3} - \frac{\rho^3}{r^5}\right), \tag{4.14}$$

$$\phi_\rho^1(\rho) = \lambda\left(\frac{3\rho^2}{r^5} - \frac{1}{r^3}\right), \tag{4.15}$$

$$\phi_\rho^2(\rho) = \zeta\left(\frac{10\rho^3}{r^7} - \frac{4\rho}{r^5}\right) + \frac{2\kappa\rho^3}{r^5}, \tag{4.16}$$

$$\phi_\theta^1(\rho) = -\frac{\lambda}{r^3}, \tag{4.17}$$

$$\phi_\theta^2(\rho) = -\frac{2\zeta\rho}{r^5}. \tag{4.18}$$

Fig. 4.7 displays the radial dependency of these amplitudes in different z-planes (color code). The black curves correspond to the median plane ($z = 0$).

A number of peculiar features in the radial dependence of the amplitudes should be noted when comparing the experimental amplitude profiles, Fig. 4.6, with the ones obtained for the model axisymmetric squirmer in an unbounded geometry (i.e. without taking into account the influence of the wall) as shown on Fig. 4.7. While for the unbounded squirmer, the amplitude ϕ_ρ^0 always presents a minimum, we observe in the experimental data that this minimum turns into a maximum when moving towards the upper hemisphere of the droplet. Similarly, the experimental amplitude ϕ_ρ^1 displays a negative minimum in the upper part of the droplet, where the squirmer model only presents a positive maximum; experimentally, ϕ_θ^1 further presents a minimum in the upper part of the droplet while this quantity is monotonously increasing in the squirmer case. Finally, regarding the quadrupolar symmetry, the experimental measurements

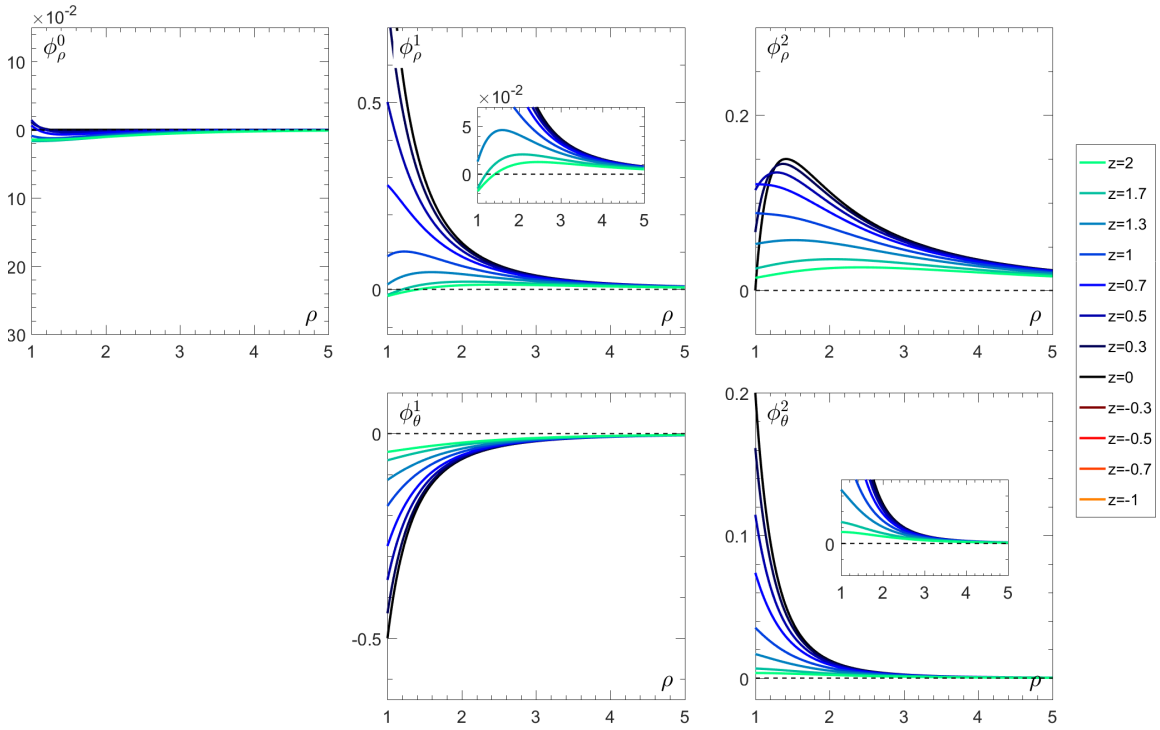

Figure 4.7: **Flow field created by a squirmer in the unbounded case**: amplitude of the monopolar (left), dipolar (middle) and quadrupolar (right) symmetries of the velocities u_ρ (top) and u_θ (bottom), as given by Eqs. (4.14)–(4.18). The z-planes are color coded according to the legend on the right; same color code as in the main text. The $z > 0$ and $z < 0$ profiles superimpose. The coefficients $\lambda = \frac{1}{2}$ and $\zeta = -\frac{1}{3}\kappa$ are given by the boundary condition at the interface of the droplet. κ is free and arbitrarily set to $\kappa = 0.3$.

for ϕ^2_ρ appear essentially similar to that of the unbounded squirmer, but ϕ^2_θ presents a systematic negative minimum for all z in the droplet case, while it is monotonically decreasing and positive in the case of the unbounded squirmer. Altogether, one sees that the flow field around the droplet is, as expected, strongly affected by the presence of the wall, and is therefore poorly accounted for by an unbounded squirmer model. It is also by far more complex than the naive intuition one could develop from an observation limited to the median plane.

4.2.3.2 Axisymmetric squirmer on a wall

The squirmer model considered is that introduced in the previous subsection. The presence of a no-slip infinite plane wall imposes a vanishing flow velocity $\mathbf{u} = \mathbf{0}$ at the wall. The methods of images followed here consists of introducing singularities at the mirror position of the swimmer with respect to the wall, such that the flow field, obtained from the superposition of the original and image singularities, satisfies the no slip condition at the wall exactly.

The appropriate singularities have been identified for a source monopole, a source dipole or a point force in the classical work of Blake and Chwang [130]. Spagnolie and Lauga [93] recently computed the image systems of higher order singularities including the Stokes dipole. The image flow field for the source quadrupole has been obtained

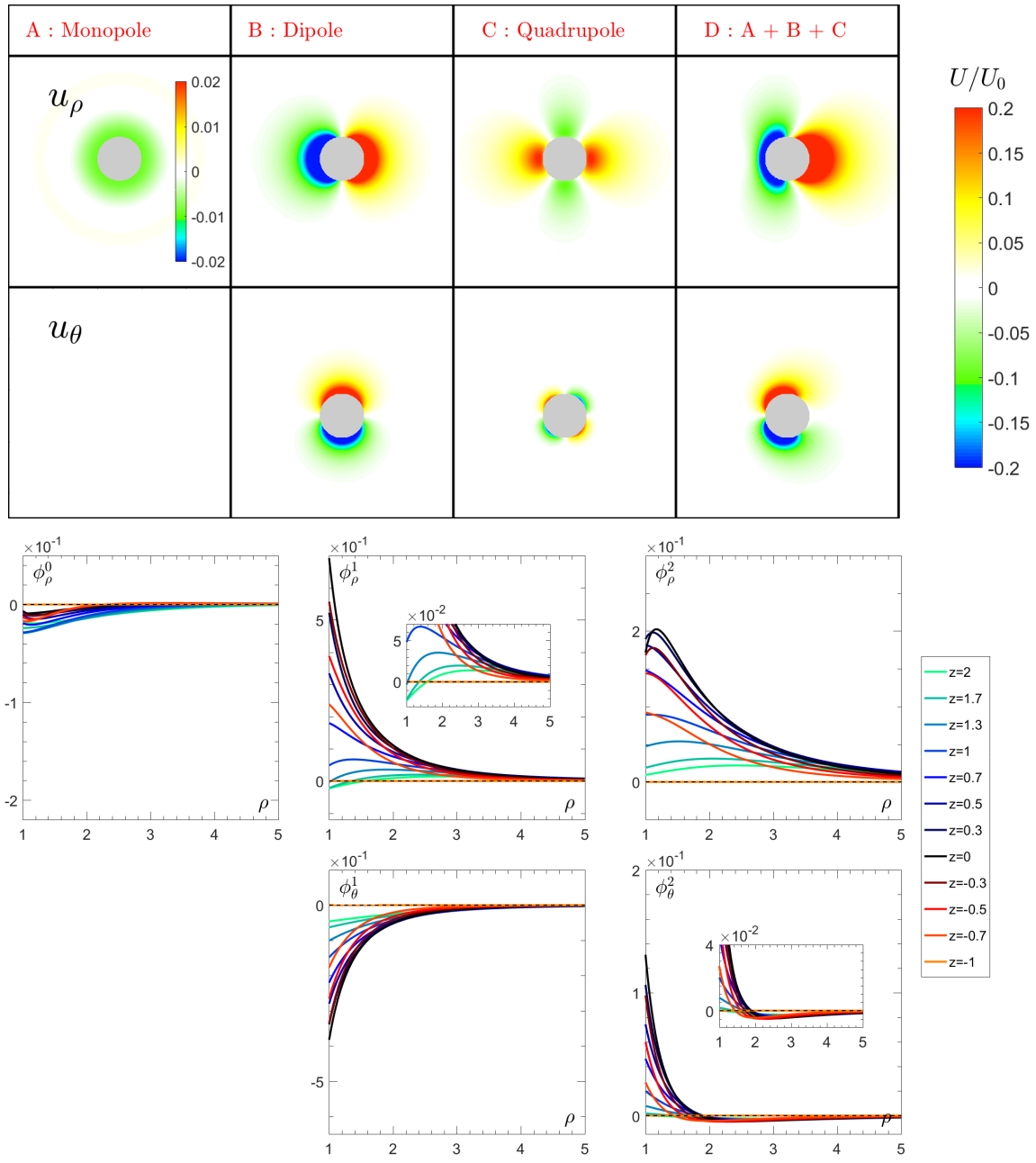

Figure 4.8: **Model flow field in the one-wall geometry:** Top: u_ρ and u_θ in the median plane, computed from the first singularities and their image systems, Eq. (4.19), using the value of κ, λ and ζ obtained from the experimental data. A: Monopolar symmetry generated by the original Stokes dipole and the original source quadrupole. B: Dipolar symmetry generated by the source dipole C: Quadrupolar symmetry generated by the Stokes dipole and the source quadrupole D: Total flow field generated by the first singularities: sum of A, B and C. The color-scale codes for the amplitude of the velocity. Bottom: Corresponding amplitudes $\phi^n_\rho(\rho, z)$ and $\phi^n_\theta(\rho, z)$, of the first three modes ($n = 0, 1, 2$) as a function of the radial coordinate ρ for different z.

similarly by Sébastien Michelin as part of this work. The general method consists again of using the fact that derivatives of the source or force singularities produce other higher-order singularity solutions of the Stokes equations: deriving the known images of lowest order singularities, one obtains the images of the higher order singularities of interest $\mathbf{u}^*_{sd}(\mathbf{r}), \mathbf{u}^*_{sq}(\mathbf{r})$ and $\mathbf{u}^*_{fd}(\mathbf{r})$. The flow field in the presence of the wall then simply reads:

$$\mathbf{u}^*(\mathbf{r}) = \lambda \mathbf{u}^*_{sd}(\mathbf{r}) + \zeta \mathbf{u}^*_{sq}(\mathbf{r}) + \kappa \mathbf{u}^*_{fd}(\mathbf{r}). \tag{4.19}$$

Note that these solutions of the Stokes equations do not satisfy the boundary conditions at the interface of the droplet, so that λ, κ and ζ are now unknown. We then want to compute the vectorial expressions of the so-obtained flow fields. We still use a set of axes centered on the sphere's center. $\mathbf{e}_z$ is a unit vector along the vertical axis and h is the distance between the center of the swimmer and the wall. Image singularities are thus positioned at a point $\mathbf{X} = -h\mathbf{e}_z$ below the wall, and we note $\mathbf{r}$ the position of the observation point (where the flow is evaluated) with respect to the sphere's center and $\mathbf{R} = \mathbf{r} + 2h\mathbf{e}_z$ the position of the same point with respect to the position of the image system. For each singularity, which leads to a velocity field $\mathbf{u}_i$ in unbounded flow, we denote by $\mathbf{u}^*_i$ the corresponding flow field near a wall (i.e. including both the original singularity and the effect of its image system). This flow field is obtained for a point source or point force as [130]:

$$\mathbf{u}^*_s(\mathbf{r}) = \overbrace{\frac{\mathbf{r}}{r^3}}^{\text{Original source}} + \overbrace{\frac{\mathbf{R}}{R^3}}^{\text{Image source}} \overbrace{- 2\left(\frac{\mathbf{R}}{R^3} - \frac{3\mathbf{R}(\mathbf{R}\cdot\mathbf{e}_z)^2}{R^5}\right)}^{\text{stresslet}} + \overbrace{2h\left(\frac{\mathbf{e}_z}{R^3} - \frac{3(\mathbf{R}\cdot\mathbf{e}_z)\mathbf{R}}{R^5}\right)}^{\text{source dipole}}, \tag{4.20}$$

$$\begin{aligned}\mathbf{u}^*_f(\mathbf{r}) = {} & \overbrace{\frac{\mathbf{e}}{r} + \frac{(\mathbf{e}\cdot\mathbf{r})\mathbf{r}}{r^3}}^{\text{Original stokeslet}} - \overbrace{\frac{\mathbf{e}}{R} - \frac{(\mathbf{e}\cdot\mathbf{R})\mathbf{R}}{R^3}}^{\text{Image Stokeslet}} + \overbrace{\frac{2h^2\mathbf{e}}{R^3} - \frac{6h^2(\mathbf{e}\cdot\mathbf{R})\mathbf{R}}{R^5}}^{\text{source dipole}} \\ & + \overbrace{\frac{2h(\mathbf{e}\cdot\mathbf{R})\mathbf{e}_z}{R^3} + \frac{6h(\mathbf{R}\cdot\mathbf{e}_z)(\mathbf{e}\cdot\mathbf{R})\mathbf{R}}{R^5} - \frac{2h(\mathbf{e}_z\cdot\mathbf{R})\mathbf{e}}{R^3}}^{\text{stresslet}}.\end{aligned} \tag{4.21}$$

In our model, the singularities used in Eq. (4.19) are all parallel to the wall. The flow field generated by higher order singularities is thus obtained by taking successive gradients of the flow field generated by a point force or point source singularity. As an example, the flow field $\mathbf{u}^*_{sd}$, generated by the source dipole singularity $\mathbf{u}_{sd}$ in the presence of a no-slip wall, is obtained by taking the gradient of the flow field $\mathbf{u}^*_s$, generated by a source monopole singularity and project it on $\mathbf{e}$. The method applies

iteratively to obtain the flow fields generated by higher-order singularities:

$$\begin{aligned}\mathbf{u}^*_{sd}(\mathbf{r}) =& -[\nabla \mathbf{u}^*_s]\cdot\mathbf{e}\\ =& -\frac{\mathbf{e}}{r^3}+\frac{3(\mathbf{e}\cdot\mathbf{r})\mathbf{r}}{r^5}+\frac{\mathbf{e}}{R^3}-\frac{3(\mathbf{e}\cdot\mathbf{R})\mathbf{R}}{R^5}-6(\mathbf{R}\cdot\mathbf{e}_z)(\mathbf{R}\cdot\mathbf{e}_z-h)\left(\frac{\mathbf{e}}{R^5}-\frac{5(\mathbf{R}\cdot\mathbf{e})\mathbf{R}}{R^7}\right)\\ &+\frac{6h(\mathbf{R}\cdot\mathbf{e})\mathbf{e}_z}{R^5},\end{aligned} \tag{4.22}$$

$$\begin{aligned}\mathbf{u}^*_{sq}(\mathbf{r}) =& -[\nabla \mathbf{u}^*_{sd}]\cdot\mathbf{e}\\ =&\frac{15(\mathbf{r}\cdot\mathbf{e})^2\mathbf{r}}{r^7}-\frac{3\mathbf{r}}{r^5}-\frac{6(\mathbf{r}\cdot\mathbf{e})\mathbf{e}}{r^5}-\frac{15(\mathbf{R}\cdot\mathbf{e})^2\mathbf{R}}{R^7}+\frac{3\mathbf{R}}{R^5}+\frac{6(\mathbf{R}\cdot\mathbf{e})\mathbf{e}}{R^5}\\ &+30h(\mathbf{R}\cdot\mathbf{e}_z-h)(\mathbf{R}\cdot\mathbf{e}_z)\left(\frac{7(\mathbf{R}\cdot\mathbf{e})^2\mathbf{R}}{R^9}-\frac{2(\mathbf{R}\cdot\mathbf{e})\mathbf{e}}{R^7}-\frac{\mathbf{R}}{R^7}\right)-\frac{6h\mathbf{e}_z}{R^5}+\frac{30h(\mathbf{R}\cdot\mathbf{e})^2\mathbf{e}_z}{R^7},\end{aligned} \tag{4.23}$$

$$\begin{aligned}\mathbf{u}^*_{fd}(\mathbf{r}) =& -\left[\nabla \mathbf{u}^*_f\right]\cdot\mathbf{e}\\ =& -\frac{\mathbf{r}}{r^3}+\frac{3(\mathbf{e}\cdot\mathbf{r})^2\mathbf{r}}{r^5}+\frac{\mathbf{R}}{R^3}-\frac{3(\mathbf{e}\cdot\mathbf{R})^2\mathbf{R}}{R^5}-\frac{6h(\mathbf{R}\cdot\mathbf{e}_z-h)\mathbf{R}}{R^5}-\frac{12h(\mathbf{R}\cdot\mathbf{e}_z-h)(\mathbf{e}\cdot\mathbf{R})\mathbf{e}}{R^5}\\ &+\frac{30h(\mathbf{e}\cdot\mathbf{R})^2(\mathbf{R}\cdot\mathbf{e}_z-h)\mathbf{R}}{R^7}-\frac{2h\mathbf{e}_z}{R^3}+\frac{6h(\mathbf{R}\cdot\mathbf{e})^2\mathbf{e}_z}{R^5}.\end{aligned} \tag{4.24}$$

These velocity fields are then projected along the axes of the cylindrical coordinate systems, using that $\mathbf{R}=(2h+z)\mathbf{e}_z+\rho\,\mathbf{e}_\rho$, $\mathbf{R}\cdot\mathbf{e}=\mathbf{r}\cdot\mathbf{e}=\rho\nu$ and $\mathbf{R}\cdot\mathbf{e}_z=2h+z$:

$$u^*_{sd,\rho}(\rho,\nu)=\left[-\frac{1}{r^3}+\frac{1}{R^3}-3\rho^2\left(\frac{1}{R^5}-\frac{1}{r^5}\right)-6(h+z)(2h+z)\left(\frac{1}{R^5}-\frac{5\rho^2}{R^7}\right)\right]L_1(\nu), \tag{4.25}$$

$$u^*_{sd,\theta}(\rho,\nu)=\left(-\frac{1}{r^3}+\frac{1}{R^3}-\frac{6(2h+z)(h+z)}{R^5}\right)L_1^1(\nu), \tag{4.26}$$

and

$$\begin{aligned}u^*_{sq,\rho}(\rho,\nu)=&\left[\frac{10\rho^3}{r^7}-\frac{4\rho}{r^5}-\frac{10\rho^3}{R^7}+\frac{4\rho}{R^5}+20h(z+h)(z+2h)\left(\frac{7\rho^3}{R^9}-\frac{2\rho}{R^7}\right)\right]L_2(\nu)\\ &+\left[\frac{5\rho^3}{r^7}-\frac{5\rho}{r^5}-\frac{5\rho^3}{R^7}+\frac{5\rho}{R^5}+10h(z+h)(z+2h)\left(\frac{7\rho^3}{R^9}-\frac{5\rho}{R^7}\right)\right]L_0(\nu),\end{aligned} \tag{4.27}$$

$$u^*_{sq,\theta}(\rho,\nu)=\left(-\frac{2\rho}{r^5}+\frac{2\rho}{R^5}-\frac{20h(z+h)(z+2h)\rho}{R^7}\right)L_2^1(\nu), \tag{4.28}$$

$$\begin{aligned}u^*_{fd,\rho}(\rho,\nu)=&\left(\frac{2\rho^3}{r^5}-\frac{2\rho^3}{R^5}-\frac{8h(z+h)\rho}{R^5}+\frac{20h\rho^3(z+h)}{R^7}\right)L_2(\nu)\\ &+\left[-\frac{\rho}{r^3}+\frac{\rho^3}{r^5}+\frac{\rho}{R^3}-\frac{\rho^3}{R^5}-10h(z+h)\left(\frac{\rho}{R^5}-\frac{\rho^3}{R^7}\right)\right]L_0(\nu),\end{aligned} \tag{4.29}$$

$$u^*_{fd,\theta}(\rho,\nu)=-4h(z+h)\frac{\rho}{R^5}L_2^1(\nu). \tag{4.30}$$

Finally, we obtain the amplitudes by projection onto the Legendre polynomials:

$$\phi_\rho^{0*}(\rho,z) = \zeta\left[\frac{5\rho^3}{r^7}-\frac{5\rho}{r^5}-\frac{5\rho^3}{R^7}+\frac{5\rho}{R^5}+10h(z+h)(z+2h)\left(\frac{7\rho^3}{R^9}-\frac{5\rho}{R^7}\right)\right] + \kappa\left[-\frac{\rho}{r^3}+\frac{\rho^3}{r^5}+\frac{\rho}{R^3}-\frac{\rho^3}{R^5}-10h(z+h)\left(\frac{\rho}{R^5}-\frac{\rho^3}{R^7}\right)\right], \tag{4.31}$$

$$\phi_\rho^{1*}(\rho,z) = \lambda\left[-\frac{1}{r^3}+\frac{1}{R^3}-3\rho^2\left(\frac{1}{R^5}+\frac{1}{r^5}\right)-6(h+z)(2h+z)\left(\frac{1}{R^5}-\frac{5\rho^2}{R^7}\right)\right], \tag{4.32}$$

$$\phi_\rho^{2*}(\rho,z) = \zeta\left[\frac{10\rho^3}{r^7}-\frac{4\rho}{r^5}-\frac{10\rho^3}{R^7}+\frac{4\rho}{R^5}+20h(z+h)(z+2h)\left(\frac{7\rho^3}{R^9}-\frac{2\rho}{R^7}\right)\right] + \kappa\left(\frac{2\rho^3}{r^5}-\frac{2\rho^3}{R^5}-\frac{8h(z+h)\rho}{R^5}+\frac{20h\rho^3(z+h)}{R^7}\right), \tag{4.33}$$

$$\phi_\theta^{1*}(\rho,z) = \lambda\left(-\frac{1}{r^3}+\frac{1}{R^3}-\frac{6(2h+z)(h+z)}{R^5}\right), \tag{4.34}$$

$$\phi_\theta^{2*}(\rho,z) = \zeta\left(-\frac{2\rho}{r^5}+\frac{2\rho}{R^5}-\frac{20h(z+h)(z+2h)\rho}{R^7}\right) - \frac{4\kappa\rho h(z+h)}{R^5}. \tag{4.35}$$

In order to compare quantitatively the experimental flow fields and the predictions of the above squirmer model, the coefficients λ, ζ and κ are extracted from the experimental data as follows. The dipolar symmetry of the flow field arises from the source dipole only, while the monopolar and quadrupolar symmetries of the flow field result from both the Stokes dipole and source quadrupole: λ is thus obtained by minimizing $\left\langle \|(\Delta\phi_\rho^1)^2\| + \|(\Delta\phi_\theta^1)^2\| \right\rangle$, where $\langle\|\Delta\phi\|\rangle$ denotes the average over the experimental realizations of the L_2-norm of the difference between the amplitudes $\phi(\rho,z)$ measured experimentally and computed analytically. Similarly κ and ζ are obtained by minimizing $\left\langle \|(\Delta\phi_\rho^2)^2\| + \|(\Delta\phi_\theta^2)^2\| \right\rangle$. We thereby obtain $\lambda = 0.35$, $\zeta = -0.08$ and $\kappa = 0.34$. This method is quite robust as for repeating the experiment for different droplets of radius of 60 and 70 μm, we obtain very similar values with interval ± 0.05. The flow fields and profiles are displayed on Fig. 4.8.

A remarkable feature is that the images of the first order singularities do induce a monopolar symmetry even in the median plane. This monopolar symmetry is however much weaker than in the experimental case, and does not contribute significantly to the reconstructed flow field at odd with the experimental observation. A closer look at the amplitude profiles on Fig. 4.8 (bottom) also reveals that the monopolar symmetry does not have the proper dependence in z: the monopolar symmetry of the experimental flow is strongest in the median plane, while it is found in this model to be largest above the droplet.

In contrast, the dipolar and quadrupolar symmetries to the experimentally-measured flow (Fig. 4.6) are surprisingly well described by this simple model (Fig. 4.8), especially for the latter. The asymmetry of the flow with respect to the median plane is properly captured, and the radial dependence of the amplitudes are also well described. This is particularly well illustrated by the non-trivial dependence on z of the amplitude and position of the maximum of $\phi_\rho^2(\rho,z)$ and of the minimum in $\phi_\theta^2(\rho,z)$ (Fig. 4.9). As far as the quadrupolar symmetry is concerned, the model predictions, together with the extraction of the parameters ζ and κ from the experimental data, perfectly

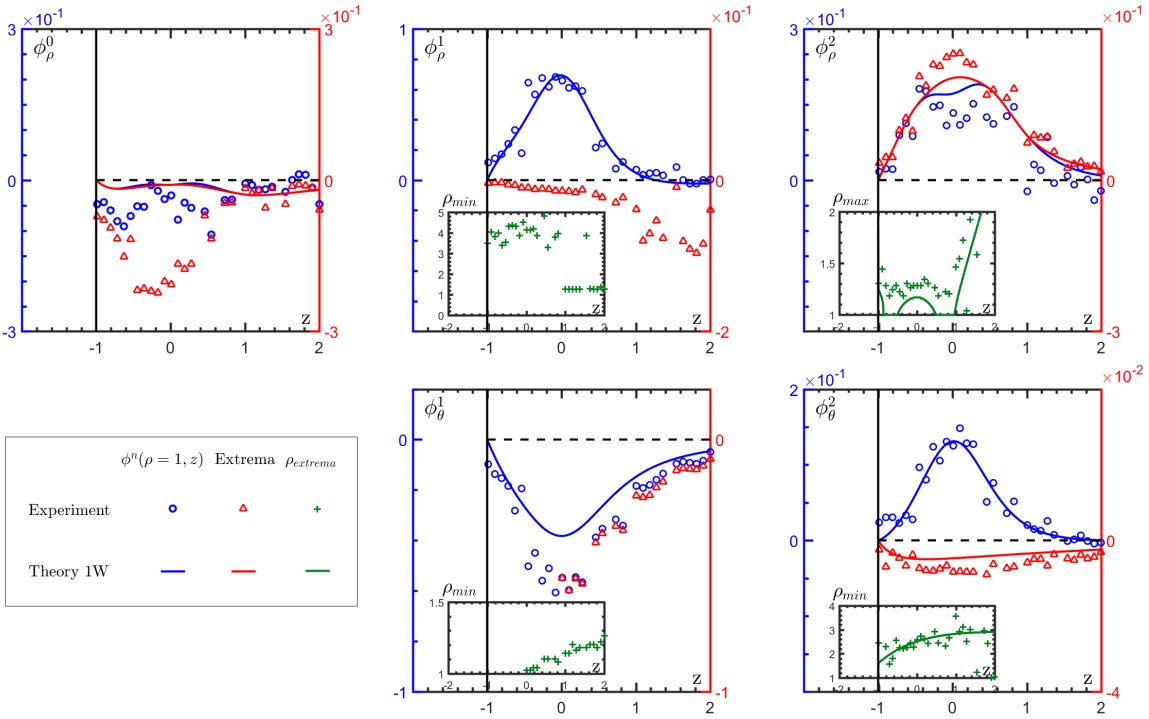

Figure 4.9: **Comparison between the characteristics of the experimental (dots) and theoretical (straight lines) velocities in the one-wall geometry:** Evolution with z of the amplitude at $\rho = 1$ (blue), of the extremum (red) and of the extremum's position (green) of the monopolar symmetry (left), the dipolar symmetry (middle) and the quadrupolar symmetry (right) of the velocities u_ρ (top) and u_θ (bottom).

describes the experimental flow field. More specifically ϕ^2_ρ has a local maximum, the position of which, varies in a non-trivial way with z, which is well captured by the model. Similarly, the amplitude and position of the local minimum of ϕ^2_θ are well reproduced. The amplitudes of the dipolar symmetry are also well captured, despite some exceptions. The magnitude of the azimuthal amplitude ϕ^1_θ is slightly underestimated by the model. Also, experimentally, ϕ^1_ρ presents a local minimum that becomes negative close to $\rho = 1$ and for $z > 0.7$, while the model predicts a negative value at $\rho = 1$ for $z > 1$, but no local minimum. Finally, ϕ^1_θ presents a local maximum close to $\rho = 1$ in experiments, that is not predicted by the theory.

In summary, the axisymmetric squirmer model presented above predicts very well the behaviour of the quadrupolar symmetry of the experimental flow field, captures the amplitude of the dipolar symmetry but not the details of the amplitude profiles very close to the droplet, and fails to describe the monopolar symmetry observed experimentally. Given the oversimplified nature of the model, it is already amazing that so many key features of the real flow are captured. For instance the fact that the amplitude profiles very close to $\rho = 1$ are not so well captured can easily be understood given that the method of images does not guarantee the boundary conditions at the swimmer interface. The main limitation of the present description lies in its failure to describe properly the monopolar symmetry of the flow observed in the experiments. This is all the more problematic since this contribution to the flow field is also observed to

dominate at long range and therefore is expected to control the interactions with other swimmers: when this monopolar symmetry is present, it dominates the Stokes dipole signature of the droplet, thereby rendering the common description of microswimmers in terms of pusher/ puller inadequate.

4.2.3.3 Origin of the monopolar symmetry of the flow

It should first be stressed that the monopolar symmetry of the flow cannot be explained by including higher order terms of the multipole expansion describing axisymmetric swimmers: although such terms do indeed contribute to a monopolar symmetry of the flow when expressed in cylindrical coordinates, their radial dependence decreases faster and faster with ρ and is therefore unable to explain a dominant monopolar symmetry at large distance. One must therefore look for the origin of the monopolar symmetry of the flow in low-order singularities. The point source singularity is the most natural candidate, especially given that the swimming mechanism of the droplet involves a water flux through the swelling of the micelles in the oil phase. This flux is however of microscopic nature and much too weak to account for a significant hydrodynamic flow.

To make further progress, one should realize that the slip velocity at the swimmer boundary is unlikely to remain axisymmetric with respect to the direction of motion, as implicitly assumed in the squirmer description presented above. This can be understood easily in the case of phoretic swimmers, as the concentration gradients at the surface (and resulting slip velocity) are likely altered by the presence of the wall. In the present case, where the swimming mechanism results from the non-linear advective coupling of the concentration and hydrodynamic fields, one expects an even stronger effect of the wall.

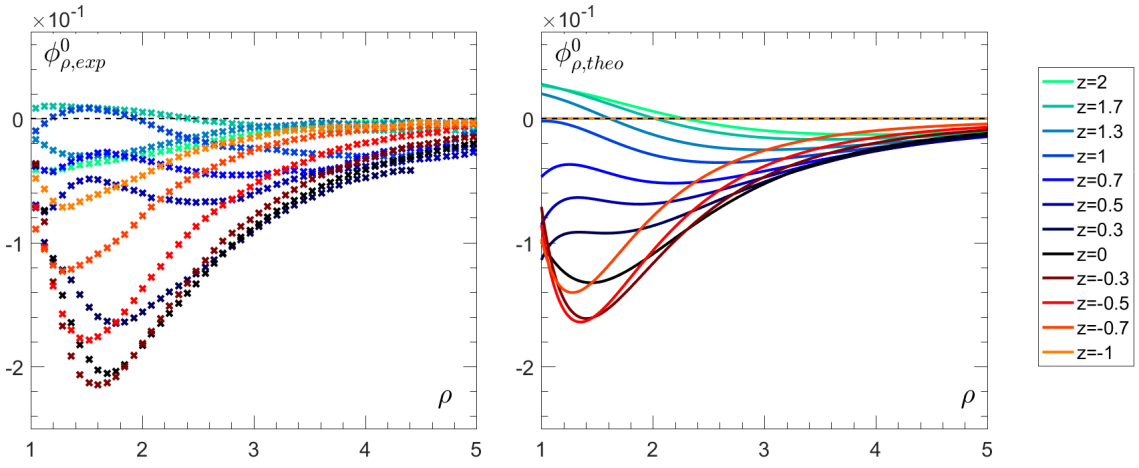

Figure 4.10: **The monopolar symmetry:** Amplitude of the monopolar symmetry of the flow field measured experimental (left), and computed in the case of a non-axisymmetric squirmer close to a wall, for which phoretic flows develop perpendicular to the wall, while the swimmer is held by gravity (right).

The full description of the coupled hydrodynamics and concentration fields, when swimming close to a wall is beyond the scope of the present work. Yet, as a first step in this direction, we may include a first correction to the axisymmetric assumption resulting from an increase of the concentration near the wall, simply because of confinement

between the wall and droplet surface [131]. This in turn generates vertical concentration gradients along the surface of the droplet, promoting its motion away from the wall [132]. The droplet being denser than the surrounding fluid, it is held vertically in place by buoyancy effects, and acts as a phoretic pump in the direction orthogonal to the wall. In this case it is no longer force-free, and a vertical point force should therefore be added. The key point to notice here is that this singularity gives rise to a flow with a dipolar symmetry in the direction orthogonal to the wall but displays a monopolar symmetry if observed in planes *parallel* to the swimming direction. We also notice that the amplitude profiles of the monopolar symmetry are non-monotonous. This suggests that more than one singularity should be considered. We thus also include the source dipole perpendicular to the wall.

The flow fields produced by the vertical point force and source dipole in the presence of the wall are again computed using the methods of images. They write in vector form:

$$\mathbf{u}^*_{pf,\perp}(\mathbf{r}) = \frac{\mathbf{e}_z}{r} + \frac{(\mathbf{e}_z\cdot\mathbf{r})\mathbf{r}}{r^3} - \frac{\mathbf{e}_z}{R} - \frac{(\mathbf{e}_z\cdot\mathbf{R})\mathbf{R}}{R^3} - \frac{2h^2\mathbf{e}_z}{R^3} + \frac{6h^2(\mathbf{R}\cdot\mathbf{e}_z)\mathbf{R}}{R^5} + \frac{2h\mathbf{R}}{R^3} - \frac{6h(\mathbf{R}\cdot\mathbf{e}_z)^2\mathbf{R}}{R^5}, \tag{4.36}$$

$$\begin{aligned}\mathbf{u}^*_{sd,\perp}(\mathbf{r}) = &- \frac{\mathbf{e}_z}{r^3} + \frac{3(\mathbf{r}\cdot\mathbf{e}_z)\mathbf{r}}{r^5} + \frac{3\mathbf{e}_z}{r^3} - \frac{9(\mathbf{r}\cdot\mathbf{e}_z)\mathbf{r}}{r^5} + \frac{-2\mathbf{e}_z}{R^3} + \frac{18(\mathbf{e}_z\cdot\mathbf{R})\mathbf{R}}{R^5} + \frac{6(\mathbf{R}\cdot\mathbf{e}_z)^2\mathbf{e}_z}{R^5} \\ &- \frac{30(\mathbf{e}_z\cdot\mathbf{R})^3\mathbf{R}}{R^7} - \frac{12h(\mathbf{e}_z\cdot\mathbf{R})\mathbf{e}_z}{R^5} - 6\frac{\mathbf{R}}{R^5} - \frac{10h(\mathbf{e}_z\cdot\mathbf{R})^2\mathbf{R}}{R^7},\end{aligned} \tag{4.37}$$

and in cylindrical coordinates:

$$u^*_{pf,\perp,\rho}(\rho,\nu) = \left(\frac{\rho z}{r^3} - \frac{\rho z}{R^3} - \frac{6h(z+h)(z+2h)\rho}{R^5}\right) L_0(\nu), \tag{4.38}$$

$$u^*_{pf,\perp,\theta}(\rho,\nu) = 0, \tag{4.39}$$

$$\begin{aligned}u^*_{sd,\perp,\rho}(\rho,\nu) =& - [\nabla\mathbf{u}^*_s]\cdot\mathbf{e}\left[\frac{3z\rho}{r^5} - \frac{3z\rho}{R^5} + 3(h+z)\left(\frac{4\rho}{R^5} - \frac{10(2h+z)^2}{R^7}\right)\right] L_0(\nu),\\ u^*_{sd,\perp,\theta}(\rho,\nu) =& 0.\end{aligned} \tag{4.40}$$

The symmetry of these contribution of these two singularities is purely monopolar in this cylindrical base. If we note ϵ the coefficients of the perpendicular point force, and σ the amplitude of the perpendicular source dipole, then the amplitude of the monopolar symmetry to the flow field, taking into account all previous singularities close to a wall is:

$$\begin{aligned}\phi^*_0(\rho,z) =& \epsilon\left(\frac{\rho z}{r^3} - \frac{\rho z}{R^3} - \frac{6h(z+h)(z+2h)\rho}{R^5}\right)\\ &+ \sigma\left[\frac{3z\rho}{r^5} - \frac{3z\rho}{R^5} + 3(h+z)\left(\frac{4\rho}{R^5} - \frac{10(2h+z)^2}{R^7}\right)\right]\\ &+ \zeta\left[\frac{5\rho^3}{r^7} - \frac{5\rho}{r^5} - \frac{5\rho^3}{R^7} + \frac{5\rho}{R^5} + 10h(z+h)(z+2h)\left(\frac{7\rho^3}{R^9} - \frac{5\rho}{R^7}\right)\right]\\ &+ \kappa\left[\frac{\rho}{r^3} - \frac{\rho^3}{r^5} - \frac{\rho}{R^3} + \frac{\rho^3}{R^5} + 10h(z+h)\left(\frac{\rho}{R^5} - \frac{\rho^3}{R^7}\right)\right].\end{aligned} \tag{4.41}$$

The contribution of these two singularities in planes parallel to the wall has a purely monopolar symmetry, so that they only contribute to the amplitude $\phi^0_\rho(\rho,\theta)$, without altering the higher-order angular amplitudes. The amplitude of the monopolar symmetry $\phi^0_\rho(\rho,\theta)$ now depends on four coefficients: ζ, κ, ϵ and σ the magnitudes of the parallel source quadrupole, $\mathbf{u}^*_{sq}$, the parallel stokes dipole $\mathbf{u}^*_{fd}$, the perpendicular point force $\mathbf{u}^*_{pf,\perp}$ and the perpendicular source dipole $\mathbf{u}^*_{sd,\perp}$, respectively. κ and ζ have already been determined from the experimental data using the higher order singularities, and thus equal to the values computed in the previous subsection. ϵ and σ are obtained by minimizing $\left\langle \|(\Delta\phi^0_\rho)^2\| \right\rangle$. The resulting amplitude profiles are provided on Fig. 4.10, together with the experimental profiles. Including the contribution of the vertical singularities resulting from confinement of the concentration field is observed to capture very well the key trends observed experimentally.

4.2.4 Effect of two walls on the flow field

We finally consider the two-wall geometry with the water droplet performing a steady linear motion between a top and a bottom walls separated by typically one droplet diameter. In this case one cannot use the method of images as it would result in an infinite set of images with respect to the two walls. Such a method is only tractable when looking at the flow field far from the droplet in the horizontal direction [133, 52, 91]. In this double-confinement geometry, there is therefore little hope to derive analytical expressions for the flow field close to the droplet even within very simple approximations. Yet, as we shall see below, it remains of interest to discuss the qualitative difference with the case of one wall confinement, from the purely experimental point of view.

The experimental results are summarized on Fig. 4.11, in the same way as for the one wall geometry. We first note (top panel) that, here also, the flow field reconstructed from the decomposition on the first three hydrodynamic multipoles conveys all the experimental signal. As in the one-wall case, the radial component of the flow field presents a monopolar symmetry. However, this monopolar symmetry is here small compared to the one-wall case, and does not dominate at long range. A natural explanation is that the effect of the vertical force singularity, which dominates at large distance in the one-wall case, is exponentially screened in the far-field in double confinement [133]. The contribution to the flow field are thus mainly dipolar and quadrupolar symmetries.

The influence of the wall is further characterized by considering the flow field symmetries, observed at different distances from the wall (see the middle panel of Fig. 4.11). The main observation is that the flow field is strongly asymmetric with respect to the median plane (asymmetry in z), despite the approximate top-down symmetry of the problem. This asymmetry is however not found on all modes. This is best observed on the amplitude profiles displayed on the bottom panel. In the case of the radial component, the dipolar and quadrupolar symmetries are dominant in the median plane, while on the contrary the monopolar symmetry dominates close to the walls. This monopolar symmetry is positive at the bottom wall and negative at the top wall. It is thus the main contributor to the flow field asymmetry. The azimuthal component, dominated by a dipolar symmetry, does not present such an asymmetry in z. There is an asymmetry carried by the azimuthal quadrupolar symmetry, but the latter being very weak, it does not affect qualitatively the flow field. Altogether the monopolar symmetry is by itself responsible for the observed asymmetry of the flow field. Since

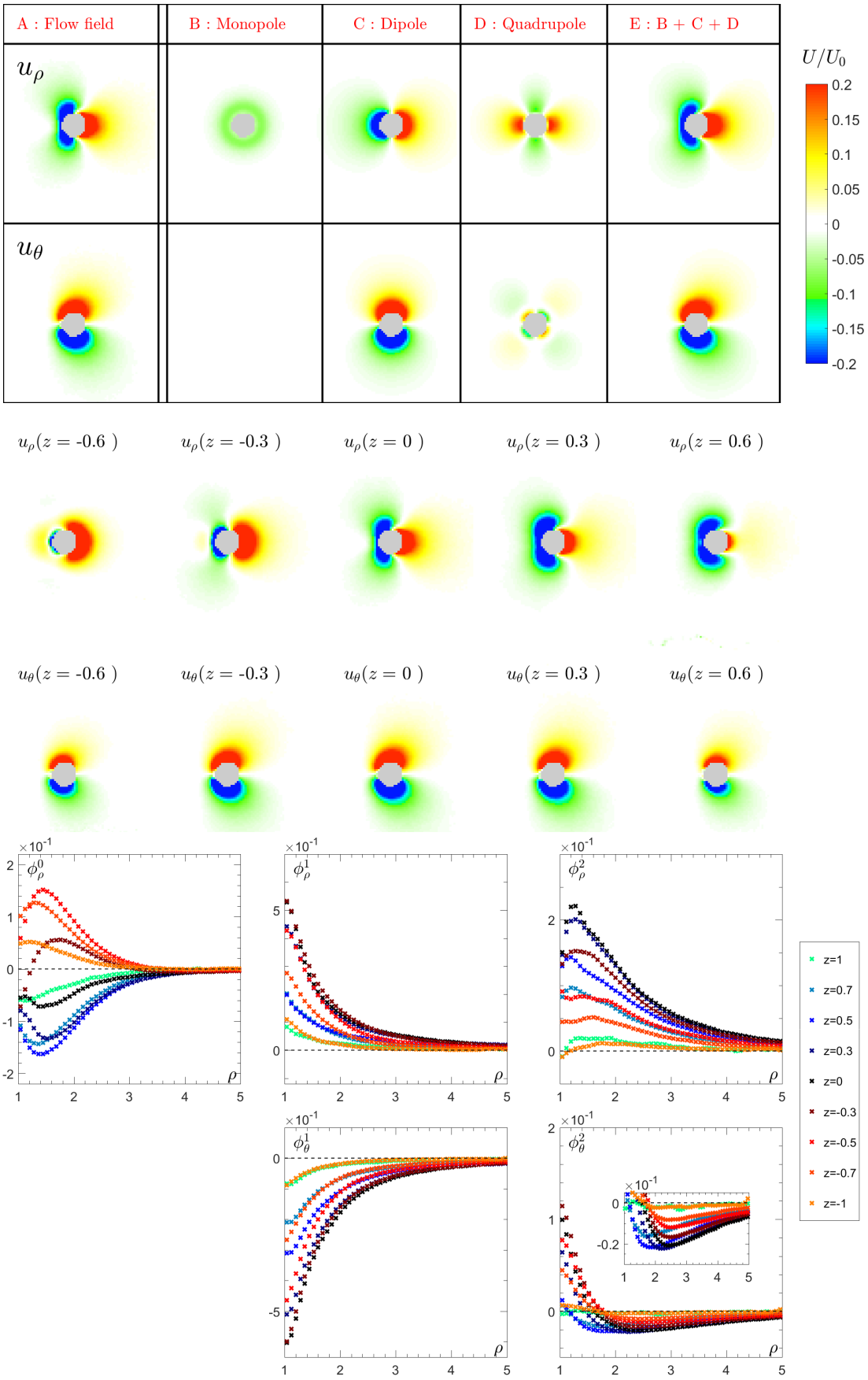

Figure 4.11: **Experimental flow field in the two-walls geometry:** Caption next page.

Caption of Fig. 4.11 Top: u_ρ and u_θ in the median plane. A. Experimental flow field. B. Monopolar symmetry i.e projection onto L_0. C. Dipolar symmetry, i.e. projection onto L_1 and L_1^1. D. Quadrupolar symmetry, i.e. projection onto L_2 and L_2^1. E. Reconstruction from only the three first symmetries, i.e. sum of B, C and D. Middle: $u\rho$ (top) and u_θ (bottom) for $z = -0.6$, $z = -0.3$, $z = 0$; $z = 0.3$; $z = 0.6$ (same color code as above). Bottom: Amplitudes $\phi_\rho^n(\rho, z)$ and $\phi_\theta^n(\rho, z)$, of the first three modes $(n = 0, 1, 2)$ as a function of the radial coordinate ρ for different z.

we never observe the reverse solution with a positive, respectively negative, monopolar symmetry at the bottom, respectively top, wall, we conclude that the symmetry is not spontaneously broken but induced by the gravity and the density mismatch between the water droplet and the surrounding oil phase.

Summary

In summary, in this chapter, we presented the kinetics of droplets swimming close to a wall, and highlited how the droplet size, the nature of the bottom wall and the confinement all played a role in two characteristics value of the droplet steady state, its steady velocity V and its shrinking rate κ.

Then, we presented first-of-a-kind measurements of the 3D flow field produced by a swimming water droplet using PIV method and confocal microscopy in two different configurations, namely that of a droplet swimming parallel and close to a single confining boundary (bottom wall), and that of a doubly-confined droplet swimming between and close to two parallel walls. In the one wall case, a simplified description of the swimming droplet was proposed as the superposition of (i) the few first axisymmetric viscous and potential singularities (and their image system), accounting for the swimming motion along the wall and (ii) a vertical point force and source dipole (and their image system), accounting for the pumping flow resulting from the top-down asymmetric modification of the chemical environment of the droplet by the confining wall. This model was observed to provide a very good description of the flow field around the droplet, with the swimming-induced singularities (i.e. parallel to the wall) able to reproduce accurately the quadrupolar and dipolar symmetries of the flow field, while the normal singularities associated with the pumping flow was further able to capture the monopolar symmetry signature of the flow field generated by the droplet. Adding this second contribution was shown to be critical to effectively capture the dominant flow field far from the droplet, which drives its interactions with its neighbors and environment.

The surprisingly good quality of this description is rooted in the possibility of superimposing the singularities parallel to and orthogonal to the wall, which in turn comes from the linearity of the Stokes equation. This is only valid in the steady state, where the slip velocity at the interface of the swimmer are, by definition, constant. If one were to solve the dynamics of the swimmer, say when approaching the wall with some angle, then the slip velocity at the interface of the swimmer would couple to the hydrodynamics through the concentration field, making the problem truly non-linear. Solving for the swimmer trajectory using a quasi-static approximation is a promising route for future work.

Another interesting perspective would be to consider interactions between two confined swimming droplets. One infers from the present results that the long distance interaction between two droplets swimming at the wall is dominated by the monopolar symmetry, which is attractive. When the interacting droplets get closer, the quadrupolar symmetry eventually dominates so that, at short enough distance, one recovers the usual pusher/puller qualification and resulting dynamics.

Finally, in the case of confinement between two walls, we observe an asymmetry with respect to the median plane, and again a monopolar symmetry, which indicates that the gravity cannot be neglected, as one could have thought at first sight. The confinement, in this case, imposes that the flows pumped by the swimmer must be evacuated laterally, inducing a recirculation at the scale of the droplet.

Chapter 5

Swimming in 1D

Motivation

The main possible application of pure water swimming droplets is their use in microfluidic channels as active components able to independently perform work (transport, local flux, mixing...). More generally, it might be very interesting to use micro-swimmers in micro-channels, as the confinement is a way to steer their motion [134]. Yet, very few studies [45] have been done in order to understand the effect of such confinement on the swimmer, while some theoretical work on weakly confined squirmers in tube [135, 136], showing in particular that pushers, pullers and neutral swimmers behave very differently.

In a 1D microfluidic devices, a droplet is essentially able to swim in one dimension, confined by the walls of the microfluidic channels. However, it is not obvious that such droplets are able to swim when they are highly confined. Indeed, in order to swim, the droplets need to advect the external fluid through the space between the wall of the channel and their interface. For droplet smaller than the channel height ($a < h$), Fig. 5.1-top, one may imagine that this space is still enough to allow the droplet to swim, but as the droplet size gets closer to the channel height, or even larger (then the droplet deforms and takes an elongated shape), Fig. 5.1-bottom, it is not obvious that the droplet is still able to swim. This may also depend on the shape of the channel: if the channel has a square section (Fig. 5.1-left), then the corners of the channel provide some space for the advection of the fluid; however if the channel has a circular section, Fig. 5.1-right, then the only space left for the outer fluid to pass is the lubrication layer between the droplet interface and the channel wall.

In this chapter, we present first-of-a-kind investigations on and characterizations of the swimming behaviour of droplets weakly to strongly confined in 1D channels, using square (section 5.1) and cylindrical (section 5.2) glass capillaries. Then we play with some more exotic geometries, such as stretched cylindrical capillaries (section 5.3), or square channels with some sharp constriction - i.e. a jump in the channel width (section 5.4). Finally, we introduce a theoretical framework in order to understand the observed experimental phenomena.

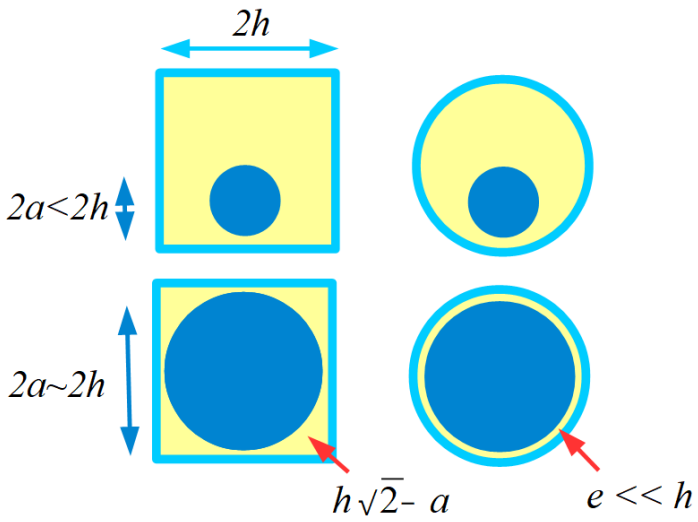

Figure 5.1: **Typical section view of droplets in capillary: top**: droplet smaller than the capillary height. **Bottom**: droplet equal to or larger than the capillary height. **Left**: Section of square capillaries. **Right**: Section of cylindrical capillaries.

Experimental realization

1D geometries

We are going to use four different 1D geometries:

Square capillaries: we use square glass capillaries of length 5 cm, and of four different inner dimensions: $2h = 400$ μm, $2h = 200$ μm, $2h = 100$ μm and $2h = 80$ μm. h is defined as half the inner dimension of the capillary, and will be compared to a, the radius of the droplet for spherical droplets, and the half-length for elongated droplets. The capillaries are either used native, or silanized beforehand, using the silanization protocol described in section (3.2.2.2).

Cylindrical capillaries: we use cylindrical glass capillaries of length 10 cm, and of two different inner dimensions: $2h = 200$ μm and $2h = 100$ μm. The cylindrical capillaries are systematically silanized[1] using the protocol described in section (3.2.2.2).

A special care should be taken for the visualization through cylindrical capillaries. Because of their shape, the light is diffracted through the capillary, and the final image is deformed. To address this problem, one usually immerses non planar interfaces into a liquid with the same refractive index as glass ($r_{glass} = 1.52$), to make the glass iso-index liquid interface optically invisible. In our case, we should be careful not to let the iso-index liquid enter inside the capillary, which is open at both ends. In particular, we had to be careful (i) to put the capillary in the iso-index liquid from the top, letting both ends out of the iso-index liquid, and (ii) not to let the iso-index liquid reaches one end of the capillary by capillarity (which would happen for instance if the capillary

[1]In not-silanized cylindrical capillaries, the droplets stick to the wall, which does not necessarily prevents them from "swimming" - some wetting droplets have been observed to move - but would drastically changes the physics at play.

was simply put on a glass slide, creating a small space between the capillary and the slice through which the iso-index liquid can advance by capillarity). The device used is

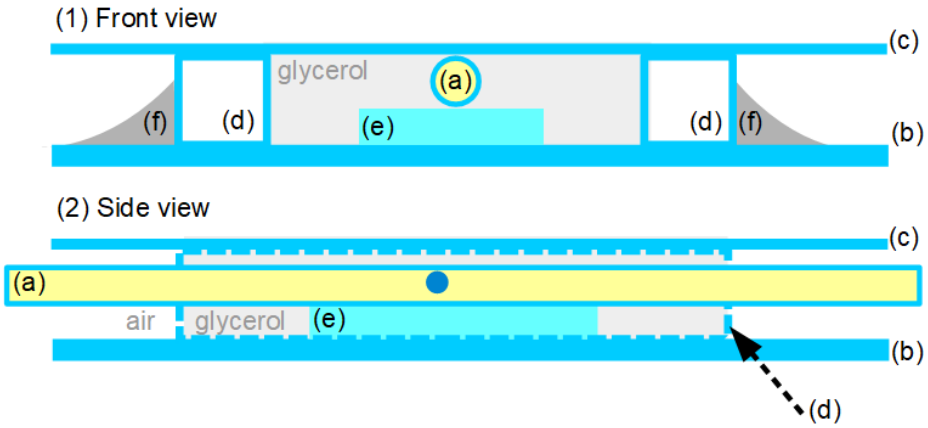

Figure 5.2: **Device for imaging through cylindrical capillaries:** (1) Front view and (2) side view of the device used to immerse a cylindrical capillary in glycerol. The cylindrical capillary (a) filled with the oil solution is placed inside a cavity filled with glycerol, constituted of a bottom glass slide (b) and a top glass coverslip (c) spaced by two square capillaries (d) glued to the glass slide using NOA epoxy glue (f). To avoid that the glycerol enters the cylindrical capillary, it is elevated using a small PDMS piece (e): then the two ends of the capillary hang in the air.

shown in Fig. 5.2: the two ends of the capillary hang in the air. The iso-index liquid we chose is glycerol ($r_{glycerol} = 1.47$): although its index does not match perfectly the one of glass, it was observed to be good enough for visualization, and it has the advantage of being water soluble, thus easily washable, and not expensive.

Stretched cylindrical capillaries: at some point, we wanted to try making droplets in conical capillaries, in order to have an *increasing* confinement. The simplest and most efficient method[2] we found out was to use a lighter: holding the capillary on one side, and adding a small weight (a glass slide) on the other side, we approach very slowly the vertical capillary with the lighter until it starts to elongate. This is a really handcrafted method, but it gives exactly the wanted result: a $h = 100$ μm capillary stretched on around 1 cm, with the smallest radius being of the order of 10 μm. The silanization of these stretched capillaries is done after the elongation (in order to not "elongate the surface properties").

Square channels with a sharp constriction: we cannot easily design a sharp constriction using glass capillaries, thus we design these constrictions in PDMS using a soft lithography process, with a mask such as the one sketched in Fig. 5.4. An inner channel is linked to an outer channel through a sharp change of width (the typical length transition is 20 μm $<<$ h_{in}). The inlet channel has a square section with

[2]To pull a capillary of 1 mm outer diameter, one usually uses a Needle Pipette Pullers (Kopf® Model 720), which allows to make very well controlled needle of controlled length and diameter. However, these apparatuses are calibrated for 1 mm capillary, and we had a very hard time obtaining a long and large elongation with our 200 μm inner diameter capillaries.

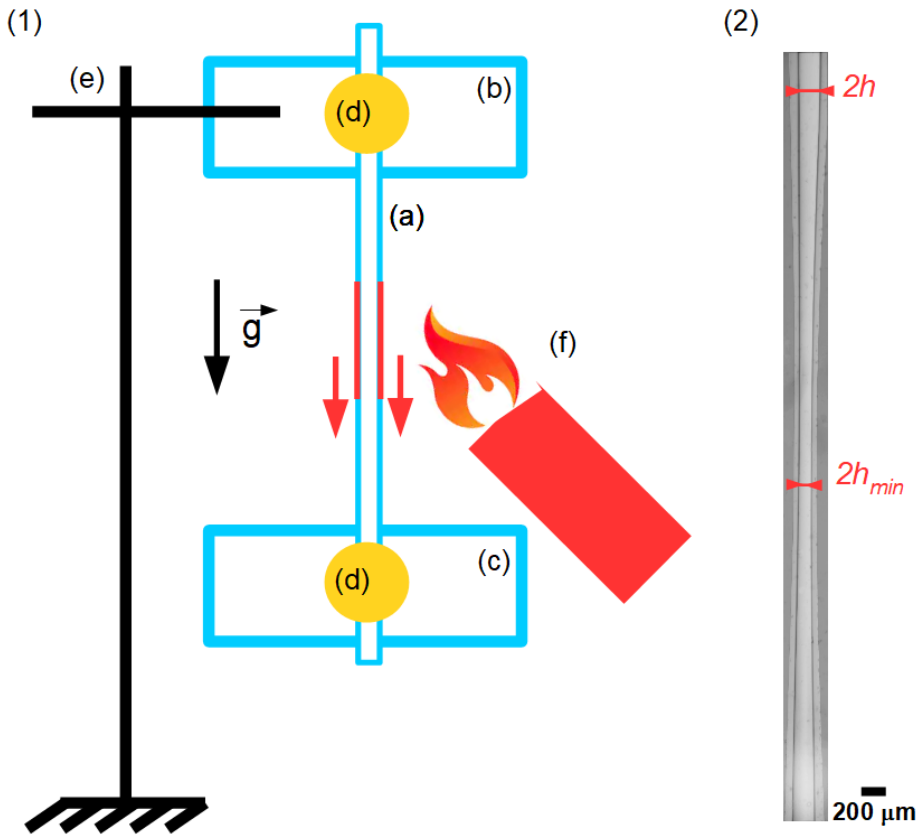

Figure 5.3: **Design of the set up dedicated to the stretching of cylindrical capillary:** (1) set up: the capillary (a) is attached at each end to two glass slides (b) and (c) with sticky pastes (d). One glass slide (b) is attached to a holder (e), while the other (c) is left hanging to act as a small weight. A lighter (f) is approached to locally heat the capillary, and removed as soon as the capillary starts stretching. (2) Images of a stretched cylindrical capillaries of initial radius h, and minimum radius h_{min}.

$w_{in} = h_{in} = 100$ μm, and the outlet channel has a rectangular one, with the same height as the inlet channel, but a different width w_{out}. Several channels are made with different w_{out}, from 10 μm to 200 μm, per step of 10 μm. Before use, the channels are filled with the oil solution, and apart from the inlet and outlet, covered by a glass coverslip. The water filled needle used to make the droplet is inserted through the left opened inlet.

Conducting an experiment

Except where indicated otherwise, all following acquisitions are performed under the macroscope (section 3.3.1.1). The droplets are made one at a time, using the femtojet apparatus (section 3.2.2). The discrete phase (water with 15% wt NaCl) filled needle is inserted inside one end of the capillary (or one end of the channel), as illustrated in Fig. 5.5, and one droplet is produced. When the droplet attains the desired size, a small kick is given through the needle. The droplet detaches and starts swimming. Statistically, the droplet swims away from the needle (the presence of the needle, or the way the droplet is produced breaks the front-back symmetry of the droplet). From time to time, the droplet swims towards the air interface, then bounces on it, swims

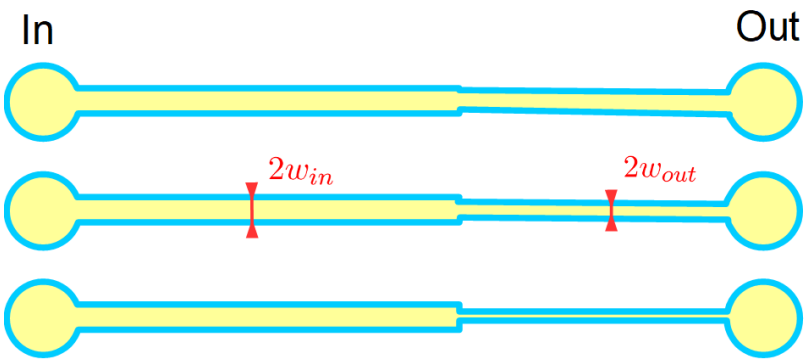

Figure 5.4: **Typical mask for designing square channel with a sharp constriction**: The resulting inlet channel has a square section with $w_{in} = h_{in} = 100$ μm, and the outlet channel has a rectangular one, with the same height as the inlet channel, but a different width w_{out}.

back slowly on its trail, and eventually passes the point where it was formed and starts swimming normally.

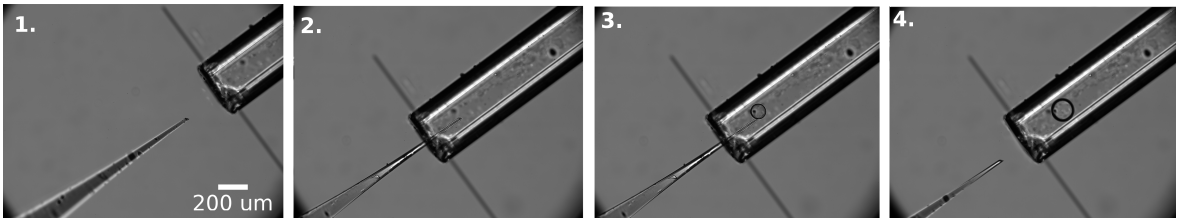

Figure 5.5: **Insertion of a needle in a capillary:** (1) the needle filled with the water phase is placed in front of the capillary, (2) and then inserted so that the tip is typically 200 μm away from the air interface. (3) the pressure is risen at the other end of the needle, and a droplet starts forming. (4) When the droplet attains the desired size, the pressure is cut and the needle simultaneously drawn quickly out of the capillary so that the droplet detaches.

5.1 Square capillary

Microfluidic channels usually have a square like section. We first study the behaviour and swimming velocity of a swimming droplet in square glass capillaries, then we look at the flow field around the droplets, and we finally focus on the interaction between two droplets in this geometry.

5.1.1 Swimming behaviour

5.1.1.1 Typical trajectories

We made several experiments of one unique water droplet with 15% NaCl in square capillaries of height $2h$ filled with a solution of 25 mM mono-olein in squalane. We vary

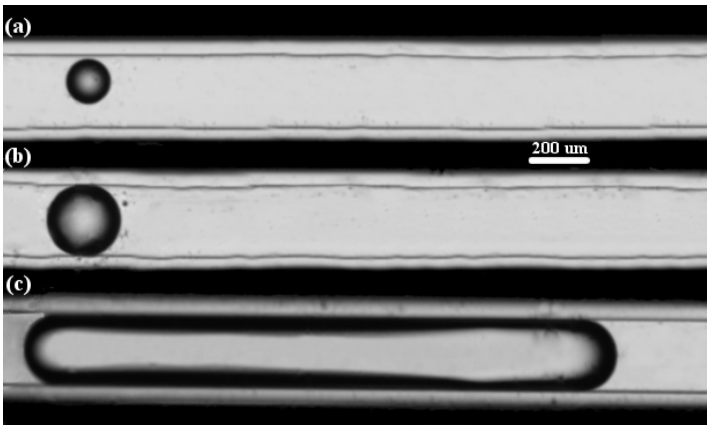

Figure 5.6: **Images of droplets swimming in a square capillaries of half-height $h = 100$ μm:** (a) droplet smaller than the capillary height $\frac{a}{h} \simeq \frac{1}{2}$. (b) droplet of the size of the capillary $\frac{a}{h} \simeq 1$. (c) droplet longer than the capillary height $\frac{L}{2h} \simeq 7$.

(1) the droplet size, from small round droplets of radius $a = 30$ μm (Fig. 5.6(a)), passing by droplets having exactly the size of the channel $a = h$ (Fig. 5.6(b)), to elongated ones of length[3] much longer than the capillary height $L = 1700$ μm (Fig. 5.6(c)), and (2) the capillary height h (defined as half the inner dimension of the capillary), $h =$ 40, 50 100 or 200 μm. We saw in the previous section that the hydrophobicity of the walls may have an influence on the swimming, so we also use $h = 100$ μm silanized capillaries for comparison. All these droplets are observed to swim, even the longest ones. Typical trajectories are provided in Fig. 5.7, together with the corresponding velocities in the capillary direction, and the size of the droplet as a function of time (for spherical droplets, the size $L = 2a$ is the diameter, and for long droplet, L is the droplets length). The droplet has the size of the capillary when $a = h$. The droplets take an elongated shape when $a > h$. Very small droplets ($a < \frac{h}{3}$, not shown here) behave almost like in 3D: they have a random direction and are able to turn back in the channel. Droplet smaller than the capillary height but bigger than the previous ones ($\frac{a}{3} < a < h$) are observed to oscillate between the two sides of the capillary with a net motion in one direction of the capillary, and a velocity that decreases before colliding with a wall, and increases after that, and thus varying a lot with time. Droplets of the same size or larger than the capillary height ($L > 2h$) are observed to swim straight, with a constant velocity. Note that the size of the droplets does not change significantly on the experiment timescale.

5.1.1.2 Velocity of the droplets

For each experiment, we measure the average velocity over the trajectory in the direction of the capillary, V, and we plot it as a function of the length of the droplet L, rescaled by the capillary height $2h$, which we call the confinement $\frac{L}{2h}$. A confinement $\frac{L}{2h} = 1$ corresponds to a spherical droplet of the size of the capillary. For small droplets, we measure only the maximum velocity during the oscillations, which corresponds to the time when the droplet is the furthest from the wall. The results are displayed on Fig. 5.8.

[3]The length of the droplet L can also be defined for spherical droplets, it is then equal to $2a$.

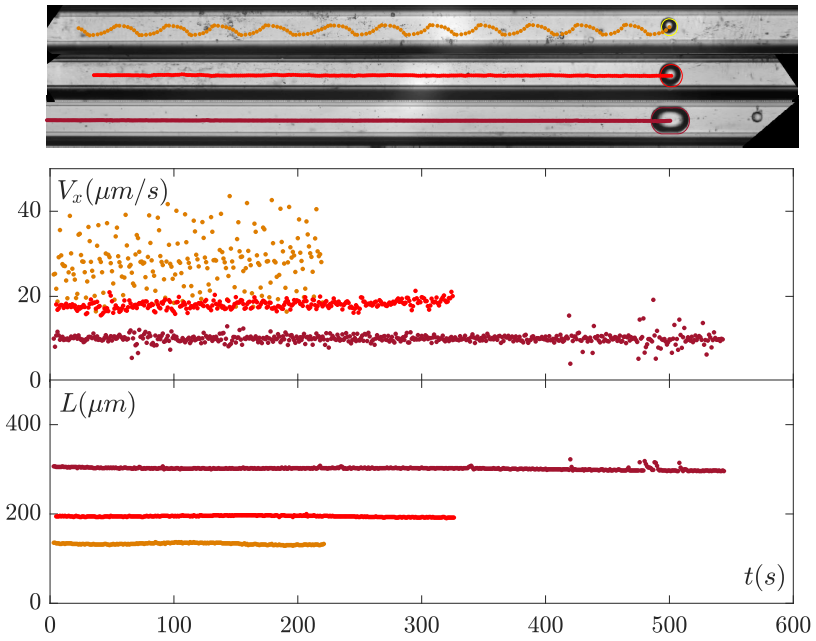

Figure 5.7: Typical behaviour of droplets of different sizes in a 100 μm square capillary. **Top:** Trajectories of the droplets. **Middle:** Velocity in the direction of the capillary versus time. **Bottom:** Length of the droplet versus time. One color corresponds to one droplet: orange for a round droplet of radius $a = 70\ \mu\text{m} < h$, bright red for a round droplet of radius $a = 100\ \mu\text{m} = h$ and dark red for an elongated droplet of length $a = 150\ \mu\text{m} > h$.

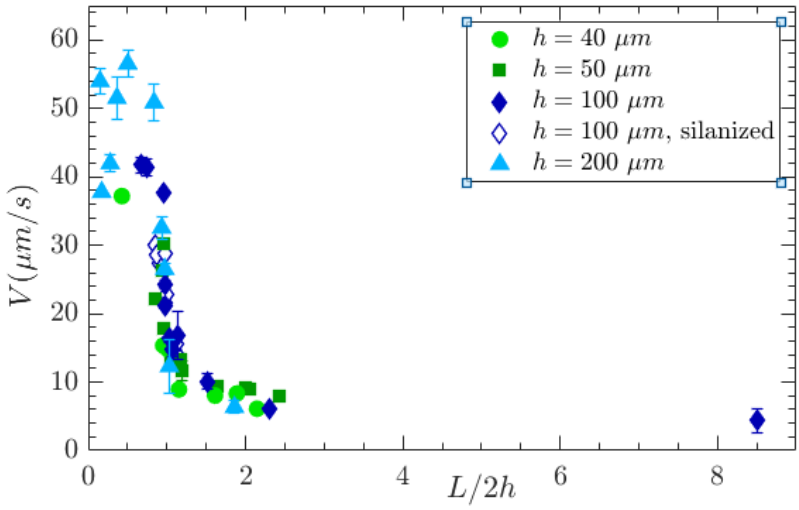

Figure 5.8: Velocity of droplets, V, swimming in square capillaries as a function on the confinement $\frac{L}{2h}$, for different capillary heights h. The error bars represent the standard deviation to the average value in time of the velocity during an experiment - limited for the small droplets to the maximum velocity during the oscillations.

We observe that the data collapse on one curve: the velocity depends only on the confinement $\frac{L}{2h}$. Furthermore, the silanization of the $h = 100$ μm capillaries do not affect the velocity. The velocity strongly decreases with the confinement for $\frac{L}{h} > 2$ (round droplet). We distinguish three behaviours, depending on the confinement:

(i) $\mathbf{\frac{L}{2h} < 1}$: small droplets have a 2D (or even 3D) motion. For not too small droplets, this motion is persistent in the direction of the capillary x, and oscillates between the two walls in the perpendicular direction y, with an almost periodic behaviour. Similarly, the velocity oscillates between a smaller value at the wall (not necessarily zero), and a maximum value between the two walls. The velocity that the droplet reaches between the two walls is most likely not its active velocity that it would reach in a steady regime, but a compromise between how much the droplet can tend toward this active velocity before starting to feel the other wall. This explains the large disparity in the velocity observed for small confinement (see below for more detailed description).

(ii) $\mathbf{1 < \frac{L}{2h} < 2}$: The droplet has a straight trajectory in one persistent direction. The velocity decreases a lot with the increasing confinement. For $L > 2h$, the droplet is not spherical anymore, and takes an elongated shape.

(iii) $\mathbf{2 < \frac{L}{2h}}$: The droplet has a straight trajectory in one persistent direction. Even very long droplets swim. The velocity of the droplet has a constant value $V_{lim} = 5$ μm/s which does not depend on the confinement anymore. Because the square capillary geometry is not a very easy geometry to deal with analytically (no axisymmetry...), we then investigate this phenomenon in more details in the next section, using cylindrical capillaries.

5.1.1.3 Discussion on the small droplets $\frac{a}{h} < 1$

The behaviour of small droplets in a tube is far from trivial. While physico-chemical interactions tend to move droplets away from walls, purely hydrodynamic interactions for pushers in 3D lead to an alignment with wall. In more confined geometries such as a tube, it has been shown [120, 137] that a pusher would oscillate in the tube, but eventually becomes trapped to the wall, and reaches a stationary state where the pusher has a circular motion along the tube wall, without any net motion in the tube direction. Recall here that the description in terms of pusher is anyhow not correct as stressed in chapter (4). These two effects oppose each other. Experimentally, we observe that droplets smaller than the capillary height oscillate between the two side walls of the square capillary. In the absence of more complete theoretical framework, we are interested in what the experimental observations can teach us on the system.

Here we study succinctly the experimental behaviour of small swimming droplets in square capillaries. A deeper analysis has been put on hold for now [4].

Fig. 5.9 shows the trajectory of the small droplets for the two largest capillary sizes (top: $h = 100$ μm, bottom: $h = 200$ μm), in which it is easier to decrease the confinement.

[4] A collaboration is in project to further explore the problem, with the LiPhy Grenoble laboratory to simulate small droplets in a confining 2D or 3D channels, and with the Laboratory of Dissipative and Biological Physics of Kyoto University to conduct complementary experiments.

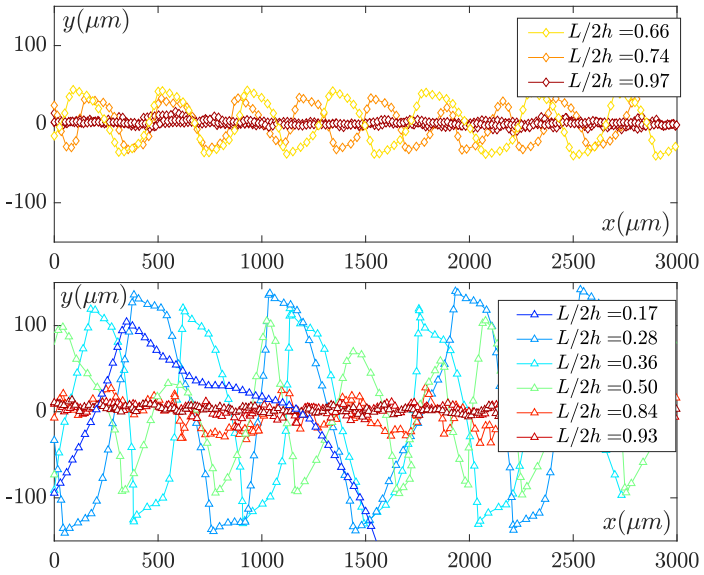

Figure 5.9: Oscillation of the center of mass of small droplets in square capillaries of $h = 100$ μm (top), and $h = 200$ μm (bottom), for different confinements (blue=low confinement ; red=strong confinement). We observe a period which depends on the confinement.

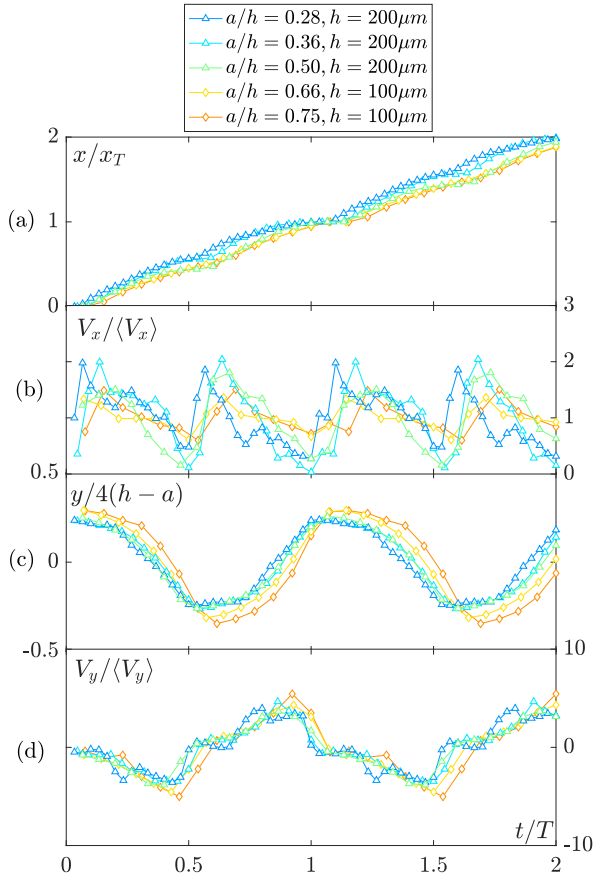

Figure 5.10: **Rescaled variable over two periods:** Evolution of different quantities for several droplets (color) as a function of the time rescaled on the period T, for two periods of oscillation. (a) the x coordinate (position in the direction of the capillary axis) rescaled by the wavelength x_T. (b) the velocity in the direction of the capillary V_x rescaled by the characteristic velocity $\langle V_x\rangle$. (c) the y coordinate (position in the direction perpendicular to the capillary axis) rescaled by the orthogonal distance covered $4(h-a)$. (d) the velocity in the direction perpendicular to the capillary axis V_y rescaled by the characteristic velocity $\langle V_y\rangle$.

Trajectories of droplets of different sizes have different colors (red: $a = h$, dark blue: $a \ll h$). The droplets are observed to oscillate periodically between the two side walls (typically between $-h+a$ and $h-a$), and on a typical wavelength $x_T(a,h)$, for a typical period T, with a velocity $\mathbf{V}(t) = V_x\mathbf{e}_x + V_y\mathbf{e}_y$ ($\mathbf{e}_x$ being the direction of the capillary). No swimming in z (direction of the gravity) is observed. The shape of the trajectory is not trivial. At the wall, (maximum and minimum of y), there is a discontinuity of the velocity, which stands for a rapid change in orientation of the droplet. The typical velocities, period and length are linked through trivial relations:

$$\langle V_x \rangle = \frac{x_T}{T}, \tag{5.1}$$

$$\langle V_y \rangle = \frac{4(h-a)}{T}. \tag{5.2}$$

We can then rescale the quantities t with the period T, x with the wavelength x_T, y with the height $4(h-a)$ (the droplet makes two round trips during one period), V_x with the typical velocity $\langle V_x \rangle$, and V_y with the typical velocity $\langle V_y \rangle$. We then observe their typical behaviour for different confinement over two periods, in Fig. 5.10. The rescaled quantities have very similar behaviour. At the beginning of one cycle (maximum of y), the droplet is at the wall. The velocity in the direction of the capillary V_x is minimum, while the perpendicular velocity V_y is zero: the droplet is almost immobile. Then the droplet velocity increases rapidly while the droplet starts swimming in the capillary direction, parallel to the wall (high V_x, low $|V_y|$). The droplet slowly drifts away from the wall (y decreases), V_x reaches a maximum and starts decreasing while $|V_y|$ increases (not in a very regular fashion). Both velocities tend toward a constant value in the middle of the capillary. Then when the droplets get closer to the other wall, both V_x and $|V_y|$ drop rapidly, V_x to a small value and $|V_y|$ to zero at the second wall, this corresponds to half a cycle. The exact same behaviour starts again, in the same direction for x and in the opposite direction for y, toward the initial wall.

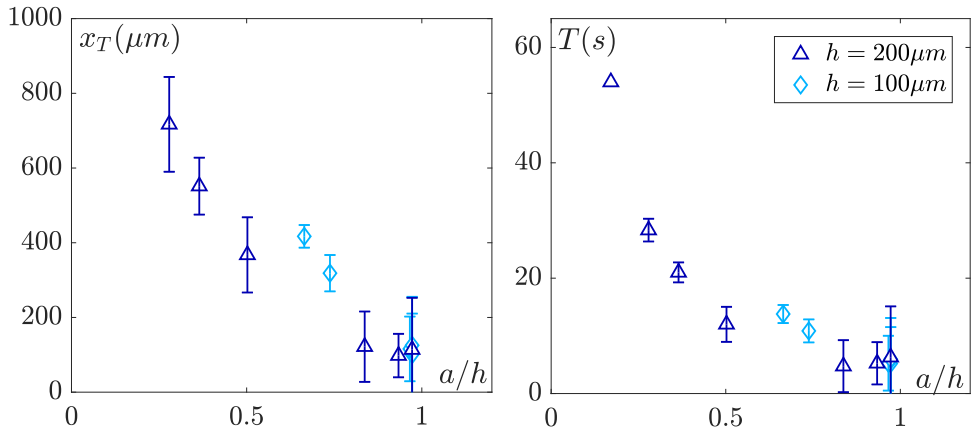

Figure 5.11: **Period and wavelength of the oscillations of small droplets:** Left - Evolution of the wavelength of oscillation x_T with increasing confinement $\frac{a}{h}$. The wavelength is averaged on all observed periods. Right - Evolution of the period of oscillation T with increasing confinement $\frac{a}{h}$. The period time is averaged on all observed periods. The errors bars are the standard deviations.

The droplet never reaches a steady state between the two walls. It strongly depends

on how much the droplet has the time to relax before reaching the other wall. But this relaxation time is likely to be strongly dependent on the confinement, making difficult further analysis in the absence of analytic or numeric support. Therefore, we limit ourselves at characterizing the oscillation per the two quantities T and x_T, in Fig. 5.11, that are direct estimation of the average velocities, through the relations (5.1) and (5.2).

5.1.2 Flow field in 1D

We also did PIV around droplets in 1D capillary. In the absence of theoretical framework, the results are very descriptive. We present and describe succinctly the typical flow field around droplets in square channels.

PIV in square glass capillaries?

In square glass capillaries, the tracers are observed to agglomerate at the back of the droplet. The formation of such agglomerates is visible in Fig. 5.12-top. The presence

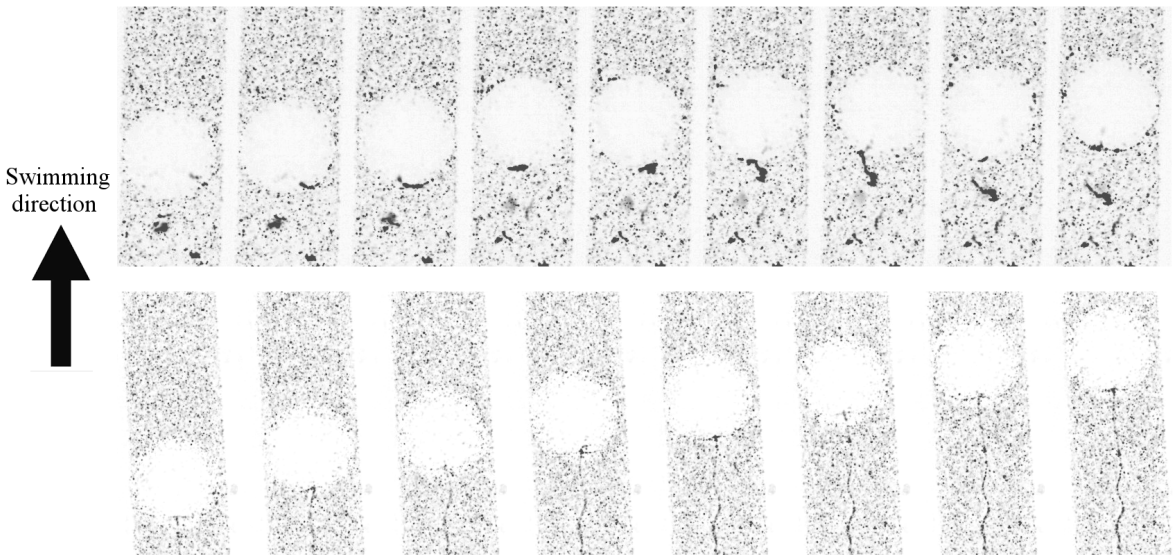

Figure 5.12: **Formation of agglomerate of colloids in square capillaries:** top - formation of agglomerate of colloids in square glass capillaries: the agglomerate forms at the back of the droplet, and detaches at some point, leaving a trail of tracer agglomerates behind the droplet. Bottom - formation of a wire like agglomerate of colloids in a square NOA microfluidic channel.

of these large agglomerates makes it difficult to perform reliable PIV. We don't know the origin of this behaviour. However, switching to NOA microfluidic square channels weakens this effect. More precisely, in NOA channel, the droplet leaves behind a wire like agglomerate of colloids which doesn't disturb the PIV as much, which is visible in Fig. 5.12-bottom.

PIV in square NOA microfluidic channel

We use the same PIV method than the one described in chapter (4), with the same acquisition parameters, experimental conditions, and post-processing treatment, but in square NOA microfluidic channels of height 200 μm ($h = 100$ μm). We make droplets of different sizes, and we present here the measurements for two droplets of size $\frac{L}{2h} = 0.9$ (spherical droplet), in Fig. 5.13, and $\frac{L}{2h}$=1.2 (slightly elongated droplet), in Fig. 5.14.

What about small droplets? We have not been able yet to obtain clean reliable PIV around a small droplet bouncing in a NOA channel such as described in the previous section for glass capillaries. The reason is mainly that because the small droplets are not in a steady state, it is much more difficult to average the flow field around the droplet.

Medium droplet: Droplets of typically the size of the channel have a steady motion, and thus it is possible to investigate the flow around the droplet in different planes in z, (Fig. 5.13). There is a lot of information in these flow fields, and we don't have yet any theoretical or analytical framework to compare these results to, so we restrict ourselves at making some clear relevant descriptive statements.

- The outer fluid is advected around the droplet in the x direction in the corners of the square channel, mainly out of the median plane, close to the side wall in the plane above the droplet: Fig. 5.13, $\frac{z}{h} = -0.88$, v_x is negative (blue) in the corners above the droplet.
- The far field is dominated by a flow pushed away from the droplet in the top plane, and pulled toward the droplet in the bottom plane, both in the front and at the back of the droplet. This is a strong indication of a re-circulation of the flow in z, which is thus not symmetric with respect to the middle plane. For droplets of the size or smaller than the capillary height, this re-circulation is always observed to have the same direction (this bias might be due to the buoyancy of the droplet).
- The droplet perturbs the outer fluid on a typical distance of a few time its radius.

Large droplet: droplets longer than the capillary height also have a steady motion, which allows us to do some PIV around them, in different planes in z, in Fig. 5.14. Once again, we try to extract a few clear statements:

- Much like for the medium size droplet, the outer fluid is mostly advected around the droplet close to the top wall, while there is much less flow in the median plane of the droplet. This advection does not happen only in the corners, but also in the lubrication layer separating the droplet from the top wall.
- The far field behaviour of the flow field is similar to the one for the spherical droplet, although inverted: the outer fluid is pulled toward the droplet in the top plane, and pushed away from the droplet in the bottom plane.
- In the median plane, we observe lateral convection of the outer fluid in the plane, in front and behind the droplet.

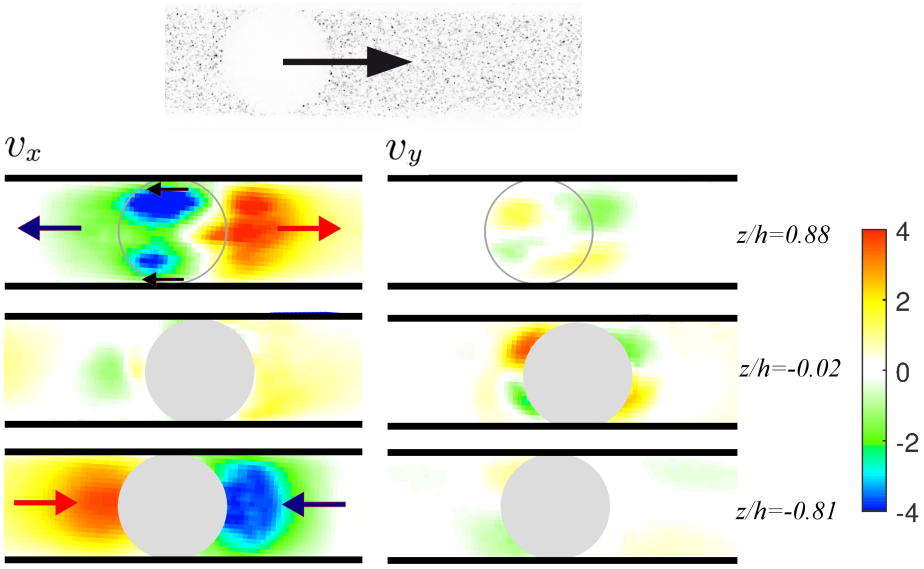

Figure 5.13: **PIV in a square capillary - $L = 2h$:** Components v_x and v_y of the flow field in the plane ($\mathbf{e}_x$,$\mathbf{e}_y$), at different heights in the capillary. $z/h = 0.88$ corresponds to a plane above the droplet, close to the top wall (z/h=1). $z/h = -0.02$ corresponds to the median plane. $z/h = -0.81$ corresponds to a plane below the droplet, close to the bottom wall (z/h=-1). The color-scale corresponds to the amplitude of the velocity rescaled by the velocity of the droplet (red for positive, blue for negative and white for zero). The arrows highlight the direction of v_x.

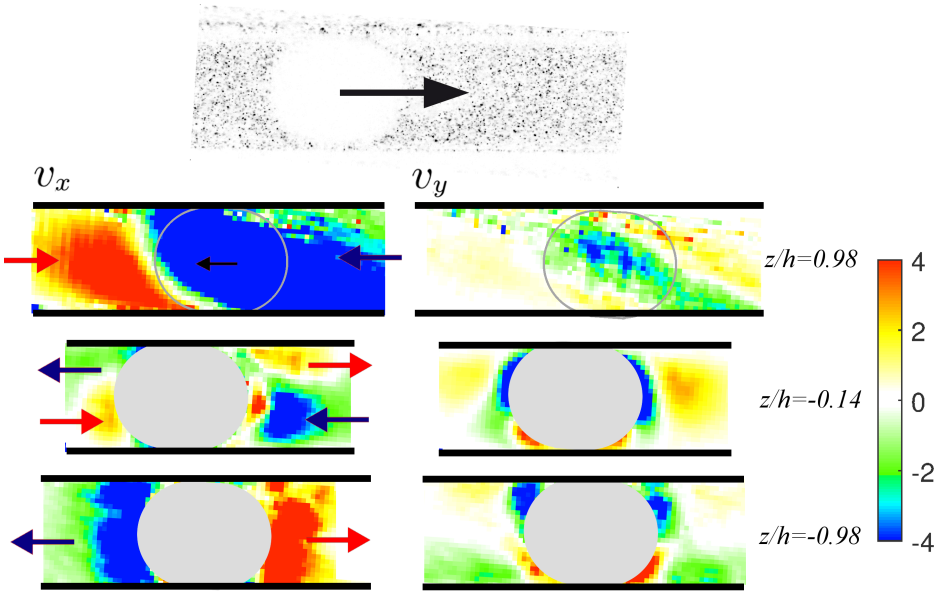

Figure 5.14: **PIV in a square capillary - $L > 2h$:** Components v_x and v_y of the flow field in the plane ($\mathbf{e}_x$,$\mathbf{e}_y$), at different heights in the capillary. $z/h = 0.98$ corresponds to a plane above the droplet, close to the top wall (z/h=1). $z/h = -0.14$ corresponds to the median plane. $z/h = -0.98$ corresponds to a plane below the droplet, close to the bottom wall (z/h=-1). The color-scale corresponds to the amplitude of the velocity rescaled by the velocity of the droplet (red for positive, blue for negative and white for zero). The arrows highlight the direction of v_x.

Even though these results are still very descriptive, simple conclusions can still be made from the previous considerations, especially for the case of the droplets of typically the capillary size, which will be of use in chapter 6: the droplets in 1D disturb the outer flow field on a distance of typically a few diameters, with repulsive long range behaviour. The droplets move in a direction which is opposite to the one of the fluid which bypass them by the corners of the channel.

5.2 Cylindrical capillaries

Microfluidic channels have generally a square-like section, which explains why we have started our experiments by using square capillaries. However, from a theoretical point of view, it is much easier to handle cylindrical capillaries, because of their cylindrical symmetry. Thus we switched to cylindrical glass capillaries to try to understand qualitatively and quantitatively the behaviour of the droplets observed in the previous section (hoping to observe the same kind of behaviour). In cylindrical capillaries, the droplets are much more eager to stick to the glass walls. To prevent this, we silanized our capillaries. The observation of cylindrical capillaries is made as explained in the experimental realization section. The experiments in this section have been conducted with Saori Suda, a PhD student from the Laboratory of Dissipative and Biological Physics of Kyoto University, during an internship at the Gulliver laboratory.

In this section, we first describe the formation of droplets in cylindrical capillaries; then we characterize the shape of the droplets, which is non-trivial. Finally, we study the swimming behaviour of the droplets.

5.2.1 Droplet formation

Unlike in the square capillary case, we were not able to produce droplets much longer than $\frac{L}{2h} > 5$. Indeed, upon formation, long droplets have a tendency to destabilize and divide into two parts (rarely three), and the division occurs at half the droplet length, producing two droplets of equivalent size swimming in opposite directions. The likelihood of such events increases with the droplet length, and the longest droplet we could achieve has length $L = 13h$. An example of such a division is given in Fig. 5.15 for a droplet of length $\frac{L}{2h} = 3.5$. Note that passive droplets in such conditions are stable - in the sense that they don't spontaneously divide (they are also likely to stick to the glass).

As passive droplets don't spontaneously divide, this effect is not likely to be due to a simple Rayleigh Plateau instability [138, 139]. We therefore suspect the activity of the droplet to play a role. In particular, we observe that while breaking, the two sides of the droplet go toward opposite directions, just like if the two sides were trying to swim independently of each other. In the lubrication layer this means that the outer fluid is pulled from one cap to the center of the droplet $\frac{L}{2}$, where the outer fluid accumulate, pinching the droplet and creating a "neck", a region of minimum radius of the cylindrical droplet. The Marangoni and phoretic effects give rise to flows that go toward maximum surface tension area, thus toward maximum concentration of swollen micelles area. Then the previous observation - the outer flow goes toward the

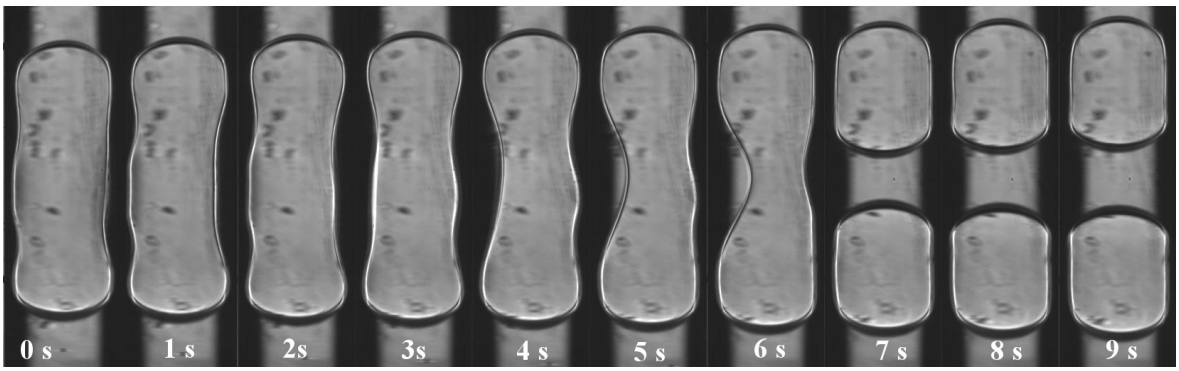

Figure 5.15: Evolution in time of a long droplet of $\frac{L}{2h} = 3.5$ in a $h = 50$ μm cylindrical capillary which destabilizes right after its production: the droplet spontaneously divide into two droplets that start swimming in opposite directions. Time frame is 1 s.

middle of the lubrication layer - would mean that there is a maximum of concentration of swollen micelles in the middle of the lubrication layer. The breaking of the droplet would then be a consequence of the formation of the neck due to the accumulation of the outer fluid in the middle of the lubrication layer. This phenomenon might be stochastic (happening from time to time at the droplet formation because of inhomogeneities in the concentration field) or systematic (always happening for long droplets, as the result of a quantifiable physical phenomenon). This will be studied in further details in section (5.3).

We made several experiments of one unique water droplet with 15% NaCl in a silanized cylindrical glass capillary of height h filled with solution of 25 mM mono-olein in squalane. We vary (1) the droplet size, from small round droplets, (Fig. 5.16(a)), passing by droplets having the exact same size as the capillary, to elongated droplets, (Fig. 5.16(c)) of length much longer than the capillary height $L = 13h$, and (2) the capillary height $h = 50$ or 100 μm. We observe that all droplets are swimming, with a very similar behaviour than in a square capillary. One striking difference is that the shape of long droplets is not trivial: in a square capillary, we observe straight cylindrical elongated droplets ended by two spherical caps; in a cylindrical capillary, we observe that the distance between the wall and the droplet interface varies along the wall (the elongated part is not a straight cylinder), the radius of the droplet changes along its length, reaching a minimum at the back of the droplet, that we call the neck.

In the following, we first investigate the shape of the droplets, before studying their swimming behaviour.

5.2.2 Non-trivial shape

The shape of the long droplet will prove to be a crucial information for understanding the physics of the phenomenon. The shape can be understood in terms of local curvature of the droplet. The long droplets take non-trivial shapes: a layer of lubrication is observed between the droplet and the wall, and its thickness is not constant along the droplet, with a local maximum toward the back of the droplet. From the droplet point

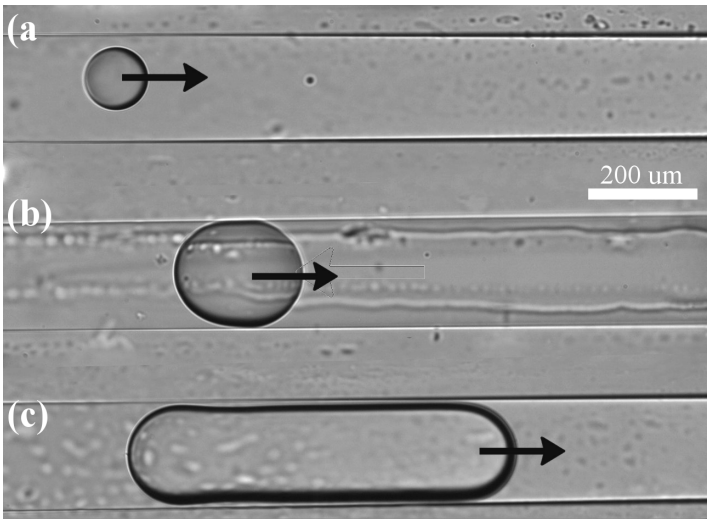

Figure 5.16: **Images of droplets swimming in a cylindrical capillaries of radius $h = 100$ μm:** (a) droplet smaller than the capillary height $\frac{a}{h} \simeq \frac{1}{2}$. (b) droplet slightly longer than the size of the capillary $\frac{L}{2h} \simeq 1.3$. (c) droplet longer than the capillary height $\frac{L}{2h} \simeq 3.5$.

of view, this corresponds to a minimum local radius leading to locally curved area, the neck. This shape does not change with time, which make us think that this is the result of an equilibrium. The surface of the droplet is characterized by two curvatures, the radial curvature (in the plane perpendicular to the observation plane) and the lateral curvature κ (in the observation plane). We focus in the following on the lateral curvature. For simplicity, we call curvature the lateral curvature κ. To compute the local curvature, we average the shape of one droplet over time, using the polar coordinates in the referential of the droplet centroid (the polar coordinates are better at conserving "circular" shape after averaging). From this averaged shape, back to the coordinates x and y, we get the local curvature using the formula:

$$\kappa(\alpha) = \frac{\Delta x(\alpha)\Delta(\Delta y(\alpha)) - \Delta y(\alpha)\Delta(\Delta x(\alpha))}{(\Delta x(\alpha)^2 + \Delta y(\alpha)^2)^{\frac{3}{2}}}, \tag{5.3}$$

Δ being the difference between two successive points of the shape. The result of the shape detection and the local curvature depending on the angle are given Fig. 5.17 for droplets with different lengths. Note that Δx, Δy, $\Delta(\Delta x)$ and $\Delta(\Delta y)$ are filtered using a low pass filter before computing κ.

- **Small droplets - $\frac{L}{2h} < 1$ - Fig. 5.17(a):** the droplets are mostly spherical (a slight flattening is observed on the side). Their curvature is a constant: $\kappa = \frac{1}{a}$.
- **Medium droplets - $\frac{L}{2h} \gtrsim 1$ - Fig. 5.17(b):** the droplets start deforming: they elongate a little through the side which is flattened (lower κ), without becoming completely flat ($\kappa > 0$). The spherical cap at the front has a radius a little lower than the one at the back: $\kappa(\alpha = 0) = 0.022$ μm $^{-1}$ (which correspond to $\frac{1}{\kappa} = 45$ μm), while $\kappa(\alpha = \pi) = 0.020$ μm $^{-1}$ (which correspond to $\frac{1}{\kappa} = 50$ μm).
- **Larger droplets - $\frac{L}{2h} \simeq 2$ - Fig. 5.17(c):** the droplets become elongated. The curvature along the elongated part decreases, and goes to zero (which means the

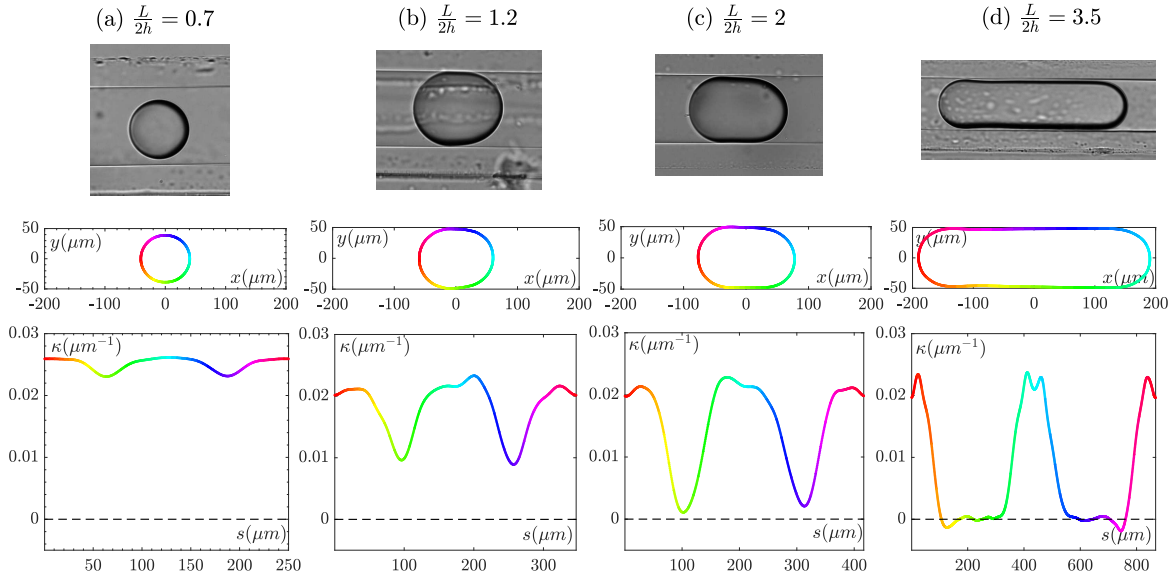

Figure 5.17: Image of droplets (top), measure of their shape (middle) and of the local curvature (bottom) for droplets of different sizes in a $h = 100$ μm capillary: (a) $\frac{L}{2h} = 0.7$, (b) $\frac{L}{2h} = 1.2$, (c) $\frac{L}{2h} = 2$, (d) $\frac{L}{2h} = 3.5$. The colors correspond to the angles, light blue for the front cap and bright red for the back cap.

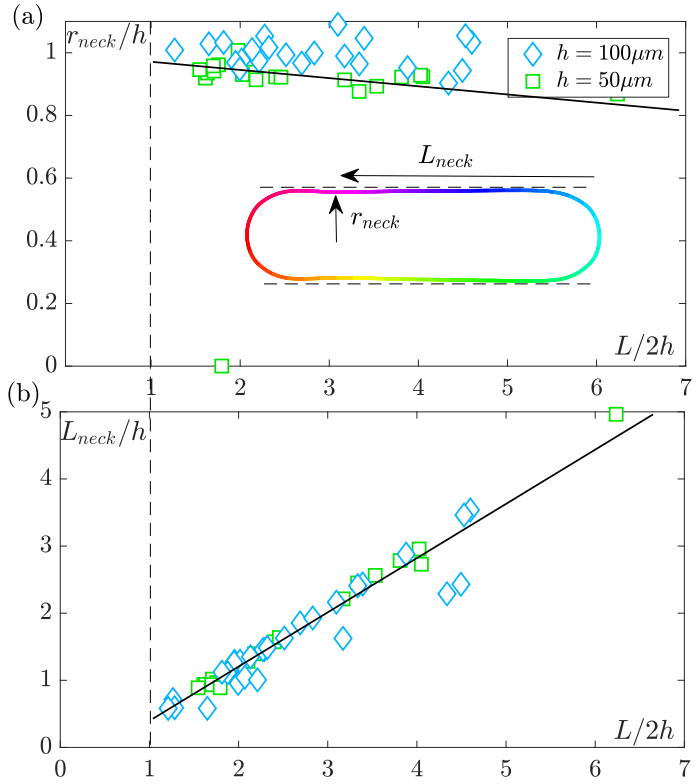

Figure 5.18: **Evolution of the neck with the confinement:** (a) evolution of the neck radius r_{neck} with the confinement $L/2h$. (b) Evolution of the neck length L_{neck} with the confinement $L/2h$. The linear fits (black line) are made on the measurements in the $h = 50$ μm capillary.

shape is cylindrical). There is still a small difference in curvature between the front and the back caps.

- **Very long droplets - $\frac{L}{2h} > 3$ - Fig. 5.17(d):** the droplets elongate even more through a long cylindrical part of curvature $\kappa = 0$. This elongated shape is deformed at the back of the droplet, and the lubrication layer thickness has a maximum value just before the spherical caps, which corresponds to an area of negative curvature. In this case, we do not measure significant difference between the radius of the front and back spherical caps. The elongated part of the droplet corresponds to the almost zero curvature part of the curve, while front and back spherical caps correspond to the large curvature part of the curves (around $\alpha = 0$ and $\alpha = \pi$). We always observe the presence of a local negative minimum of the curvature (local maximum of the lubrication layer thickness) at the back of the droplet, right before the back spherical cap. This minimum corresponds to a minimum in the droplet width, which we call the neck.

The particularities of the shapes described above are the difference of curvature between the front and back caps, for droplets of $\frac{L}{2h} \simeq 2$, and the presence of the neck for long droplets. If we focus on this second phenomenon, we can measure the position and the radius of the neck for droplets of different lengths in capillaries of different heights. The neck is at a position L_n from the front of the droplet, and l_n from the back of the droplet: $L = l_n + L_n$

The position of the neck collapse on a curve which is roughly a line of equation $\frac{L_{neck}}{2h} = 0.81\frac{L}{2h} - 0.43$ (linear fit on the data for $h = 50$ μm, which are better defined). When the neck first appears ($\frac{L}{2h} \gtrsim 2$), the neck forms at the middle of the droplet. Then for longer droplet, the neck is always situated at the back of the droplet $\frac{L_{neck}}{2h} > 0.5\frac{L}{2h}$. The radius of the neck decreases very slowly with increasing length. For $h = 50$ μm capillaries, the neck is less pronounced, and its radius harder to measure. Also, the radius decreases roughly linearly with increasing confinement, with the equation $\frac{r_{neck}}{h} = -0.02\frac{L}{h} + 0.96$.

5.2.3 Swimming behaviour

5.2.3.1 Typical trajectories

Just like in the square capillaries case, we look at the trajectory of the droplets in cylindrical capillaries, Fig. 5.19. This behaviour is very similar to what is observed in square capillaries: small droplets oscillate, although in a less regular fashion than in a square capillary, while medium and large droplets swim straight at a constant velocity.

5.2.3.2 Velocity of the droplets

For each experiment, we measure the average over the trajectory of the velocity in the direction of the capillary $\langle V \rangle$, and we plot it as a function of the length of the droplet L, rescaled by the capillary height $2h$ (the confinement). For small droplets, we measure only the maximum velocity during the oscillation, which corresponds to the time when the droplet is the furthest from the wall, as we did for the droplets in square channels. The results are shown in Fig. 5.20.

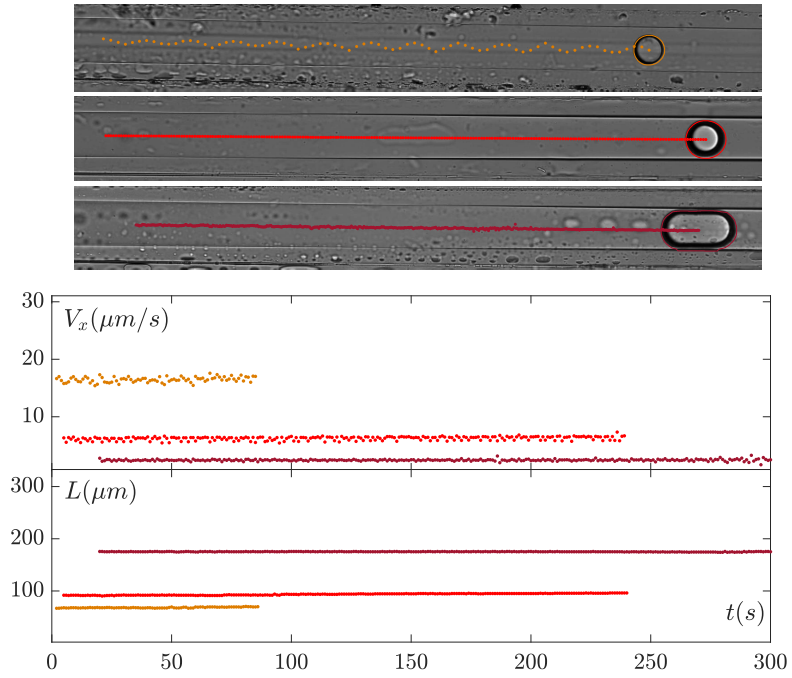

Figure 5.19: **Typical behaviour of droplets of different sizes in a 50 μm cylindrical capillary. Top:** Trajectory of the droplets. **Middle:** Velocity in the direction of the capillary versus time. **Bottom:** Length of the droplet versus time. One color corresponds to one droplet: orange for a round droplet of radius $a = h = 40$ μm, bright red for a round droplet of radius $a = 50$ μm $= h$ and dark red for an elongated droplet of half-length $a = 100$ μm $> h$.

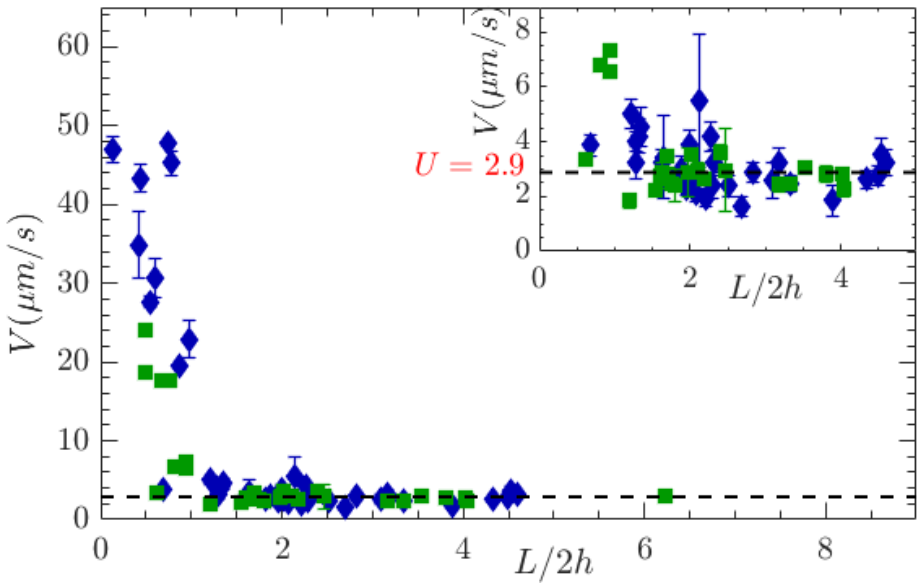

Figure 5.20: Velocity of droplets V in cylindrical capillaries depending on the confinement $\frac{L}{2h}$, for different capillary diameters h. The error bars represent the standard deviation of the average value in time of the velocity during an experiment.

We observe that again, the data collapse on one single curve. The velocity of the droplets depends only on the confinement $\frac{L}{h}$. The velocity decreases strongly with the confinement, even for small droplets. We observe two different behaviours - the transition from the "fast fluctuating" to the "slow regular" motion that was observed in section (5.1) is now abrupt and the intermediate regime $1 < \frac{l}{2h} < 2$ has disappeared in favor of the "slow regular" one.

(i) $\mathbf{\frac{L}{2h} < 1}$: the droplet has a 3D motion. If the droplet is not too small, this motion is persistent in the direction of the capillary x, oscillate in the cylinder in the perpendicular directions y and z (the motion in z correspond to the droplet going out of the focus plane)- the behaviour is not periodic. The velocity varies a lot during these oscillations. The main difference between the behaviour of the small droplets in square and cylindrical capillaries is the dimension: in square capillaries, the droplets remain in one plane - the bottom plane of the capillary, and oscillate between the two sides wall on this plane[5]. In cylindrical capillaries however, the bottom is not plane, and thus when the droplet moves in the y direction, confined to the bottom by the gravity, it also moves in z. In this case, the gravity has a strong influence on the oscillation of the droplet, adding some complexity to the case of square capillary.

(ii) $\mathbf{\frac{L}{2h} > 1}$: The droplet has a straight trajectory in one persistent direction. Even very long droplets swim. The velocity of the droplet converges toward a constant value $V_{lim} = 2.5$ μm/s that does not depend on the confinement anymore. This behaviour is very similar to the one observed in the square capillaries, except for the value of V_{lim} which is smaller in the cylindrical capillary case.

5.3 Stretched cylindrical capillaries

The experiments in this section have been conducted with Saori Suda, a PhD student from the Laboratory of Dissipative and Biological Physics of Kyoto University, during an internship at the Gulliver laboratory.

We saw in the previous section that long droplets were not stable upon production, and that this instability was not simply due to an instability of the surface (such as Rayleigh-Plateau), but is likely to be driven by flow fields in the lubrification layer induced by non-trivial concentration gradient of swollen micelles. This instability might be linked to the production process, which perturbs the droplet - this is likely the case discussed in the previous section, as medium size droplets were observed to sometime destabilize at production, and sometimes remain stable and swim - but it could also be intrinsically linked to the droplet length - as no matter how careful we were when producing the droplet, we were not able to produce long stable droplets ($\frac{L}{h} > 13$).

[5]For really small droplet, $\frac{L}{h} < \frac{1}{6}$, as mentioned before, the droplets is not confined to the bottom wall by gravity, and a 3D behaviour is observed

5.3.1 Swimming behaviour

Then one may wonder what would happen if we were able to progressively increase the length of a droplet while it is swimming, by varying the height of the capillary. Would we be able to produce stable long droplets, or would the droplet destabilize and spontaneously divide? In order to address this question, we use stretched cylindrical glass capillary, whose geometry is described in Fig. 5.21.

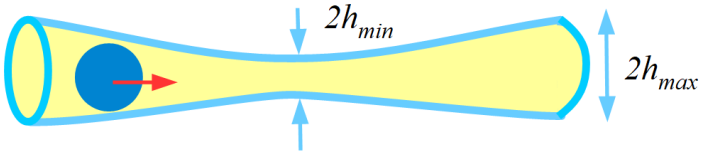

Figure 5.21: Sketch of a stretched capillary.

We made several experiments of one unique water droplet with 15% NaCl in a stretched silanized cylindrical glass capillary of initial half-height $h = 100$ μm filled with a solution of 25 mM mono-olein in squalane.

We vary (1) the droplet initial length, from round droplets of radius $a = 100\mu$m, to long droplets of a few times the capillary height, and (2) the capillary shape, that we characterize mainly by two parameters: h_{min} the minimum radius of the capillary and g_h the gradient of radius to go from the initial radius to h_{min} ($g_h < 0$), then back to the initial radius ($g_h > 0$). $|g_h|$ is typically between 0 and 0.05, and h_{min} varies from $h = 100$ μm (straight capillary) to $h = 10$ μm. We observe that all droplets are swimming, and that there are two different kinds of behaviours.

1. "Short" droplets passing through "large" constrictions are observed to simply elongate and then shrink along the radius gradient with the volume conservation, and little perturbation. Such a behaviour is illustrated in Fig. 5.22-left.

2. "Long" droplets passing in "narrow" constrictions are observed to destabilize at their back (at the neck position), and spontaneously divide, eventually several times, until they pass through the constriction. The "daughter droplets" formed do not swim, and their size at formation decreases with the capillary height at the place of the division. Such behaviour is illustrated in Fig. 5.22-right.

In the absence of division, the velocity of the center of mass of the droplet is almost constant [6] and equal to the one measured for elongated droplets in straight cylindrical capillary (section (5.2.3.2)): $V \simeq 3\mu$m/s. Long droplets are observed to have a neck, and when a division occurs, it is always observed at the neck. However, the presence of a neck does not systematically lead to division. For different experiments, with capillaries of different h_{min} and droplets of different initial length, the droplets are observed to undergo various numbers of division, from none (simple elongation), or only one division, to up to thirteen successive divisions. After passing the smallest capillary radius, the droplet continues swimming, without further division.

[6] The slight variation of velocity can be associated with the tension force exerted on the droplet because of the difference of curvature of the front and back meniscus - in a convergent tube the droplet is slowed down, while in a divergent tube its accelerated.

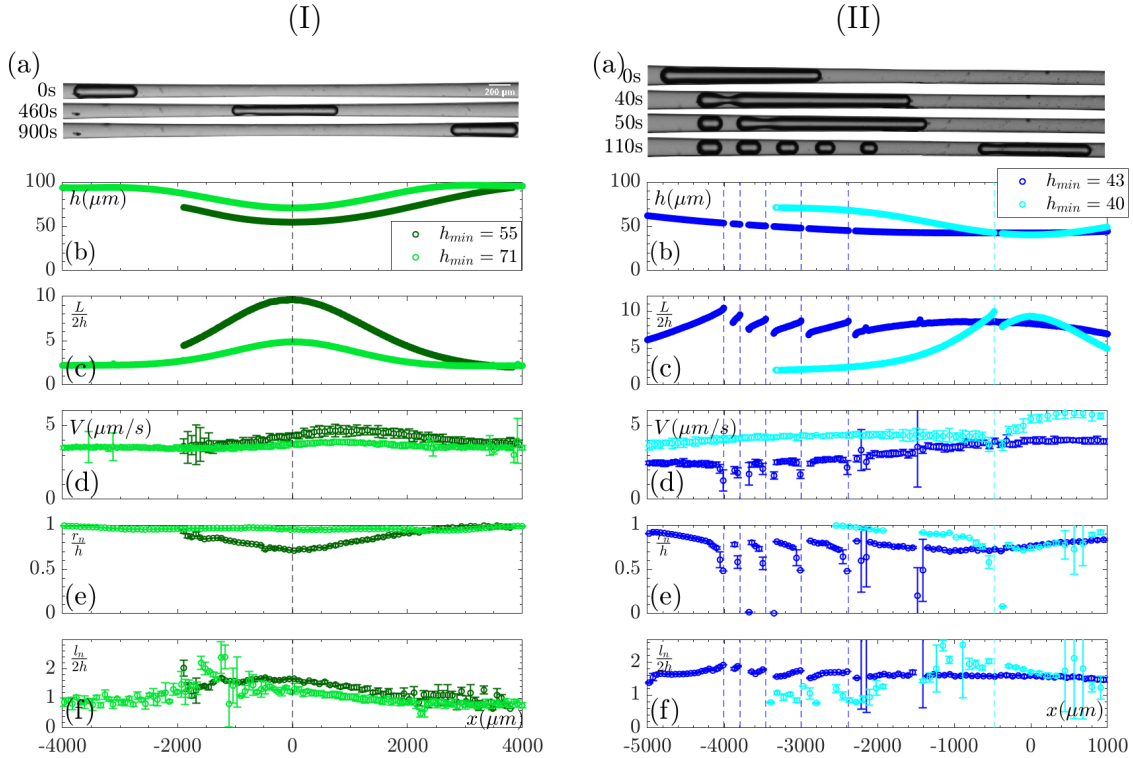

Figure 5.22: **behaviour of droplets passing through stretched capillaries:** both capillaries have a gradient $g_h \simeq 0.02$. **I** - Passing: the droplet successively elongates and shrinks along the capillary radius. **II** - Division: the droplet undergoes spontaneous divisions. It divides at its tail, forming smaller non-swimming droplets ("daughter droplets") whose length decreases with the capillary radius. (a) Snapshot of the droplets in time. Evolution of (b) the capillary radius h, (c) the dimensionless droplet length $\frac{L}{2h}$, (d) the velocity of the center of mass V, (e) the dimensionless neck radius $\frac{r_n}{h}$ and (f) the dimensionless neck position $\frac{l_n}{h}$.

5.3.2 Study of the elongation

We focus on one experiment without division, and look in Fig. 5.23 at the influence of the confinement on the velocity and shape of the droplet. rescaling all length by the radius of the capillary h, which has a trivial influence; we observe that the radius and position of the neck depend on the length of the droplet. This result might be surprising, as it indicates that there is another length-scale than h that has an influence on the droplet shape. This phenomenon will be investigated in further details in section (5.5).

We also observe that while the shape of the droplet changes with increasing confinement (converging tube), this change is reversible when decreasing the confinement (diverging tube); the droplet goes back to its initial shape. This means that the phenomenon that in this regime determine the shape of the droplet is quasi-static.

5.3.3 Study of the division

Focus on one division event

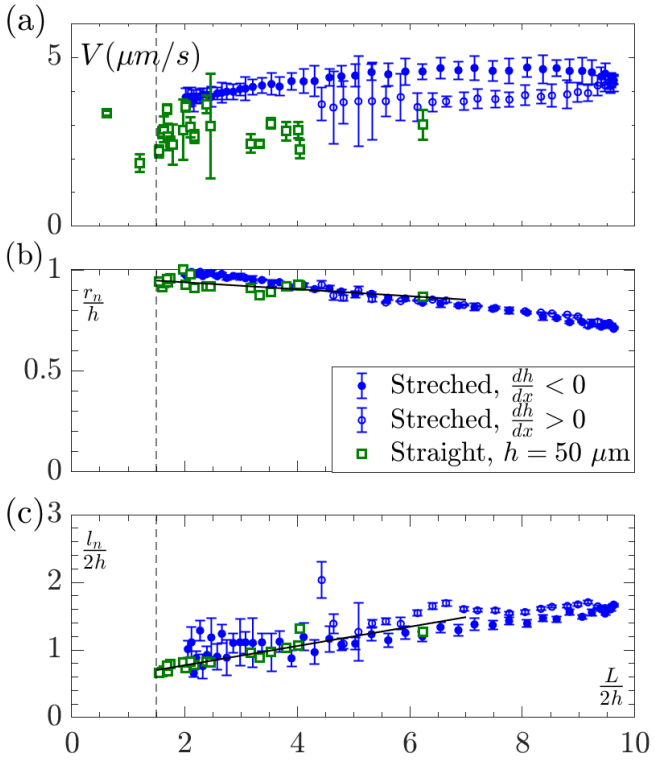

Figure 5.23: Evolution of the droplet characteristic during an elongation (blue), and for many droplets of various length in straight cylindrical capillaries of radius $h = 50$ μm: (a) the velocity, (b) the dimensionless neck radius and (c) the dimensionless neck position, depending on the confinement.

We first focus on only one division event (the first one for a droplet), and we look at the evolution of the shape of the droplet during this division, in Fig. 5.24.

We start the observation from 100 s before the division. While the capillary radius does not change much during this time, (from $h = 57$ μm to $h = 53$ μm), the shape of the droplet varies a lot: its length varies from $L = 1000$ μm to $L = 1110$ μm, and the neck deepens. The variation of L is trivially linked to the radius of the capillary and the neck radius through the volume conservation of the droplet. In Fig. 5.24(c), we plot the evolution of this neck radius with time. We observe two regimes, from $t = -200$ s to $t = -20$ s, the neck radius decreases slowly in time. From $t = -20$ s to $t = 0$, the neck radius decreases quickly with time, until it reaches a minimum value, at which it divides (or more precisely, the time needed to go from this minimum value to zero is less than 1 s, therefore is not observed). We call r_n^d the neck radius at the transition between the two regimes (r_n^d is extracted roughly by hand where the slop of the curves starts increasing).

In search of a rule for division:

Why, or in which configuration the droplet divides, is not trivial. We measure for all

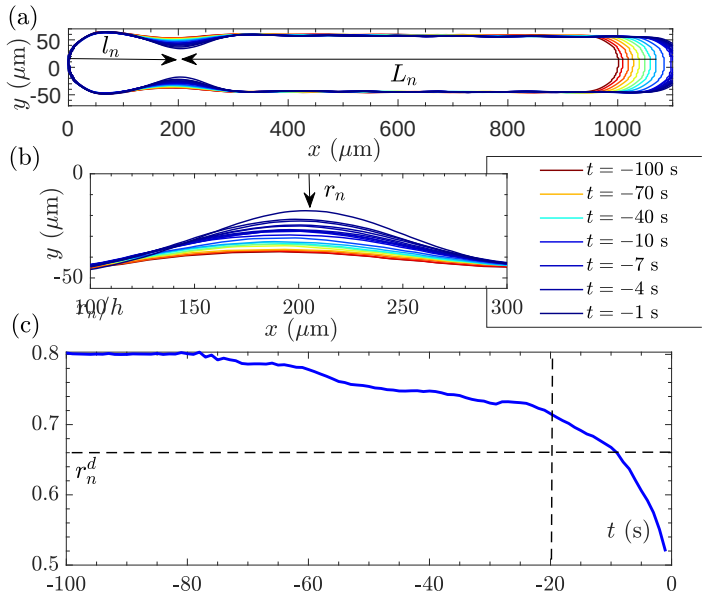

Figure 5.24: **Example of the behaviour of a droplet from 100 s before division:** during this time, the radius of the capillary does not vary a lot $h = 55 \pm 2$ μm, and the length varies from $L = 1000$ μm to $L = 1110$ μm. (a) Evolution of the droplet shape with time (colors). (b) Zoom on the neck. (c) Evolution of the neck radius r_n with time. $t = 0$ s is the time of division. r_n^d is the neck radius from which the division accelerates.

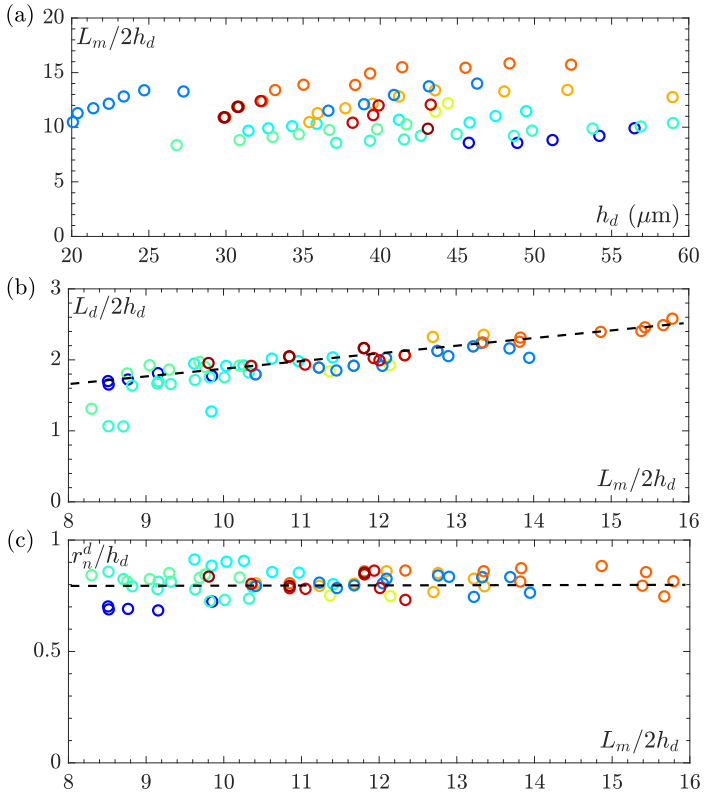

Figure 5.25: **Quantities at which the droplet divides, for all experiments:** (a) evolution of the mother length with the capillary height. (b) Evolution of the daughter size with confinement. (c) Evolution of the neck size at division as a function of the confinement. The colors stand for the experiment: the same color is used for the different divisions of the same droplet.

experiments and divisions different quantities at the division time: the size of the capillary at division h_d, the mother length L_m, the daughter length L_d and the neck radius at division r_n^d. All these quantities are shown in Fig. 5.25. In Fig. 5.25(a), we observe that the confinement at division $\frac{L_m}{h_d}$ varies a lot for the different experiments, and even for the different divisions of the same droplet. This means that the confinement is not the key parameter of the problem (at least not directly). There must be another length scale in the problem. The Fig. 5.25(b) shows the evolution of the daughter length L_d rescaled by h_d with the confinement. All data collapse on a single line: this means that although the confinement does not control the division, it imposes the distance at which the droplet breaks (the position of the neck). Finally, the Fig. 5.25c shows the evolution of r_n^d rescaled by h_d with the confinement: all data collapse on a constant line of value approximately $\frac{r_n^d}{h_d} = 0.8$. This is a strong indication that $\frac{r_n^d}{h_d}$ is a critical value below which the droplet starts dividing. Note that the temporal resolution of our experiments is strongly limiting a thorough investigation of the dynamics of the neck. Further experiments using fast camera are in progress.

From the previous observations, we can define two successive behaviour of our droplets. The first one is the one described in sections (5.2) and (5.3.2): when swimming in cylindrical capillary, an elongated droplet gets a non-trivial shape with a minimum lateral curvature which defines the neck. This shape is stable, and it is possible to vary continuously the confinement of the droplet to measure the quasi-static evolution of the shape. However, when the neck size goes below a critical value, as described in the current section, a dynamical non-reversible regime happens, leading to the division of the droplet. In the theoretical section 5.5.1, we introduce theoretical tools in order to understand these two phenomena.

5.4 Square constriction

The way we designed our stretched cylindrical capillaries prevented us to explore a large variety of constriction shape - the height gradient were always small $g_h \ll 1$. To have an idea of what would happen for the other limit, $g_h \gg 1$, we also investigate the behaviour of droplets in sharp constriction: a simple design square NOA channel with a width jump in the y direction, as described in section (5). The half-width before the constriction is $w_{in} = 100$ μm, and the half-width after the constriction is $w_{out} \leq w_{in}$. The height remains the same. The geometry and the notation of this constriction are illustrated in Fig. 5.26.

Conceptually, if $w_{out} = w_{in}$, there is no constriction, and the droplet should simply pass. At the opposite $w_{out} = 0$, there is a wall in front of the droplet, and the droplet should stop, and eventually bounce on the wall and turn back. We are interested in what happens between these two extreme situations. Does the droplet pass through? Does it deform? Does it stop at the constriction? Does it bounce back?

Most experiments of this section were conducted by Hong Po, a student from ESPCI Paris during an internship at the Gulliver laboratory under my supervision.

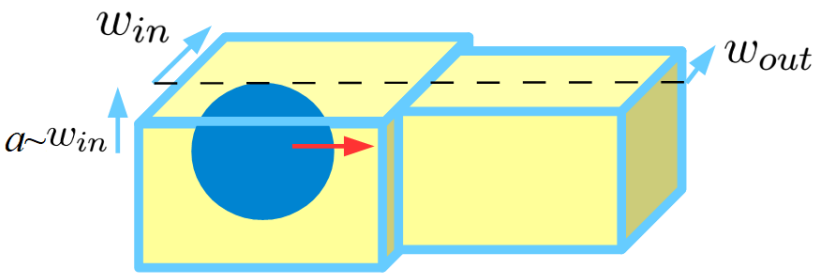

Figure 5.26: **Sketch of the geometry and notations for a rectangular constriction:** The square constriction in constituted of an inner square channel of half-height and half-width $h = w_{in}$, and of an outer channel of the same height, but of smaller half-width $w_{out} \leqslant w_{in}$. The droplet has typically the size of the inner channel $a = w_{in}$, and initially swims toward the outer channel.

5.4.1 Passing or stopping

In a first time, we made many droplets of typically the inner channel size $L \simeq 2a \simeq 2w = 200$ μm. We vary only the second channel size between $w_{out} = 5$ μm and $w_{out} = 100$ μm.

We observe that either the droplet is stopped at the constriction, or it passes through by deforming itself (very rarely, the droplet bounces on the constriction, and turns back). In both case, the shape of the droplets (in Fig. 5.28), is not trivial. More precisely:

- The droplet passing while deforming - Fig. 5.28(a) - goes from a spherical shape in the inner channel, to an elongated shape in the outer channel, passing by a composite shape at the constriction.
- The droplet blocked on the constriction initially has a spherical shape, and deforms at the constriction. Surprisingly, the final state reached by the droplet is not spherical, the front cap of the droplet remains stuck in the constriction. This behaviour is unlike the one observed for passive droplets [140], which, driven by the difference of pressure imposed by the difference of curvature (Laplace law), are driven out of the narrowest channel (and reach a spherical shape).

We measure the curvature at the front κ_f, and at the back κ_b of the droplets, as well as the velocities at the front V_f and back V_b of the droplet. We look at their dynamical behaviour for three different cases: a first droplet passing through a very large constriction for reference, in Fig. 5.29(1), a second passing through a narrow constriction, in Fig. 5.29(2), and a last one stopping at a narrow constriction, in Fig. 5.29(3):

1. **Droplet passing through a constriction - large outer channel, Fig. 5.29(1):** when the droplet arrives at the constriction, its velocity (a) drops a little, without stopping. The curvature (b) almost doesn't change, from the inverse of the inner channel half-width $\frac{1}{w_{in}} = 0.01$ μm $^{-1}$ to the inverse of the outer channel half-width $\frac{1}{w_{out}} = 0.0105$ μm $^{-1}$. The passage through the constriction is almost instantaneous.

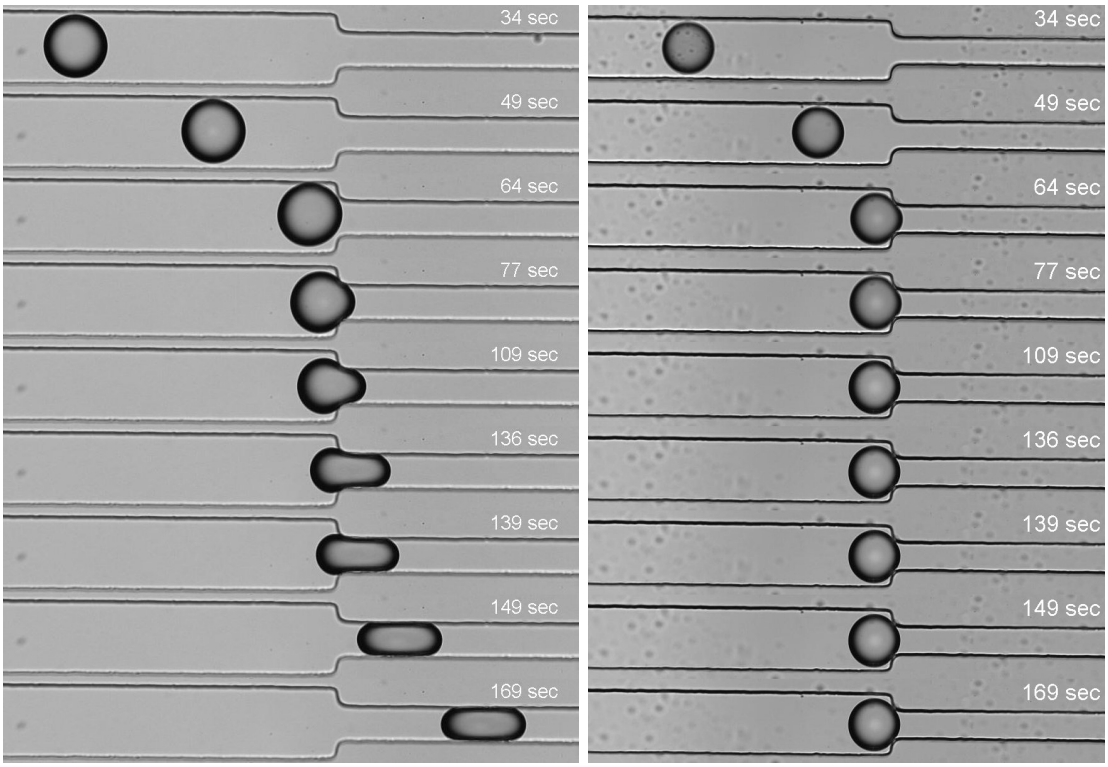

Figure 5.27: **Image of droplets at a constriction:** (a) droplet passing through a constriction of $w_{out} = 50$ μm and (b) droplet stopped at a constriction of $w_{out} = 40$ μm.

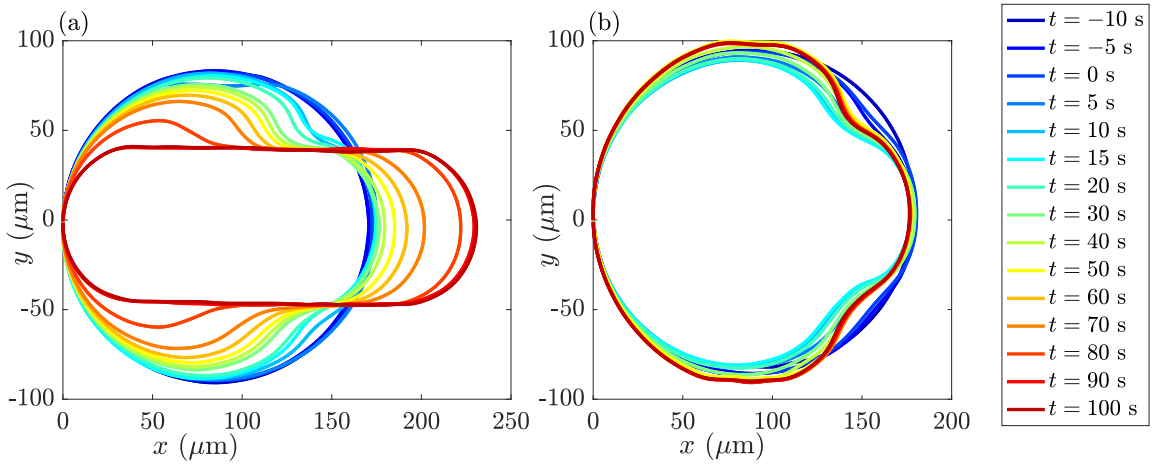

Figure 5.28: **Shape of droplets at constriction:** (a) shape of a droplet passing through a constriction $w_{out} = 45$ μm. (b) shape of a droplet stopped at a constriction $w_{out} = 40$ μm. The color-scale stands for the time (dark blue = right before reaching the constriction, bright red = long time after first reaching the constriction).

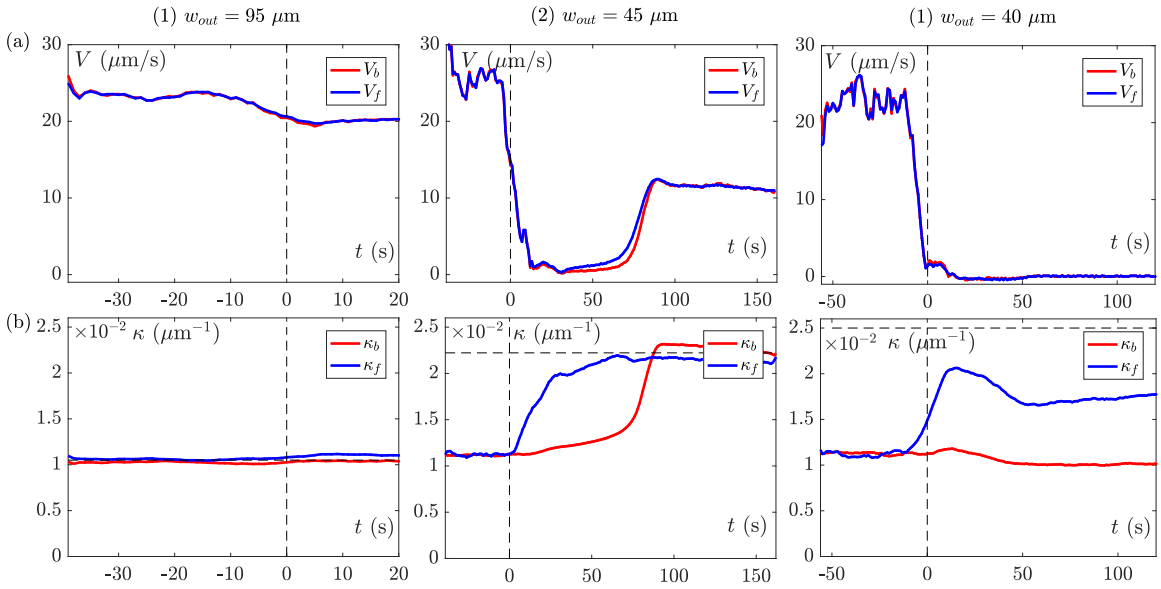

Figure 5.29: **behaviour of droplets at a rectangular constriction:** The inner channel is square with a half-width w_{in}=100 μm, and the outer channel rectangular with a fixed half-height $h = 100$ μm, and half-width: (1) $\frac{w_{out}}{w_{in}} = 0.95$, droplet passing through a large constriction. (2) $\frac{w_{out}}{w_{in}} = 0.45$, droplet passing through a narrow constriction. (1) $\frac{w_{out}}{w_{in}} = 0.4$, droplet stopping at a narrow constriction. $t = 0$ correspond to the time at which the droplet front first attains the constriction, and is highlighted by a horizontal black dashed line. We give (a) the velocity of the front of the droplet (in red) and of the back of the droplet (blue) with time, and (b) of curvature at the front of the droplet (in red) and at its back (blue) with time. We also gives $\frac{1}{w_{out}}$ (black horizontal dashed line).

2. **Droplet passing through a constriction - narrow outer channel, Fig. 5.29(2):** in this case, when the droplet arrives at the constriction, its velocity (a) drops rapidly to zero, and the droplet stops moving. However the droplet does not stop being active: the front cap enters the outer channel, and starts deforming. Its curvature (b - blue) increases, from the inverse of the inner channel half-width $\frac{1}{w_{in}} = 0.01\ \mu\text{m}^{-1}$ to the inverse of the outer channel half-width $\frac{1}{w_{out}} = 0.022\ \mu\text{m}^{-1}$. Then the droplet starts penetrating the outer channel by elongating (the velocity (a) of the front cap (blue) starts increasing). The spherical volume still in the inner channel decreases rapidly, and thus the curvature of the back cap (red) increases, until the droplet completely passes into the outer channel. In the outer channel, the droplet reaches a steady state with a constant velocity V_{out}, and a fixed shape.

3. **Droplet stopped at a constriction, Fig. 5.29(3):** when the droplet arrives at the constriction, its velocity (a) drops rapidly to zero, and the droplet stops moving. Once again, the droplet does not stop being active: the cap stuck in the small channel starts deforming, and the curvature (b) of the front cap (blue) increases, much like in the previous case. Unlike the previous case however, the curvature will never reaches the inverse of the outer channel half-width $\frac{1}{w_{out}} = 0.025\ \mu\text{m}^{-1}$: after attaining a maximum $\kappa_{front} = 0.021\ \mu\text{m}^{-1}$, the curvature decreases and stabilize at a lower value $\kappa_{front} = 0.017\ \mu\text{m}^{-1}$. The droplet does not evolve anymore, and remains stuck at the constriction for the remaining of the experiment.

The two droplets (2) and (3) that respectively passes through and stops at narrow channels have very similar behaviours when they arrive at the constriction: their velocity goes to zero, and the cap entering the channel starts deforming (increasing its curvature). The difference between them is that the droplet (2) continues deforming and engages in the outer channel, while the droplet (3) does not increase its radius of curvature high enough to reach the inverse of the outer channel width, thus cannot engage in the outer channel, and finally somewhat stops trying and reaches steady state while half stuck in the outer channel. We can imagine two reasons as for why the droplet (3) does not pass through the constriction: the first being that the droplet cannot deform itself enough to pass - it cannot attain a low enough curvature to enter the second channel (geometrical reason), and the second being that while stopping for too long at the constriction, the droplet poisons itself, saturating all micelles around (dynamical reason).

In order to further investigate this phenomena, we measure for all experiments, the velocity in the final state of the droplet V_{out} (which is non/zero when the droplet passes, and zero if the droplet is stuck at the constriction), and the time of passage t_{pass} defined as the difference between the time at which the droplet meets the constriction for the first time, and the time at which the droplet reaches its maximum curvature (which correspond to the last attempt to enter the outer channel). The geometrical constrain imposed by the constriction is quantified by the radius the cap needed to reach to enter the outer channel w_{out}, and the ratio of the initial radius of the droplet a. In Fig. 5.30, we plot the passing time as a function of the geometrical constrain for passing (orange) and stopped (blue) droplets.

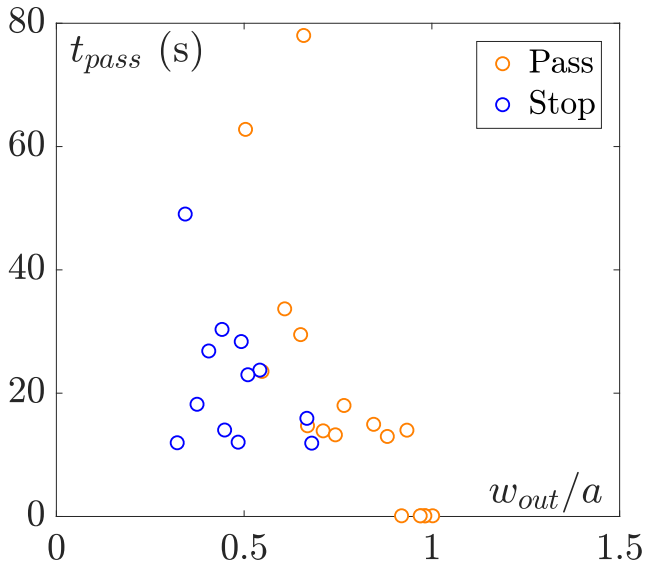

Figure 5.30: Time of passage t_{pass} for different geometrical constrain w_{out}/a: the droplets passing through the constrictions are in orange, whereas the ones stopped at the constriction are in blue.

If the problem was purely dynamic (poisoning), then we would expect that the longer the droplet spends at the constriction, the less likely it is to pass in the end. For a given geometry (for instance $\frac{w_{out}}{a} = 0.5$, we observe the opposite behaviour. We can conclude that poisoning is not at the origin of the stopping of some droplets. On the contrary, if the problem was purely geometric, then we would expect that the narrower the outer channel is, the less likely the droplets are to pass. This is roughly what is observed, although there isn't a clear critical value $\frac{w_{out}}{a}$ to separate the two domains. Actually, the two domains separation seems to be a function of both t_{pass} (whose influence is then something else than poisoning), and $\frac{w_{out}}{a}$.

5.4.2 Discussion

For droplets stopped at the constriction, we made two observations: (i) unlike passive droplets, the droplet remains partially stuck in the outer channel, keeping a stable non spherical shape, and (ii) the poisoning of the droplets doesn't seems to happen (or at least to play a critical role on the droplet behaviour) on the time scales observed. These two observations make us think that although they are not swimming, droplets stuck at constriction remain active, *i.e.* they still induce a flux around themselves.

From a hydrodynamics perspective, two phenomenon are at play: the swimming of the droplet, which - because of the initial conditions - imposes a flux toward the constriction - and the passive geometrically driven flux which comes from the difference of curvature between the front and the back of the droplet. If there was no activity, then the difference in Laplace pressure should drive the droplet in the large channel, while if the activity was dominant, the droplet should be able to pass. Then, the passing or stopping of droplets is ruled by the balance between the activity and the Laplace pressure difference (which might itself be affected by activity). Note that whether this

stopped state is a steady state or a transient state toward another state (complete passing or withdrawal) is not clear, further investigations are in progress in order to answer this question.

5.5 Theoretical approach for an elongated droplet

This whole theoretical section is the result of fruitful discussions between Saori Suda, and professor Masatoshi Ichikawa from the Laboratory of Dissipative and Biological Physics of Kyoto university, and Vincent Bertin, Mathilde Reyssat, Olivier Dauchot, and me, at the Gulliver laboratory.

5.5.1 Elongated droplet in a straight capillary

Section (5.2) highlighted two important observations on the swimming of droplets in cylindrical channels:

- When the droplet is bigger than the channel height, its velocity does not depend on the droplet length L, nor on the capillary height h.
- In cylindrical capillaries, the lubrification layer around the droplet is of micron size, and has a non-trivial thickness that varies along the droplet, reaching a local minimum at the back of the droplet which defines the neck.

In order to capture the physics behind these observations, we develop a theoretical approach to understand the swimming of active droplets in a cylindrical tube. This problem intricates two phenomena: (i) the activity, consequence of the physico-chemical interactions between the inner and outer phases (production of micelles, concentration gradient...) and (ii) the lubrication, which considers the hydrodynamic of a moving thin liquid film. These two concepts are linked through the physical quantities in our system: the concentration field c of the swollen micelles (source of activity), the velocity field $\mathbf{v}$ around the droplet, and the thickness e of the liquid film between the droplet and the tube (which characterize the shape of the droplet).

5.5.1.1 Lubrication problem: the Bretherton approach

The lubrication layer problem (sections (5.5.1.1)) has been studied by Vincent Bertin, from the Gulliver laboratory in the framework of an inter-PhD collaboration.

The lubrication phenomenon of self propelling long droplet (of viscosity smaller than the external fluid) in a tube is similar to an existing problem in the literature, the so called Bretherton problem [2], which considers the motion of an elongated bubble in a tube, pushed by an external gradient of pressure. The main difference is the driving mecanism behind the motion of the droplet/bubble. Using a similar approach than the one used by Bretherton (that we first briefly describe), we propose a theoretical description of our system by including the activity of the swimming droplet.

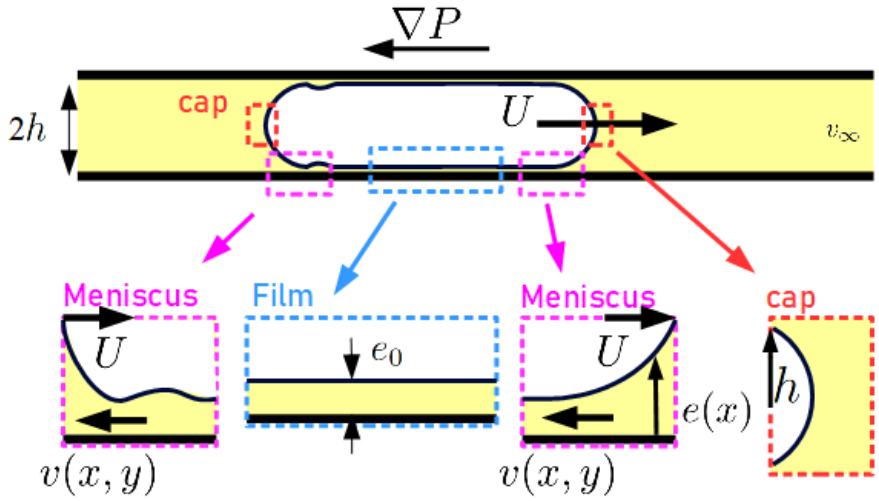

Figure 5.31: The Bretherton approach consist in separating the bubble in five regions, two spherical caps (red dashed lines), at the front and rear, one lubrication film of constant thickness (blue dashed line), and two dynamical meniscus (violet dashed lines), that connect the two caps and the lubrication film.

The classical Bretherton problem

The Bretherton problem considers a bubble (a fluid whose viscosity is small compared to the outer fluid), in a cylindrical tube filled with an outer fluid. The outer fluid is driven by an external pressure gradient; and the bubble moves at a velocity U pushed by the outer fluid. A lubrication film forms between the droplet and the wall of the tube.

The theoretical approach consists in separating the bubble in five regions (illustrated in Fig. 5.31), two spherical caps, at the front and rear, one lubrication film of constant thickness, and two dynamical meniscus, that connect the two caps and the lubrication film. In the following, we will assume a full separation of length scales, namely that (i) the thickness of the lubrication film e is small compared to the length of the dynamical meniscus, and the length of the droplet L, which allows the use of the lubrication approximation in the dynamical meniscus and in the lubrication film; that (ii) e is small compared to the half height of the capillary h, which allows to approximate the lubrication layer as planar and that (iii) h is small compared to L: which allows to neglect what happens at the other end of the droplet.

The five regions are treated independently, then the curvature of the interface between the inner and outer liquid is matched asymptotically between the different regions.

The caps: in the front and tail menisci, the mechanism governing the shape of the droplet is the surface, or energy minimization. In the case of a bubble in a tube, these caps are typically supposed to be spherical with a curvature $\frac{1}{h}$.

The lubrication film is supposed as a first approximation to have a constant thickness e_0, and thus a zero curvature. For a passive bubble, the velocity in the lubrication film at the interface with the droplet is equal to the velocity of the droplet, and we consider

a plug flow:

$$v(y) = U, \tag{5.4}$$

which yields to a flux of liquid in the lubrication film $\varphi = Ue_0$.

The dynamical meniscus: based on the asymptotic matching [141], the dynamical meniscus corresponds to section of the droplet over which the curvature evolves from $\sim \frac{1}{h}$ to 0. We introduce a typical length ℓ to quantify the size of the matching region. In this region, there is a curvature gradient that then induces a pressure gradient, which itself leads to a flow in the film.

In the dynamical meniscus, we assume the lubrication approximation[7]. Here, the thickness of liquid $e(x)$ is not constant leading to pressure gradient. The governing equations in the fluid are then:

$$\eta \partial_y^2 v = \partial_x p, \tag{5.5}$$

$$0 = \partial_y p, \tag{5.6}$$

and the boundary conditions are the same than in the lubrication layer. The normal stress balance in the lubrication approximation yields to

$$p(x) = -\gamma \partial_x^2 e(x), \tag{5.7}$$

Considering that their is no shear stress at the interfac, we can solve this problem and find a flow

$$v(x,y) = -\frac{\gamma \partial_x^3 e(x)}{2\eta}\left(y^2 - 2ye\right) + U. \tag{5.8}$$

The problem is stationary and then the flux of liquid is uniform which means that

$$\varphi = \int_0^e \mathrm{d}y v(x,y) = \frac{\gamma e^3 \partial_x^3 e}{3\eta} + Ue \tag{5.9}$$

where φ is the flux in the lubrication film introduced before. Then the governing equation of the interface $e(x)$ is

$$\frac{\gamma e^3 e'''}{3\eta} + Ue = Ue_0 \tag{5.10}$$

where prime is the derivative with respect to x. We introduce $\ell = e_0\left(\frac{\gamma}{3\eta U}\right)^{1/3}$ as the typical length scale of matching region and use dimensionless variables such that

$$E(X) = \frac{e(x)}{e_0}, \tag{5.11}$$

$$X = \frac{x}{\ell} \tag{5.12}$$

[7]This approximation describes the flow of fluids in a geometry in which one dimension is significantly smaller than the others, here $e \ll \ell$. Then the Stokes equations are expanded in the parameter $\frac{e}{\ell}$, and only the leading-order equations are considered. The underlying hypothesis are that the velocity is almost uni-directional, and that the orthoradial velocity gradients are strong.

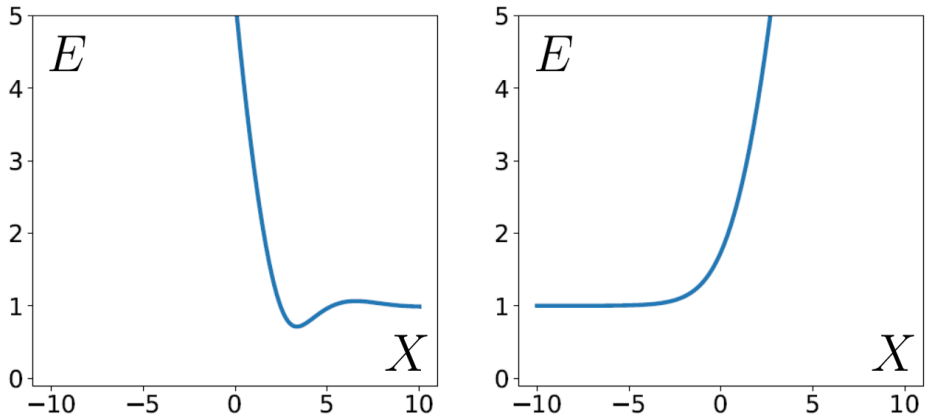

Figure 5.32: Shape of the front dynamical meniscus (right) and rear dynamical meniscus (left) of a passive droplet pushed by a pressure gradient in a tube, solution of the equation 5.13 computed numerically using a Runge-Kutta algorithm of order 4.

and the governing equation becomes

$$E''' = \frac{1-E}{E^3} \tag{5.13}$$

For the front dynamic meniscus, the matching conditions are:

$$E(X \to -\infty) = 1, \tag{5.14}$$
$$E''(X \to \infty) = cste, \tag{5.15}$$

the constant being given by the matching, while for the rear dynamic meniscus, the matching conditions are:

$$E(X \to -\infty) = cste, \tag{5.16}$$
$$E(X \to +\infty) = 1. \tag{5.17}$$

If one solves the equation 5.13, with each set of boundary conditions, one then finds two shapes for the front and rear dynamical meniscus. Vincent Bertin computed numerically these shape using a Runge-Kutta algorithm of order 4, and the result is given in Fig. 5.32 (these are the same shapes than the ones that were computed in the original article of Bretehrton).

Toward the caps (toward $+\infty$ for the front meniscus, and toward $-\infty$ for the rear meniscus), the thickness increases and diverges with a constant curvature. For the front meniscus, the matching then consists in matching the curvature given by this model to the one in the cap region:

$$\lim_{x\to-\infty} e''(x) = \frac{e_0}{\ell^2} \lim_{X\to-\infty} E''(X) = \frac{1}{h}. \tag{5.18}$$

The quantity $\lim_{X\to-\infty} E''(X)$ is a numerical pre-factor. Then:

$$\frac{e_0}{h} \sim \left(\frac{3\eta U}{\gamma}\right)^{2/3} \tag{5.19}$$

The front meniscus thickness decreases monotonically toward e_0. The rear meniscus, however, presents a non-monotonic variation of the thickness, a local minimum, much

like what was observed in our experiment for the long active droplets. This shape of the rear (in particular what we defined as the size of the neck r_n, and its position L_d in the experiments) is fixed by the thickness of the lubrication film, e_0, which itself scales only with the half-height of the capillary h, and the velocity of the bubble U: this means that for a fixed U, and a fixed size of capillary, the shape is fixed. This is unlike what was observed in the experiments; for instance in Fig. 5.18, the neck deepen for longer droplet.

The active Bretherton problem

In the case of the swimming droplets, there is no external pressure gradient, the flux is local and come from the gradient of swollen micelles at the interface between the droplet and the outer oil[8]. We use the same approach as Brethreton, the droplet being divided in five regions.

The caps: we observe experimentally, that the curvature is constant, indicating that the menisci are simply spherical caps. We thus consider that within a good approximation, the activity does not affect the shape of the menisci. In the following, we consider spherical caps of curvature $\frac{1}{h}$ (which is typically what is observed experimentally).

The lubrication film: we don't have access experimentally to a precise measurement of the lubrication layer thickness. In contrast with in the Bretherton case, we cannot make the hypothesis that it is constant. This will be of great importance, as will be seen in the following. Note that the concentration field of swollen micelles is not constant in this region. On the contrary, in the present system the origin of all flows are gradients in the concentration field of swollen micelles at the interface. There is a velocity jump v_s (phoretic effect) and a stress jump σ_s (Marangoni effect) across the interface. In 3D for our system, the Marangoni effect is dominant (see (2). Thus as a first approximation, we neglect the phoretic effect. Furthermore, the inner fluid being less viscous than the outer fluid, most dissipation happens in the outer fluid, and we consider that $\sigma^i \ll \sigma_s = \sigma$ (that is to say we neglect the viscous stress exerted by the water on the oil). Then we have:

$$\eta \frac{\partial v}{\partial y}|_{y=0} = \sigma_s. \tag{5.20}$$

Adding the no-slip condition at the wall, the flow is then given by

$$v(y) = \frac{\sigma_s y}{\eta}, \tag{5.21}$$

which yields to a flux of liquid $\varphi = \frac{\sigma_s e_0^2}{2\eta}$. Note that in the previous computation, σ_s is not necessarily constant along the interface, however, as the flux is conserved, this would means that the thickness of the film e_0 varies along the interface; this will be discussed later.

[8]This problem is similar to a problem considered before [142], of the thermocapillary migration of long bubbles in cylindrical capillary tubes.

The dynamical meniscus: once again, the gradient of curvature of the thickness of liquid $e(x)$ is not constant, leading to pressure gradients. The hydrodynamics equations are as before:

$$\eta\partial_y^2 v = \partial_x p, \tag{5.22}$$
$$0 = \partial_y p, \tag{5.23}$$

For the boundary conditions, we consider the no-slip condition at the wall, *i.e.* $v(y = 0) = 0$ and stress balance at the interface. The normal stress balance in the lubrication approximation yields to

$$p(x) = -\gamma\partial_x^2 e(x), \tag{5.24}$$

and the tangential stress is assumed to be the same as in the lubrication film, which is the main difference with the classical case of Bretherton:

$$\eta\partial_y v|_{y=e} = \sigma_s. \tag{5.25}$$

We can solve this problem and find a flow

$$v(x,y) = \frac{\partial_x p}{2\eta}\Big(y^2 - 2ye\Big) + \frac{\sigma_s y}{\eta} \tag{5.26}$$

The problem is stationary and then the flux of liquid is uniform which means

$$\varphi = \int_0^e \mathrm{d}y v(x,y) = -\frac{e^3\partial_x p}{3\eta} + \frac{\sigma_s e^2}{2\eta} \tag{5.27}$$

Then the governing equation of the interface $e(x)$ is

$$\frac{\gamma e^3 e'''}{3\eta} + \frac{\sigma_s e^2}{2\eta} = \frac{\sigma_s e_0^2}{2\eta} \tag{5.28}$$

We introduce $\tilde{\ell} = e_0\left(\frac{2\gamma}{3\sigma_s e_0}\right)^{1/3}$ as the typical length scale of matching region and use dimensionless variables such that

$$E(X) = \frac{e(x)}{e_0}, \qquad X = \frac{x}{\tilde{\ell}} \tag{5.29}$$

and the governing equation becomes

$$E''' = \frac{1 - E^2}{E^3}. \tag{5.30}$$

Note here the difference with the standard Bretherton equation, for which the numerator of the right term is $1 - E$, instead of the quadratic dependence in E found here. For the front dynamic meniscus, the matching conditions are still:

$$E(X \to -\infty) = 1, \tag{5.31}$$
$$E(X \to \infty) = cste. \tag{5.32}$$

an for the rear dynamic meniscus:

$$E(X \to \infty) = cste, \tag{5.33}$$
$$E(X \to -\infty) = 1. \tag{5.34}$$

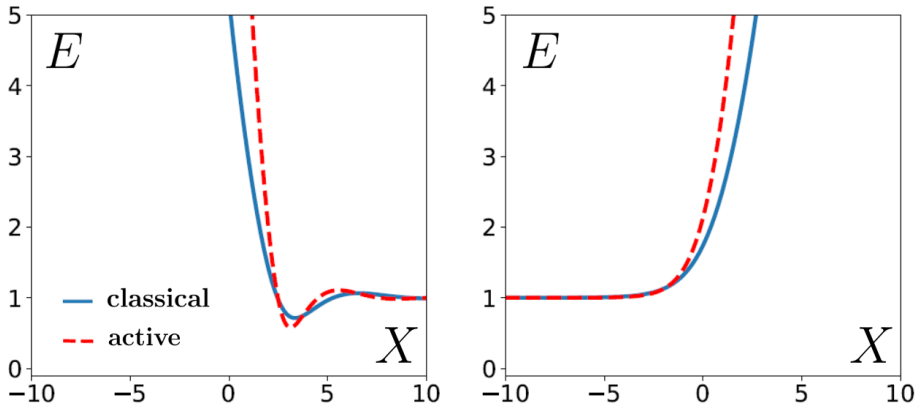

Figure 5.33: Shape of the front dynamical meniscus (right) and rear dynamical meniscus (left) of an active droplet (red dashed line) in a tube, solution of the equation 5.30 computed numerically using a Runge-Kutta algorithm of order 4, and for comparison the shape a passive droplet (blue continuous line).

Vincent Bertin solved this equation numerically using a Runge-Kutta algorithm of order 4. A typical solution is given in Fig. 5.33. We observe that the thickness increases as $X \to -\infty$. Again, the shape of the front meniscus can be matched with the curvature of the cap at $+\infty$.

$$\lim_{x\to-\infty} e''(x) = \frac{e_0}{\tilde{\ell}^2} \lim_{X\to-\infty} E''(X) = \frac{1}{h}. \tag{5.35}$$

The quantity $\lim_{X\to-\infty} E''(X)$ is again a numerical pre-factor (different from the classic Bretherton case, and found to be equal to 1.8). The important thing is that the thickness scales as:

$$\frac{e_0}{h} \sim \left(\frac{\sigma_s e_0}{\gamma}\right)^{2/3} \tag{5.36}$$

Interestingly, this result is identical to the classical Bretherton scaling law. If we don't use σ_s as a variable but the typical velocity in the film U as $\sigma_s = \frac{\eta U}{e_0}$, we find: $\frac{e_0}{h} \sim \left(\frac{\eta U}{\gamma}\right)^{2/3}$, which is exactly the equation 5.19, therefore not altered by the fact that the precise thickness profile within the matching region is indeed different from the classical case.

The shape of the rear still depends on the lubrication film thickness e_0; however, this time this thickness depend on the active stress σ_s, which is still unknown at this point.

5.5.1.2 Concentration field

If the active stress was fixed (for instance for a squirmer), then the shape of the swimmer would also be fixed. In the case of our swimming droplet however, the active stress depends on the local concentration gradient of swollen micelles along the droplet interface[9]:

$$\sigma_s = K \frac{\partial c}{\partial x}\Big|_{y=e_0}. \tag{5.37}$$

[9]The difference in sign with equation (2.125) comes from the orientation of the x axis.

This concentration field is governed by three phenomena: the emission of swollen micelles at the interface with a rate that we consider constant j_0; their diffusion in the lubrication layer and their advection with the flux of velocity v. Assuming steady state, the concentration is governed by the advection-diffusion equation:

$$\mathbf{v} \cdot \nabla c = D\Delta c, \tag{5.38}$$

with for the boundary solutions, a constant flux at the liquid-liquid interface ($y = e_0$),

$$-D\partial_y c|_{y=e_0} = j_0. \tag{5.39}$$

A first naive approach would consist in taking the thickness of the lubrication film to be constant. The following analytical calculations and numerical computations have been done by Vincent Bertin.

Analytical results for a plug flow

We first assume the flow field to be uniform (plug flow)[10]. We also neglect the diffusion of concentration alog the interface.

The equation (5.38) becomes then the diffusion equation,

$$\frac{\partial c}{\partial x} = \frac{D}{v}\frac{\partial^2 c}{\partial y^2}, \tag{5.40}$$

where x is analogous to time and $\frac{D}{v}$ is the analogous diffusion coefficient. We rescale the concentration field by a typical value C_0, x by the lubrication thickness e_0 and the Peclet number defined as $\mathrm{Pe} = \frac{ve_0}{D}$, $X = \frac{x}{e_0 Pe}$ and we invert and rescale the y axis $Y = \frac{1-y}{e_0}$ such that Y=0 corresponds to the liquid-liquid interface, and Y=1 corresponds to the wall. The equation can then be written as:

$$\mathrm{Pe}\,\partial_X C = \partial_Y^2 C. \tag{5.41}$$

The diffusion equation [143, 144] is known to have some self-similar solution with the variable $x/\sqrt{Dt}$. Similarly, we can look for self-similar solutions of the second kind with a diffusive profile as $Y \sim \sqrt{X}$:

$$C(X, Y) = AX^{\alpha} f(\frac{Y}{X^{\beta}}). \tag{5.42}$$

Choosing $C_0 = \frac{j_0 e_0}{AD}$, the boundary condition at the liquid-liquid interface is then $f'(Y = 0) = -1$. For simplicity for the analytical solution, we also chose as a boundary condition $f(Y \to \infty) = 0$, which means that the concentration vanishes far from the interface, this hypothesis neglects the influence of the wall on the concentration field.

We then inject this self similar solution in the equation (5.41). We find

$$\alpha f(u) - \beta u f'(u) = X^{1-2\beta} f''(u), \tag{5.43}$$

[10]This last assumption is very strong as it does not fulfil the boundary conditions at the wall $v(y = 0) = 0$

which exhibits solution when $\beta = 1/2$ and for all alpha. The value the scaling parameter α must be determined with the boundary conditions. The equation then becomes

$$\alpha f(u) - \frac{u}{2} f'(u) = f''(u). \tag{5.44}$$

In a lot of diffusion processes [145], the solute is at thermodynamic equilibrium at the boundary, resulting in a boundary condition $C(X, Y = 0) = c_0$, which imposes a scaling parameter $\alpha = 0$.

In the active droplet problem, we assume that it is the flux of swollen micelles at the interface that is fixed:

$$\partial_Y C|_{Y=0} = -\frac{e_0 j_0}{D C_0} \tag{5.45}$$

$$= J_0. \tag{5.46}$$

Which gives

$$A X^{\alpha - 1/2} f'(0) = J_0 \tag{5.47}$$

Then, the scaling parameter in accordance with this boundary condition is $\alpha = 1/2$. We notice that a positive scaling $c(x, y = 0) \sim x^{1/2}$ make sense because micelles are constantly ejected from the interface and therefore accumulates with the advection toward the back of the droplet. The self similar function follows the equation

$$f''(u) = \frac{-u f'(u) + f(u)}{2}, \tag{5.48}$$

whose general solutions are of the form

$$u \to K_1 u - K_2 \left(\frac{\sqrt{\pi}\, u}{2} \operatorname{erf}\left(\frac{u}{2} \right) + \exp\left(-\frac{u^2}{4} \right) \right), \tag{5.49}$$

and the particular solution for $f'(0) = -1$ and $f(\infty) = 0$ is

$$f(u) = \frac{2}{\sqrt{\pi}} \exp\left(-\frac{u^2}{4} \right) + u \left(\operatorname{erf}(\frac{u}{2}) - 1 \right). \tag{5.50}$$

In dimensional unit, this leads to

$$c(x, y) = \frac{2 j_0}{D} \sqrt{\frac{x e_0}{\pi}} \left(\exp(-\frac{y^2 v}{4 D x}) - \frac{y}{2} \sqrt{\frac{\pi v}{x D}} \left[1 - \operatorname{erf}(\frac{y}{\sqrt{4 D x / v}}) \right] \right). \tag{5.51}$$

Thus, the concentration diffuses vertically as $y \sim \sqrt{x}$, and with an increasing mass $\sqrt{x}$ in x.

Numerical results for a shear flow

The computation of the same problem as before, but with a shear flow (the velocity is then space dependent $v(y)$) has been done numerically. Without further details on the numerical procedure, we simply give in Fig. 5.34 the concentration field obtained by using a Runge Kutta algorithm of order 4 (RK4) for a plug flow (for reference), and for a shear flow. For the plug flow in the panel (a), we recover the typical field

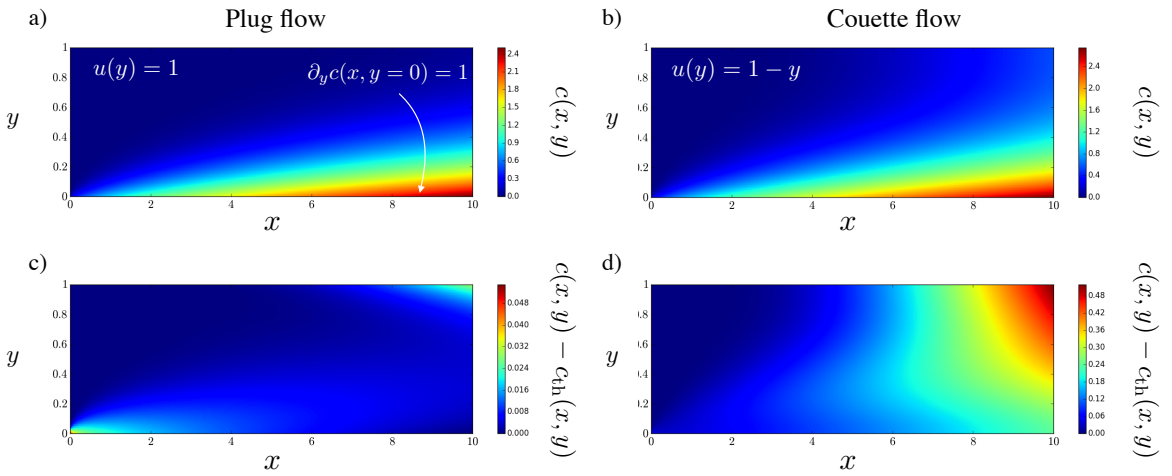

Figure 5.34: Concentration fields of solute solving numerically Eq.the shear flow problem on the right and the plug flow problem on the left (panel (a) et (b)). The flux of micelle is fixed at the oil-water interface $Y = 0$. The bottom panels shows the difference of the numerical solution with the corresponding self-similar solution derived from teh plug flow problem with vanishing concentration at $Y \to \infty$.

of a boundary layer that grows as $y \sim \sqrt{Dx/v}$. This numerical solution is compared with the self-similar solution derived analytically in panel (c). We find a very good agreement between the two solutions. A very small deviation is observed in the top right corner because of the presence of the wall. There is also a small difference observed in the bottom left corner, that is due to the fact that the initial concentration field is not exactly the self similar one. Still, the numerical converges toward the universal self-similar attractor [146] derived in the previous section in Eq.5.51 at $x \gg 1$.

The results in shear flow, in Fig. 5.34 (c) and (d) are very similar, although the solute diffuses slightly more in this case as the advection is less important as $Y \to 1$. In particular, the concentration profile at the water-oil interface increases as the square root of the distance, *i.e.* $c(x, y = 0) \sim \sqrt{x}$, due to the accumulation of micelles.

Limit of this approach

From the previous computation comes out that the gradient of concentration at the liquid-liquid interface is not constant:

$$\nabla_{\parallel} c \sim \frac{1}{\sqrt{x}}. \tag{5.52}$$

Then the stress jump across the interface is not a constant along the droplet:

$$\sigma_s \sim \frac{1}{\sqrt{x}}, \tag{5.53}$$

Because of the conservation of the flux, $\varphi \propto e_0 \sigma_s$, this imposes that the thickness of the film also varies along the droplet:

$$e_0(x) \sim \sqrt{x}, \tag{5.54}$$

which means that $e_0(x)$ increases while going toward the back of the droplet.

One of the building hypothesis of this model was that the thickness of the lubrication film was constant, therefore this model is not self-consistent: the thickness of the lubrication must vary along the droplet.

Finding the solutions of the diffusion equation in a film of varying thickness, limited by a wall on one side, and an interface that generates a constant flux of concentration on the other side is still an ongoing project conducted by Vincent Bertin.

We can still discuss about the implications of such solutions. Unlike in the classical Bretherton case, where the lubrication film thickness is constant; if the thickness of the film varies along the droplet, then the asymptotic matching of the shape of the dynamical menisci at the front and the rear will be done for different thickness. More precisely, at the front dynamical meniscus the thickness $e_{0,front}$ is fixed by the velocity of the droplet; but at the rear dynamical meniscus the thickness $e_{0,rear}$ depends on (increases with) the length L of the droplet, thus with the asymptotic matching, the shape of the rear meniscus depends on the length of the droplet, in particular the size and the position of the neck. This is what is observed experimentally in Fig. 5.3.2.

The next (on going) step is to build the complete theoretical model for the lubrication field, to get the exact shape of the droplet, and eventually compare it with the experimental data).

5.5.2 Division phenomenon

The last section gave first insights on the behaviour of elongated droplets in straight cylindrical capillaries. Here we discuss the origin of the division phenomena in stretched capillaries. Obviously, the spatial dependence of $e_0(x)$ must now play a crucial role.

5.5.2.1 First step: micelles saturation

As the swollen micelles are emitted at a constant flux at the interface, and are simultaneously advected downstream, the concentration of swollen micelles increases along the droplet length. However, the quantity of empty micelles in the oil solution is finite (it depends on the initial concentration of surfactant). Then in stretched capillaries, as the length increases, the concentration at the back of the droplet should attain a maximum swollen micelles concentration c^* by saturating all present empty micelles with water. On another hand, the flux in the lubrication layer is driven by a Marangoni flow, and thus by the gradient of concentration: the outer fluid is attracted by region of high swollen micelles concentration. Then if one region attains a maximum concentration, all outer fluxes are driven toward this region. This accumulation of fluid produces a thickening of the lubrication layer, but also bring in empty micelles and dilute the swollen micelles. This phenomenon could be the origin of an instability deepening the neck, which would eventually lead to its breaking.

We assume for simplicity that the capillary thickness h is constant (the variation of

radius in the timescale of a division is small compared to the droplet length increase and the lubrication layer thickness increase), and that the fraction of swollen micelles increases linearly from the head of the droplet towards its tail (starting from zero at the start of the lubrication layer, we neglect what happens in the front cap). The concentration at the back of the droplet should then scale as:

$$c(x) = \frac{A}{ve_0} L. \tag{5.55}$$

In this vision, the division length, which is the size of the mother droplet, L_m should scale as $\frac{\sigma_s e_0^2 c^*}{\eta A}$. Using the conservation of volume in the lubrication film, $hU = e_0 v = \frac{e_0^2 \sigma_s}{\eta}$, this rewrites as:

$$\frac{L_m}{2h} = \frac{Uc^*}{2A}. \tag{5.56}$$

Numerical application: the initial concentration of empty micelles in the oil solution is $c^* = (c_{surfactant} - CMC)/100$, if we consider that the micelles are constituted of typically 100 surfactant molecules. $c_{surfactant} = 25$ mM, $CMC = 5$ mM, thus $c^* = 10^{23}$ m^{-3}. Then using the typical measured velocity $V = 2 \cdot 10^{-6}$ m, one find $L_m = 1$ mm, *i.e.* a confinement $\frac{L_m}{2h} = 10$.

This numerical result is of the same order than the mother length measured experimentally (we typically measure $\frac{L_m}{h}$ between 10 and 20. However, as mentioned in the experimental section, this typical confinement do not really collapse onto a single constant curve. This observation made us inclined to think that another phenomenon is then at play.

5.5.2.2 Second step: instability

Although active droplets are observed to have a steady shape with a neck at the back of the droplet, it is likely that this shape will become unstable if the neck become too thin, through for instance a Rayleigh-Plateau instability [75]. A complete calculation of the Rayleigh-Plateau instability in the case of an active droplet confined by wall is ongoing by Masatoshi Ichikawa from the Laboratory of Dissipative and Biological Physics of Kyoto university. We can still have a very simple geometric and passive approach to get the idea of what is going on.

Let's consider a passive droplet (the surface tension γ is constant), in a viscous fluid (the flows outside the droplet are considered small compared to the flow inside the droplet), with the shape of an infinite straight cylinder with a radius h (region I), except in a region that we call the neck (region II), where the radius decreases to a minimum r_n (the geometry and notations are presented in Fig. 5.35(a)). In both regions, the Laplace law applies, and we have a relation between the pressure inside P_i^I and P_i^{II} and outside the droplet P_o^I and P_o^{II}, and the local radius of curvature. In the region I, the cylinder is straight, the tangential curvature is zero and the azimuthal curvature is $\frac{1}{h}$. In the region II, the tangential curvature is $\frac{-1}{R}$, and the azimuthal curvature is $\frac{1}{r_n}$. Then the Laplace law in the two regions gives:

$$P_i^I - P_o^I = \frac{\gamma}{h},$$
$$P_i^{II} - P_o^{II} = -\frac{\gamma}{R} + \frac{\gamma}{r_n}.$$

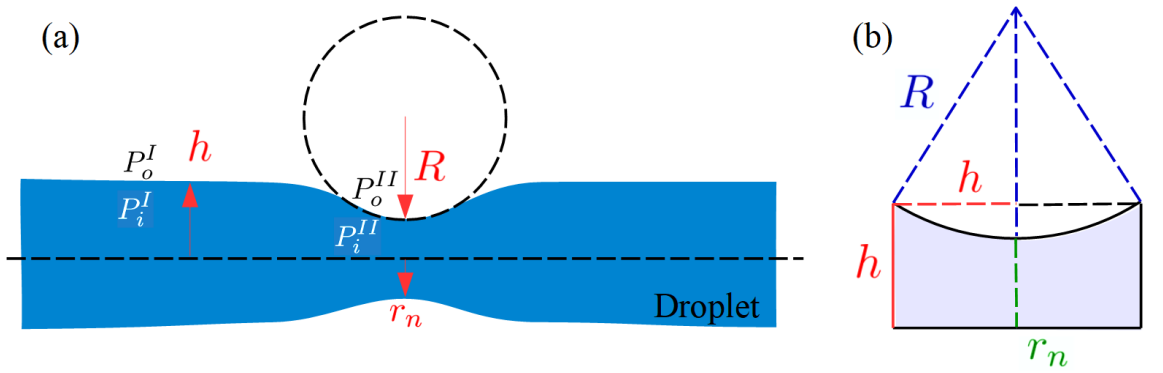

Figure 5.35: **Simple geometric approach of the stability of a neck:** (a) a long droplet with a mostly cylindrical shape of curvature $\frac{1}{h}$ (region I), except in a region where the thickness varies (region II), called the neck, of radial curvature $\frac{1}{r_n}$, and of azimuthal curvature$\frac{1}{R}$. P_i^I and P_o^I are respectively the inner and outer pressure in region I, and P_i^{II} and P_o^{II} are respectively the inner and outer pressure in region II. (b) Sketch of the neck geometry: the neck deforms the droplet on a typical length h, and on a typical thickness $R - h + r_n$.

If we consider that the pressure in the outside fluid is constant: $P_o^I = P_o^{II}$, then inside the droplet:

$$\Delta P_i = P_i^{II} - P_i^I = \gamma(\frac{1}{R} + \frac{1}{r_n} - \frac{1}{h}). \tag{5.57}$$

A flux v develops in response to the pressure gradient (through the Stokes equation). The direction of the flow depends on the sign of ΔP_i: if $\Delta P_i < 0$ the flux goes from the region I to the region II: the neck thickens: there is no rupture. If $\Delta P_i > 0$ the flux goes from the region II to the region I: the neck thins out and the droplet divides.

In order to compute the conditions on the neck for the division to occurs, we need to establish a simple model for the shape of the neck. We suppose that the deformation due to the local thinning happens on a typical length h. The Fig. 5.35(a) then shows the simplified geometry of the neck. Then R can be expressed as a function of h and r_n:

$$R = \frac{2h^2 - 2r_n h + r_n^2}{2(h - r_n)}. \tag{5.58}$$

ΔP_i thus becomes:

$$\Delta P_i = \gamma(h - r_n)\frac{r_n^2 - 4r_n h + 2h^2}{r_n h(r_n^2 - 2r_n h + 2h^2)}. \tag{5.59}$$

Trivially, when $r_n = h$, $\Delta P_i = 0$: the droplet is a straight capillary, and the inner pressure is homogeneous. The second part of the expression of ΔP_i (the fraction) has two zero, one for $r_n^c > h$, which is not a physical case studied here, and one for $r_n^c = 0.42h$. Between $r_n = h$ and $r_n = r_n^c$, ΔP_i is negative: the flow induced stabilizes the droplet. However, when $r_n < r_n^c$, ΔP_i becomes positive: the flow induced destabilizes the droplet, and a division occurs. r_n^c is then a critical value of the neck under which the droplet spontaneously divides.

Obviously, we stress that this model is way too simplified [11] to account for any numerical results in our experiment. In particular, we completely neglected the confinement by the wall in the outer flow, that might invalidate our hypothesis $\Delta P_o = 0$, but we also neglected the activity, which because of its effect on the boundary condition modifies the classical Laplace law used for passive and quasi-static problems. Still, this approach illustrates simply in term of pressure gradient and local curvature, that there might exist a critical neck radius, r_n^c under which the shape of the droplet becomes unstable and spontaneously break.

Experimentally, in Fig. 5.25(c), we do observe that the spontaneous breaking of the droplet always starts at a fixed value of r_n (around $r_n^c = 0.8h$), independently of all other factors. This is a strong indication that the division itself of the droplet is an instability phenomena, akin to the usual Rayleigh Plateau instability, but that only occurs when the droplets have reached a certain shape, namely presents a thin enough neck.

5.5.3 Discussion

The combination of the experimental observations and theoretical considerations conducted in the previous sections allows us to present a very likely scenario for the complex behaviour of swimming droplets confined in cylindrical capillaries.

Long swimming droplets in cylindrical capillaries swim at a constant and fixed velocity, independent of the geometry. This velocity is a result of the coupling between the hydrodynamics of the outer fluid in the lubrication fluid, and the advection-diffusion of swollen micelles along the droplet interface. Naive theoretical considerations of the concentration profile inside the lubrication layer reveals that swollen micelles accumulate at the rear of the droplet, inducing a variation in the lubrication layer thickness. This has an influence on the shape of the rear of the droplet, that then depends on the droplet's length, which is what is observed experimentally (its radius is measured to decrease when the confinement increases). Using stretched capillary, we then observe swimming droplets whose confinement increases continuously. When the neck attains a certain thickness, the droplets spontaneously divide, and eventually, the droplets may undergo successive divisions as the confinement continues to increase. The instability leading to this division division phenomenon needs to be further studied.

Conclusion

In this chapter, we thoroughly investigated the behaviour of highly confined swimmer, in simple and exotic geometries, and we propose some theoretical tools to better apprehend the physical phenomenon beneath our observation. One of the most striking result of this chapter is yet one of the simplest observation: droplets are able to swim even when strongly confined, advecting the outer fluid in a thin lubrication layer between their interface and the wall. In this lubrication layer, the outer fluid may attain

[11] It is actually too simple to even account for passive problems, for instance the Rayleigh-Plateau approach also take into account the stability of perturbation waves.

velocities of the order of 100 μm/s, on a thickness of a few microns, to be able to displace the droplet at a velocity of 3 μm/s. The only founds limitation of swimming under confinement is the spontaneous division of droplets observed under continuous increase of the confinement, in stretched capillaries. This spontaneous division is a combination of the activity of the droplet which leads to the deepening of a neck at the rear of the droplet, and of the geometry that constrains the shape of the droplet, and leads to an instability at the origin of the division. This phenomenon is the second most attractive result of this chapter. Indeed, as exposed in chapter (1), the ability to divide is one of the hallmarks of living system: our swimming droplets share yet another particularity of the living systems.

Chapter 6

Swimming together in 1D

Motivation

Brief introduction to phase transition at equilibrium

A complete and pedagogical introduction to phase transition in 1D is given in [147]. We restrict ourselves here to simple arguments and discussions that will highlight the particularity of our current system.

In an equilibrium thermodynamic description, phase transitions take place when there is a non-analytic change in the free energy F of the system, in the thermodynamic limit. This statement can be understood simply with the following example: let us consider a system that has two possible states I (for instance global alignment), and II (for instance disordered state), whose free energies vary as a function of a parameter (for instance a "temperature" T): $F_I(T)$ and $F_{II}(T)$. At a temperature T, the system goes in the state of lower free energy. In Fig. 6.1 are represented two different possibilities for the relative free energy: (a) if one free energy is always smaller than the other, then the system always keep the same state - there is no phase transition; (b) if for a certain critical finite value of T the two free energies cross each other, then the stable state of the system changes - there is a phase transition.

Now to a 1D system: let us consider a 1D Ising model, a network of L spin, of value ± 1, in a 1D periodic lattice (Fig. 6.2(a)). If all spin are aligned, then there is a global alignment in the system. Otherwise, the system is considered disordered. The spins have short range interactions, and the energy cost of two misaligned neighbor spin is called j, while the energy cost of two aligned neighbor spins is zero. If we call N the number of boundaries between domains of aligned spin in the system, a state of the system of N boundaries has an energy $E = Nj$, and $\frac{L!}{N!(L-N)!}$ realization, thus an entropy $S = kT \log \frac{L!}{N!(L-N)!}$. The system might undergoes any macroscopic state between the two extremes "only one domain" ($N = 0$), and "all spin misaligned" ($N = L$): the system has $L + 1$ possible state, of free energy $F = E - TS$. For a given temperature different than zero, we trace in Fig. 6.2(b) the typical curves for E, S and F. F has a finite non zero local minimum for a certain N. Thus the stable state of the system is a system with a certain number of different domains, the system is disordered. This result is valid for all temperature expect for $T = 0$ which

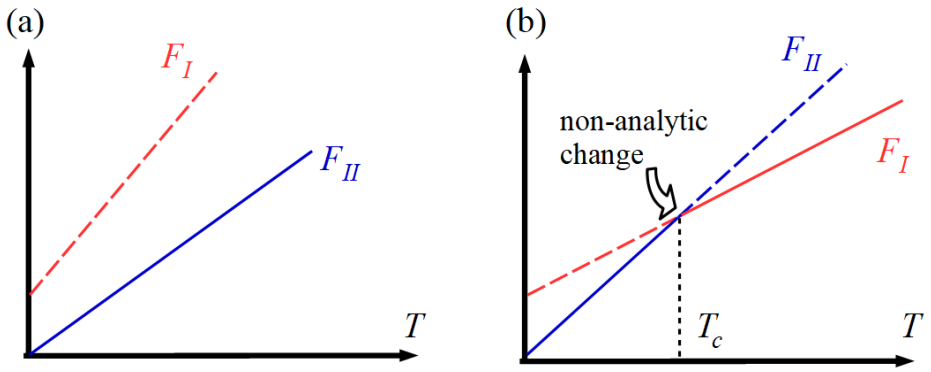

Figure 6.1: **Two states system and phase transition:** (a) one free energy is always smaller than the other. (b) the two free energies cross each other at T_c. The free energy of the first state is represented in red. The free energy of the second state is represented in blue. The sable state (the lowest in free energy) is represented in continuous line, while the other state is represented in dashed line.

is not attainable physically. This system is always disordered, thus there is no phase transition in this 1D system (and this result can be generalized to other model than the Ising model, with the conditions that the interaction are short range, and the system is homogeneous). This approach is called the Landau-Peierls argument, and predicts that no equilibrium phase transition is possible for 1D homogeneous[1] and short range interactions systems.

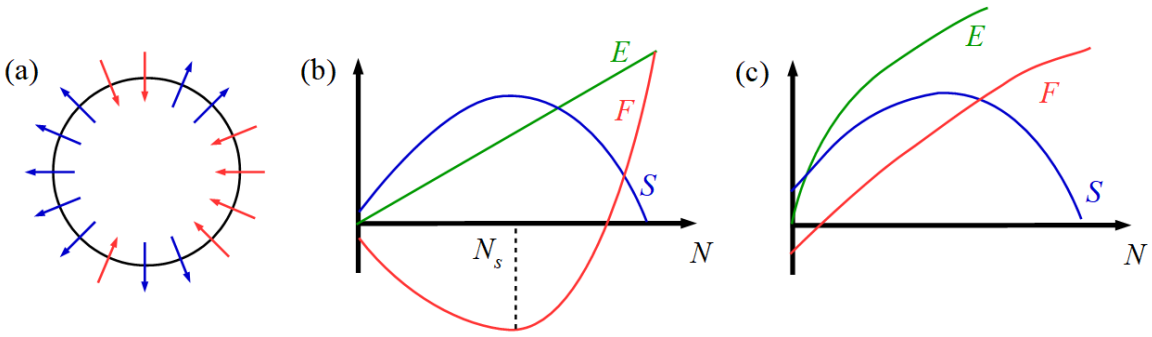

Figure 6.2: **1D Ising system:** (a) 1D Ising system of L spins on a periodic lattice, with spin ± 1 and N domains (blue and red). (b) System with short range interactions: free energy F (red) resulting from the energy E and the entropy S of the system, at a non zero temperature. F presents a local minimum at $N = N_s$. (c) System with long range interactions: free energy f (red) resulting from the energy E and the entropy S of the system, at a non zero temperature. The minimum of F is for $N = 0$.

As precised before, a way to overcome the no phase transition rule in 1D is to introduce long range interactions in the system, for instance decaying as a power law with distance. This long range interaction increases the cost of boundary, and thus increases E. One may then notice that for a $S(N, T)$ fixed, if $E(N)$ increases fast enough, then the local minimum of F might disappear for temperature low enough, but non zero. This is illustrated in Fig. 6.2(c). Then the lowest energy of the system is for $N = 0$:

[1]By homogeneous, we mean equally spaced

all spin are aligned, at a non zero small temperature. The system undergoes a phase transition from global alignment at small T to disorder at high T.

What should be kept in mind from this very brief and simple introduction to the phase transition in 1D system at thermodynamical equilibrium is that such system does not usually present phase transition.

Context

The above discussion is valid only in 1D and at equilibrium. Active system, such as our swimming droplets[2], are out of equilibrium. Phases transitions and collective behaviours in systems of active particles have motivated a significant amount of experimental [39] and theoretical works, combining both hydrodynamics and statistical approaches [42, 148]. Several phenomena peculiar to the activity have been observed, notably the emergence of collective behaviours [149, 150], or the motility induced phase separation [151] (commonly called MIPS). Most of these studies have been conducted in 2D.

Even in the absence of activity, the behaviour of 1D system is expected to be different than 2D systems. In particular, in 1D, the interactions between particles play a predominant role. Still, it has been demonstrated that phase transition could occur in an active 1D system [152], and a few models of active particle in 1D have been developed, taking into account either volume-exclusion [153] or alignment [154], but never combining both.

In order to design a 1D system of active particles, one possibility is to confine them (with walls for instance). One experimental challenge is then that the confinement may hinder the activity of the particles, especially in the case where the activity comes from an interaction with the external medium. From a theoretical perspective difficulties also arise from the confinement, as correlation emerges because of the geometrical constrains (in particular, the fact that the particles cannot bypass each-other [155]).

We saw in the previous chapter (5) that swimming droplets conserved their activity even when highly confined, which make them a good candidate to explore the collective behaviour of active particle in 1D. In the following, we present in section (6.1), what is, to the best of our knowledge, the first experimental realization of a 1D system of active particles. We observe the emergence of a rich variety of behaviours, which we try to understand in section (6.2) by building a model based on the simple experimental observation of the binary collisions between two droplets.

6.1 Experimental realization

6.1.1 Materials and Methods

6.1.1.1 Set up and observation

To produce and observe a lot of monodisperse droplets, we use a NOA microfluidic device composed of two parts, a first part to produce the droplets, and a second part

[2]For reminder, the thermodynamically stable state of our system is when all micelles in solution are saturated with water. Then, eventual remaining water droplet are not moving.

for observation. The first part for the production of droplets has been described in section 3.2.3. It allows to make droplets of typically the channel size ($a = 100$ μm), at various density (we define the linear density d of droplets as the fraction of the number of droplets N on the maximum number of droplets that could enter a portion of a channel of length L, without being deformed: $d = \frac{Na}{L}$). We typically make densities between $d = 0.1$ to $d = 0.8$ (from 50 to 400 droplets). The size of the droplets being the size of the channel section, the motion of the droplet is essentially 1D. The observation chamber is a 1D square channel of length $L = 10$ cm and section 200 μm per 200μm, folded in the shape of a "snake" (see in Fig. 6.3) to be contained in the 1cm per 1cm visualization area. Note that the device is thus not strictly 1D: the droplets need to "turn" to pass through the curved part of the channel that link two straight lines. This might have an influence on the droplet swimming. The discrete phase is a solution of 15% wt NaCl in water. As explained before, the salt helps the swimming of the droplet in 1D. The continuous phase is a solution of 25 mM mono-olein in oil. We tried two different oils, tetradecane and squalane. The droplets are driven inside the snake with

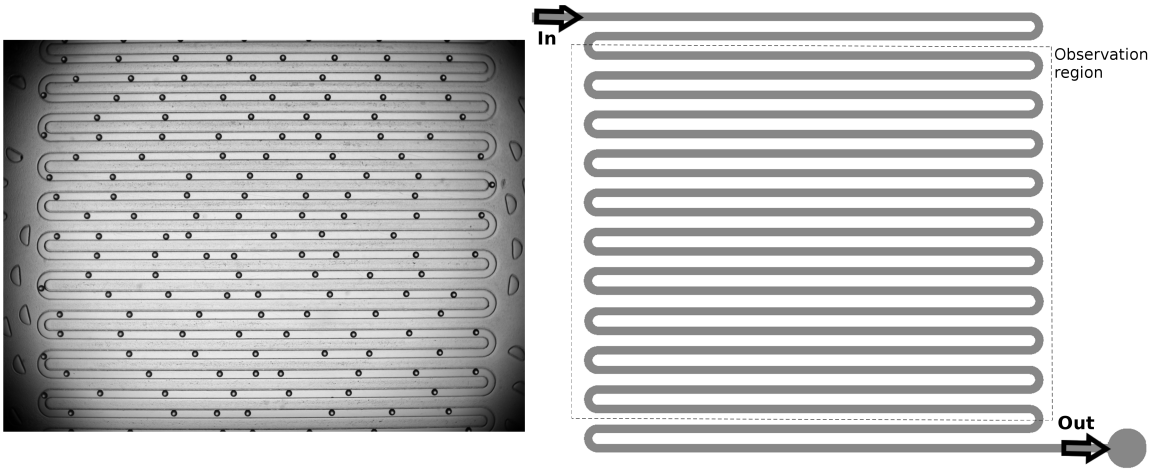

Figure 6.3: **Snake observation device:** 1D channel, the droplets enter from the top left, and exit at the bottom right. The droplets typically have the size of the channel width, thus the motion of the droplets is basically 1D.

an external flux, and then this external flux is cut. The residual fluxes are left to equilibrate for a few minutes, and then the outlet is closed and the inlet is linked to the trash. After around one minute, the droplets start swimming in a "random" direction. The observation is done using the macroscope (details section (3.3.1.1)), images are recorded at a frequency of one frame per second, for typically 1 to 2 hours. The pixel size is typically 3μm.

The experiments in squalane have been conducted by Yang Liu during an internship in the Gulliver lab prior to my arrival. The experiments in tetradecane, and the data analysis have been started during my internship at Gulliver, and continued during my PhD.

6.1.1.2 Data analysis

In order to get quantitative results from the experiments, a first step to extract the data is needed. During the internship of Yang Liu, some programs had been made,

which I completed and improved. There are four main steps to go from the images of the droplets to their positions and velocities:

Detection of the droplets: The rough detection of the droplets is made by morphological segmentation on the image. Then a sharp detection is made by using the matlab function for detecting circle, "imfindcircles", which uses a circular Hough transform. This function is very slow. This explains the need for the first detection, which reduces considerably the computation time. The total time of this function depends on the density of the droplets in the experiment, and varies from one hour to one night. At the end of this first step, we get the planar coordinates and the radius of each droplet (with the precision of one pixel, $\pm 3\mu$m, which is 3% of the droplets radius). This function may miss some droplets, or count twice the same droplet. These errors will be corrected later.

Computation of the curvi-linear abscissa: The droplets are evolving in a snake, and the relevant parameter is the curvi-linear abscissa along the snake. This is computed by first fitting a snake shape with the 2D positions of the droplets at all times, and then projecting the positions of the droplets on the snake. The computation time of this step depends on the density of droplets and of the resolution of the snake, and varies from ten minutes to a few hours. At the end of this second step, we get the curvi-linear abscissa and the radius of each droplet.

Determination of the trajectory of a droplet: At this point, we have the abscissa of each droplet at each time, but not yet the trajectory of each droplet at all time. We consider that the droplet cannot pass each other (this has indeed never been observed in the experiments). Then through the experiment, the droplets order remains the same. We order the droplets in three steps: first we correct droplets that have been detected twice (when the distance between two droplets is smaller than a droplet diameter), then we select the droplets that remain in the snake from the beginning to the end of the experiment (we remove the one that goes in and out of the snake), and finally we look for missing droplets (when the droplet goes at a velocity of more than one diameter per second, its typical velocity being 0.1 diameter per second). This step takes a few minutes. At the end of this third step, we get the trajectories of all droplets.

Smoothing of the data: A simple final step is used to smooth the data. The positions are smoothed by a low band filter. The velocity is computed by an iterative average filter on the time derivative of the position. At the end of this final step, we get the smoothed abscissa, the velocities, and the radius of the droplet.

6.1.1.3 The residual flow

After cutting all fluxes, we observe that there is a strong global velocity at the start of the experiments. This residual flow is due to the relaxation of all the microfluidic circuits (tubing, NOA), after the high flow imposed for the droplets production. Although the device was designed to minimize this residual flow (use of NOA instead of PDMS, use of rigid tubing...) it is still present, not negligible, and last for a long time (30 min). Then, to compute the active velocity of the droplets (their velocity relative

to this residual flow), we need to compute the residual flow. Assuming that the presence of an external flow does not affect the active velocity of the droplet, we have in our system a fraction of n particle going upward (toward the upper right exit) with an active velocity $+V_0$, and (1-n) going downward (toward the lower left exit), with an active velocity $-V_0$. The number of droplets going up or down is random ($n \neq 0.5$), so taking the average velocity of all droplets at one time wouldn't give us the velocity of the outer flow V_f:

$$\langle v \rangle = V_f + (2n-1)V_0. \tag{6.1}$$

However, using the average velocity of the droplet going right (respectively left):

$$\langle v_r \rangle = V_f + V_0, \tag{6.2}$$

$$\langle v_l \rangle = V_f - V_0, \tag{6.3}$$

one finds:

$$V_f = \frac{\langle v_r \rangle + \langle v_l \rangle}{2} \tag{6.4}$$

The residual flow V_f is computed this way, and subtracted to all individual velocities V. The position of the droplets S relative to this residual flow is computed from the integral of the new velocities also noted V, and used from now on.

Discussion on the effect of an external flow: we considered above that the velocity of the external flow can be simply added to the inner velocity of the droplets. However, the droplets swim by interacting with the solute, and have a certain concentration profile around them. The presence of an external flow may change this profile (for instance wash away the solute from the droplet),so that the the velocity of the droplets may depend on the residual flow. More dramatically, this dependency is likely to be not symmetric, so that in presence of a flow, the active velocity of the droplets going to the right is not simply the opposite of the droplets going to the left, leading to a systematic error on the residual flow computed before. In particular, one should be careful about three things: first the residual flow is sometimes observed to change sign with time, before relaxing to zero. Second "catastrophe" events happen from time to time (abrupt fluctuation of the external flow), where the residual flow is punctually disturbed by what we think is an external event (vibration, closing door...), which are difficult to avoid in such long experiments. Third, the initial conditions might be biased by the residual flow, which may favor one direction compared to the other. All these considerations must be kept in mind for the coming analysis.

6.1.1.4 The influence of the oil

The experiments are conducted at several droplet densities, for two different oils, squalane and tetradecane. First results can be extracted from direct observation.

In squalane:
The experiments in squalane have been realized by Yang Liu, when he was a student at ESPCI Paris, during an internship at the Gulliver laboratory prior to my arrival. At the beginning of the experiment, the droplets start swimming in "random[3]" directions.

[3]The droplets being brought in the snake channel by an outer flow, it is likely that the initial conditions around the droplets are not symmetric, and thus the initial velocities might be biased.

They are observed to swim straight, until they meet one another, events that we call collisions. This collision event describes the meeting and interaction between two droplets when they are close enough to feel (hydrodynamically or chemically) each other. The two droplets do not necessarily touch each other. The collision event is described in more details in the following. After the collision, the droplet may turn back (most of the time), or persist in its initial direction (from time to time), and start swimming straight again, until the next collision. The droplets continue swimming for one to two hours, although the velocity is observed to decrease slowly with time.

In Tetradecane:
Experiments were also done in tetradecane. The droplets are observed to swim slower and for shorter time than in squalane. Their motion is not regular; it alternates between swimming for a few dozen of minutes, and not moving for the same order of time. After stopping, their direction of swimming may change. The interaction with the wall seems to be more present than in squalane, as droplets a little smaller than the channel width stick to one side of the channel. This is not observed in squalane. Furthermore, the droplets seem to stick to the wall and to stick together at long times.

In the following, we thus concentrate on the study of the 1D swimming in squalane, for which the droplets swim more regularly.

6.1.1.5 Evolution of the droplet size

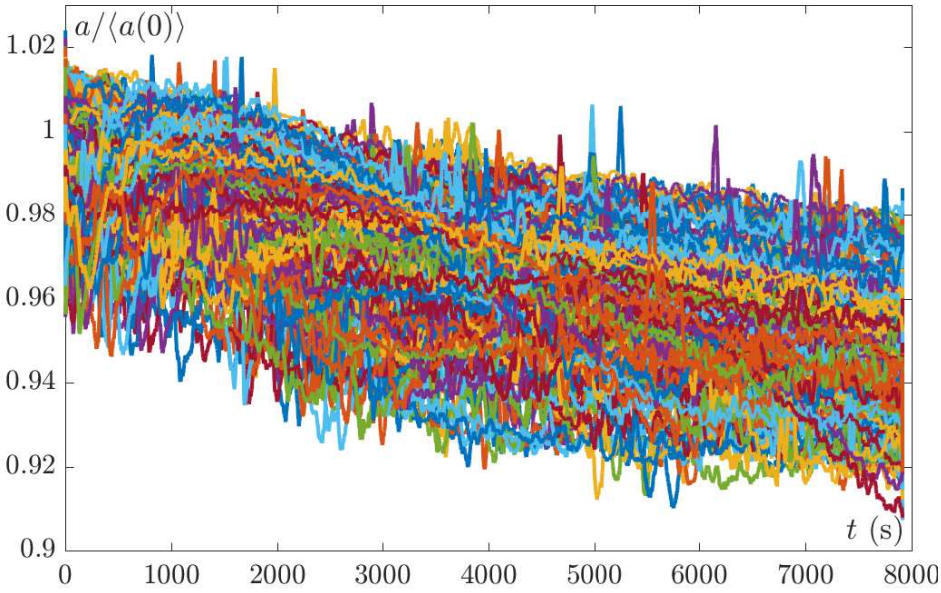

Figure 6.4: Radius of the droplets after tracking, for an experiment at intermediate density $d = 0.2$. The radius abscissa is rescaled by the average radius at time $t = 0$ s.

Fig. 6.4 shows the evolution of the radii, rescaled by the average radius at time $t = 0$ s, for all droplets in a typical experiment. The size of the droplets is observed to be quite mono-disperse (variation of $\pm$ 2%). The droplet size decreases with time, very slowly (less than 3% in one hour). Essentially, we can consider the size of the droplets to be the same for all the droplets, and constant in time.

6.1.1.6 Typical phenomenology at various densities

Fig. 6.5 shows the spatio-temporal diagram, the velocity histogram and the computed residual flow for typical experiments with various numbers of droplets.

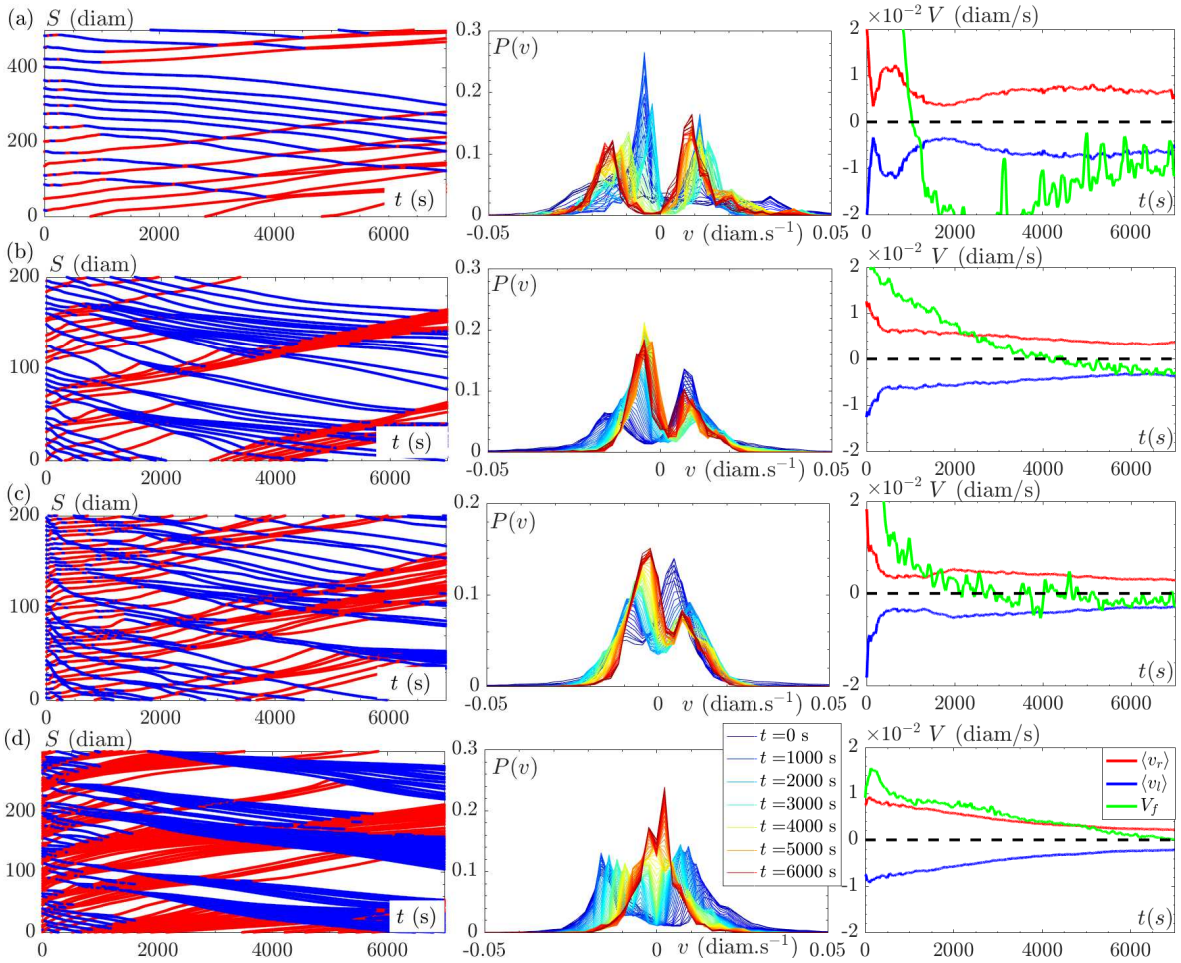

Figure 6.5: Typical experiments for various densities. From top to bottom: (a) $d = 0.05$, (b) $d = 0.25$, (c) $d = 0.35$, (d) $d = 0.4$. **Right**: spatio-temporal diagram of the droplets positions; the color codes for is the direction of the droplet (red toward the top, blue toward the bottom). **Middle**: histograms of the droplet velocities, the color codes for is the time (blue=beginning, red=end). **Left**: Velocity of the subtracted residual flow (green), of the average of the "positive" active velocity (red) and of the "negative" active velocity (blue).

Focusing on the velocity histograms in Fig. 6.5(b), one observes at a certain time (one color) the presence of two peaks of probability, one for positive velocity and one for negative one. These are the active velocity of the droplet going right (positive), or left (negative). The amplitudes of these pics vary with time: the number of droplets going right or left is not conserved. The positions of these peaks do not vary a lot with time, except for very dense experiments (for instance in Fig. 6.5(d)). Note that even though the velocities are centered around the active velocities, they have large fluctuations.

With our definition of the residual flow, equation (6.4), the positive and negative active velocities should be symmetrical after subtraction of this residual flow: this is indeed observed in the histogram, the two peaks are centered around zero. Fig. 6.5(c) shows

the evolution in time of these active velocities, as well as the computed residual flow. At the beginning of the experiment, the residual flow is large compared to the active velocities. Then it decreases (in general monotonically) to zero with timescales, which vary from one realization to another. Its value remains of the same order than the active velocities for long time (2000 s). The active velocities decreases rapidly at the start of the experiment, and tend toward a constant after some time (2000 s), except for the experiment at high density. For high density experiments, the active velocities are observed to decrease through the experiment. This could be due to two reasons: a global reduction of the droplets activity (decrease in size or saturation of the micelles), or a local behaviour due to the "regime" they are in. This will be discussed more precisely later on, but we consider the second option to be more likely.

Finally, looking at the spatio-temporal diagram in Fig. 6.5(c), one observes a rich variety of behaviours: binary collisions between droplets, where the droplets exchange direction, but also at the scale of the experiment, emergence of dense structures, where the droplets are aligned, which we shall call trains. These trains interact with single droplets, but also with other trains. We now focus on these collective behaviours in the next section.

6.1.2 Experimental observations: a rich variety of behaviours

Our system is composed of active droplets swimming in a 1D channel, that can "meet" other droplets through what we call a collision. At the scale of the system, collective behaviours, such as trains are observed. As was presented in this chapter introduction, the emergence of a collective behaviour is surprising. Are these regimes stable organized phase? What mechanism lies behind the formation of the train structure? We shall try in this section to understand from experimental observations how these aligned regimes come to be, and, in particular, if the understanding of the binary collisions between droplets can explain these collective behaviours. We progressively increase the density of our system to observe phenomena of increasing complexity.

6.1.2.1 Droplet swimming alone

For low density, a droplet that does not collide with another droplet can be considered to swim alone. Trajectories and velocities of such droplets are given in Fig. 6.6. The droplets are observed to swim in one persistent direction (there is no tumbling), with a velocity that fluctuates with time. The absolute value of the droplet velocity is in average around $V_0 = 5$ μm/s - this value varies from one experiment to the other, but remain of this order of magnitude. In this diluted experiment, we do not observe a global slowing down of the droplets.

This velocity is lower than the one observed in 2D, where it has been measured to be around $V_0^{2D} = 5-20$ μm/s (section (5)), but also lower from the ones measured in 1D for one droplet experiments, where it has been measured to be around $V_0^{2D} = 10-50\mu$m/s (section (4)). This difference might come from the fastest filling of the micelles in the confined environment when the density of droplets is high.

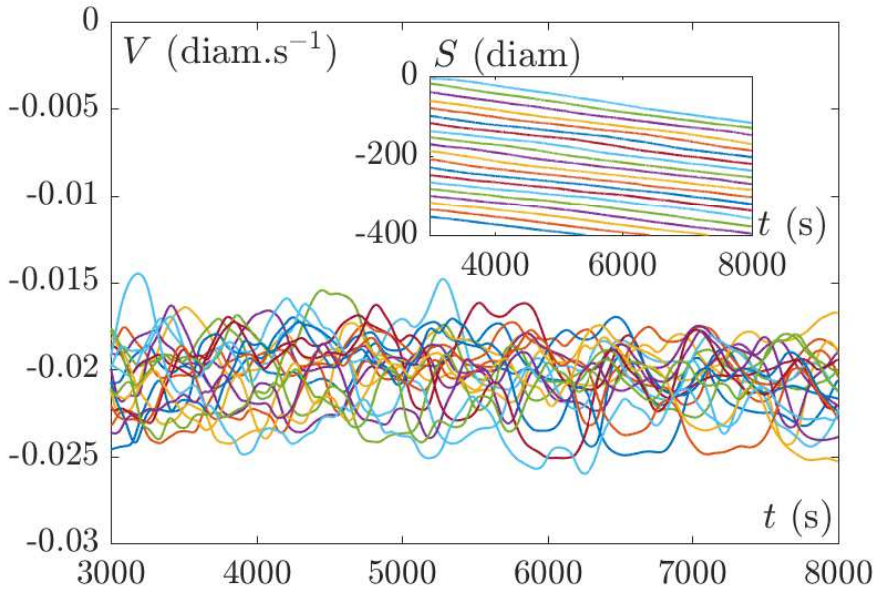

Figure 6.6: **behaviour of diluted droplets without collisions:** Velocities V of droplets swimming in the same direction rescaled by the droplet diameter $2a$ in a diluted experiment. Insert: corresponding curvilinear abscissa of the droplet S rescaled by the droplet diameter $2a$.

6.1.2.2 Very dilute experiment $d = 0.06$ - binary collision

For very dilute experiments, such as the one presented in Fig. 6.5(a), the droplets swim alone most of the time in one given direction, and from time to time, collide with other droplets. Several of these collision events are represented in Fig. 6.7. A collision takes a certain time (typically 200 s), and is composed of (i) a deceleration time, from the moment the droplets start to feel each other, until they reach a minimum distance (note that both the "feeling" distance and the "minimum distance" might be larger than a droplet diameter: the two droplets might not touch each other at all through the collision); (ii) a response time, which is the consequence of the collision, and lasts until the droplets relax toward a "swimming alone" behaviour. This response time is not well-defined yet, but its understanding will be of importance for the following.

Let us call n_1 the droplet going upward before the collision (in continuous line) with a velocity $V_1 > 0$ and n_2 the droplet going downward before the collision (dashed line), with a velocity $V_2 < 0$, and V_1' and V_2' their respective velocity after the collision. Then the consequences of the collision can be (i) n_1 and n_2 exchange direction, $V_1' < 0$ and $V_2' > 0$ (ex: Fig. 6.7(a) and Fig. 6.7(b)) ; (ii) n_1 persists in its direction, and n_2 changes direction, $V_1' > 0$ and $V_2' > 0$ (ex: Fig. 6.7(c) and Fig. 6.7(e)); (iii) n_2 persists in its direction, and n_1 changes direction, $V_1' < 0$ and $V_2' < 0$ (ex: Fig. 6.7(d)). The first behaviour is the most common, while the second and third ones, that lead to an alignment of the droplets, are less frequent at low dilution.

Looking more precisely at collisions between droplets that exchange direction in Fig. 6.7-top, we observe that the velocity of the center of mass (in black) is constant, but the droplets lose velocity (kinetic energy) after collision. Generally, these collisions are well described by an inelastic collision law with conservation of the momentum,

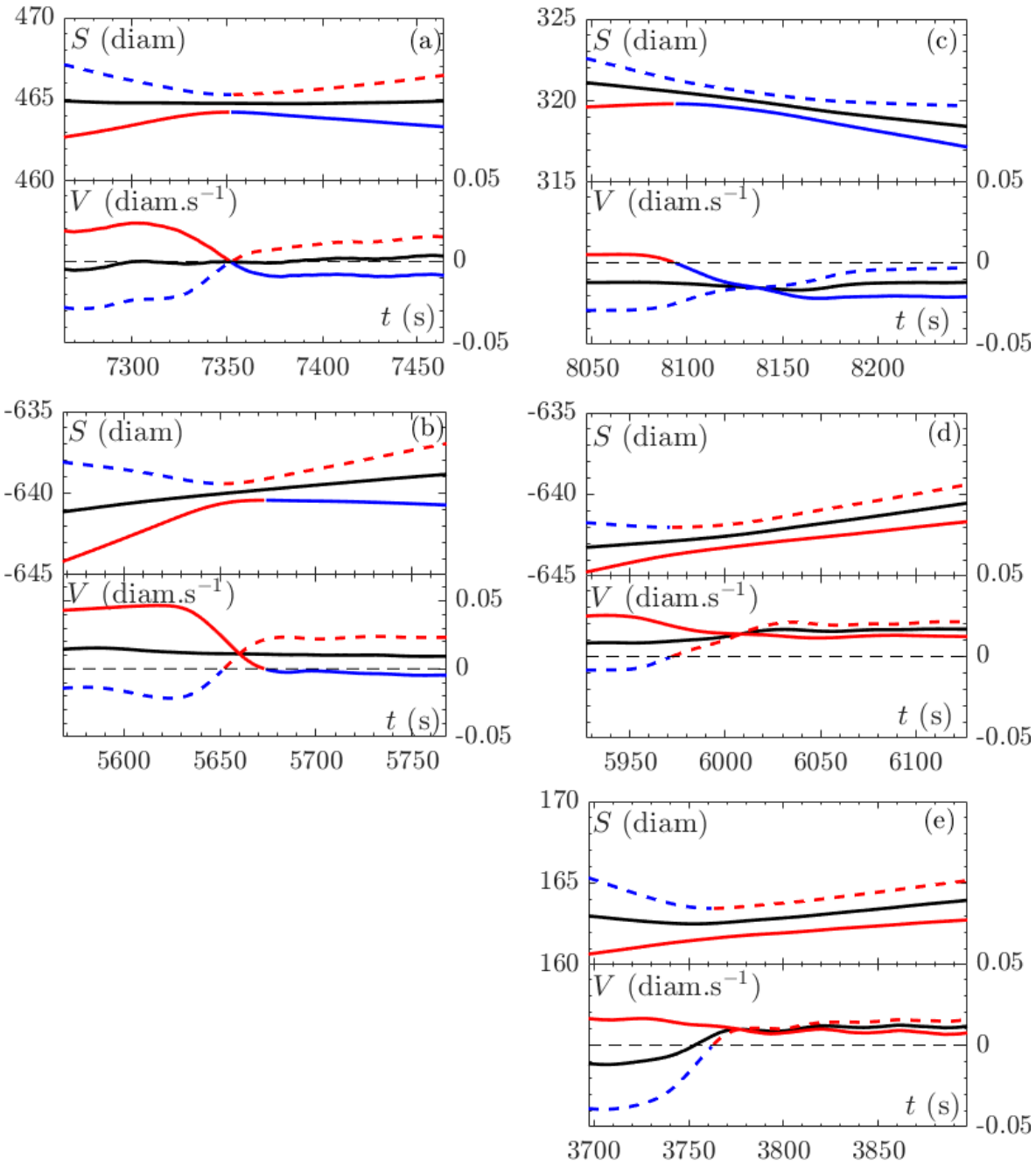

Figure 6.7: **All kinds of collision observed in diluted experiments:** the droplet going upward before the collision is in continuous line; the droplet going downward before the collision is in dashed line. The color codes for the velocity sign, red is positive (going upward) and blue negative (going downward). The center of mass is in black. **Left**: collisions between droplets that exchange direction. (a) The velocity of the center of mass is zero; symmetric inelastic collision. (b) The velocity of the center of mass is constant but non-zero; asymmetric inelastic collision. **Right**: Collision between droplets that leads to alignment. (c) and (d) The velocity of the centers of mass are constant, but non-zero: asymmetric inelastic collision that leads to an alignment. (e) The velocity of the center of mass is non-constant, a droplet persists in its direction with almost unchanging velocity: persistent droplet collision.

and non-conservation of the kinetic energy (these law are presented in more details in section (6.2.1). If one now looks at the collisions Fig. 6.7(c) and Fig. 6.7(d), which lead to alignment, one may notice that these collisions can be described using the same inelastic collision rules, with conservation of the momentum, but loss of velocity after collision. The difference is that before the collision, one droplet goes much faster than the other, and thus although the velocities are exchanged in the referential of the center of mass, they remain of the same sign after the collision. Note that although the collisions (a), (b) (c) and (d) would look the same in the referential of the center of mass of the two incoming droplets, the large velocities difference in the referential of the lab leads to alignment in the case of the collisions (c) and (d). Hence the fluctuations of velocities play a key role in the possibility (or impossibility) of alignment events.

Finally, there is another kind of collision, illustrated in Fig. 6.7(e): the velocity of the center of mass is not constant and even changes sign, and, more surprising, the two droplets align with the slower one, which is the opposite of the more intuitive behaviour of the inelastic collision presented before. These persistent droplet collisions are observed throughout all experiments.

To summarize, we have two kinds of collisions:

1. Inelastic collisions, with conservation of the momentum and non-conservation of the kinetic energy. Such collisions may lead to alignment with the fastest droplet if the velocities are different enough.

2. Persistent droplet collisions, where one droplet persists in its direction with almost constant velocity. This droplet might be slower than the other, resulting in an alignment with the slowest droplet.

Note that the large variety of collision behaviours (alignment, exchange of velocity...) is possible thanks to the fluctuation of velocities in our system.

6.1.2.3 Dilute experiment $d = 0.1/0.2$ - Propagation of collisions

In one "rare" experiment, all droplets go in the same direction, except for one. The spatio-temporal diagram of the droplet positions is given in Fig. 6.8(a).

One can observe through this experiment the propagation of one collision. Although each droplet displacement is not much, the collision propagates through the whole system. The propagation velocity decreases with time. There are two possible interpretations to this slowing down: it may come either from the decreasing of global active velocity with time (because the droplet size decreases, or because the micelles in solution saturate), or it could come from the collision itself (the velocity of the droplet is not conserved after collision). To answer this question, one may notice that the velocity of a droplet swimming alone has not been observed to decrease significantly with time (Fig. 6.6), and also, one remember that during an inelastic collision event, we indeed observe a loss of velocity after the collision.

Fig. 6.9 shows the successive collision events throughout the collision wave. At each collision event i, a droplet going upward n_1^i (continuous line) before the collision meets a droplet going downward n_2^i (dashed line) before the collision. For all collisions, except for the last one, the droplets exchange velocities. After the collision, n_2^i goes upward,

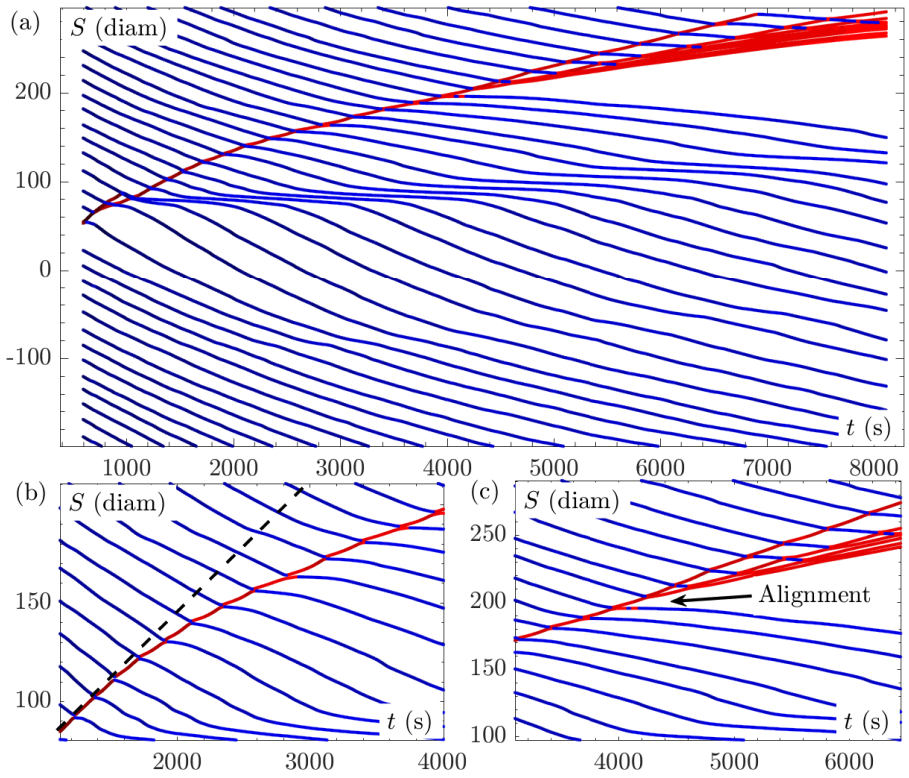

Figure 6.8: **Collision wave:** (a) Spatio-temporal diagram of a very dilute experiment $d = 0.1$, where all droplets except one go in the same direction at $t = 0$. The droplet going upward are colored in red, while the droplets going downward are colored in blue. (b) Zoom on the propagation of the collision (c) Zoom on the first absorption event.

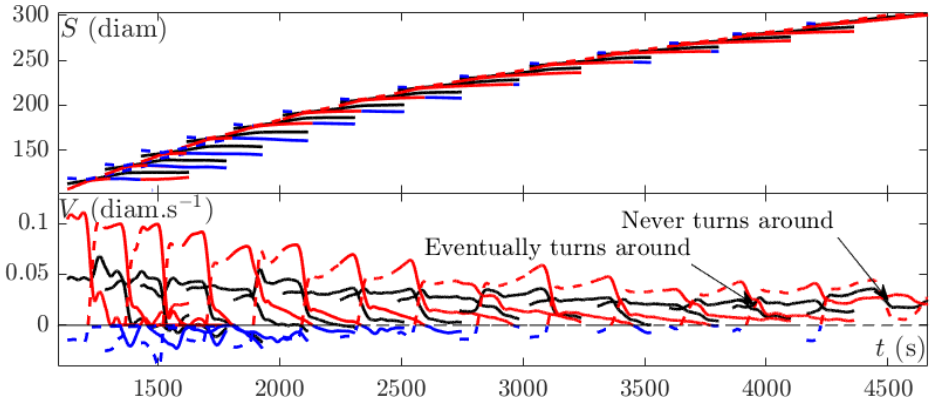

Figure 6.9: **Successive collisions through the collision wave:** (a) Position, (b) Velocity: for each collision, the droplet going upward before the collision is in continuous line; the droplet going downward before the collision is in dashed line. The droplet that goes downward before the collision (dashed line, blue), exchange velocity and goes upward after the collision (dashed line, red), becomes the droplet going upward for the next collision (continuous line, red), exchange velocity and goes downward again after the second collision (continuous line, blue). The color is the velocity sign, red is positive and blue negative. The center of mass is in black

and becomes the n_1^{i+1} droplet for the next collision. As observed before, the velocity of the droplet going upward before collision (red continuous line) - decreases after each collision. The velocity of the droplet going downward before collision (blue dashed line) is relatively constant. The velocity of the center of mass before collision (black line) decreases through the collision wave. This collision wave ends with a persistent droplet collision: the droplet going upward persists in its direction. This alignment event is followed by other alignment events, forming a regime of aligned droplets going upward: a train. This "alignment event" is what we consider to be necessary for the nucleation of the train regime.

Now let's look at another experiment, a little denser $d = 0.2$, and with more random initial conditions (Fig. 6.10(a)).

Initially, there are mostly collisions, during which the droplets exchange direction, leading to a regime that we call "quasi-elastic" regime (Fig. 6.10(b)). At some point, some alignment event occurs (Fig. 6.10(c)), leading to the nucleation of trains: a dense aligned regime emerges. These trains are absorbent, (Fig. 6.10(d)): they are likely to absorb incoming droplet and grow.

In these dilute experiments, there are only a few collisions, and thus the investigation of their long term consequences is limited. However, one can keep in mind a few observations:

1. A collision between two droplets:
   (a) lasts a certain time
   (b) does not conserve the kinetic energy
   (c) may lead to alignment
2. Collisions propagate through the system. As consequences:
   (a) the initial conditions have a strong influence on the system behaviour: the system has a long-lasting memory (remember that there is no tumbling, hence the dynamics is deterministic);
   (b) although the droplets do not browse long distance, information does.
3. Alignment in the system leads to the formation of dense aligned groups of droplets: the trains.

6.1.2.4 Denser experiment $d > 0.2$ - Train behaviour

For denser experiment, the trains are observed to form very quickly, to grow by absorbing droplets, and to interact with other trains (Fig. 6.11(a)). If one focuses on the behaviour of only one N droplets long train colliding with another droplet, the growing process can be described as follow: the droplet $n = 0$ arrives face to face with the $\{N\}$-train, it collides with the first droplet of the train $n = 1$. The two droplets turn around, losing some velocity. The first droplet $n = 1$ is now oriented against the train, and collide with the second droplet of the train $n = 2$. Once again, they exchange velocity while losing some. This means that at each successive collision during the

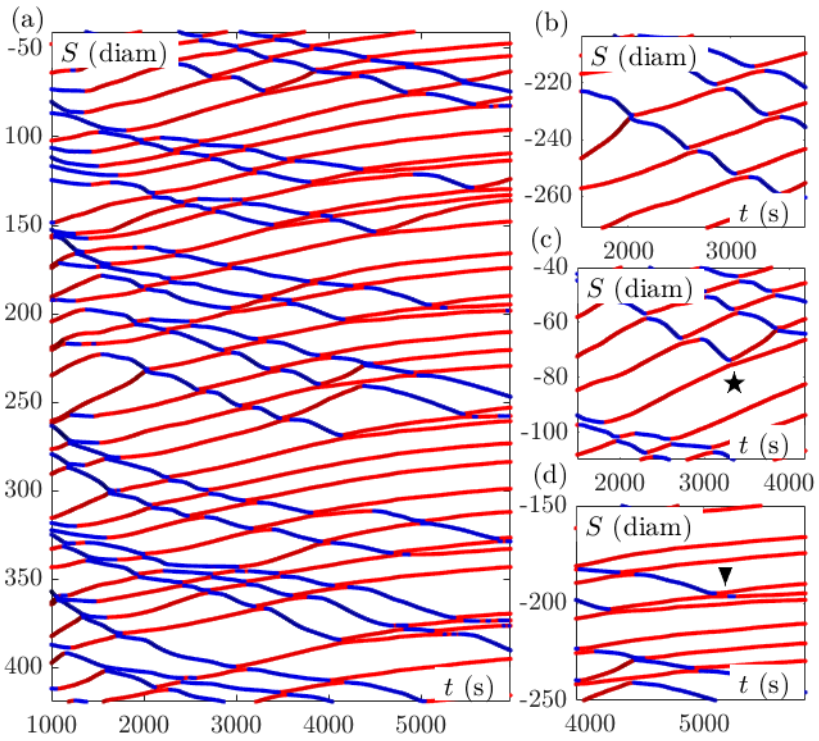

Figure 6.10: (a) Spatio-temporal diagram of a dilute experiment $d = 0.2$, with random initial conditions. The droplet going upward are colored in red, while the droplets going downward are colored in blue. (b) Elastic regime: mostly collision events with exchange of direction. (c) Alignment event (black star). (d) Nucleation of trains (black triangle).

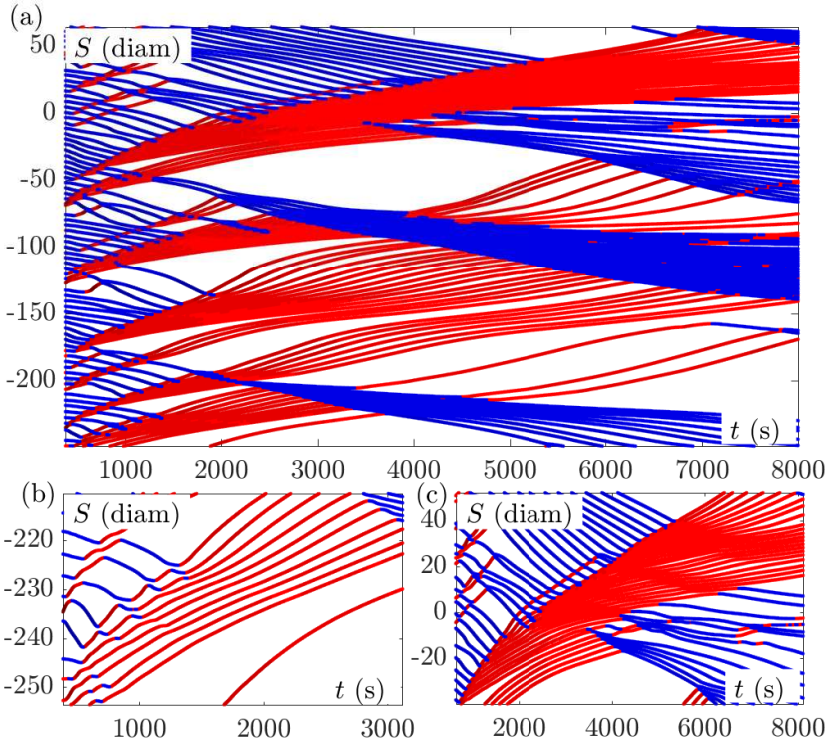

Figure 6.11: (a) Spatio-temporal diagram of a dense experiment $d = 0.6$. The droplet going upward are colored in red, while the droplets going downward are colored in blue. (b) Train absorbing droplets and growing. (c) Two trains crossing each other.

transmission of the initial "impulsion[4]" of the droplet $n = 0$ colliding with the train, this impulsion loses velocity, until at some point it disappears: the $n+1$ droplet in the train does not turn back while colliding with the n droplet: the impulsion has been completely absorbed by the train. and the system one droplet + a $\{N\}$-train becomes the system $\{N+1\}$-train: it gained alignment. This behaviour is intrinsically linked with the non-elasticity of the collisions.

In the absence of absorption or interaction with another train, a train is still observed to increase in volume (Fig. 6.12): the distance between droplets increases because

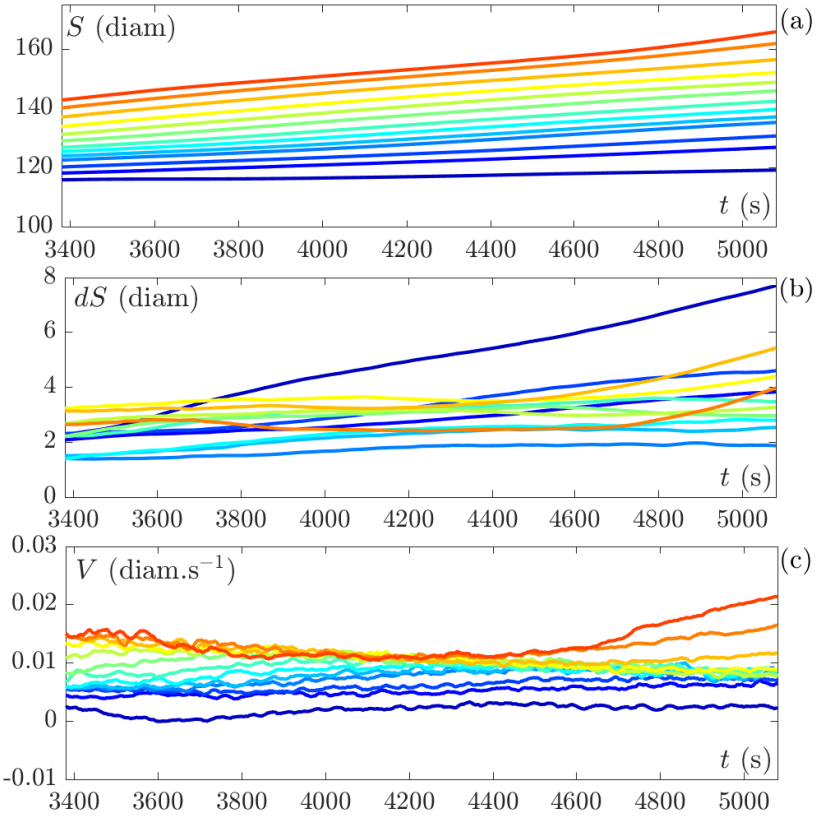

Figure 6.12: (a) Abscissa (b) distance between droplets and (c) velocity of droplets in a train without absorption nor interaction with other train, in the experiment presented in Fig. 6.11(a)

the droplet at the head of the train are faster than the one at the tail of the train. The active velocity of the droplet is measured to be around $V = 0.02$ diam/s. "Free" droplets go at this active velocity, while droplets in trains go slower. When a droplet leaves a train, it becomes a free droplet and accelerates toward its free active speed. If we look at the velocity of the droplet through the experiment, Fig. 6.13, we indeed observe the droplets to go slower inside the trains (black), and to regain velocity outside of trains (red and blue), in the quasi-elastic regime.

We can also observe the collision between two trains, Fig. 6.11(c). This is a really complex event: the two trains exchange some droplets, but are also observed to cross

[4]Obviously, our system is over-damped and out of equilibrium, thus there is strictly speaking no "conservation" or "transmission of impulsion" - we simply use these terms for an effective description of what happens in the system.

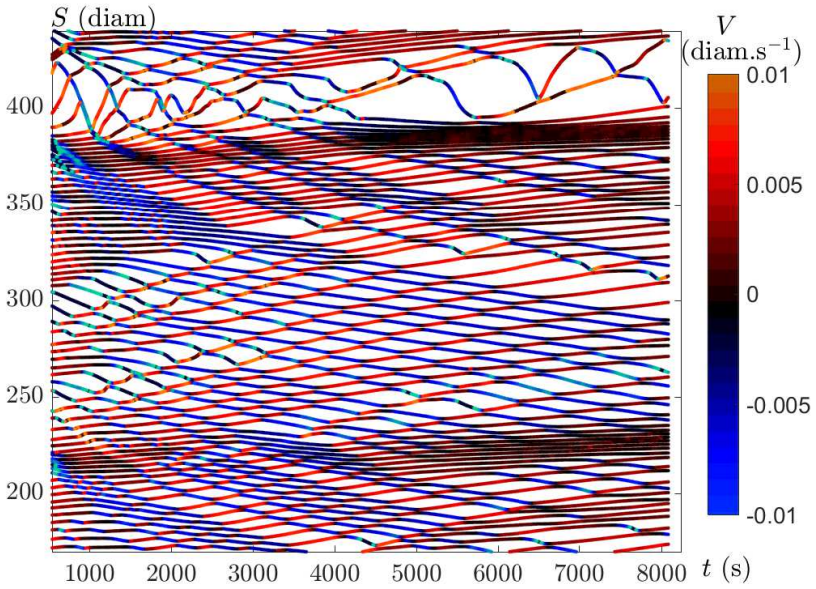

Figure 6.13: **Formation of cloggs:** spatio-temporal diagram of the position of the droplet, with a colormap proportional to the velocity: the free droplets goes fast (red for the droplets going up and blue for the droplets going down). During a collision between two trains, the droplets are almost immobile (black).

each other, not fusing to form only one train. This train collision lasts some time (several thousands of seconds). Furthermore, during the collision between the two trains, the droplets are almost immobile (dark blue), forming what we call a clogg.

To summarize the train behaviour:

- A train is a dense group of droplets going in the same direction.
- The nucleation of the trains happens through alignment during a binary collision between two droplets.
- The trains are absorbent: they grow by absorbing the droplets they meet.
- Droplets in trains are slower than when swimming alone.
- A train without interaction tends to expand, and the droplet inside accelerate progressively leading to the formation of a diluted aligned regime.
- When two trains meet each other, they form a clogg. The droplets inside the cloggs are almost immobile. The trains can leave the clogg.

6.1.3 Discussion - physical origin of the behaviours

Our previous observations show that the swimming droplet may have many different behaviours, that depend on its history and its environment: (i) if the droplet is alone, it can either be in its stationary state (going at its active velocity V_0), or relaxing toward this stationary state, if previous event changed its velocity; (ii) if there are two droplets, they either enter an inelastic collision, or a persistent droplet collision; (iii) if the droplet is in a dense phase, it is either in a train (dense aligned droplets going

at slow velocity), or in a clogg (dense droplets almost immobile). In this section, we want to understand the physical origin of these behaviours.

6.1.3.1 The relaxation toward activity

When just made, a swimming droplet has a zero velocity. Through the instability described in section (2.2.3), it starts swimming in a random direction, and reaches its stable state with a steady active velocity V_0. If at some point, because of some perturbation, the velocity of the droplet changes, then it will relax once again toward its active velocity. This is what is observed for instance when a droplet leaves a train, where because of the environment its velocity was slower than its active velocity: the droplet accelerates until it reaches once again its active velocity. Similarly, this is what should be observed after a collision: the collision slows down the droplets, putting them out of their steady state dynamics. They then relax back to their free-swimming speed. Such relaxation after an inelastic collision is showed in Fig. 6.14. This relaxation is

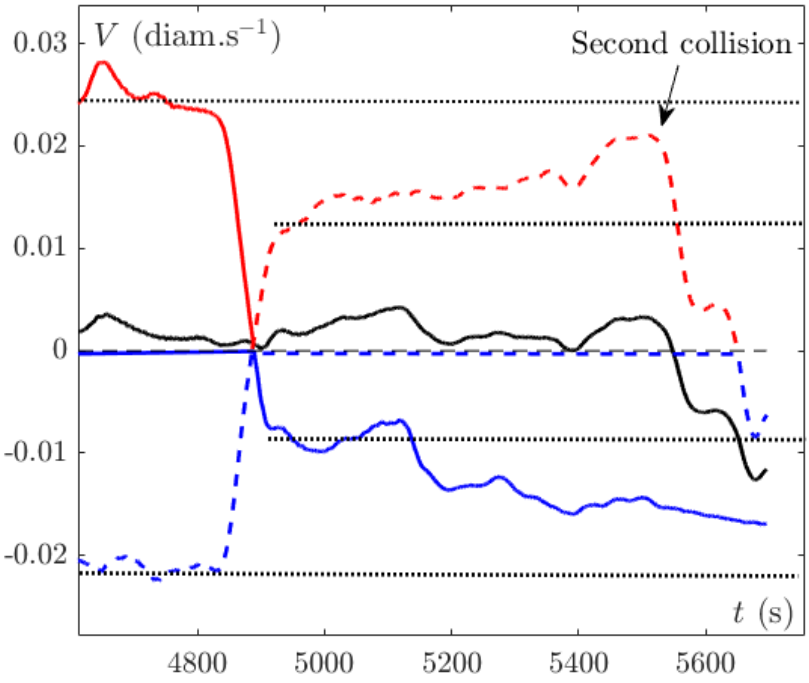

Figure 6.14: A collision between two droplets followed by a long time without collision: the droplets velocities relax toward their steady active velocity. This relaxation is interrupted by another collision.

very slow, and is not a direct consequence of the collision. Therefore we differentiate two time scales in our system, the collision time, which is the time the droplet takes to exchange their velocity, of the order of 200 s, and the relaxation time, which is the characteristic time at which the droplet reaches its steady velocity, of the order of 1000 s. Because the relaxation takes so long, it is very rare to see the droplets reaching their steady velocity before entering in another collision: the droplets are constantly out of their steady state, relaxing toward their active velocity, while being slowed down by

the collisions. This relaxation toward equilibrium plays a very important role when considering collisions that lead to alignment. Indeed, in such case, after the collision, the droplets have the same direction, and therefore relax toward active velocities of the same sign. This means that while the velocity of the center of mass is conserved through an inelastic collision, it is not during the relaxation time. Phrased differently, the system gains momentum after the collision. We believe that this effect plays a very important role in the formation of the train regimes.

6.1.3.2 Origin of the collision behaviour

Collision with exchange of direction

Let's look first at the most common collision: the inelastic collision that does not lead to alignment. The trajectory and the velocity during a typical collision, and the notation we are going to use are given in Fig. 6.15(a) and (b). Before the collision, the

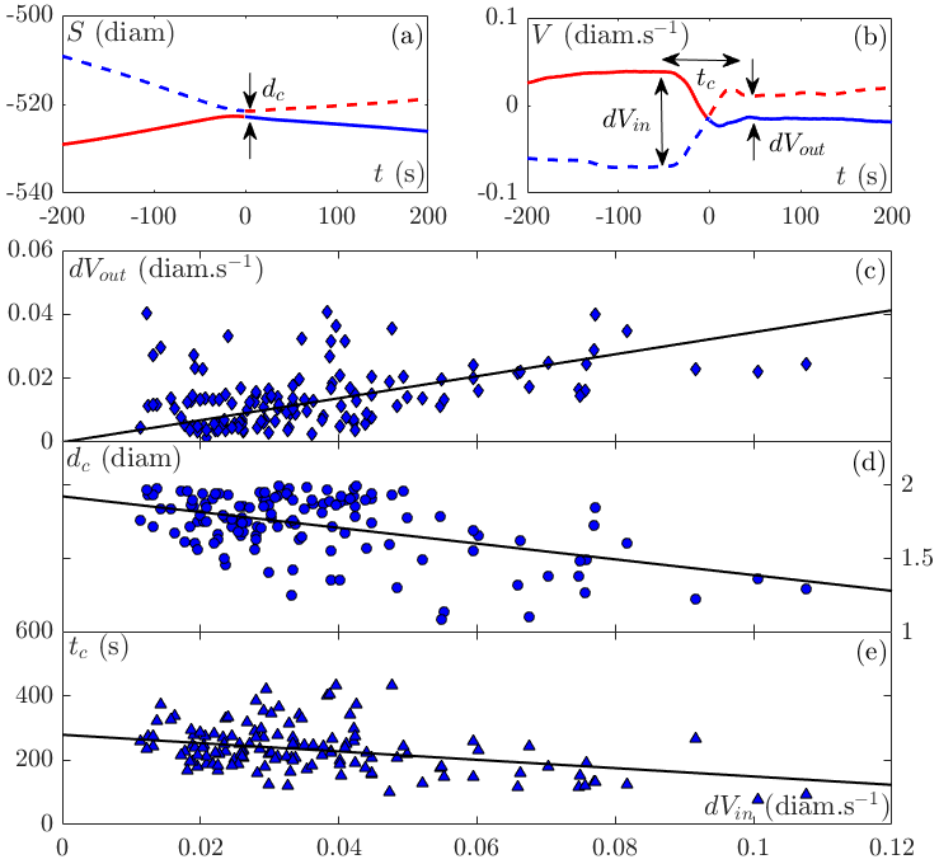

Figure 6.15: **Characterization of well-defined collisions for an experiment of density $d = 0.1$:** (a) Trajectories of two colliding droplets, d_c is the minimum distance between the droplets, which defines the time of collision. (b) Velocities of the same two droplets: dV_{in} is the relative velocity of the droplets before the collision; dV_{out} is the relative velocity of the droplets after the collision. t_c is the total collision time, defined as the time from when the droplets start feeling each other, to the time they stop feeling each other. (c) dV_{out} vs dV_{in} for all well defined collisions, and linear fit (black line). (d) d_c vs dV_{in}, and linear fit (black line). (e) t_c vs dV_{in}, and linear fit (black line).

droplets n_1 and n_2 swim toward each other at a velocity which vary slightly around their average velocities $V_{1,in}$ and $V_{2,in}$ which may not be the same. At a certain time t_{in} (time at which they start feeling each other), the velocities of the two droplets start to decrease. This happens when the droplets are at a distance d_{in}. This distance varies from one droplet diameter to a few droplet diameters. If the entrance velocities of the two droplets are different, the velocity of the center of mass is non-zero. In the referential of the center of mass, the velocities decrease symmetrically toward zero. In the referential of the lab, this means that one of the velocities might change sign before the other. The time at collision and the distance at collision d_c are defined when the distance between the two droplets is minimum. Note that with this definition, the relative velocity of the droplets is zero at the collision. After turning back, the droplets speeds increase until they reach new steady velocities $V_{1,out}$ and $V_{2,out}$. The time at which the drops stop feeling each other is called t_{out}, and this happens at a distance d_{out}. Even after this time, the velocity is not observed to be constant, but to increase slowly (relaxation time). The total collision time is defined as $t_c = t_{out} - t_{in}$.

One may then inquire on the effect of the initial velocity $V_{1,in}$ and $V_{2,in}$ on the collision behaviour. As the velocity of the center of mass is constant, the important parameter to characterize these collisions is the relative velocity, $dV_{in} = \frac{V_{1,in} - V_{2,in}}{2}$. These effects are presented in Fig. 6.15(c), (d) and (e). A few observations can be made:

- dV_{out}, the relative velocity after collision increases with dV_{in} the relative velocity before the collision, but is always lower;

- d_c, the distance at collision decreases with the relative velocity before the collision, but is often larger than $2a$, which is the minimum distance at which the droplet can be (when they touch each other). This means that the collision happens at a finite non-zero distance, of typically two diameters between the two droplets.

- The duration of a collision t_c decreases with the relative velocity before the collision.

The droplets start to interact far from each other, and often collide without touching. The interaction of these droplets can only be made through a modification of the swollen micelles concentration field. This concentration field can be disturbed by the swollen micelles emitted by the other droplet, or the hydrodynamics flow field produced by the other droplet. Actually, as in our system the hydrodynamics and chemistry are coupled, it is likely to be the two at the same time. The mechanisms at play are very complex, and we are not able to solve them exactly. We may however discuss on the basis of the previous measurement: the droplets are colliding at a certain distance d_c, of typically two droplets diameter. In front of the droplet, micelles are emitted, which diffuse with a diffusion coefficient D, and are advected at the typical velocity V_{in}. A characteristic distance on which the micelles are transported in front of the droplet emerges from these two parameters: $d_{micelles} = \frac{D}{V_{in}} \simeq 100$ nm. This distance alone is too small to explain how the droplets feel each other from so far. This consideration makes us think that the interactions between droplet during inelastic collision are dominated by the hydrodynamics.

6.2 Development of a simple model

We have described in details the phenomenology observed in the dense phase. What we would like to understand now is if these dense phases are caused directly by the activity and the binary interactions of these droplets. For that, we are going to introduce a numerical model for these droplets, using only this activity and these binary interaction as ingredients, and see if they are sufficient to observe the same collective behaviour than the one observed experimentally: the trains and the cloggs.

6.2.1 The model ingredients

We want to implement two key ingredients in our system: the activity of the droplet (and thus the relaxation toward activity), and the binary collisions, which behave as inelastic collisions. We consider particles of finite radius a, at a global density d, with an active velocity $\pm V_0$, moving on a periodic 1D axis (continuous or discrete), oriented by the vector $\mathbf{e}_x$.

Binary collision

As in our experiment the collision time is smaller than the relaxation time, we suppose an "instantaneous" inelastic collision as a first approximation. For the general case of an inelastic collision between two particles n_1 and n_2 of different masses m_1 and m_2, at different velocity V_1 and V_2; the velocity of the center of mass U, and the differential velocity dU are defined by:

$$U = \frac{m_1 V_1 + m_2 V_2}{m_1 + m_2}, \tag{6.5}$$

$$dU = V_1 - V_2. \tag{6.6}$$

Then the velocities rewrite as:

$$V_1 = U + \frac{m_2}{m_1 + m_2} dU, \tag{6.7}$$

$$V_2 = U - \frac{m_1}{m_1 + m_2} dU. \tag{6.8}$$

We consider inelastic collisions that conserve momentum, but not the kinetic energy. These rules can be translated as:

$$U' = U,$$
$$dU' = \alpha dU,$$

where α is the restitution coefficient. Under such rules, the velocity of the particle after collision are;

$$V_1' = \frac{1}{m_1 + m_2}\Big(\alpha m_2 (V_2 - V_1) + m_1 V_1 + m_2 V_2\Big), \tag{6.9}$$

$$V_2' = \frac{1}{m_1 + m_2}\Big(\alpha m_1 (V_1 - V_2) + m_2 V_2 + m_1 V_1\Big). \tag{6.10}$$

As a first approximation in the model, we consider that all particles have the same mass, which amounts to neglect the persistent particle collisions. Then the above expression rewrite as:

$$V_1' = \frac{1}{2}\Big((1+\alpha)V_2 + (1-\alpha)V_1\Big), \tag{6.11}$$

$$V_2' = \frac{1}{2}\Big((1+\alpha)V_1 + (1-\alpha)V_2\Big). \tag{6.12}$$

For elastic collisions, $\alpha = 1$, the particles simply exchange their velocity. For perfectly inelastic collision, $\alpha = 0$, the particles align on the velocity of the center of mass. An inelastic collision between two particles that exchange direction is shown in Fig. 6.16(a), and between two particles that come out with the same direction in Fig. 6.16(b). In

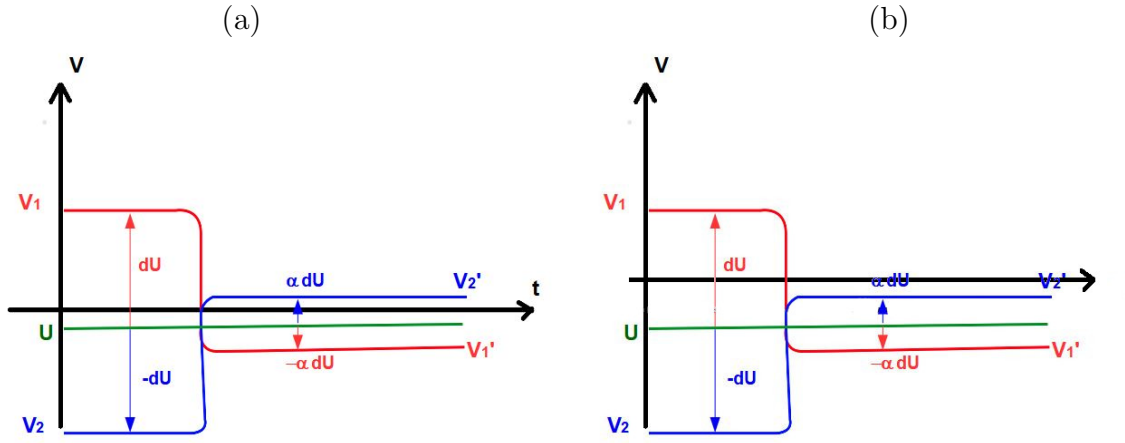

Figure 6.16: (a) Model collision for an inelastic collision leading to an exchange in direction ($\alpha dU > |U|$). (b) Model collision for an inelastic collision between two particles that come out with the same direction of motion ($\alpha dU < |U|$).

these inelastic collisions, a simple rule tells us if the particle will exchange direction or come out with the same direction: if $\alpha dU > |U|$, then $V_1' = U - \alpha dU$ cannot have the same sign than $V_2' = U + \alpha dU$. However if $\alpha dU < |U|$, then V_1' and V_2' have the same sign.

Relaxation toward activity

In the absence of any systematic experimental information on how the particles relax, we choose our relaxation to be conceptually the simplest one: an exponential relaxation. This exponential relaxation occurs at a typical rate $\lambda = \frac{1}{\tau_r}$, τ_r being the typical relaxation time.

One important point to notice is that there are actually two steady states in this bi-directional system, corresponding to the two directions the particle can have ($\pm\mathbf{e}_x$)

6.2.2 Numerical implementation of the model

We tried two different implementations of this model. In a first time, we used a continuous coordinate (1D axis), but we encountered difficulties in dealing with dense region.

We then switched to discrete coordinates (1D lattice). The analytic consideration has been made for the continuous model. The continuous implementation of the model has been taken over by Pierre Illien during a Post doc at the Gulliver laboratory, and we will briefly discuss the result at the end of this section.

6.2.2.1 Continuous model

We consider particles of finite radius a, at a global density d, with an active velocity $\pm V_0$, and moving on a periodic 1D axis. These particles interact with inelastic collisions of restitution coefficient α, and when their velocity is not the active velocity, they relax toward it at an exponential rate $\lambda = \frac{1}{\tau_r}$.
If at a time t_0, a particle i at a position $x_i(t_0)$ has a velocity $V_i(t_0)$, and a direction $s_i = \pm 1$, then in the absence of collision, its velocity and position at time t are:

$$V_i(t) = V_i(t_0)e^{\lambda(t_0-t)} + s_i(t_0)V_0(1 - e^{\lambda(t_0-t)}), \tag{6.13}$$

$$x_i(t) = x_i(t_0) - \frac{1}{\lambda}V_i(t_0)(e^{\lambda(t_0-t)} - 1) + s_i(t_0)V_0(t - t_0) + s_i(t_0)V_0\frac{1}{\lambda}(e^{\lambda(t_0-t)} - 1) \tag{6.14}$$

Then we know the position of the particles at all times depending on the last time it had a collision t_c^n, and until the next collision occurs at a time t_c^{n+1}. In the system of N particles, it is then possible to compute the position of all particles at all times from binary collision to binary collision, by computing after each binary collision the next collision event (the one that will happen the soonest). Knowing that a collision has happened at a time t_c^n, we want to compute the next collision time t_c^{n+1}. For each pair i and $i+1$ of particles, a collision event is such that $x_i - x_{i+1} = 0$, which gives an equation in t_c^{n+1}:

$$\begin{aligned}(s_i - s_{i+1})V_0 t_c^{n+1} + \frac{1}{\lambda}e^{\lambda t_c^n}(V_i(t_c^n) - V_{i+1}(t_c^n) \\ + (s_i - s_{i+1})V_0)e^{-\lambda t_c^{n+1}} = x_{i+1}(t_c^n) - x_i(t_c^n) + (s_i - s_{i+1})V_0(t_c^n + \frac{1}{\lambda}),\end{aligned} \tag{6.15}$$

which is of the form $at + be^{-\lambda t} = c$. This kind of equation is not solvable analytically, but using the numerical Lambert W function, we can express the solution as

$$t = \frac{c}{a} + \frac{1}{\lambda}W(\frac{-b}{a}\lambda e^{\frac{-c}{a}\lambda}). \tag{6.16}$$

This time of collision is computed for each pair of particles, and the minimum of all these times is the time at which the next collision will happen t_c^{n+1}. Using this, we can numerically compute the trajectory of all particles. However, a problem arises in very dense region: if the particles are blocked in a configuration where they are side by side (for instance in a clogg), then they are in permanent collision, and we cannot deal with this phenomenon with our simple implementation. For this reason, we decided to switch to a discrete model, which is simpler to implement, and keep the key ingredients that we are interested in.

6.2.2.2 Discrete model

We consider a system of N particles at a density d on a 1D periodic lattice of step a, which is also the size of our particles. These particles are active, with a steady velocity $V_0 = 1$, and a direction $s = \pm 1$, the sign being the direction of motion. These particles collide with an inelastic coefficient α, and relax toward activity with a rate λ. The implementation is as follows:

1. The particles are initially placed randomly on the lattice, with random direction and a velocity $V(t = 0) = \pm 1$.
2. At each time step, all particles are considered in a random order, and attempt to move to the next site with probability V in direction s.
   (a) If the next step is free, the particle moves with a probability V, and the velocity relaxes exponentially toward V_0 with a rate λ:
   $$V(t+1) = V(t) + \lambda s(t)(V_0 - V(t)). \tag{6.17}$$
   (b) If the next step is occupied, the particle collides with the other particle with the same inelastic behaviour than before. Its position doesn't change, but its velocity evolves with the rule:
   $$V_1(t+1) = \frac{1-\alpha}{2} V_1(t) + \frac{1+\alpha}{2} V_2(t). \tag{6.18}$$

This discrete model is really simple, and should be viewed as a first approach at understanding the effect of our key ingredients - the inelastic collision and the relaxation toward activity - on the behaviour of the system. This model is the one that we use for all following results.

6.2.3 Simulation with parameter values close to the experiments

The typical velocity in the experiment is $V_0 = 0.02$ (diam/s^{-1}), and the density varies between $d = 0.1$ and $d = 0.8$. Experimentally, we can measure the inelastic coefficient for the different experiments. Although it is relatively constant in the same experiment, it varies from $\alpha = 0.2$ to $\alpha = 0.8$ from one experiment to anther. We also evaluate roughly the relaxation time $\tau_r = 1000$ s.

Discussion - Collision with alignment:

The inelastic collision that leads to alignment are not conceptually different from the inelastic collision where the droplet exchange direction. It is likely that they come from the same physical mechanism, the only difference being the velocity of the droplet before collision. More interesting is the persistent droplet collision: during these collision, one droplet is persistent, its velocity is almost constant, just like if it didn't feel the other droplet. There are two possible explanations for that: (i) the droplet swims under a high gradient of swollen micelles, then the addition of more swollen micelles by

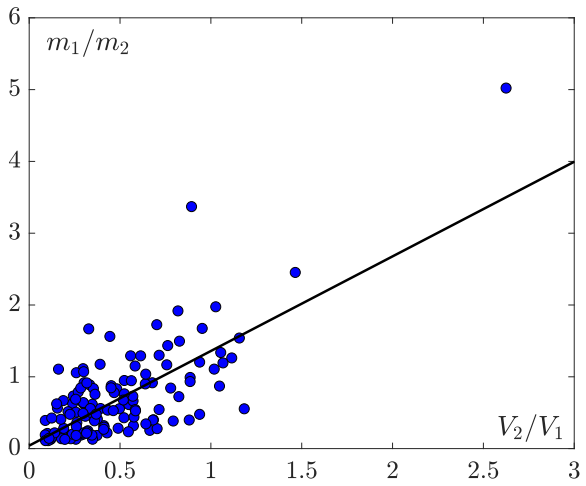

Figure 6.17: **Persistent collision - mass ratio:** mass ratio between two colliding droplets as a function of the inverse ratio of velocities, for all well-defined collision of an experiment at $d = 0.1$, and linear fit (black line).

the other droplet would not change much this gradient, thus not disturb the persistent droplet. However in that case, the persistent droplet should go very fast, but they are experimentally observed to be slower than other droplet. (ii) The channel behind the persistent droplet is locally saturated in swollen micelles - preventing completely the persistent droplet to turn back. This may happen in an area of the channel where collisions have happened multiple times. This analysis is coherent with the fact that the persistent droplet is slow (the channel being almost saturated, the droplet can only generate a small gradient to swim); but also with the fact that persistent droplets often appear after a lot of collisions - for instance at the end of a collision wave. To relate these persistent droplets with the inelastic collision from before, one can conceptualize these slow droplets with high swollen micelles concentration around them as particle with "higher mass". Then these persistent droplets move with higher momentum and kinetic energy than the other "normal" droplet: they are much harder to perturb, and thus to be turned back. To check this hypothesis, we compute the "mass ratio" of particles during a collision such that the momentum is conserved:

$$\frac{m_1}{m_2} = -\frac{V_2' - V_2}{V_1' - V_1}. \tag{6.19}$$

We can then check that during binary collision, relatively slower droplets indeed have a relatively heavier "mass", in Fig. 6.17, and that droplets of similar velocity have the same "mass" (ratio of order 1).

In the simulation we supposed the mass of the particles to be always the same, that is we neglect the persistent like collisions.

Running the simulation for typical parameters, $d = 0.2$ $\alpha = 0.6$ and $\lambda = 10^{-3}$, we typically obtain the spatio-temporal diagram presented in Fig. 6.18. Although the behaviour from one numerical run to another may vary, on the typical time scale of 10000 s, we observe that:

- At short time scale, the particles collide with each other and exchange direction.

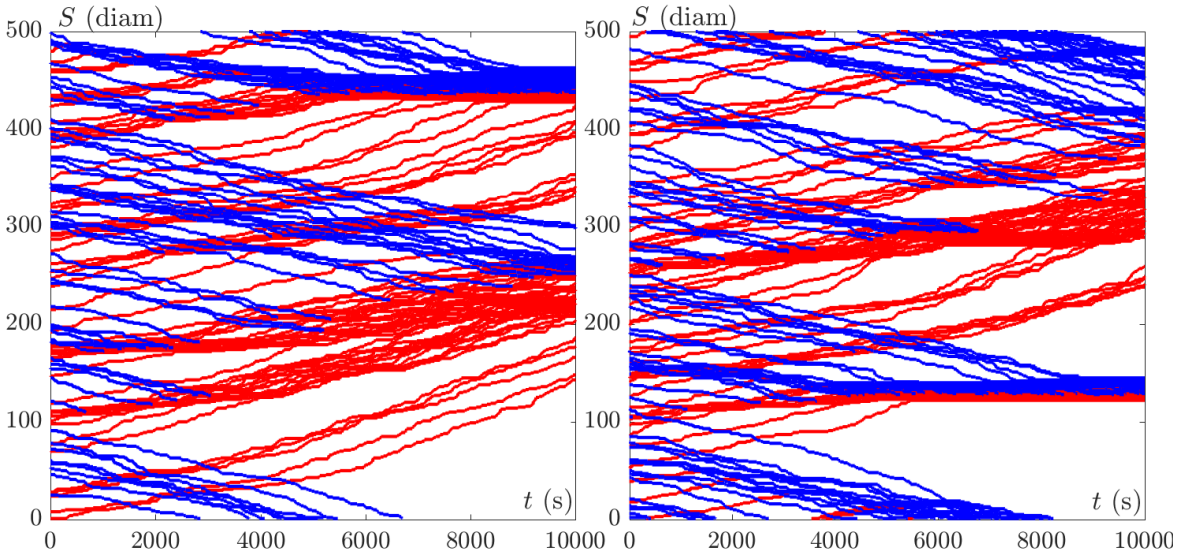

Figure 6.18: Spatio-temporal diagrams for two simulations with parameters $V_0/2a = 0.02$ s^{-1}, $dt = 1$ s, $d = 0.2$ $\alpha = 0.6$ and $\lambda = 10^{-3}$, which are parameters close to the experimental ones.

- Alignment happens in the system, nucleating trains.
- Trains absorb particles and grow.
- Two trains can meet each other, forming a clogg, a region where the particle do not move. The cloggs may evaporate.

These observations are very similar to the ones observed experimentally. In that sense, these simulations confirm that the collective behaviour of our swimming droplet may rise from our simple considerations about the binary interactions and the activity that have been implemented in our model. Note that over this time scale, the system does not seem to have reached a steady state, trains are still forming and growing, and other cloggs may appear when two trains collide. In other words, in the experiments, we are always in a transient regime. This could be expected given the very long relaxation time τ_r and the absence of noise to randomize the dynamics.

At this point, one may want to go a little further in the exploration of our model behaviour by exploring the parameter space α, λ and d (d, V_0 and dt play an equivalent role in our system), and try to catch the steady regime - if there is one, by running longer experiments.

6.2.4 Exploration of the parameter space

6.2.4.1 Observation of different regimes

For random initial conditions, we want to explore and characterize the behaviours of the system for different parameters α, λ and d. To characterize what we are observing, we introduce a few order parameters: the average velocity amplitude V_m, the magnetization (the average orientation) M and the participation ratio $R(t) = \frac{\langle D \rangle_g^2}{\langle D^2 \rangle_g}$, D being

the distance between two neighbor particles, and $\langle\cdot\rangle_g$ the average over all particle at a time t. V_m quantifies how fast the particles go (if $V_m = 0$, all particles are not moving, and if $V_m = 1$, all particles have their maximum velocity), M quantify how aligned they are (if $S = 0$, there is as many particles going upward than downward, and if $|S| = 1$, all particles go in the same direction), and R quantifies how homogeneous they are (if $R = 1$, all particles are at an equal distance from their neighbors, and if $R \to 0$, all particles are at the same place in space).

All simulations presented here are made for a number of particles $N = 100$, a number of time step $N_t = 10^5$, a density $d = 0.1$, a time step $dt = 1$ and a velocity $V_0 = 0.1$, which gives a ratio $\frac{1}{dV_0dt} = 100$ (which is similar to the experimental conditions).

Starting with quasi-elastic collision (α close to one), we observe basically a regime of binary, quasi-elastic collisions (see Fig. 6.19. In this regime, the particles loose almost no velocity after collision, and retrieve it almost immediately. Therefore, the average velocity is almost one. In such system, alignment is not observed; and the impulsion is conserved. The magnetization is constant, and fixed by the initial condition. For random initial direction, and for a large number of particles, this magnetization tends to zero as $\frac{1}{\sqrt{N_d}}$. The participation ratio R is non-zero, as the distance between the particles is homogeneous and does not vary much during the simulation.

Then if we decrease the restitution coefficient (Fig. 6.20), a different behaviour is observed. At the beginning, the behaviour is the same than for the quasi-elastic collision: the particles collide and exchange direction. Then we start to observe collisions that lead to alignment. These alignments nucleate the formation of trains: dense structures of aligned particles. These trains then interact with each other and fuse together, forming larger trains. A train is a region with high density, if there are only a few large trains in the system, it leaves large empty spaces between two trains, a characteristic of that is the decrease of the participation ratio. The magnetization tends to 1 (in absolute value) as one train finally takes over the whole experiment, until only one train remains: all the particles are aligned ($M = \pm 1$), and the whole system becomes homogeneous ($R \to$ constant). The train regime is thus a transient one that leads to a stable regime: the homogeneous globally aligned state.

Looking at system where the global aligned state develop faster (lower λ, which leads to more fluctuation in velocity), we can study more precisely its properties (Fig. 6.21). When the particles are all aligned ($M = 1$), there is no more collision, and thus the velocity has the time to relax towards the active velocity $V_m = 1$, even when the restitution coefficient α is low. The density becomes fixed, $R \to$ constant (no more interaction between particles, but there might still be statistical fluctuations).

Finally, throughout the low α experiment, but especially for very low relaxation time, we observe the apparition of cloggs: regions of the lattice where the particles are completely packed, and are blocked (Fig. 6.22). The participation ratio R then tends to zero, as particles are very localized. Although the particles are immobilized in these structures, they still have an orientation, and are constantly simultaneously trying to relax and collide with their neighbor particles, being unable to escape. These structures typically appear when two trains of comparable size collide. The two trains compete with each other inside the clogg, for a long time. One can observe the front between

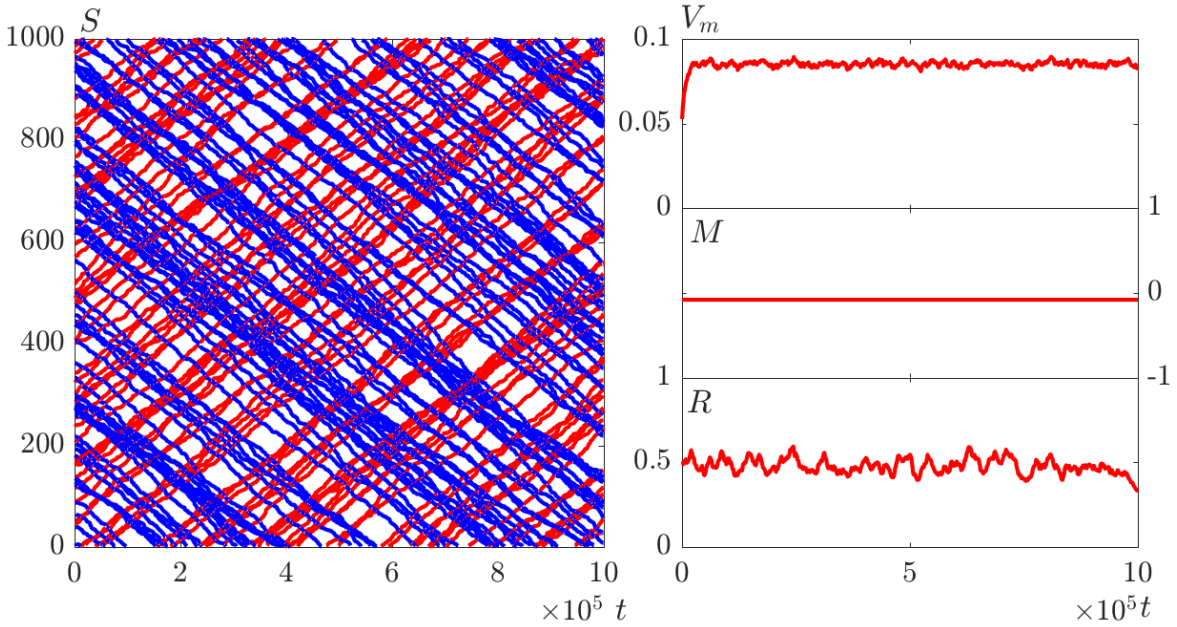

Figure 6.19: **Quasi-elastic regime:** Simulation for the parameters $\alpha = 0.8$, $\lambda = 0.01$. **Left:** Spatio-temporal diagram, the color stand for the sign of the velocity, red for positive and blue for negative. **Right:** temporal evolution of the parameters V_m, M and R.

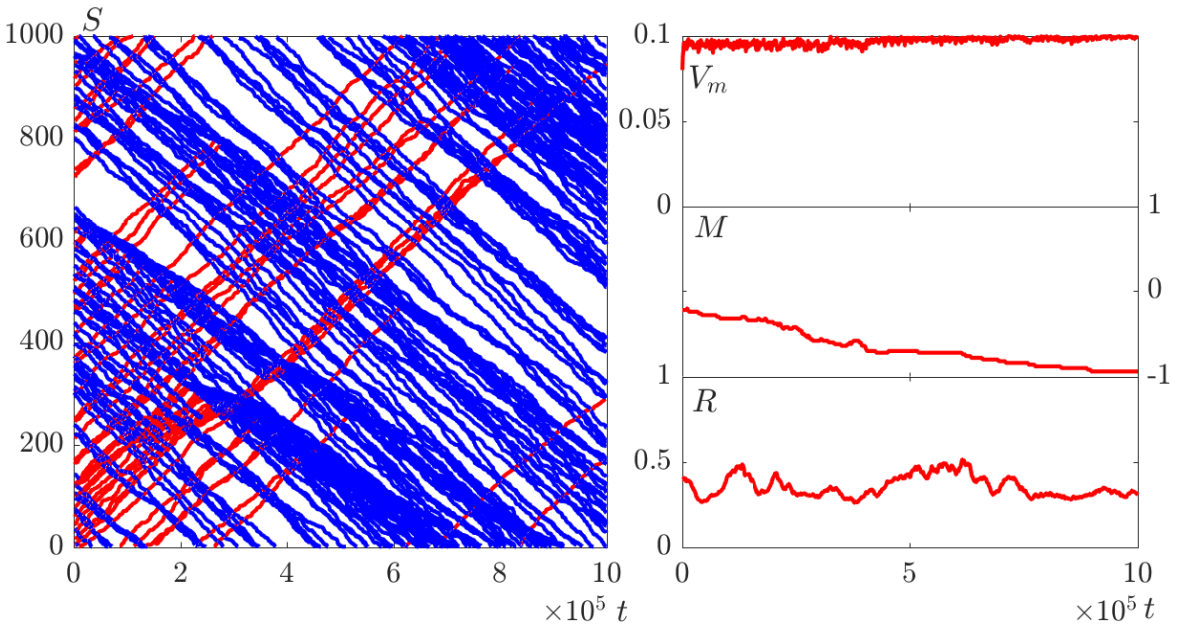

Figure 6.20: **Transient regime of train formation:** Simulation for the parameters $\alpha = 0.4$, $\lambda = 0.1$. Same representation than in Fig. 6.19.

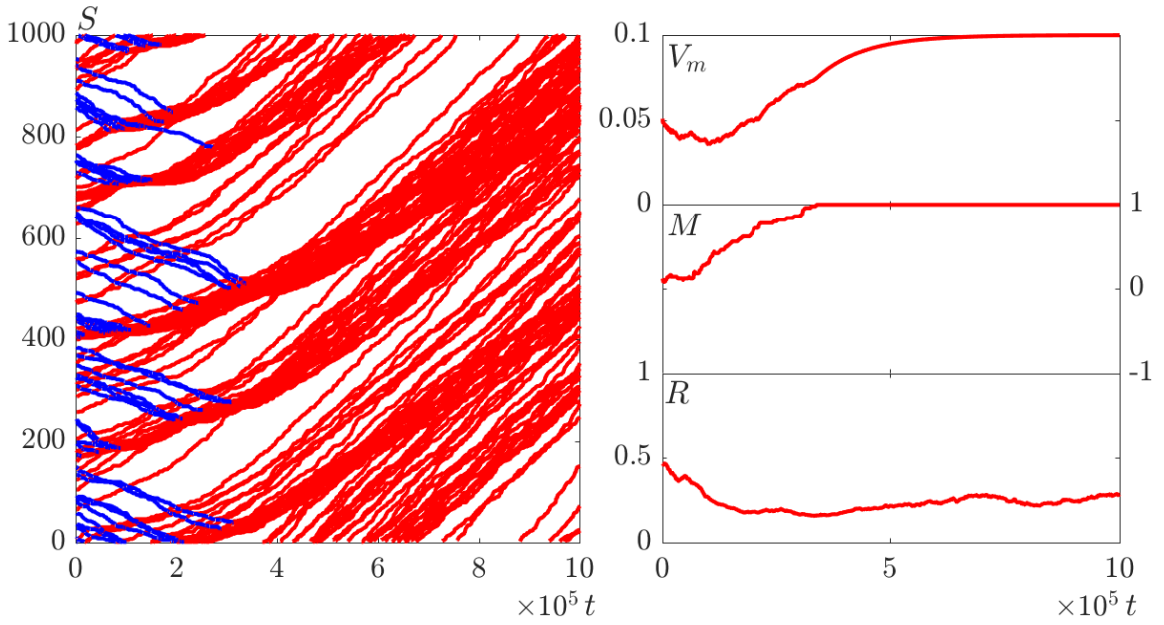

Figure 6.21: **Global alignment of the particles:** Simulation for the parameters $\alpha = 0.6$, $\lambda = 0.001$. Same representation than in Fig. 6.19.

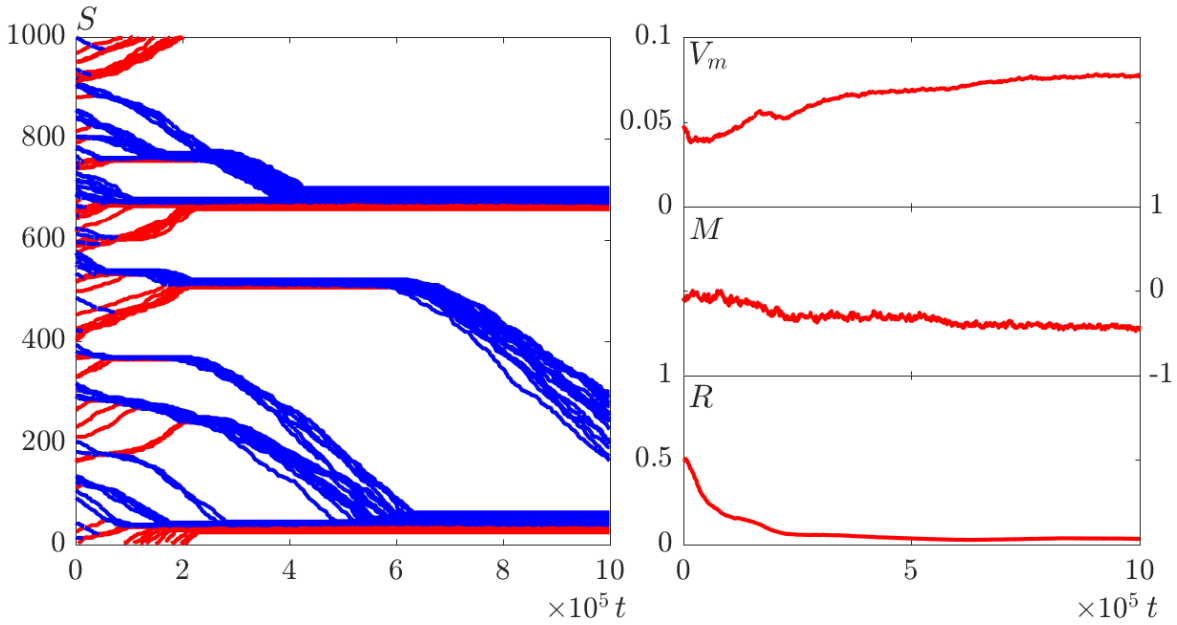

Figure 6.22: **Apparition of cloggs in the system:** Simulation for the parameters $\alpha = 0.2$, $\lambda = 0.001$. Same representation than in Fig. 6.19.

the two trains with time, it seems to follow some stochastic evolution. At some point, this front will reach one of the clogg end, then all the particles in the cloggs are aligned, and are freed in a train structure, that slowly relaxes toward a final aligned regime. Several cloggs can be observed at the same time.

6.2.4.2 Phase diagrams

The observed regimes in our system are: the quasi-elastic collision state, the train state, the globally aligned state, and the clogg state. Using the previous parameter, one can try to establish a "phase" diagram of these regimes, although whether these regimes are truly stable phases or not has yet to be discussed.

Regime	V_m	M	R
Quasi-elastic collision regime	$V_m \to$ constant - the constant being a compromise between the loss in velocity after collision, and the regained velocity during relaxation.	$M \to 0$ (it is actually of the order of $\frac{1}{\sqrt{N}}$ - fixed by the initial conditions.	R non zero - there is no large variation of density in the system.
Train regime (transient)	$V_m \to 1$ but is controlled by large events - it decreases fast during train fusion, and increase slowly inside trains, thus is very experiment dependent.	$\lvert M \rvert$ increases slowly - one train win over all others.	R - is experiment dependent.
Global alignment regime	$V_m = 1$ - all particles relaxed toward the active velocity	$M = 1$ - all particles are aligned	$R \to$ finite value - the spacing between particles does not evolve.
Clogg regime (transient)	$V_m \neq 0$, but small - the particles are blocked and constantly collide with each other.	M is small, but dynamic - a collision front separate two sizes of the clogg that go in opposite direction.	R is small - particles are condensed in cloggs.

Table 6.1: Summary of the different regimes and their characteristic parameters.

Table 6.1 summarize how the quantities V_m, M and R behave in the different phases. Using these observations, we can plot these variables as function of λ and α in Fig. 6.23, for a dilution of $d = 0.1$.

Fig. 6.23(a) shows the value of the average velocity: $V_m = 0$ (blue) corresponds to the clogg regime. $V_m = 1$ (red) corresponds to global alignment regime or quasi-elastic

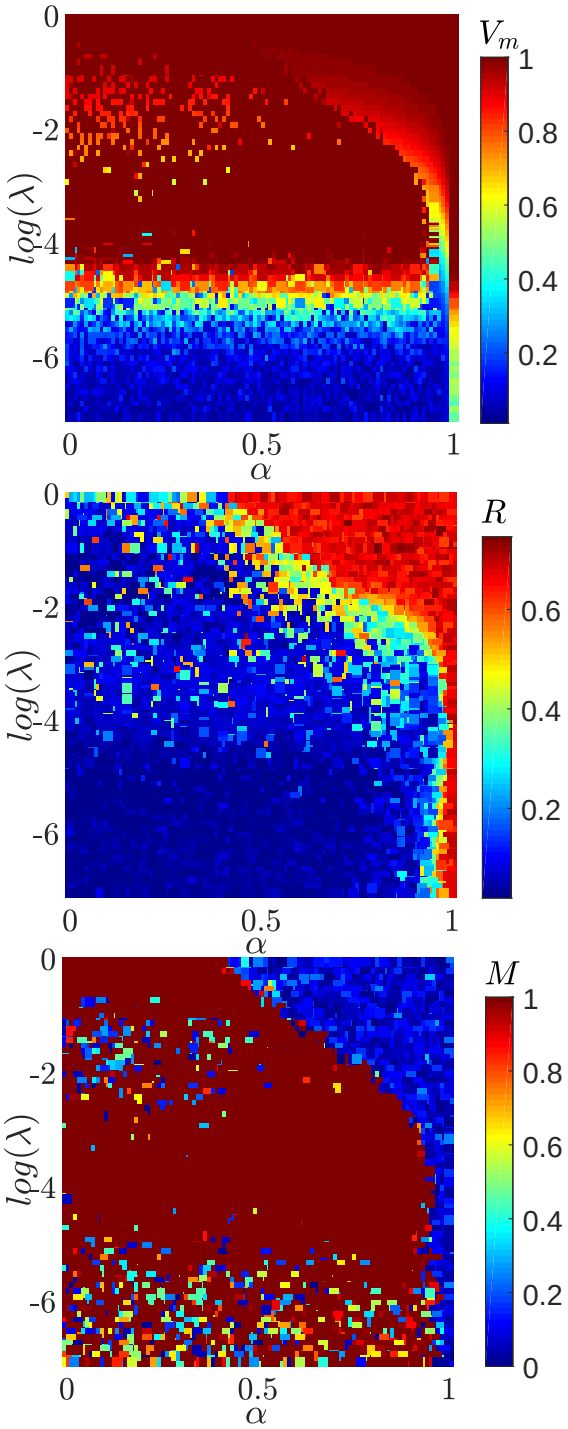

Figure 6.23: **Phase diagram computed from the system variable:** Top - average velocity at the end of the experiment ($V_m = 0$ is blue and $V_m = 1$ is red). Middle - Participation ratio at the end of the experiment ($R = 0$ is blue and $R \to 1$ is red). Bottom - magnetization at the end of the experiment ($M = 0$ is blue and $M = 1$ is red).

regimes, intermediary colors may correspond to a transient regime that had not yet reached a steady state (trains, intermediary cloggs), or to a quasi-elastic regimes whose velocity is not one.
Fig. 6.23(b) Shows the value of the magnetization: $M = 0$ (blue) corresponds to the not globally aligned regimes, like the cloggs and the quasi-elastic regime, $M = 1$ (red) corresponds to the global alignment regime, intermediary colors correspond to transient regime such as not balanced clogg, or train regimes.
Fig. 6.23(c) shows the participation ratio: high R (blue) corresponds to very homogeneous regimes such as the quasi-elastic regime, intermediary R (blue-green) corresponds to a global alignment, low R (light green) corresponds to locally dense domains that leave a lot of empty space around it, such as cloggs or large trains.

Using all the above consideration, one may draw a schematic "phase diagram" of the different regimes, in the two parameter space $\{\alpha, \lambda\}$, Fig. 6.24, for a number of particles $N = 100$, a number of time step $N_t = 10^5$, a velocity $V_0 = 1$ and a density $d = 0.01$.

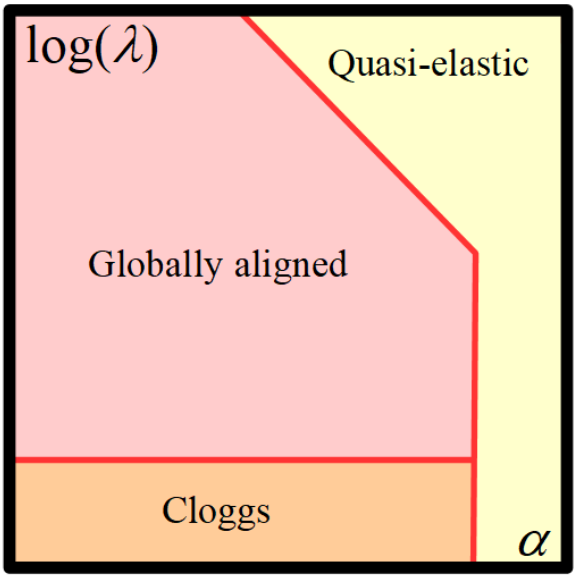

Figure 6.24: **Schematic phase diagram:** we observe three long lasting regime, the quasi-elastic regime for high α, the globally aligned regime, for low α and high λ, and the cloggs, for low α and low λ.

Interpretation:
When λ is very small, the particles never have time to retrieve their velocity. As a consequence, they will be slower in the dense region, where they collide a lot. Particles spend more time in the dense area, making them even denser, until particles are blocked, creating cloggs. This is the bottom area of the phase diagram. This clogg phase could be interpreted in term of Motility Induced Phase Separation (MIPS) [151], which is a widely studied phenomena in the field of active mater. The lower the λ parameter is, the longer the cloggs last, until we can no longer see them break. It is difficult to say if these cloggs are always a transient regime, or if they become a stable phase at some low enough λ.

When there is disparity of velocity in the system, collision may lead to alignment, creating trains. Such trains absorb other particles and grow, making dense aligned structures that interact with each other. These trains are only transient regimes however, and one train is always observed to win over the other, leading to a globally aligned system. This is the upper left part of the diagram. In this region, transient cloggs can also appear, always transient, but this contribute to decrease the average velocity and magnetization of the system, which corresponds to the blue dot observed in the V_m and M phase diagrams, in the middle of the globally aligned regime. This regime forms a steady phase: as there is no noise, nothing in our system can undo the alignment, and thus the aligned phase is stable.

Finally, when α is large, the collisions are quasi-elastic; particles collide without aligning. One could still discuss on the stability of such regime, indeed, the system is stochastic, thus a local heterogeneity in the system could lead to aligning collisions. As said before, nothing in the system can undo alignment, thus each aligning collision increases effectively and definitively the whole system alignment. One can then wonder if after waiting for a long enough time, the system will evolve into trains, then to a globally aligned regime. This is definitively false for $\alpha = 1$, as a system with only elastic collision will never lead to alignment.

Discussion on the influence of the density : when the density decreases, it is more difficult to form cloggs: the clogg regime happens for lower λ. The increased spacing between particle makes it also easier for them to relax toward activity: aligning collision in the system are more unlikely, and thus the transition between the globally aligned and elastic regime will happen for lower α. The global shape of the phase diagram is otherwise unaltered.

6.2.5 Some theoretical considerations

In our experimental system, as well as in our simulation system, we observe a variety of transient phases and two "long-lasting" phases which are the quasi-elastic regimes and the global alignment. The initial conditions being misaligned (random), the most striking effect is the emergence of a globally aligned phase. From the implementation of the simulation, we know that these behaviours emerge from very simple rules at the scale of one active particle, and from binary collisions. One collision may lead to alignment, for certain sets of velocities prior to collision, and parameter α (Fig. 6.16). Yet this consideration does not explicit how the system reaches such a collision. We are still lacking a set of rules, or at least a physical understanding that would help us predict why one system would tend toward a global alignment state, or a quasi-elastic state. In order to answer this question, we present in the following two simple analytic approaches that highlight the physical phenomenon leading - or not - a system toward alignment.

6.2.5.1 First approach: two particles system

A first approach consists in investigating the case of two particles, n_1 initially starting with a velocity $V_1 > 0$ and n_2 with a velocity $V_2 < 0$, on a periodic lattice (Fig. 6.25). The particles will collide with each other as long as they do not reach an aligned state.

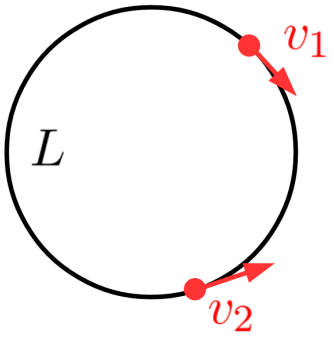

Figure 6.25: **Two particles case:** To particle moving at velocities v_1 and v_2 on a periodic 1D network of size L.

$U = |\frac{V_1+V_2}{2V_0}|$ is the velocity of the center of mass made dimensionless by the active velocity V_0, and we define dU the difference in velocities also dimensionless such as $dU = |\frac{V_1-V_2}{2V_0}|$. In the referential of the lab:

$$V_1 = sV_0(U + dU), \tag{6.20}$$
$$V_2 = sV_0(U - dU), \tag{6.21}$$

where s is the direction of the first particle, which changes after each collision. This convention allows us to conveniently keep $dU > 0$.

The purpose of this section is to predict the behaviour of two particles at long time: would they align or would they collide forever? We consider a continuous space and a discrete time of step dt.

In the absence of collision: as long as the particles are not aligned (n_1 has a direction s and n_2 has a direction $-s$), at each time step:

$$V_1(t + dt) = V_1(t) + \lambda(sV_0 - V_1(t)), \tag{6.22}$$
$$V_2(t + dt) = V_2(t) + \lambda(-sV_0 - V_2(t)), \tag{6.23}$$

where λ is as defined before, the relaxation rate toward activity. In the referential of the center of mass, it gives:

$$dU(t + dt) = (1 - \lambda)dU(t) + \lambda, \tag{6.24}$$
$$U(t + dt) = (1 - \lambda)U(t). \tag{6.25}$$

After n time iteration:

$$dU(t + ndt) - 1 = (1 - \lambda)^n(dU(t) - 1), \tag{6.26}$$
$$U(t + ndt) = (1 - \lambda)^n U(t). \tag{6.27}$$

The position of the particle with time is:

$$x_1(t + ndt) = x_1(t) + dtV_0 \times \sum_{i=1}^{n} U(t + idt) + sdU(t + idt), \tag{6.28}$$

$$x_2(t + ndt) = x_2(t) + dtV_0 \times \sum_{i=1}^{n} U(t + idt) - sdU(t + idt). \tag{6.29}$$

$$\tag{6.30}$$

If the periodic lattice has a size L, right after the collision the two particles are at a distance L from each other (note that L is signed). Then we want to know the time $n_c dt$ needed before the next collision, and their velocity at the time of collision:

$$L = s(x_1(t + n_c dt) - x_1(t)) - s(x_2(t + n_c dt) - x_2(t)), \tag{6.31}$$

$$= 2dtV_0 \sum_{i=1}^{n_c} dU(t + idt), \tag{6.32}$$

$$= 2dtV_0 \sum_{i=1}^{n_c} (1-\lambda)^i (dU(t) - 1) + 1), \tag{6.33}$$

$$= 2dtV_0 * \Big(\frac{1-(1-\lambda)^{n_c}}{\lambda} (dU(t) - 1) + n_c \Big). \tag{6.34}$$

This last equation is non trivial, but gives n_c, the time between two collisions. We are more interested in a recursive form in dU of this equation. Using equation 6.26, we get:

$$n_c = \Big(\frac{L}{2dtV_0} + \frac{1}{\lambda} (dU(t + n_c dt) - dU(t)) \Big), \tag{6.35}$$

which injected in equation (6.26), gives an equation between the velocity $dU(t)$ and the velocity $dU(t + n_c dt)$, in the absence of collision:

$$dU(t + n_c dt) - 1 = \exp\Big[\frac{L}{2dtV_0} + \frac{1}{\lambda} (dU(t + n_c dt) - dU(t)) \ln(1-\lambda) \Big] (dU(t) - 1). \tag{6.36}$$

Rewritten cleverly, this gives:

$$\frac{\ln(1-\lambda)}{\lambda} \Big(dU(t + n_c dt) - 1 \Big) \exp\Big(- \frac{\ln(1-\lambda)}{\lambda} (dU(t + n_c dt) - 1) \Big) \tag{6.37}$$

$$= \frac{\ln(1-\lambda)}{\lambda} \Big(dU(t) - 1 \Big) \exp\Big(- \frac{\ln(1-\lambda)}{\lambda} (dU(t) - 1 - \frac{L\lambda}{2V_0 dt}) \Big) \tag{6.38}$$

Once again, this equation of the form $x \exp(x) = y$ have a numerical solution using the Lambert W function: $x = W(y)$. Then:

$$dU(t + n_c dt) = 1 - \frac{\lambda}{\ln(1-\lambda)} W\Big\{ \frac{\ln(1-\lambda)}{\lambda} (dU(t) - 1) \exp\Big[- \frac{\ln(1-\lambda)}{\lambda} (dU(t) - 1 - \frac{L\lambda}{2V_0 dt}) \Big] \Big\}. \tag{6.39}$$

We finally have an analytic recurrence equation for dU in the absence of collision: $dU(t + n_c dt) = f(dU(t), L, \lambda)$. Note that this function f is an increasing function, but also that $f(x) \geqslant x$ (physically, in the absence of alignment, the two particles velocities increase toward their active velocities, with different sign, thus dU grows.)

We use a similar reasoning for U:

$$\begin{aligned}U(t+n_c dt) &= (1-\lambda)^{n_c} U(t)\\ &= \frac{dU(t+n_c dt)-1}{dU(t)-1}U(t)\\ &= -\frac{U(t)}{dU(t)-1}\frac{\lambda}{\ln(1-\lambda)}\\ &\quad * W\Big\{-\exp(\frac{d\ln(1-\lambda)}{2dt}) * \frac{\ln(1-\lambda)}{\lambda}(dU(t)-1)\exp\Big[-\frac{\ln(1-\lambda)}{\lambda}(dU(t)-1)\Big]\Big\}\end{aligned}$$

Which is an equation of the form $U(t+n_c dt) = \frac{1-f(dU(t),d,\lambda)}{1-dU(t)}U(t)$.

During a collision: After the first collision which occurs at t^-, the two particles exchange their velocity with inelasticity. In the referential of the center of mass:

$$U(t^+) = U(t^-), \tag{6.40}$$
$$dU(t^+) = \alpha dU(t^-). \tag{6.41}$$

After many collisions: We define two sequences U_k and dU_k which stand for the velocities right after the k^{th} collision. The relations defining these sequences are:

$$\begin{aligned}U_{k+1} &= \frac{1-f(dU_k,d,\lambda)}{1-dU_k}U_k,\\ dU_{k+1} &= \alpha f(dU_k,d,\lambda).\end{aligned}$$

where f is a numerical function that uses the Lambert W function, as defined before. Plotting $\alpha f(x)$ with x between 0 and 1 for $\alpha = 0.8$ and $\lambda = 0.01$ in Fig. 6.26, we see that this function can cross the identity function.

In this case, the sequence dU is convergent: in the absence of alignment, the difference of velocity between the two particles right after a collision reaches a constant value after a certain number of collisions. Plotting the same curve for different α (Fig. 6.27(a)), and different λ (Fig. 6.27(b)), we can make a few observations.

- If $\lambda = 1$ (instantaneous relaxation), then the velocity of the particle right before the collision is always $\pm V_0$, and thus right after the collision, their velocity is $\pm\alpha V_0$. $U_k = 0$ and $dU_k = \alpha V_0$.

- If $\lambda = 0$ and $\alpha \neq 1$, there is no relaxation, the particles loose velocity after each collision, and provided that there is no alignment after the first collision, the velocity of the particles tends to zero. $U_k \to 0$ and $dU_k \to 0$.

- If $\lambda \neq 1$ and $\alpha = 0$, the particles align after the first collision $dU_1 = 0$ and $U_1 = V_0$.

- If $\lambda \neq 1$ and $\alpha = 1$, the particles never loose any velocity. There is no alignment. Both particles velocities go toward $\pm V_0$, exchanging sign after each collision.

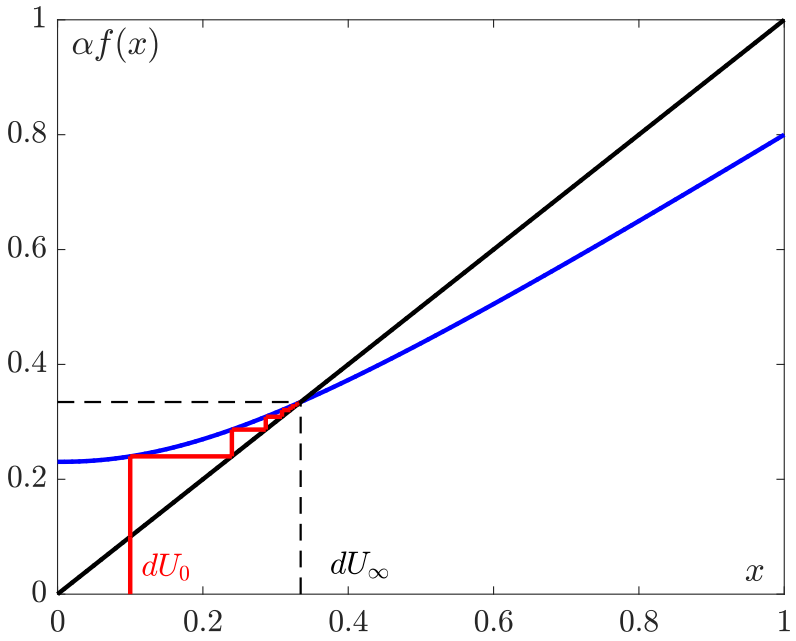

Figure 6.26: function $\alpha f(x)$ (in blue) for $\alpha = 0.8$, $\lambda = 10^{-2}$ and $L = 10$. In black, the identity function. In red the recurrence of dU from dU_0 to dU_∞.

- If $0 < \lambda < 1$ and $0 < \alpha < 1$: the particles loose velocity after each collision, and eventually regain some of it by relaxing between two collisions. Providing there is no alignment, this converges [5] toward a certain dU_∞ which is the solution of the equation $f(x) = x$, and can be computed numerically. These solutions depend on α, λ and L. Fig. 6.28 gives the evolution of dU_∞ with λ and α, for $L = 10$.

Interestingly, the curves of iso-value of dU_∞ share some similarities with the boundary separating the disordered from the globally aligned phase, in the phase diagram computed previously (Fig. 6.23). We observe basically that the value dU_∞ increases with α and λ. This statement is quite intuitive as if α is low, the particles loose a lot of velocity after collision, and if λ is low, it doesn't have time to recover much velocity before the next collision.

If one now looks at the evolution of the sequence U_k, because $f(x) > x$, $\frac{1-f(x)}{1-x} < 1$, thus the sequence U_k is decreasing after each collision. Actually, because $dU \to dU_\infty$ such that $\alpha f(dU_\infty) = dU_\infty$, $\frac{U_{k+1}}{U_k} \to \frac{1-\frac{1}{\alpha}dU_\infty}{1-dU_\infty} < 1$, thus the sequence U_k tend to zero. Knowing the limit of $dU_k \to dU_\infty$ and $U_k \to 0$, we know, in the absence of alignment, the final state of the system.

We have yet to discuss the conditions that lead to this "alignment" event that changes the equations: as soon as there is alignment, both particles go in the same direction and stop colliding. Provided that $\lambda \neq 0$, both velocities then relax toward the active velocity $\pm V_0$, of the same sign. The prediction of this alignment event is the crucial information we are lacking in order to be able to predict beforehand the final state of

[5] This statement is purely the product of an observation, we have not demonstrated that this sequence converges for all α and λ.

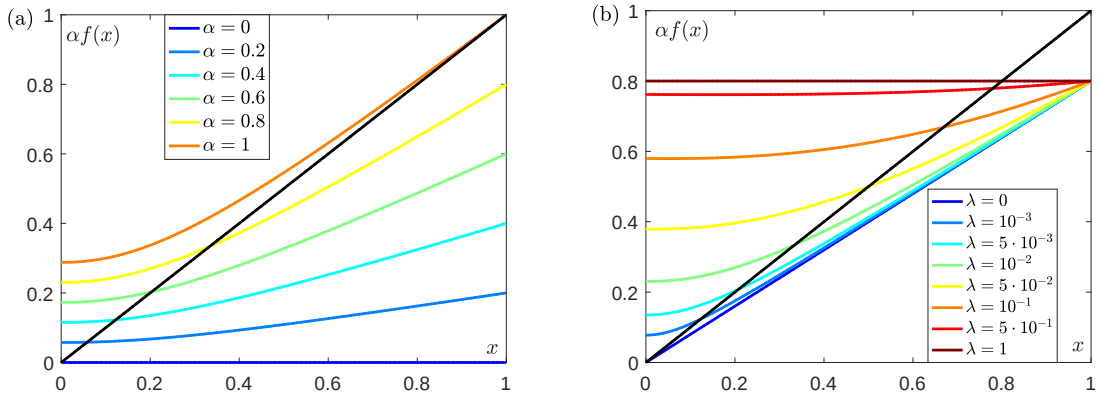

Figure 6.27: (a) Evolution of the function $\alpha f(x)$ for different values of α, at $\lambda = 0.01$ and $L = 10$. (b) Evolution of the function $\alpha f(x)$ for different values of λ, for $\alpha = 0.8$ and $L = 10$.

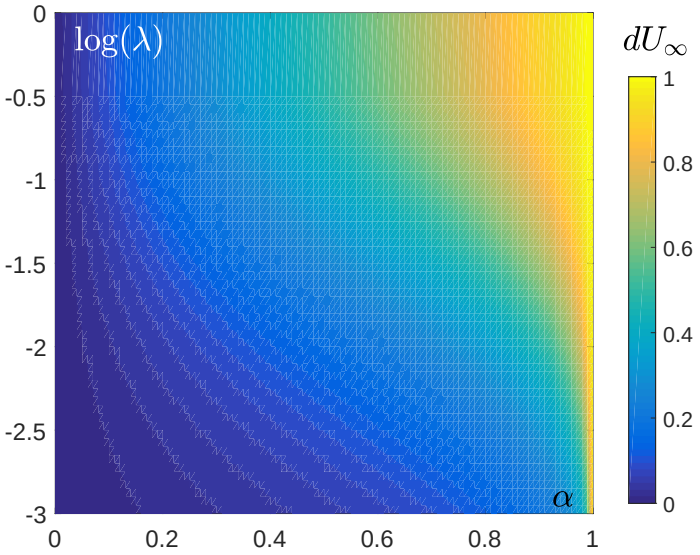

Figure 6.28: Value of dU_{inf} computed numerically as a function of the two parameters α and λ, for $V_0 = 1$ and $L = 10$.

the system.

The alignment or non-alignment of particles can be translated in terms of the comparison between the velocity of the center of mass, and that of the difference of velocity, or in term of their ratio. If we note Q_k the sequence of the ratio of U_k and dU_k: $Q_k = \frac{dU_k}{U_k}$ (Fig. 6.16 illustrates the following rules);

Non alignment $\Leftrightarrow U_k < dU_k \Leftrightarrow Q_k > 1$

Alignment $\Leftrightarrow U_k > dU_k \Leftrightarrow Q_k < 1$

Then two non-aligned particles are aligned by the collision k if $Q_k < 1$. The sequence Q_k does not have a simple recurrence law - it depends on dU_k in a highly non trivial way:

$$Q_{k+1} = \frac{\alpha f(dU_k)(1 - dU_k)}{dU_k(1 - f(dU_k))} Q_k \tag{6.42}$$

If we note $g(x) = \frac{\alpha f(x)(1-x)}{x(1-f(x))}$, we can plot this function on the same graph as $f(x)$ (Fig. 6.29). The evolution of dU after each collision follows the function f (in blue). Like before, for any initial condition of dU_0, we finds that dU converges toward a finite, non-zero value dU_∞. Each iteration of dU is represented in red continuous lines. Then to each dU also correspond a value of $g(dU) = \frac{Q_{k+1}}{Q_k}$, represented in red dashed lines. Then at each iteration, we know the value of $\frac{Q_{k+1}}{Q_k}$.

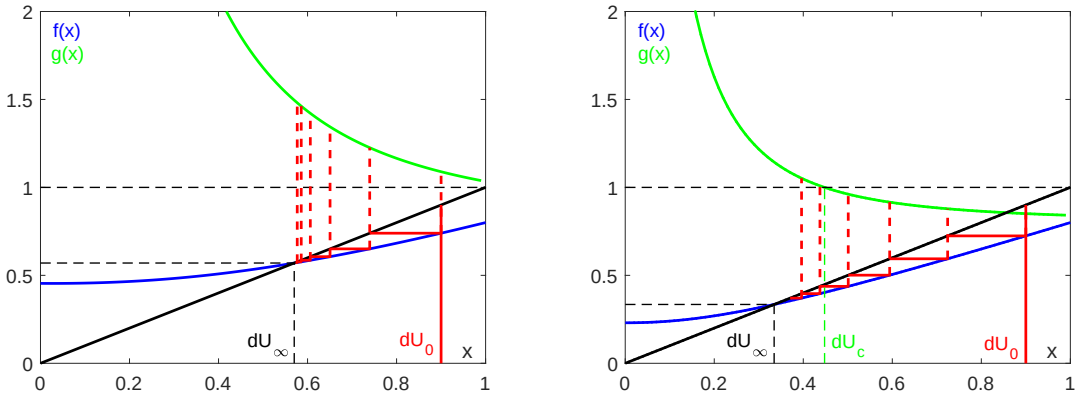

Figure 6.29: function f(x) (in blue) and g(x) (in green) (a) for $\alpha = 0.8$, $\lambda = 0.05$ and $L = 10$ (b) for $\alpha = 0.8$, $\lambda = 0.01$ and $L = 10$. In black, the identity function. In red the recurrence of dU from dU_0 to dU_∞. In (b) $g(x)$ has value lower than one for $dU > dU_c$.

Knowing that $Q_0 > 1$ (the particles are initially not aligned), we can pinpoint some cases where the successive collisions cannot lead to alignment:

- if $dU_0 < dU_\infty$: dU_k is an increasing sequence, while U_k is a decreasing one: the successive collisions cannot lead to $U_k > dU_k$.
- if $g(x) > 1$ for all x between 0 and 1; then the sequence Q_k is increasing, and being initially larger than unity, it cannot lead to a $Q_k < 1$.

Then two necessary (but not sufficient) conditions to have alignment are that $dU_0 > dU_\infty$ and that g(x) goes smaller than unity. We call dU_c the value of dU such as $g(dU_c) = 1$, when it exists between 0 and 1. We can compute numerically this dU_c as a function of λ and α (Fig. 6.30).

We observe that this dU_c exists ($g(x)$ has value under one) for low λ and low α.

Phrased differently, the existence of this dU_c means that for certain dU, the sequence U_k decreases slower that the sequence dU_k, thus there is a chance to attain $U_k > dU_k$. However, this "chance" depends on the initial value of the two sequences. For a given function g (λ, α and L fixed), with $dU_0 > dU_c$, the function $\frac{Q_{k+1}}{Q_k}$ decreases until $dU_k = dU_c$. Thus the lowest Q_k will be attained right after the k_c collision, such as $dU_{k_c} > dU_c$ and $dU_{k_c+1} < dU_c$. We define $A_c(dU_0) = \prod_{k=0}^{k_c} \frac{Q_{k+1}}{Q_k}$ such that $Q_{k_c}{=}A_c(dU_0)Q_0$ (Note graphically that this coefficient depends on dU_0, as the number of collision depends on dU_0, but is maximum for $dU_0 = 1$). Then $U_{k_c} > dU_{k_c}$ (*i.e.* $Q_{k_c} < 1$) means for the initial conditions that $U_0 > A_c(dU_0)dU_0$. It is not possible to always impose such rule.

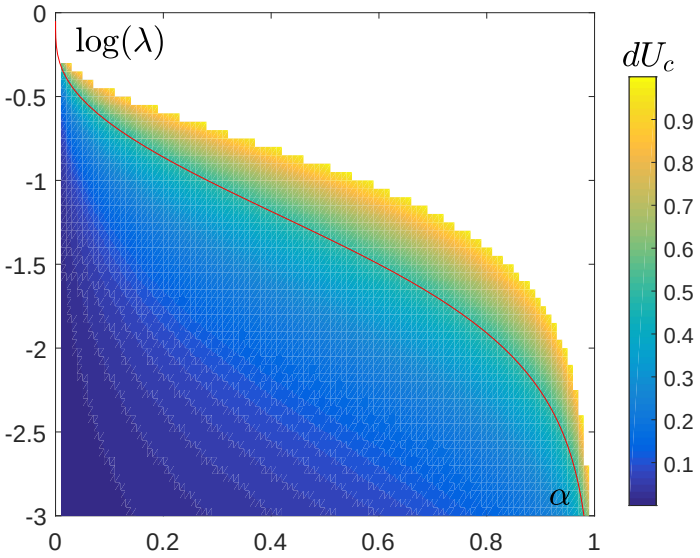

Figure 6.30: Value of dU_c computed numerically as a function of the two parameters α and λ. White color means that dU_c does not exist between 0 and 1. In red is the curve $dU_c = 0.5$.

Indeed, we restricted our velocity to be smaller than the active velocity, this means that $U_0 < 1 - dU_0$. Thus we can find $U_0 > A_c dU_0$ only if $A_c(dU_0)dU_0 < 1 - dU_0$, that is if $(A_c(dU_0) + 1)dU_0 < 1$. Observing a number of experiments, we observe that the function $(A_c(dU_0) + 1)dU_0$ is an increasing function in dU_0, thus that its smallest value is at dU_c. Then the last, but not least, condition that allows the system to have alignment, for at least some value of U_0 and dU_0 is that $(A_c(dU_c) + 1)dU_c < 1$. Note that as $A_c(dU_c) = 1$, then the condition rewrites very simply as $dU_c < 0.5$.

The critical curve that separate the two regimes "possible alignment", and "no alignment" is then $dU_c = 0.5$, with $g(dU_c) = 1$. After some arrangement, this gives us an equation between α, λ and L:

$$\alpha = -1 + \frac{1}{f(x = \frac{1}{2}, \lambda, L)} \tag{6.43}$$

We can inverse the f function, to get a more explicit relation between α, λ and L. We get:

$$\ln(1-\lambda)\Big(\frac{1}{\lambda} - \frac{\alpha+1}{\alpha-1}\frac{L}{V_0\Delta t}\Big) = -2\frac{\alpha+1}{\alpha-1}\ln\Big(\frac{2\alpha}{\alpha+1}\Big) \tag{6.44}$$

This curve is plotted in Fig. 6.31. $dU_c < 0.5$ means that I can chose $dU_0 = 0.5 > dU_c$, and find a U_0 close enough but smaller than dU_0, $U_0 = 0.5 - \epsilon$ such that $U_0 > A_c(dU_0)dU_0$. Rewritten as $\epsilon < 0.5(1 - A_c(dU_0))$, we find that since $A_c(dU_0) < 1$, this is always possible. We can study the asymptotic behaviour of this relation:

- $\alpha \to 0$: then $\ln(1-\lambda)\Big(\frac{1}{\lambda} + \frac{L}{V_0\Delta t}\Big) = 2\ln(2\alpha)$. We see graphically that $\ln(\lambda) \underset{\alpha\to 0}{\longrightarrow} 0$, which corresponds to $\lambda \underset{\alpha\to 0}{\longrightarrow} 1$, and thus to $\ln(1-\lambda) \underset{\alpha\to 0}{\longrightarrow} -\infty$. Then more precisely λ goes to 1 as:

$$\lambda \underset{\alpha\to 0}{\longrightarrow} 1 - \exp\Big(\frac{2}{1 + \frac{L}{V_0\Delta t}}\ln(2\alpha)\Big). \tag{6.45}$$

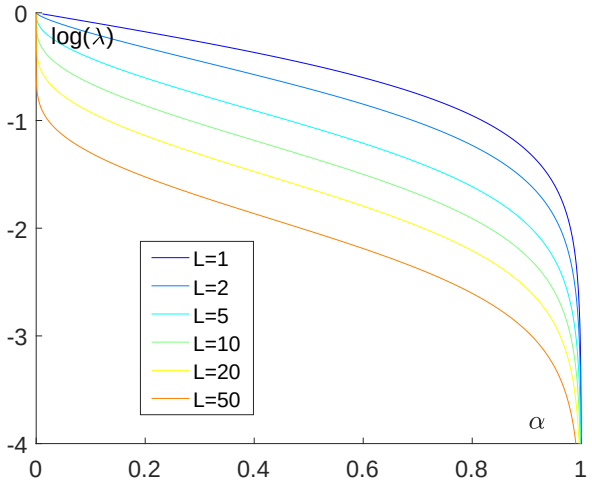

Figure 6.31: Curve separating the two regimes alignment and non alignment depending on the parameters α and λ, and for different L, for the two particles system.

- $\alpha \rightarrow 1$: graphically $\ln(\lambda) \underset{\alpha\to 1}{\longrightarrow} -\infty$, which means that $\lambda \underset{\alpha\to 1}{\longrightarrow} 0$, and $\ln(1-\lambda) \underset{\alpha\to 1}{\longrightarrow} -\lambda$. If we note $\alpha = 1-\epsilon$, then the equation (6.44) can be simplified as $1 + \lambda\frac{2-\epsilon}{\epsilon}\frac{L}{V_0\Delta t} = (2-\epsilon)$, thus:

$$\lambda \underset{\alpha\to 1}{\longrightarrow} \frac{V_0\Delta t}{2L}(1-\alpha). \tag{6.46}$$

- L $\rightarrow +\infty$: then for $\lambda \neq 0$, the equation (6.44) simplifies as:

$$\lambda \underset{L\to\infty}{\longrightarrow} 1 - \exp\Big(\frac{2V_0\Delta t}{L}\ln(\frac{2\alpha}{\alpha+1})\Big) \tag{6.47}$$

$$\underset{L\to\infty}{\longrightarrow} 0 \tag{6.48}$$

Discussion

The above analysis gives us insight on what conditions lead to alignment: alignment asks for a combination of the density, $\frac{1}{L}$, the inelastic coefficient α and the relaxation λ such that the system is "not too elastic", and "relax slowly enough" or on a "long enough distance", as described by the critical curve equation (6.44). But that is not enough - alignment can only happen for certain initial velocities (for instance, if $U_0 = 0$, the system will never reach alignment). Thus, the final behaviour of our system has a strong dependency on the initial condition.

How is this relevant to the system with many particles? Fig. 6.32 shows the superposition of the critical curve and the phase diagram obtained by measuring the final magnetization in the simulation (the other phase diagram obtained using V_m and R could have been also used). For $\alpha < 0.9$, the critical curves greatly underestimate the critical λ at which alignment occurs. For our numerical system, alignment happens for a wider range of λ, at the expense of the quasi-elastic region. There is a simple explanation for that. The main difference between the two particles system and the many particle system is that in the two particles system, the distance between the two

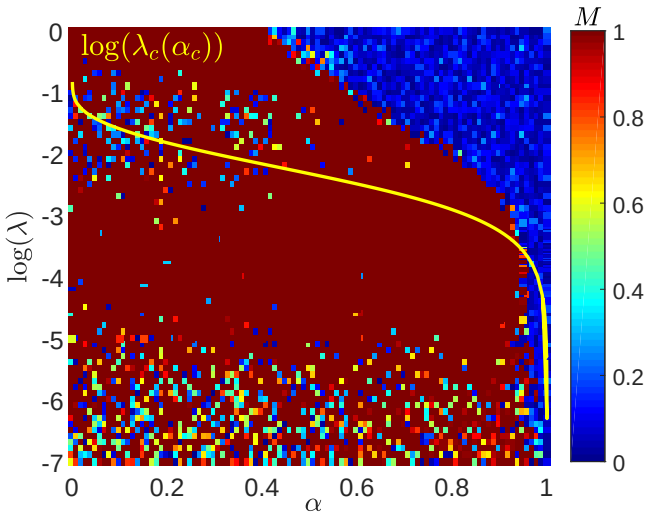

Figure 6.32: **Comparison between the simulations and the two particles system phase separation:** Phase diagram obtain through the simulations by considering the value of the magnetization and the critical curve computed from analytically solving the two particles case (yellow).

particles after collision L is fixed. In the many particle system, the particles change their collision partner after each collision, and the distance also changes. We saw in this section that the alignment rule depended on L: more fluctuation in the distance between particles then mean more opportunity for alignment events. This is particularly visible for $\lambda = 1$ ($\log(\lambda) = 0$): (1) in the two particles system, $\lambda = 1$ means that at collision, the particles may loose some velocity, but at the next time step, they will instantaneously relax toward the active velocity. The two particles always meet symmetrically, with velocities $+V_0$ and $-V_0$, thus alignment never happens. (2) In the many particle system, alignment may still happen if the particles undergo successive collisions, that is to say if the particles do not have the one necessary time step (in our implementation of the model) to relax toward the active velocity. The fact that the transition between the quasi-elastic and globally aligned regimes in the phase diagram is not $\alpha_c \to 0$ when $\lambda_c \to 1$ is thus intrinsically linked with the discrete time implementation of our model.

Another phenomenon absent from the two particles model is of course the formation of cloggs.

At this point, we should gather a few remarks:

- The behaviour of the system depends on the number of particles (more particles seem to favor alignment).
- The behaviour of the system also depends on the observation time - some transient long lasting regime are at play in the system: the cloggs and the trains.
- Because of the absence of noise in the system, only alignment events may happen, there is no source of misalignment.

Then stochastically, in an infinite system with an infinite number of combinations of initial conditions, and if we wait long enough, we could always reach an L between

two droplets small enough so that with the α and λ parameters of the experiment, a collision leads to alignment. This alignment may nucleate a train, which itself will relax toward the globally aligned phase. One may then wonder about the stability of the regime observed, in particular the stability of the quasi-elastic regime, where a train nucleation could happen stochastically even after a long time, and leads to the global alignment regime.

6.2.5.2 Second approach: Continuous model

During his Post-Doc at Gulliver, Pierre Illien worked on the development of the model for more robust and long-lasting simulation, and considering continuous time. I will summarize part of his work which is strongly related to what I have exposed. In his work, the relaxation toward activity is then written:

$$V_i(t) = s_i V_0 + \Big(V_c^i - s_i V_0\Big) \exp -\gamma(t - t_{c,i}), \tag{6.49}$$

where $t_{c,i}$ is the time of the last collision, and V_c^i the velocity right after this last collision. γ is related to the coefficient λ that we use in the discrete model: $\gamma = -\frac{\ln(1-\lambda)}{dt}$. Then:

$$\ln(\lambda) \to -\infty \Leftrightarrow \lambda \to 0 \Leftrightarrow \gamma \to 0 \Leftrightarrow \ln(\gamma) \to -\infty, \tag{6.50}$$

$$\ln(\lambda) \to 0 \Leftrightarrow \lambda \to 1 \Leftrightarrow \gamma \to +\infty \Leftrightarrow \ln(\gamma) \to +\infty. \tag{6.51}$$

He also studied more precisely the phase diagram of the particles collective behaviour, in the plane (α;γ), and the phase diagram computed is shown in Fig. 6.33.

The main difference with our phase diagram is that for the limit between the two regimes quasi-elastic and globally aligned regime (red and blue point) $\alpha_c \to 0$ when $\gamma_c \to \infty$ ($\lambda \to 1$), which is expected as the behaviour in $\lambda_c \to 1$ of our discrete model was intrinsically linked with the discretization of the relaxation toward activity.

Pierre Illien also computed analytically the transition curve for a growing train in the continuous model. The growing train system is a system of an infinite number of particles, with special initial condition: one particle going in the direction $\mathbf{e}_x$, in front of "a lot" of particles going in the direction $-\mathbf{e}_x$, with an homogeneous density. Then we expect successive collisions to happen in the system, in a similar way than what happened for the experiment in Fig. 6.8. After each inelastic collision, the particle looses some velocity, and regains it in some extent before the next collision. The question to answer is then if the particle turns back at some point (global alignment), or not. Solving this problem, Pierre found a critical curve $\gamma_c(\alpha_c)$ separating the cases when the droplet finally align, and when the droplets never align (represented with a black continuous line in Fig. 6.33):

$$\begin{aligned} &\textit{Growing train (continuous)}: && \frac{\gamma L}{V_0} = -2\ln\Big(\frac{2\alpha}{1+\alpha}\Big) - \frac{1-\alpha}{1+\alpha}, \\ &\textit{Two droplets (discret)}: && \frac{\gamma L}{V_0} = -2\ln\Big(\frac{2\alpha}{1+\alpha}\Big) - \frac{1-\alpha}{1+\alpha}\Big(\frac{\gamma dt}{1-\exp(-\gamma dt)}\Big). \end{aligned}$$

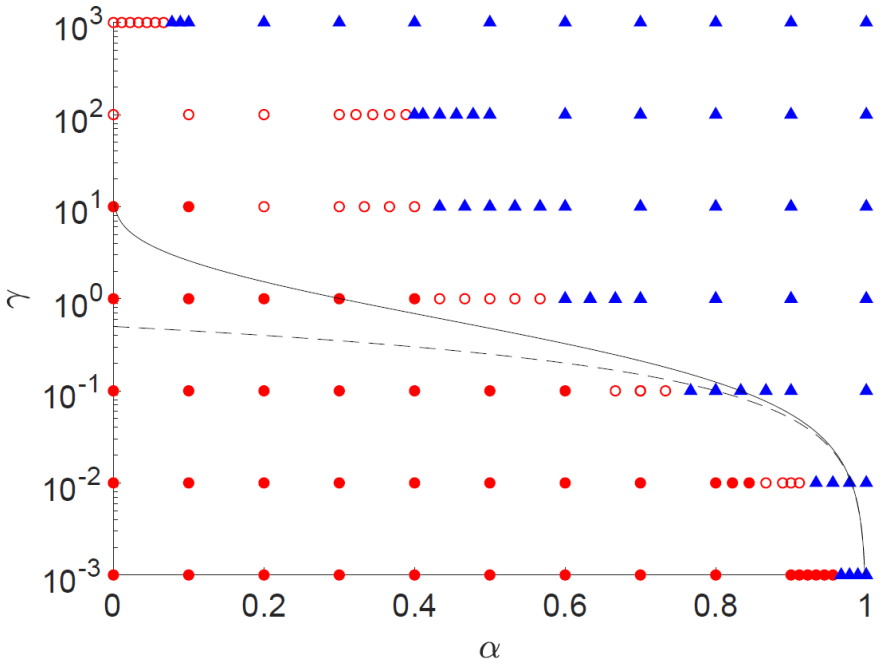

Figure 6.33: Phase diagram computed by Pierre Illien in the plane (α;γ), representing sets of parameters that allow the formation of 'trains' (going to the ordered state after an arrested cluster state (•), or continuously (○) or not (▲). Simulations performed with N = 100 particles on a lattice of L = 1000 sites. The solid line represents the critical value of the relaxation rate that allows an infinite train to grow by one unit.

The two relations are very similar, with a supplementary factor in the case of the discrete system that depends on the time step dt: $\left(\frac{\gamma dt}{1-\exp(-\gamma dt)}\right) \underset{dt\to 0}{\longrightarrow} 1$.

Pierre's continuous model and the previous discrete model give similar results. Pierre's model being faster and more robust, it allows to explore the parameter space for longer experiments, and for more droplets. Pierre studied the evolution of the transition curve between the quasi-elastic and global alignment phase with the observation time: the longer the experiment, the more the curve shift toward large α (global alignment happens for larger α). However, this shifting seems to saturate for time long enough, which suggests that a quasi-inelastic stable phase does exist. Note that $\alpha = 1$ and $\lambda = 1$ are still limit at which there might not be alignment in the system. These results and considerations are still under discussion.

6.2.5.3 Short discussion on the Clogg regime

The clogg is a regime where all particles condense in a small spatial region, and are blocked with a zero apparent velocity (they do have a inner velocity, the probability of moving is non zero, but they are blocked by the presence of other particles).

Inside a clogg, two regions going in two opposite directions face each other. The boundary between the two regions is dynamic and move inside the clogg. At some point, the boundary reaches one end of the clogg: all particle become aligned, and the clogg explode into a unique train. Although they can last a very long time, cloggs are transient regimes.

The clogg regime might remind of the MIPS behaviour: the motility in a clogg being reduced (the particle are blocked), particles accumulate in the clogg region, leading to a density mismatch between the cloggs (all sites are occupied), and the "bulk" (outside the cloggs, the density is smaller, or could even be zero if all particles are in cloggs). We still stress that the clogg regime is different than the MIPS behaviour in the sense that (i) although particles can condensate from the bulk to the clogg (as soon as they collide with the clogg), the opposite is not true, the particles do not leave the clogg (except for the final transition to a train). There is therefore, unlike in MIPS, no phase coexistence: and (ii) the dense phase in MIPS reaches a stable state, while cloggs in our model are transient.

Conclusion

In this chapter, we studied the collective behaviour of swimming droplets in a 1D geometry. We observed a rich variety of behaviours, from the binary interaction between droplets to the formation of collective structures such as trains (dense regions of aligned droplets) or cloggs (regions in which droplets are so densely packed that they are blocked). We showed that the interaction between two droplets is well described by an effective inelastic collision. Furthermore, we observed that the activity of the droplets makes their velocities always relax toward an active velocity, although this relaxation time is long compared to the collision time.

We then implemented in section (6.2) a very simple numerical model taking into account these two ingredients, the inelastic collision (quantified by a restitution parameter α) and the relaxation toward activity (quantified by a relaxation rate λ), to see if they could explain the observed collective behaviours. Using parameters close to the ones we measure experimentally, we retrieved phenomena similar to the ones observed experimentally: the formation of trains and of cloggs. Investigating further this model by looking at times longer than the experimental ones, we determined that both trains and cloggs are transient states, and that, at long times, the system has only two states, the globally aligned state and the disordered quasi-elastic state, depending on the two parameters α and λ.

We want to pinpoint three important features of the model:

1. **The absence of noise:** no noise was implemented in our system, which make it purely deterministic.

2. **The effect of the observation time:** the transient state in our system (trains and clogg) might last a really long time. The train state lasts longer as α gets closer to the critical value that separate the global alignment state to the quasi elastic state. The clogg state lasts longer as λ gets smaller.

3. **The effect of a finite number of particles:** a finite number of particle implies a finite number of initial conditions - it is then unlikely that "special" initial conditions happens - the presence of an already formed train at the start of the experiment for instance. If the number of particles - and so the initial conditions - was infinite, then all combination of initial conditions could be found somewhere in the system.

The difference between the two observed final states of our system is the alignment between particles. On one hand, the nucleation of trains seems to be the crucial event for reaching the globally aligned state. On the other hand, in the absence of noise, there is no source of misalignment in our system. One may then ponder on the stability of the quasi-elastic state.

For systems with a finite number of particles, initial conditions plays a crucial role: independently of the parameters α and λ there is always at least two peculiar sets of initial conditions, one that leads to the global alignment state (for instance all droplet are initially aligned), and another that leads to the quasi elastic state (for instance all particles are placed at the same distance, and are given alternatively the velocities $\pm V_0$). Such initial conditions remain rare on a high enough number of realization, and Pierre Illien's study lead to think that for long observation time, there indeed exists a region in the parameter space λ and α where the quasi-elastic state is stable. Our numerical system then present a phase transition between the globally-aligned state, and the quasi-elastic state.

However, for a system with an infinite number of particles, it is very likely that for all parameter λ and α, except for $\alpha = 1$, some local initial conditions leads to the formation of a train. If a train absorbs other particles and grows, it will propagate into the whole system, which will then reach a globally aligned state. But Pierre Illien's study (section (6.2.5.2)) demonstrated that all trains do not grow. The final system could then be a globally aligned state, with trains of finite and globally constant size. The system with an infinite number of particles is complex, and the eventual existence of a phase transition is still under discussion.

Chapter 7

Ongoing work: swimming under gravity

Motivation

In the biological world, many microorganisms are observed to undergo gravitaxis [156, 62, 157, 64, 61, 60, 158, 63] - a response in motility to a gravitational field. This behaviour fights against sedimentation, and its interest is most likely the possibility to explore a widest part of the environment. Yet how these microorganisms feel the gravitational field is not fully understood. Several possible origins have been pinpointed: physiological mechanisms [62, 157, 159]; bottom heaviness [64, 61] (inhomogeneity in the swimmer density) or fore-aft asymmetry [160, 161, 158, 63, 162].

Some experimental and theoretical studies [163, 164, 65, 165] suggest that the activity alone might be enough to fight against gravity to some extent, by increasing the sedimentation length. This effect can be understood as an increase of the effective temperature of the active particles due to the activity [163, 65]. But if activity has an influence on sedimentation, it doesn't mean that the swimmer "feels" the gravity field. The gravity effect might be only a passive one (additivity of the effects of activity and gravity). It is the case for instance for squirmers, as discussed in chapter 2, section 7: the flow field of a squirmer under a gravitational field is simply the superposition of the flow field of the swimmer in absence of gravity, and the flow field of a passive particle under gravity.

Yet, the behaviour of many experimental swimmers cannot be explained by such a model. Under sedimentation, some phoretic particles are observed to partially align, oriented against the gravitational field [65, 66, 67]. A more subtle effect is when the gravity confine the swimmer close to a bottom or top interface, then interesting phenomena happens, that cannot be explained by the presence of the wall alone [50, 51, 166, 1]. This has been partially addressed in chapter 4.

This means that in several cases, the gravity has an effect on the activity of the swimmer itself. For auto-phoretic swimmers, just like in the case of the presence of a wall, this effect is non-trivial: the gravity modifies the flow field; which modifies the solute concentration; which modifies the activity of the swimmer. A first theoretical approach, conducted by Sébastien Michelin gave some insight on the behaviour of auto-phoretic swimmers under an external field. This preliminary work motivated parallel experimental studies.

The present chapter exposes the preliminary experimental work that has been done in such a context. We study the swimming behaviour of water droplets on an inclined plane (2D) and in square and cylindrical capillaries (1D). Although this work is still quite exploratory, it provides us with some interesting insight on the non-trivial effect of gravity on phoretic swimmers in general, and on swimming droplets in particular.

7.1 Gravity in 2D

7.1.1 Experimental realization

We study the behaviour of swimming and passive droplets (for comparison) in an inclined NOA arena (section 3.2.2.2) under the macroscope (section 3.3.1.1). The discrete phase is made of a solution of water with 15% wt NaCl. For swimming droplet, the continuous phase is made of a solution of 25 mM mono-olein in squalane. For passive droplet, the continuous phase is made of a solution of 4 mM mono-olein in squalane. The arena (schematized in Fig. 7.1) is inclined using a rotation platform, with an angle α with the horizontal, measured precisely using a dual-axis digital angle protractor (TLL-90s, Jingyan®). The macroscope remains fixed, thus the chamber is not parallel to the focal plane, limiting the angle α to values at which the droplet imaging is still acceptable (roughly $\alpha = 45^o$). For each experiment, one droplet is made in the middle of the chamber, then is observed to swim at various angle from $\alpha = 0^o$ to $\alpha = 45^o$ for typically 200 s per angle. The whole experiment is limited to 1 h, so that the droplet radius might be considered constant. The tilting direction is alternated between each angle, to keep the droplet in the middle of the chamber, $\mathbf{e}_x$ is always taken in the direction of the projection of gravity on the chamber plane. The gravity force exerted on the droplet along the chamber plane is then $\mathbf{F}_g = \frac{4\pi}{3} a^3 \rho g \sin\alpha \mathbf{e}_x$. For

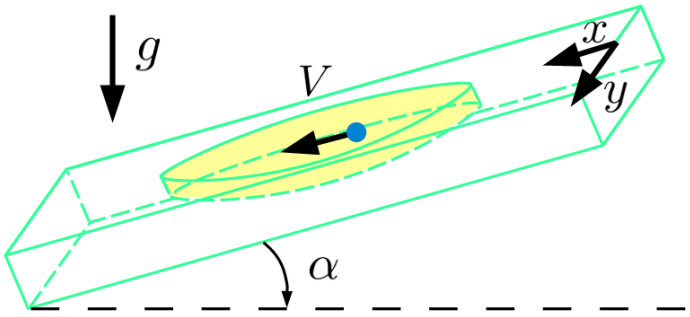

Figure 7.1: **Tilted NOA chamber:** The chamber is tilted with an angle α from the horizontal. x is the direction of the projection of the gravity in the chamber plane. y is the orthogonal coordinates in the chamber plane.

all experiments, the droplet radius (20 μm $< a <$ 150μm) is small compared to the arena height (5 mm), and the droplets are always far from the side walls, so that the droplets "see" only the bottom wall. e_x is defined as the direction of the tilting; and $\mathbf{e}_y$ the normal direction such that $\{\mathbf{e}_x, \mathbf{e}_y\}$ is the plane parallel to the bottom wall, in which the droplet swims (2D motion). We use matlab and image processing tools (described in section (3.3.1.2)) in order to extract the trajectory $\{x(t),y(t)\}$ of the droplet. From this trajectory, we compute the velocity $\mathbf{V}(t)$.

Fig. 7.2 presents typical trajectories of (a) and (b) active, and (c) passive droplets, at different angles, for droplets of typical size $a = 100$ μm. Fig. 7.3 shows a scatter plot of the velocities of the corresponding experiments. Passive droplets have an expected behaviour: they do not move at $\alpha = 0^o$, and fall straight in the direction of gravity when $\alpha > 0^o$. Their velocity increases with increasing angle. For active droplets, two kinds of behaviours are observed. Most often the droplets swim straight Fig. 7.2(a), but sometimes they exhibit curly trajectories Fig. 7.2(b). In both cases, there is a net displacement in the direction of gravity, and the velocity in the direction of gravity V_x increases with increasing angle, in an equivalent manner for the two behaviours. Unlike the passive case, there is also a non-zero normal contribution to the velocity, V_y. This contribution decreases with time for $\alpha > 0$: the droplet aligns progressively with gravity, but also with increasing angle. The droplets with curly trajectories explore more the velocity space than the droplets with straight trajectories.

In the following, we are first going to characterize the behaviour of the passive droplets, before comparing it with the behaviour of the active ones.

7.1.2 Passive droplets

In 3D, far from any wall, a passive droplet falling in a viscous liquid because of an external force $F_g = \frac{4\pi}{3}a^3\rho g \sin\alpha$ goes at a velocity (see section (2.1.4.5)):

$$V = \frac{2a^2\rho g}{3}\sin\alpha\frac{(\eta+\eta_i)}{\eta(2\eta+3\eta_i)} \tag{7.1}$$

$$\simeq \frac{a^2\rho g}{3\eta}\sin\alpha \tag{7.2}$$

In the presence of a wall, this relation is modified. Let's consider as a first approximation that in the presence of a wall, we can still write:

$$V = \kappa_{pass}a^2\sin\alpha \tag{7.3}$$

$\kappa_{3D} = \frac{\rho g}{3\eta} = 0.015$ μm $^{-1}$ s^{-1} is the slope of this curve for passive droplets in 3D. We can plot the velocity of the passive droplets as a function of $a^2\sin\alpha$. All the data collapse on a single line of director $\kappa_{pass} = 0.005$ μm $^{-1}$ s^{-1} $< \kappa_{3D}$. The falling of the droplet compared with the 3D case is indeed slowed down by the presence of the wall. In Fig. 7.4, the passive droplets velocities as a function of $a^2\sin\alpha$ are represented by grey cross and the black continuous line is the linear fit.

7.1.3 Active droplets

7.1.3.1 Dynamic

For each angle, the droplet is initially swimming *against* gravity (this initial condition is due to our experimental protocol, during which we alternate the angles). We observe that the droplet quickly turns round to follow the gravity direction (within

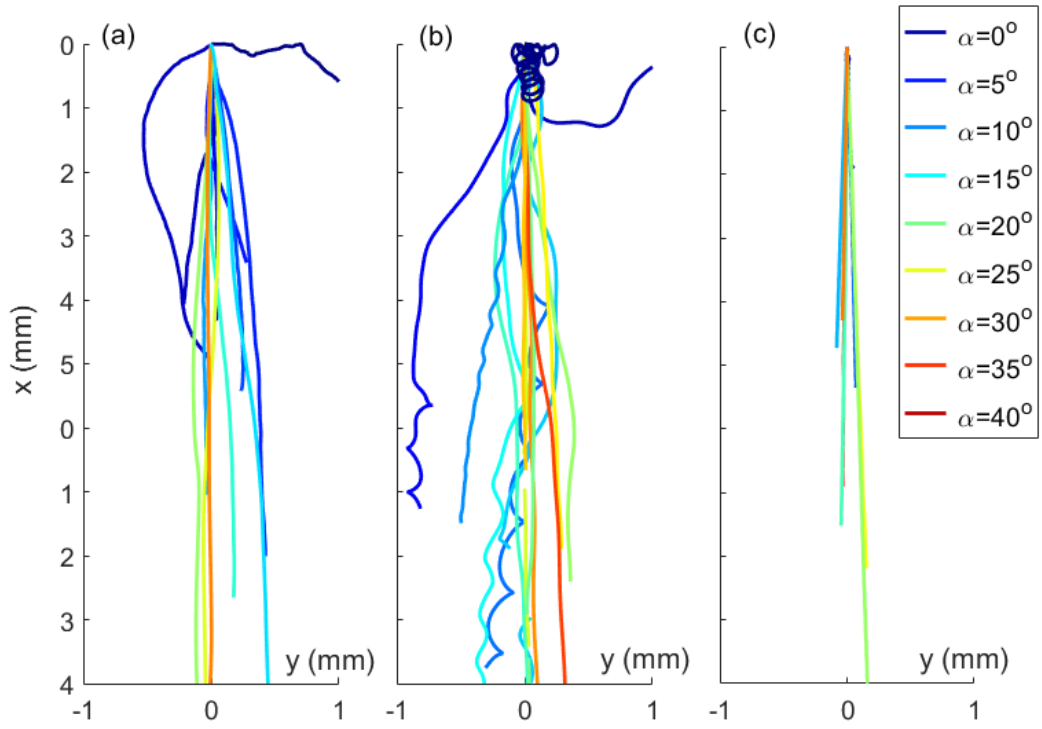

Figure 7.2: **Trajectories of droplets of radius $a = 100$ μm on an inclined plane:** (a) a droplets swimming straight (b) a swimming droplet oscillating (c) a passive droplet.

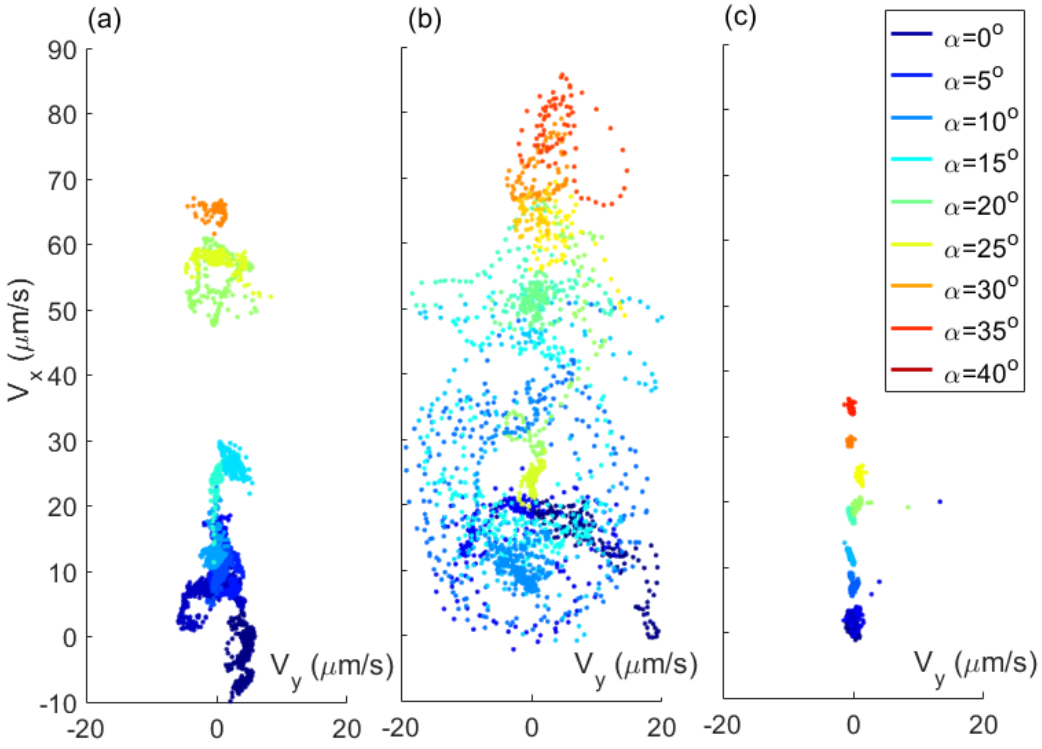

Figure 7.3: **Scatter plot of the velocities of droplets of radius $a = 100$ μm on an inclined plane:** (a) a droplet swimming straight (b) a swimming droplet oscillating (c) a passive droplet.

the few seconds before the acquisition starts), and that the higher α, the quickest this relaxation is. This transient should provide very useful information on the dynamic of the droplet swimming under gravity; and will constitute one of the main leads for future work.

Similarly, the curly behaviour of some droplets has not been yet studied. It is not without reminiscing the trajectory of the swimming of liquid crystal swimming droplets [51], whose curly trajectory is attributed to the coupling between the nematic director field and the convective flow, which leads to an instability in the swimming mechanism (due to a symmetry breaking). Similarly, the curling trajectory of our water droplet in presence of gravity could be due to an instability.

In the following, we are first interested in the droplet swimming steadily: with a constant velocity (in amplitude and direction).

7.1.3.2 Steady state

The average velocity of droplets in the direction of gravity V_x is represented in Fig. 7.4 as a function of $a^2 \sin\alpha$, in order to compare with the velocity of the passive droplets. We observe that the velocity of active droplets in presence of gravity is always higher

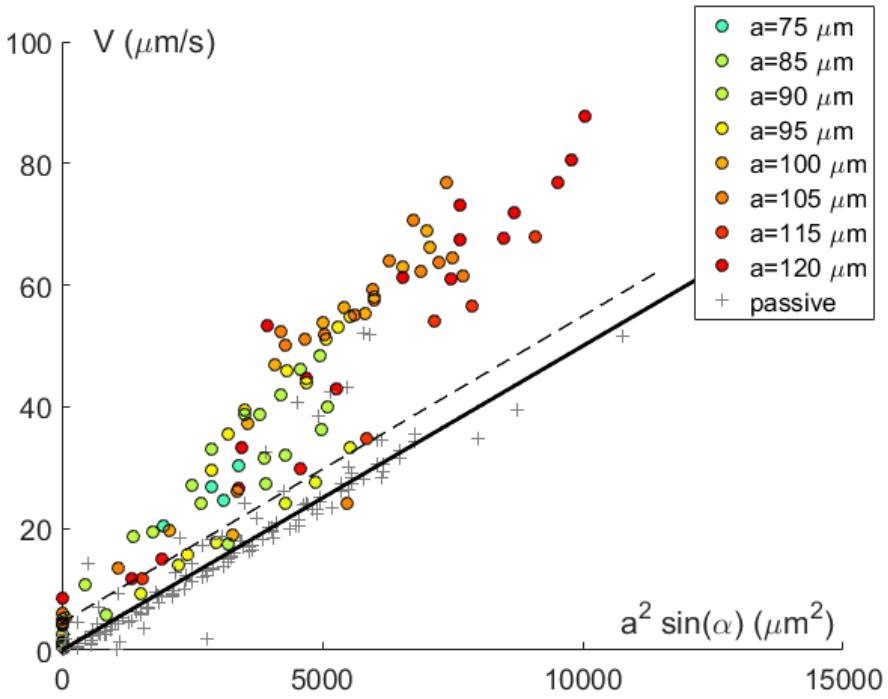

Figure 7.4: Velocity component parallel to gravity V_x averaged on a steady state trajectory, for swimming droplets of different sizes a (color) and at different angles, as a function of $a^2 \sin\alpha$. The velocity of passive droplets is added in grey, and the black line stands for the linear regression of all passive droplets. The dashed straight line corresponds to the expected asymptotic swimming velocity in the presence of gravity, according to the law of velocity addition.

than the velocity of passive ones. The droplets are swimming *toward* gravity. We also observe that the velocity of active droplets grows further away from the velocity of the passive ones as the angle increases. This is unlike what would happen if the velocity of active droplets under gravity was simply the sum of their passive velocity and their active velocity in absence of gravity (in black dashed line in the Fig. 7.4). This observation means that the presence of gravity indeed modifies the activity of the swimmer.

These experiments of droplets swimming on a tilted plane are still in their infancy; and these are only preliminary results. More experiments are planned in the future. We can still compare them to the simplest modeling which is the case of a squirmer under gravity.

We consider a model swimmer whose activity is not modified by the presence of gravity (i.e a squirmer). As seen in section 2.3.2, the velocity of such swimmer under gravity is simply the composition of the active velocity in the absence of force, and the velocity of the equivalent passive particle under gravity:

$$V = V_a + V_g \tag{7.4}$$
$$= \frac{a\langle\sigma_s\rangle - 3\eta_i\langle v_s\rangle}{2\eta + 3\eta_i} - \frac{2a^2\rho g \sin\alpha}{3}\frac{(\eta+\eta_i)}{\eta(2\eta+3\eta_i)} \tag{7.5}$$
$$= V_a(\alpha = 0) + V_g. \tag{7.6}$$

For a phoretic swimmer, we can still write the active velocity in presence of gravity as a composition of a passive effect, due to the gravity, and an active effect, due to the concentration field, but this concentration field is modified by the presence of gravity (section (2.2.3.2)):

$$V = V_a + V_g \tag{7.7}$$
$$= -\frac{K + 3\eta_i M}{2\eta + 3\eta_i}\langle\nabla_\parallel c(r=a,g)\rangle - \frac{2a^2\rho g \sin\alpha}{3}\frac{(\eta+\eta_i)}{\eta(2\eta+3\eta_i)} \tag{7.8}$$
$$\neq V_a(\alpha = 0) + V_g. \tag{7.9}$$

We observe that for small angles, the velocity of the droplets follows the additivity of an active and a passive velocities (within the noise); but for higher angles, the velocity of the swimming droplets becomes much higher. This observation confirms the fact that our swimmer is *not* a squirmer and that the presence of gravity indeed modifies the activity of the swimmer. The theoretical study of the effect of gravity on the whole hydrodynamics and concentration fields is currently conducted by Sébastien Michelin from the LadHyX, in the Département de Mécanique, Ecole Polytechnique. Although not trivial if one takes into consideration the effect of gravity on the whole hydrodynamics field and concentration field, one can have a simplified and intuitive visualization of how the gravity can affect the swimming droplet, Fig. 7.5. The gravity field enhances the spontaneous gradient. A swimming droplet in the absence of gravity (a), through an instability mechanism, develops a certain concentration field of swollen micelles around itself (see (3)). This concentration field is "thinner" in front of the droplet and thicker at its back, generating a gradient of concentration that makes the

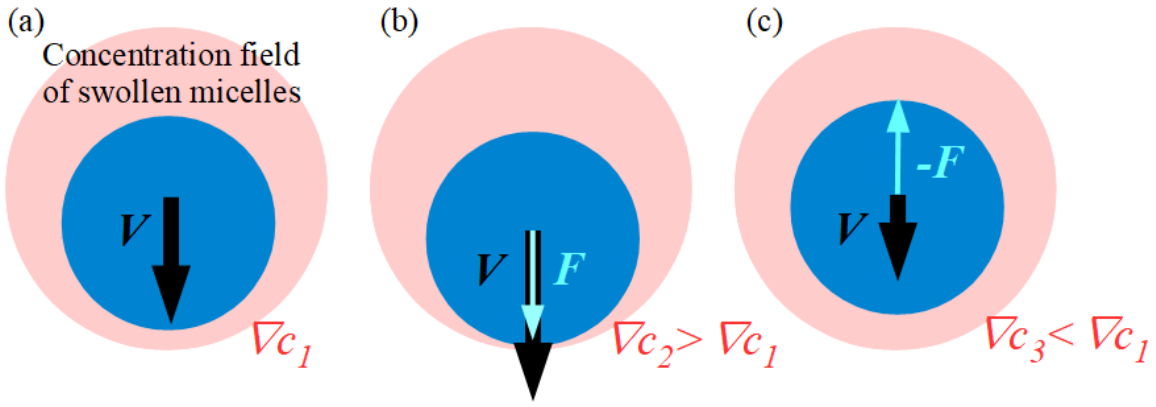

Figure 7.5: **Simplified visualization of the effect of gravity on a swimming droplet:** (a) in absence of gravity, a concentration field of swollen micelles (pale red) develop around the droplet, inducing a gradient ∇c_1 between the front and the back of the droplet. (b) In presence of a force $\mathbf{F}$ in the same direction than the swimming, the droplet accelerates, and the concentration field and the induced gradient ∇c_2 are modified. (c) In presence of a force $-\mathbf{F}$ in the opposite direction than the swimming, the droplet slows down, and the concentration field and the induced gradient ∇c_3 are modified.

droplet swim. If we add a gravity force in the swimming direction (b), the droplet accelerates, and thus is shifted in its concentration field: the concentration field becomes even thinner in front of the droplet and even thicker at its back. The gradient between the front of the back increases, and so does the active velocity. If we add a gravity force in the direction opposed to swimming (c), the droplet slows down, and thus is shifted in its concentration field: it becomes thicker in front of the droplet and thinner at its back. The gradient between the front of the back decreases, and so does the active velocity.

7.2 Gravity in 1D

In 2D, we know the direction of gravity, and we observe in which direction the droplet is swimming. However, we do not have any information on the actual direction of the swimmer (the one that comes from the boundary conditions). To avoid this issue, one possibility is to impose the swimmer direction, for instance by geometrical means: in a tilted capillary, a droplet of the size or bigger than the capillary height is strongly steered in the capillary direction and thus can only swim with or against the gravity. Hence in this section, in a similar way than in 2D, we explore the effect of gravity on a droplet in 1D channels.

7.2.1 Experimental realization

Developing the experimental set-up and running experiments have been done by Victor Maquart, a 3$^{\text{rd}}$ year student (M2) at ESPCI Paris, during an internship at the Gulliver laboratory under my supervision.

We use 200 μm inner diameter cylindrical capillaries ($h = 100$ μm), which are silanized beforehand using the same method as in chapter (5). The capillary is first filled with the continuous phase. In order to observe a droplet in such a capillary under gravity,

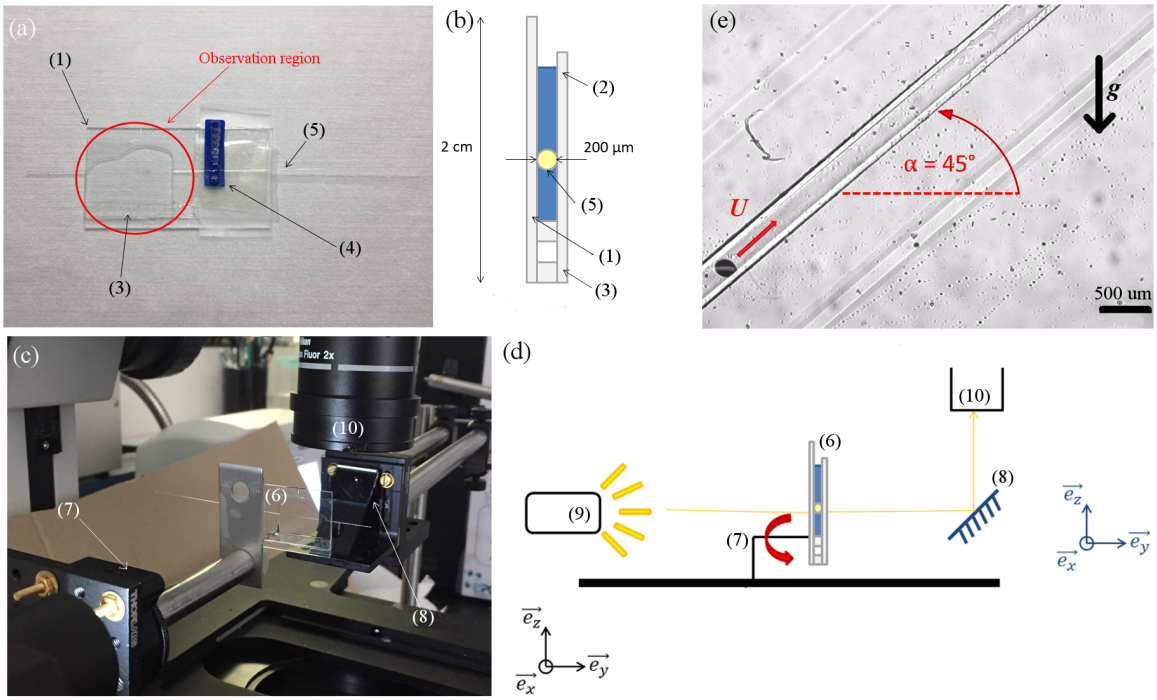

Figure 7.6: **Droplet in a tilted capillary - Set up:** (a) photo and (b) sketch of the device used to immerse the cylindrical capillary in glycerol; (c) photo and (d) sketch of the set up used to tilt the device, and observe the capillary through the macroscope. (d) image of a droplet in a cylindrical capillary obtained through the macroscope. The different components are (1) a rectangular glass slide (2) a square glass coverslip (3) a square capillary (4) a 3D printed holder (5) the cylindrical capillary (6) the whole device (7) a rotation arm (8) a mirror (9) a light source and (10) the macroscope objective.

the capillary must be immersed in glycerol (iso-index with glass), but the whole device should be easy to tilt, up to $\alpha = 90^o$ (once again α is the angle made with the horizontal plane). To achieve this, a slightly different device than the one developed in section (5) has been designed, and is illustrated in Fig. 7.6(a) and (b). The glycerol is trapped between a rectangular glass slide (1) and a square glass coverslip (2) spaced with a square capillary (3) of outer height 330 μm, which is the size of our cylindrical capillary outer diameter. A holder (4), which is simply a succession of pillar spaced 500 μm apart designed with a 3D printer (Ultimaker 3 Extended), is fixed on the other side of the glass slide. The cylindrical capillary (5) is inserted in the glycerol, and held by the holder. Both ends of the cylindrical capillary hang in the air, to prevent the glycerol to enter. The visualization of the capillary is made through the glass coverslip. With this simple design, the whole device can be tilted easily.

Then the device is fixed to a rotation platform, Fig. 7.6(c) and (d): to avoid the problem of focusing on a tilted plane, that we had with the chamber in the previous section, the whole device (6) is fixed in a plane perpendicular to the one of the macroscope (7), and rotated in this plane, and a lamp (8) and a mirror (9) are added so that the light

comes from the lamp, pass through the capillary, reflect on the mirror and goes in the macroscope's objective (10). That way we can tilt the capillary in the focal plane, and keep the droplet focused independently of the angle. This trick uses the fact that we can image through the side of the capillary, which is not possible for a chamber.

A typical image of a droplet in a tilted cylindrical capillary is shown in Fig. 7.6(e). α, the angle with the horizontal is taken positive when the droplet is swimming *against* the gravity, and negative when the droplet is swimming *with* the gravity. Although the imaging after reflection in the mirror is not excellent (this could be improved by using a higher quality mirror), this is sufficient to track the droplet accurately.

An experiment is conducted as follows: the droplet is made at one end of the capillary (in the exact same way as in section (5), while the capillary is horizontal ($\alpha = 0$, no gravity). A first acquisition is made for typically 200 s. Then successive acquisitions are made for the same droplet, but changing the angle α. Using Matlab® and image analysis tools (described in section (3.3.1.2), we compute the trajectory, and then the velocity of the droplet over time.

This is done for many different droplets. In a first time, we make spherical droplets of typically the size of the capillary $0.8 < \frac{a}{h} < 1$, then we look at a few longer droplets, up to $\frac{L}{2h} = 2.4$. We also make passive droplets - although we are limited in their size: passive droplets longer than the capillary height stick to the wall. Note that we consider that the droplet direction does not change during one experiment, which is confirmed experimentally (in particular, the droplet doesn't turn back to swim on its trail).

7.2.2 Result

Typical trajectories and velocities for a droplet of size $a = 100$ μm going with the gravity ($\alpha < 0$), are given in Fig. 7.7. We observe that the droplet feels the gravity, and accelerate as the tilting angle increases.

We then look at a series of droplets of typically the capillary size: 80 μm $< a < 105$ μm. We compute the average velocity of the droplets over the trajectory, and we compare it with the one of passive droplets of similar size. The result are shown in Fig. 7.8

A first direct observation is that active droplets go faster than passive ones. A second observation is that the influence of gravity remains small, unlike in 2D: the velocity of passive droplet falling under gravity is small compared to the velocity of swimming droplet without gravity (no more than one half). In presence of gravity, droplets swimming downward go faster than active droplets without gravity, while droplet swimming upward go slower, but gravity never overcome the swimming: swimming droplets are able to ascend a vertical capillary.

With in mind the purpose of studying droplets on which the gravity force would be greater, we made droplets longer than the capillary height $1 < \frac{a}{h} < 2.5$, a being in the case of elongated droplet the half-length. We represent in Fig. 7.9 the average velocity over the trajectory of spherical and long droplet as a function of $\sin(\alpha)$.

The blue triangle stands for spherical droplets, whose behaviour was just discussed. We observe two surprising behaviours: first, droplets slightly larger than the capillary height (a =105 μm, blue diamond) going against gravity *accelerate* when the gravity in-

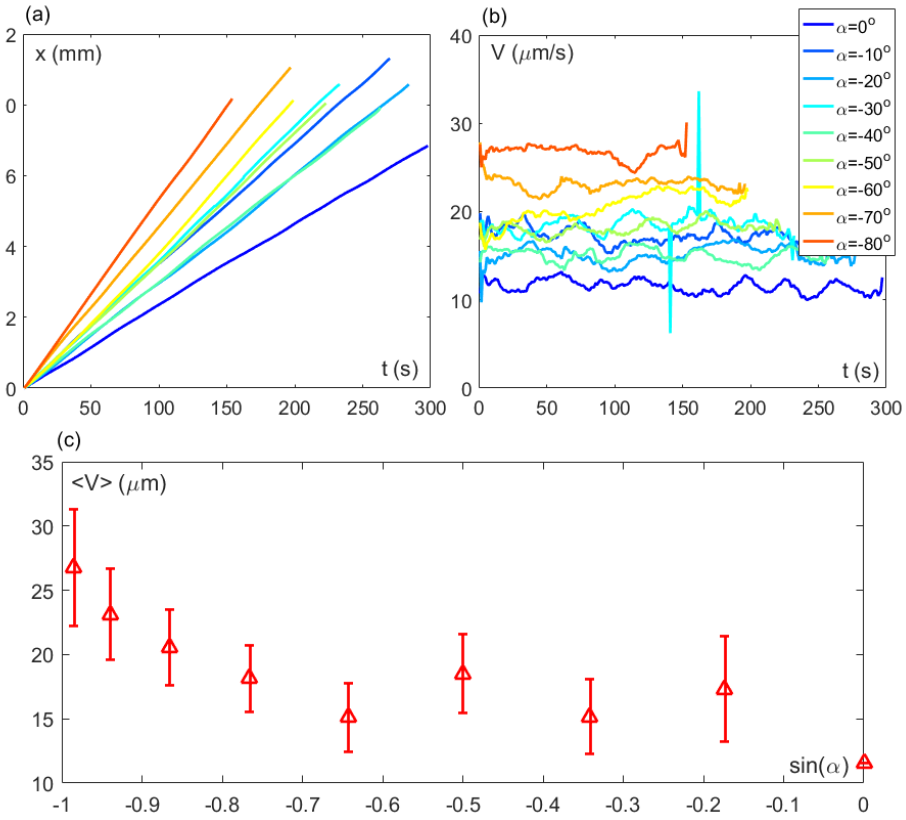

Figure 7.7: **Trajectories and velocities of a droplet swimming with gravity:** (a) Trajectories and (b) velocities of a droplet of size $a = 100$ μm at different angles (color code) from $\alpha = 0$ (dark blue) to $\alpha = -90^o$ (red). The droplet swims in the direction of gravity. (c) Average velocity over the trajectory for the different angles. The error bars represent the standard deviation over the trajectory.

creases while their equivalent going with the gravity behave just like spherical droplets. Second, droplets larger than that ($a > 120$ μm, from light blue to red diamond) do not seem to feel gravity: their velocity is always around $V = 2.5$ μm with or against gravity, which is the value of velocity in absence of gravity found for long droplets in a cylindrical capillary, and measured in chapter (5).

7.2.3 Discussion

Unlike in the 2D case, the velocity of passive particles do not collapse on a single curve linear in $a^2 \sin(\alpha)$. In order to study the role of gravity on the activity of the droplets, for droplets of typically the capillary size, we subtracted the velocity of equivalent passive droplets (same size, same angle) to the velocity of active droplets under gravity. The result is shown in Fig. 7.10. Roughly, this active velocity does not depend much on $\sin(\alpha)$. With a lot of twist (maybe too much at this stage of the experiments) in the data, one observes a non monotonous effect of the gravity on the active velocity when the droplet is going *with* the gravity: at intermediate angles, the gravity decreases the active velocity. This result is counter-intuitive if we compare it with the interpretation of what happened in 2D. At higher angles, the tendency reverses, and the gravity increases the active velocity when the droplet goes with the gravity, which is more like

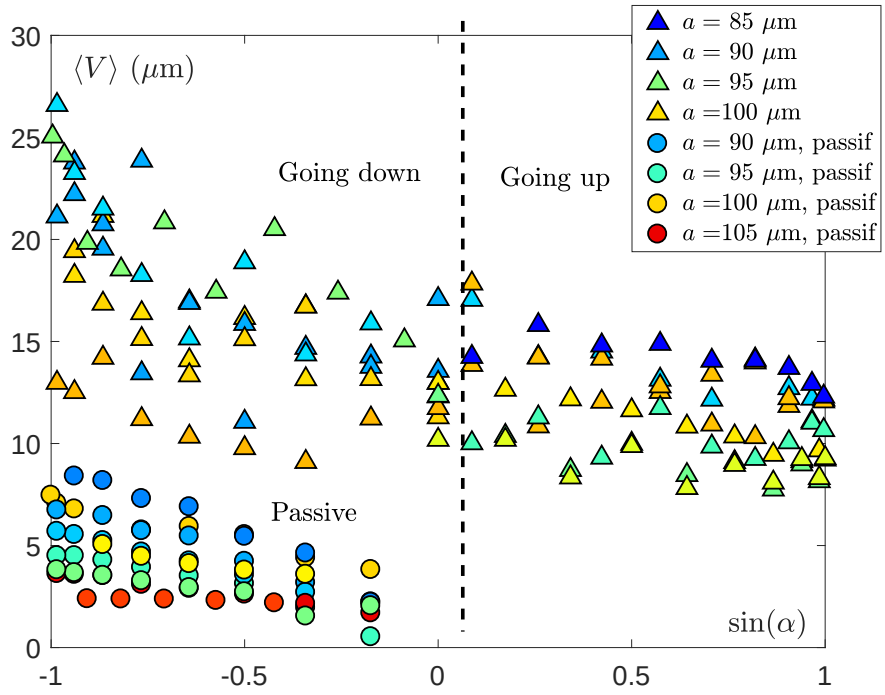

Figure 7.8: **Average velocity of spherical droplets in 1D under gravity:** Average velocity over the trajectory of spherical active (triangle) and passive (circle) droplets as a function of sin(α) for droplet of different size (color-scale).

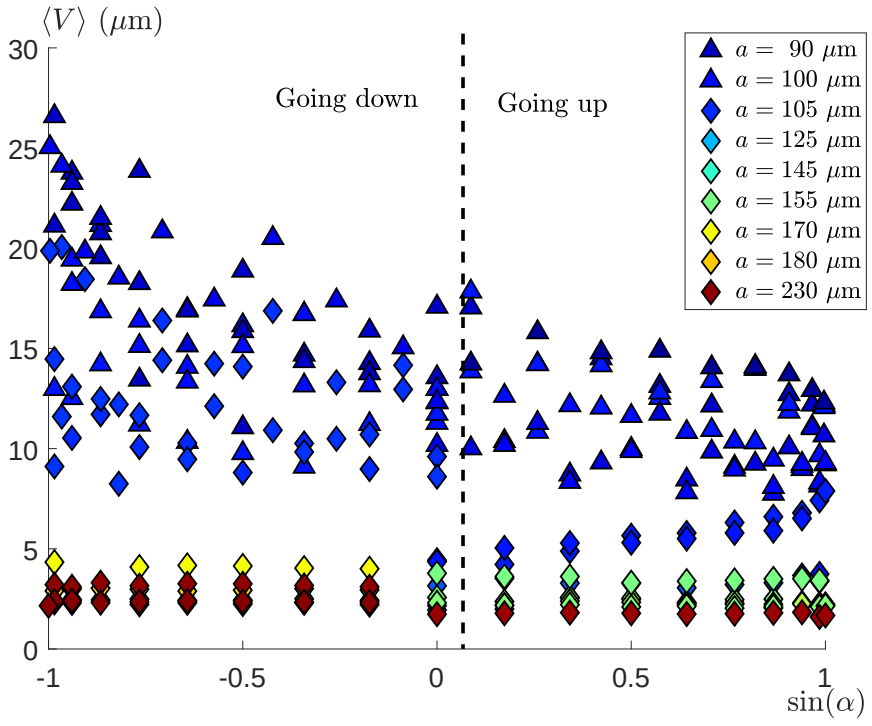

Figure 7.9: **Average velocity of spherical and long active droplets in 1D under gravity:** Average velocity over the trajectory of spherical (triangle $a < 1$) and long (diamond, $a > 1$) active droplets as a function of sin(α) for droplet of different size (color-scale).

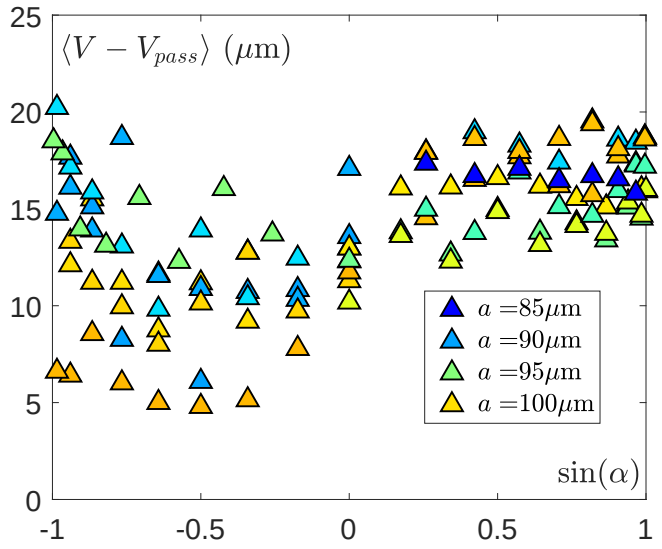

Figure 7.10: **Average velocity of spherical droplets in 1D under gravity:** Average velocity over the trajectory of spherical active (triangle) and passive (circle) droplets as a function of $\sin(\alpha)$ for droplet of different size (color-scale).

what is observed in 2D. These tendencies have to be confirmed with more experiments.

Conclusion

This chapter presented ongoing work on the effect of gravity on swimming, by looking at swimming droplets on tilted planes or in tilted capillaries. In 2D, gravity strongly orients the swimming of the droplet. First measures of the droplets velocity under gravity show that at large gravity (large tilting angle), the velocity is not the simple additivity of the effect of activity and gravity, at odd with the prediction for a squirmer. The presence of gravity increases the active velocity of the swimmer, by enhancing the spontaneous gradient of swollen micelles concentration around the droplet. The next step of this study is to make more experiments in order to quantify the effect of gravity on the activity, and eventually to compare it with theoretical predictions, on which Sébastien Michelin is working.

In 1D, first measurements of the velocity of droplets in silanized cylindrical capillaries show promising results. The droplets are observed to swim against gravity, even for angles up to 90^o. Looking more closely at the influence of gravity on the active velocity itself, by subtracting the measured velocity of an equivalent passive droplet, one may discuss on the subtle non-monotonous evolution of the velocity. More experiments are required to capture more precisely the phenomenon. Finally, and surprisingly, the gravity does not have any visible effect on the swimming of long droplets, that swim downward and upward at the same velocity than the one measured in absence of gravity

This work is still at the stage of purely experimental observations of the droplet swimming behaviour. We still lack the tools to interpret what is going one. Finding such tools is left for future prospect.

General Conclusion

Intermediate conclusions and discussions have been made along this manuscript, for each experimental chapter. In this final conclusion, we intend to bring together and synthesize a few major results.

This work, which is essentially fundamental in nature, explores experimentally through a model swimmer the influence that external factors can have on the behaviour of microswimmers. The pure water swimming droplet swims using a self induced concentration gradient of swollen micelles. We observed them in several situations: in presence of a wall, in chapter (4), confined in 1D, in chapter (5), with many other droplets in 1D, in chapter (6), and finally under gravity, in chapter (7) (which is still an ongoing work). These external factors influence the hydrodynamics around the droplet, but, through the coupling between the hydrodynamics and the swollen micelles concentration, they also modify the swimmer itself. We saw in chapter (4) that a wall changes the long range behaviour of the swimmer. In chapter (5), the high confinement trivially modifies the shape of the swimmer, which does not prevent it from swimming, and even allows for complex phenomena such as spontaneous divisions to happen. Finally in chapter (6), we saw that collective behaviours, such as trains or cloggs, can emerge from the droplets interactions. In all cases, what could have been thought as simple constrains that would impede the swimming, leads to a richer and more complex phenomenology. Beyond the simple understanding of our peculiar system, these studies give insight on various phenomena at the interface of hydrodynamics, physico-chemical engineering and active matter.

Most of the time, a water swimming droplet behaves "as expected": it swims in a regular way, shrinks slowly, and eventually interacts with another droplet. Sometimes, its behaviour is unexpected. This work presented and analyzed some surprising behaviour of these water droplets (for instance division and strong shape deformation under confinement, in chapter (5)). During this PhD, we met with other situations in which the droplet acted in a strange way. We did not further study these situations, but we present some of the most stunning ones briefly, in Fig. 7.11. (a) Throughout our experiments, we used only closed chambers (with no air interface). In one experiment, we forgot to do so, and all the water droplets started to "disappear". Taking a closer look at one droplet(Fig. 7.11(a)), we observed that the droplet was shrinking (most likely the water is evaporating), leaving behind a small black agglomerate of a few microns (most likely a surfactant agglomerate). (b) To look through cylindrical

capillaries, we immerse the capillary into glycerol, and we are very careful that no glycerol enters the oil phase. It still happened a few times, and we then observed a glycerol droplet that, to our surprise, was swimming. Even more amazing, one glycerol droplet met a long water droplet (Fig. 7.11(b)). After meeting, the two droplets stuck together, and the refractive index of the glycerol droplet started to change, until it reached the same refractive index than the water droplet, while the volume of the glycerol droplet was increasing (most likely, the glycerol droplet was "drinking" water from the water droplet). After a while, the swelling of the glycerol droplet stopped, and the two droplets started swimming, still stuck together. (c) During an experiment, the room temperature is kept above 25^oC , to prevent the crystallization of the mono-olein. Sometimes, crystallization still happens (Fig. 7.11(c)). When a swimming droplet sees a mono-olein crystal (almost transparent in the picture), it swims toward it, and "eats" it. After eating a few mono-olein crystals, the droplet stops swimming. (d) Under some conditions (we believe that the droplets need to be made very closely from each other, and before they start swimming), swimming droplets assemble into a "crystal", and swim together without breaking this assembly (Fig. 7.11(d)). Their swimming then consists in turning around each other, in what we call a waltz. This phenomenon is currently being studied in the team of professor Masatoshi Ichikawa from the Laboratory of Dissipative and Biological Physics of Kyoto university.

A final remark: the system studied in the current work is quite simple, composed of water, oil and surfactant. Amazingly, it presents many of the hallmarks of life detailed in chapter (1), namely compartmentalization (a droplet), division (under high confinement), energy transduction (that empowers the activity by thermodynamic relaxation), and motility, which is the very reason for which this system was studied. All these behaviours are achieved in the absence of chemical reaction, using only physical and physico-chemical phenomena. Without the intention of building an actual probiotic system, we want the reader remember how startling it is, that the living world and the physico-chemical world can be so closely related.

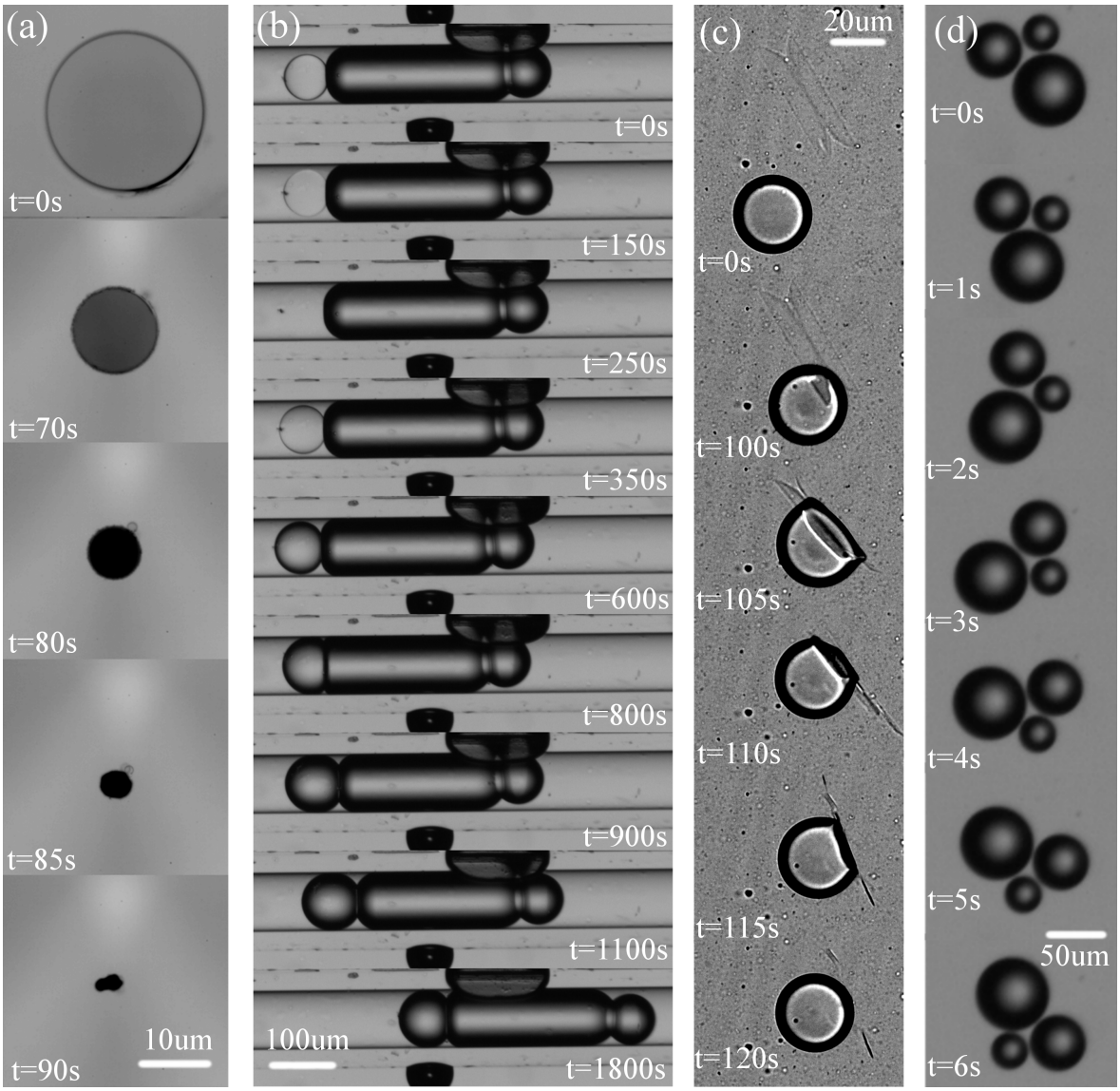

Figure 7.11: **Strange behaviour of our pure water swimming droplets:** (a) disappearance of a droplet close to an air interface. (b) Meeting of a glycerol droplet (light grey, left) and a long water droplet (darker grey, right). The refractive index of the glycerol droplet progressively changes as the glycerol droplet swell. (c) A water droplet eating a crystal of mono-olein. (d) A waltzing crystal of three water droplets.

Bibliography

[1] C. De Blois, M. Reyssat, S. S. Michelin, and O. Dauchot, "Flow field around a confined active droplet," *Physical Review Fluids*, may 2019.

[2] F. P. Bretherton, "The motion of long bubbles in tubes," *Journal of Fluid Mechanics*, 1961.

[3] N. Amy Yewdall, A. F. Mason, and J. C. Van Hest, "The hallmarks of living systems: Towards creating artificial cells," 2018.

[4] S. Arsène, S. Ameta, N. Lehman, A. D. Griffiths, and P. Nghe, "Coupled catabolism and anabolism in autocatalytic RNA sets," *Nucleic Acids Research*, 2018.

[5] S. Chatterjee and S. Yadav, "The Origin of Prebiotic Information System in the Peptide/RNA World: A Simulation Model of the Evolution of Translation and the Genetic Code," *Life*, 2019.

[6] Y. Sowa and R. M. Berry, "Bacterial flagellar motor," 2008.

[7] M. Hanczyc, "Droplets: Unconventional Protocell Model with Life-Like Dynamics and Room to Grow," *Life*, 2014.

[8] A. M. Brizard and J. H. Van Esch, "Self-assembly approaches for the construction of cell architecture mimics," *Soft Matter*, 2009.

[9] A. J. Dzieciol and S. Mann, "Designs for life: Protocell models in the laboratory," 2012.

[10] K. Powell, "How biologists are creating life-like cells from scratch," *Nature*, 2018.

[11] Supramaniam, Ces, and Salehi-Reyhani, "Microfluidics for Artificial Life: Techniques for Bottom-Up Synthetic Biology," *Micromachines*, 2019.

[12] C. Martino and A. J. DeMello, "Droplet-based microfluidics for artificial cell generation: A brief review," 2016.

[13] S. Rasmussen, M. A. Bedau, L. Chen, D. Deamer, D. C. Krakauer, N. H. Packard, and P. F. Stadler, "Protocells: Bridging Nonliving and Living Matter," *Phenomenology and the Cognitive Sciences*, 2008.

[14] M. G. Simon and A. P. Lee, "Microfluidic droplet manipulations and their applications," in *Microdroplet Technology: Principles and Emerging Applications in Biology and Chemistry*, Springer, New York, NY, 2012.

[15] D. Zwicker, R. Seyboldt, C. A. Weber, A. A. Hyman, and F. Jülicher, "Growth and division of active droplets provides a model for protocells," *Nature Physics*, vol. 13, no. 4, pp. 408–413, 2017.

[16] P. A. Bachmann, P. Walde, P. L. Luisi, and J. Lang, "Self-Replicating Micelles: Aqueous Micelles and Enzymatically Driven Reactions in Reverse Micelles," *Journal of the American Chemical Society*, 1991.

[17] K. P. Browne, D. A. Walker, K. J. Bishop, and B. A. Grzybowski, "Self-division of macroscopic droplets: Partitioning of nanosized cargo into nanoscale micelles," *Angewandte Chemie - International Edition*, 2010.

[18] F. Caschera, S. Rasmussen, and M. M. Hanczyc, "An oil droplet division-fusion cycle," in *ChemPlusChem*, 2013.

[19] A. Courbet, F. Molina, and P. Amar, "Computing with Synthetic Protocells," *Acta Biotheoretica*, 2015.

[20] E. Lauga and T. R. Powers, "The hydrodynamics of swimming microorganisms," *Rep. Prog. Phys.*, vol. 72, no. 9, 2009.

[21] E. M. Purcell, "Life at low Reynolds number," *American Journal of Physics*, 1977.

[22] H. C. Berg and R. A. Anderson, "Bacteria swim by rotating their flagellar filaments," *Nature*, 1973.

[23] R. Dreyfus, J. Baudry, M. L. Roper, M. Fermigier, H. A. Stone, and J. Bibette, "Microscopic artificial swimmers," *Nature*, 2005.

[24] E. Lauga, "Bacterial Hydrodynamics," *Annu. Rev. Fluid Mech.*, vol. 48, pp. 105–130, 2016.

[25] B. M. Friedrich, I. H. Riedel-Kruse, J. Howard, and F. Julicher, "High-precision tracking of sperm swimming fine structure provides strong test of resistive force theory," *Journal of Experimental Biology*, 2010.

[26] W. Gao, S. Sattayasamitsathit, K. M. Manesh, D. Weihs, and J. Wang, "Magnetically Powered Flexible Metal Nanowire Motors," *Journal of the American Chemical Society*, vol. 132, no. 41, pp. 14403–14405, 2010.

[27] S. L. Tamm and G. A. Horridge, "The relation between the orientation of the central fibrils and the direction of beat in cilia of Opalina," *Proc. R. Soc. Lond. B*, vol. 175, no. 1040, pp. 219–233, 1970.

[28] J. Gray and J. S. Gardiner, "The Mechanism of Ciliary Movement," *Proceedings of the Royal Society of London. Series B, Containing Papers of a Biological Character*, vol. 93, no. 650, pp. 104–121, 1922.

[29] J. L. Anderson, "Colloid Transport by Interfacial Forces," *Annual Review of Fluid Mechanics*, vol. 21, no. 1, pp. 61–99, 1989.

[30] R. F. Ismagilov, A. Schwartz, N. Bowden, and G. M. Whitesides, "Autonomous movement and self-assembly," *Angewandte Chemie - International Edition*, 2002.

[31] L. Turner, W. S. Ryu, and H. C. Berg, "Real-time imaging of fluorescent flagellar filaments," *Journal of Bacteriology*, 2000.

[32] H. Machemer, "Ciliary activity and the origin of metachrony in Paramecium: effects of increased viscosity.," *The Journal of experimental biology*, 1972.

[33] G. Volpe, I. Buttinoni, D. Vogt, H. J. Kümmerer, and C. Bechinger, "Microswimmers in patterned environments," *Soft Matter*, 2011.

[34] S. Sanchez, A. A. Solovev, S. M. Harazim, C. Deneke, Y. Feng Mei, and O. G. Schmidt, "The smallest man-made jet engine," *Chemical Record*, 2011.

[35] S. J. Ebbens and J. R. Howse, "In pursuit of propulsion at the nanoscale," 2010.

[36] A. Najafi and R. Golestanian, "Simple swimmer at low Reynolds number: Three linked spheres," *Physical Review E - Statistical Physics, Plasmas, Fluids, and Related Interdisciplinary Topics*, 2004.

[37] M. J. Lighthill, "On the squirming motion of nearly spherical deformable bodies through liquids at very small Reynolds numbers.," *Commun. Pure Appl. Math.*, 1952.

[38] J. R. Blake, "A note on the image system for a stokeslet in a no-slip boundary," *Mathematical Proceedings of the Cambridge Philosophical Society*, vol. 70, no. 1971, pp. 303–310, 1971.

[39] C. Bechinger, R. Di Leonardo, H. Löwen, C. Reichhardt, G. G. Volpe, and G. G. Volpe, "Active particles in complex and crowded environments," *Reviews of Modern Physics*, 2016.

[40] P. D. Frymier, R. M. Ford, H. C. Berg, and P. T. Cummings, "Three-dimensional tracking of motile bacteria near a solid planar surface," *Proceedings of the National Academy of Sciences*, vol. 92, no. 13, pp. 6195–6199, 1995.

[41] A. P. Berke, L. Turner, H. C. Berg, and E. Lauga, "Hydrodynamic attraction of swimming microorganisms by surfaces," *Physical Review Letters*, 2008.

[42] A. Zöttl and H. Stark, "Emergent behavior in active colloids," 2016.

[43] D. Takagi, J. Palacci, A. B. Braunschweig, M. J. Shelley, and J. Zhang, "Hydrodynamic capture of microswimmers into sphere-bound orbits," *Soft Matter*, 2014.

[44] S. Das, A. Garg, A. I. Campbell, J. Howse, A. Sen, D. Velegol, R. Golestanian, and S. J. Ebbens, "Boundaries can steer active Janus spheres," *Nature Communications*, 2015.

[45] P. Denissenko, V. Kantsler, D. J. Smith, and J. Kirkman-Brown, "Human spermatozoa migration in microchannels reveals boundary-following navigation," *Proceedings of the National Academy of Sciences*, 2012.

[46] M. S. Davies Wykes, X. Zhong, J. Tong, T. Adachi, Y. Liu, L. Ristroph, M. D. Ward, M. J. Shelley, and J. Zhang, "Guiding microscale swimmers using teardrop-shaped posts," *Soft Matter*, vol. 13, no. 27, pp. 4681–4688, 2017.

[47] R. Di Leonardo, D. Dell'Arciprete, L. Angelani, and V. Iebba, "Swimming with an image," *Physical Review Letters*, 2011.

[48] W. R. DiLuzio, L. Turner, M. Mayer, P. Garstecki, D. B. Weibel, H. C. Berg, and G. M. Whitesides, "Escherichia coli swim on the right-hand side," *Nature*, 2005.

[49] Y. Magariyama, M. Ichiba, K. Nakata, K. Baba, T. Ohtani, S. Kudo, and T. Goto, "Difference in bacterial motion between forward and backward swimming caused by the wall effect," *Biophysical Journal*, 2005.

[50] K. Drescher, K. C. Leptos, I. Tuval, T. Ishikawa, T. J. Pedley, and R. E. Goldstein, "Dancing volvox: Hydrodynamic bound states of swimming algae," *Physical Review Letters*, 2009.

[51] C. Krüger, C. Bahr, S. Herminghaus, and C. C. Maass, "Dimensionality matters in the collective behaviour of active emulsions," *European Physical Journal E*, vol. 39, no. 6, p. 64, 2016.

[52] S. Thutupalli, D. Geyer, R. Singh, R. Adhikari, and H. A. Stone, "Flow-induced phase separation of active particles is controlled by boundary conditions," *Proceedings of the National Academy of Sciences*, vol. 115, no. 21, pp. 5403–5408, 2018.

[53] H. Wioland, F. G. Woodhouse, J. Dunkel, J. O. Kessler, and R. E. Goldstein, "Confinement stabilizes a bacterial suspension into a spiral vortex," *Physical Review Letters*, 2013.

[54] R. Di Leonardo, L. Angelani, D. Dell\textquoterightArciprete, G. Ruocco, V. Iebba, S. Schippa, M. P. Conte, F. Mecarini, F. De Angelis, and E. Di Fabrizio, "Bacterial ratchet motors," *Proceedings of the National Academy of Sciences*, vol. 107, no. 21, pp. 9541–9545, 2010.

[55] J. Elgeti, R. G. Winkler, and G. Gompper, "Physics of microswimmers single particle motion and collective behavior: a review," *Reports on Progress in Physics*, pp. 1–50, 2015.

[56] J. Henrichsen, "Bacterial surface translocation: a survey and a classification.," 1972.

[57] H. P. Zhang, A. Be'er, E. L. Florin, and H. L. Swinney, "Collective motion and density fluctuations in bacterial colonies," *Proceedings of the National Academy of Sciences of the United States of America*, 2010.

[58] J. Gachelin, A. Rousselet, A. Lindner, and E. Clement, "Collective motion in an active suspension of Escherichia coli bacteria," *New Journal of Physics*, 2014.

[59] J. Palacci, S. Sacanna, A. P. Steinberg, D. J. Pine, and P. M. Chaikin, "Living crystals of light-activated colloidal surfers," *Science*, 2013.

[60] A. M. Roberts, "Geotaxis in motile micro-organisms.," *The Journal of experimental biology*, 1970.

[61] J. O. Kessler, "Hydrodynamic focusing of motile algal cells," *Nature*, 1985.

[62] D.-P. Häder and R. Hemmersbach, "Graviperception and graviorientation in flagellates," *Planta*, 1997.

[63] Y. Mogami, J. Ishii, and S. A. Baba, "Theoretical and experimental dissection of gravity-dependent mechanical orientation in gravitactic microorganisms," *Biological Bulletin*, 2001.

[64] W. M. Durham, J. O. Kessler, and R. Stocker, "Disruption of vertical motility by shear triggers formation of thin phytoplankton layers," *Science*, 2009.

[65] J. Palacci, C. Cottin-Bizonne, C. Ybert, and L. Bocquet, "Sedimentation and Effective Temperature of Active Colloidal Suspensions," *Phys. Rev. Lett.*, vol. 105, no. 8, p. 88304, 2010.

[66] M. Enculescu and H. Stark, "Active colloidal suspensions exhibit polar order under gravity," *Physical Review Letters*, 2011.

[67] K. Wolff, A. M. Hahn, and H. Stark, "Sedimentation and polar order of active bottom-heavy particles," *European Physical Journal E*, 2013.

[68] G. Arfken and H. J. Weber, *Mathematical Methods for Physicists, 4th ed.* Academic Press, 1972.

[69] S. Kim and S. J. Karrila, *Microhydrodynamics: Principles and selected applications*. Dover, 2005.

[70] H. Brenner, "The Stokes resistance of a slightly deformed sphere," *Chemical Engineering Science*, vol. 19, no. 8, pp. 519–539, 1964.

[71] S. Rybalko, N. Magome, and K. Yoshikawa, "Forward and backward laser-guided motion of an oil droplet," *Physical Review E - Statistical Physics, Plasmas, Fluids, and Related Interdisciplinary Topics*, 2004.

[72] J. R. Howse, R. A. L. Jones, A. J. Ryan, T. Gough, R. Vafabakhsh, and R. Golestanian, "Self-Motile Colloidal Particles: From Directed Propulsion to Random Walk," *Phys. Rev. Lett.*, vol. 99, p. 48102, jul 2007.

[73] J. Thomson, "XLII. On certain curious motions observable at the surfaces of wine and other alcoholic liquors," *The London, Edinburgh, and Dublin Philosophical Magazine and Journal of Science*, 1855.

[74] C. Marangoni, *Sull'espansione delle goccie d'un liquido galleggianti sulla superficie di altro liquido (On the expansion of a droplet of a liquid floating on the surface of another liquid).* Pavia, 1869.

[75] P.-G. de Gennes, F. Brochard-Wyart, and D. Quéré, *Capillarity and Wetting Phenomena*. Springer, New York, NY, 2004.

[76] E. Ruckenstein, "Can phoretic motions be treated as interfacial tension gradient driven phenomena?," *Journal of Colloid and Interface Science*, vol. 83, no. 1, pp. 77–81, 1981.

[77] L. S. Mok and K. Kim, "Motion of a gas bubble inside a spherical liquid container with a vertical temperature gradient," *Journal of Fluid Mechanics*, 1987.

[78] K. D. Barton and R. Shankar Subramanian, "The migration of liquid drops in a vertical temperature gradient," *Journal of Colloid And Interface Science*, 1989.

[79] J. W. Gibbs, "On the equilibrium of heterogeneous substances," *American Journal of Science*, 1878.

[80] J. D. van der Waals, "The thermodynamic theory of capillarity under the hypothesis of a continuous variation of density," *Journal of Statistical Physics*, 1979.

[81] A. Ch. Mitropoulos, "What is a surface excess?," *Journal of Engineering Science and Technology Review*, vol. 1, 2008.

[82] R. Golestanian, T. B. Liverpool, and A. Ajdari, "Designing phoretic micro- and nano-swimmers," *New Journal of Physics*, 2007.

[83] S. Michelin, E. Lauga, and D. Bartolo, "Spontaneous autophoretic motion of isotropic particles," *Physics of Fluids*, vol. 25, no. 6, p. 61701, 2013.

[84] A. Walther and A. H. Müller, "Janus particles: Synthesis, self-assembly, physical properties, and applications," 2013.

[85] T. Nisisako, "Recent advances in microfluidic production of Janus droplets and particles," 2016.

[86] S. Michelin and E. Lauga, "Phoretic self-propulsion at finite Péclet numbers," *Journal of Fluid Mechanics*, 2014.

[87] Z. Izri, M. N. Van Der Linden, S. Michelin, and O. Dauchot, "Self-propulsion of pure water droplets by spontaneous marangoni-stress-driven motion," *Physical Review Letters*, vol. 113, no. 24, p. 248302, 2014.

[88] J. R. Blake, "A spherical envelope approach to ciliary propulsion," *Journal of Fluid Mechanics*, vol. 46, no. 1, pp. 199–208, 1970.

[89] S. Michelin and E. Lauga, "Efficiency optimization and symmetry-breaking in a model of ciliary locomotion," *Physics of Fluids*, 2010.

[90] O. S. Pak and E. Lauga, "Generalized squirming motion of a sphere," *Journal of Engineering Mathematics*, vol. 88, pp. 1–28, oct 2014.

[91] E. Kanso and S. Michelin, "Phoretic and hydrodynamic interactions of weakly confined autophoretic particles," *Journal of Chemical Physics*, vol. 150, p. 44902, 2019.

[92] S. H. Lee, R. S. Chadwick, and L. G. Leal, "Motion of a sphere in the presence of a plane interface. Part 1. An approximate solution by generalization of the method of Lorentz," *Journal of Fluid Mechanics*, vol. 93, no. 4, pp. 705–726, 1979.

[93] S. E. Spagnolie and E. Lauga, "Hydrodynamics of self-propulsion near a boundary: predictions and accuracy of far-field approximations," *Journal of Fluid Mechanics*, vol. 700, pp. 105–147, 2012.

[94] D. Papavassiliou and G. P. Alexander, "The many-body reciprocal theorem and swimmer hydrodynamics," *EPL (Europhysics Letters)*, vol. 110, no. 4, p. 44001, 2015.

[95] Y. Ibrahim and T. B. Liverpool, "The dynamics of a self-phoretic Janus swimmer near a wall," *EPL (Europhysics Letters)*, vol. 111, no. 4, pp. 48006–48008, 2015.

[96] M. N. Popescu, W. E. Uspal, Z. Eskandari, M. Tasinkevych, and S. Dietrich, "Effective squirmer models for self-phoretic chemically active spherical colloids," *The European Physical Journal E*, vol. 41, no. 12, p. 145, 2018.

[97] A. Mozaffari, N. Sharifi-Mood, J. KOPLIK, and C. Maldarelli, "Self-diffusiophoretic colloidal propulsion near a solid boundary," *Phys. Fluids*, vol. 28, no. 5, pp. 53107–53136, 2016.

[98] C. D. Bain, G. D. Burnett-Hall, and R. R. Montgomerie, "Rapid motion of liquid drops [8]," 1994.

[99] F. D. Dos Santos and T. Ondarçuhu, "Free-running droplets," *Physical Review Letters*, 1995.

[100] S. W. Lee, D. Y. Kwok, and P. E. Laibinis, "Chemical influences on adsorption-mediated self-propelled drop movement," *Physical Review E - Statistical Physics, Plasmas, Fluids, and Related Interdisciplinary Topics*, 2002.

[101] Y. Sumino, H. Kitahata, K. Yoshikawa, M. Nagayama, S. I. M. Nomura, N. Magome, and Y. Mori, "Chemosensitive running droplet," *Physical Review E - Statistical, Nonlinear, and Soft Matter Physics*, vol. 72, no. 4, pp. 1–8, 2005.

[102] P. Lazar and H. Riegler, "Reversible self-propelled droplet movement: A new driving mechanism," *Physical Review Letters*, 2005.

[103] Y. Sumino, N. Magome, T. Hamada, and K. Yoshikawa, "Self-running droplet: Emergence of regular motion from nonequilibrium noise," *Physical Review Letters*, vol. 94, no. 6, pp. 1–4, 2005.

[104] Y. Sumino and K. Yoshikawa, "Self-motion of an oil droplet: A simple physicochemical model of active Brownian motion," *Chaos*, 2008.

[105] K. Ichimura, S. K. Oh, and M. Nakagawa, "Light-driven motion of liquids on a photoresponsive surface," *Science*, 2000.

[106] T. Toyota, H. Tsuha, K. Yamada, K. Takakura, T. Ikegami, and T. Sugawara, "Listeria -like Motion of Oil Droplets ," *Chemistry Letters*, 2006.

[107] M. M. Hanczyc, T. Toyota, T. Ikegami, N. Packard, and T. Sugawara, "Fatty acid chemistry at the oil-water interface: Self-propelled oil droplets," *Journal of the American Chemical Society*, 2007.

[108] Y. J. Chen, Y. Nagamine, and K. Yoshikawa, "Self-propelled motion of a droplet induced by Marangoni-driven spreading," *Physical Review E - Statistical, Nonlinear, and Soft Matter Physics*, 2009.

[109] T. Toyota, N. Maru, M. M. Hanczyc, T. Ikegami, and T. Sugawara, "Self-Propelled Oil Droplets Consuming "Fuel" Surfactant," *Journal of the American Chemical Society*, vol. 131, no. 14, pp. 5012–5013, 2009.

[110] T. Ban, T. Yamagami, H. Nakata, and Y. Okano, "PH-dependent motion of self-propelled droplets due to marangoni effect at neutral pH," *Langmuir*, 2013.

[111] S. Thutupalli, R. Seemann, and S. Herminghaus, "Swarming behavior of simple model squirmers," *New Journal of Physics*, vol. 13, no. 7, p. 73021, 2011.

[112] H. Kitahata, N. Yoshinaga, K. H. Nagai, and Y. Sumino, "Spontaneous motion of a droplet coupled with a chemical wave," *Physical Review E - Statistical, Nonlinear, and Soft Matter Physics*, 2011.

[113] A. N. Zaikin and A. M. Zhabotinsky, "Concentration wave propagation in two-dimensional liquid-phase self-oscillating system," *Nature*, 1970.

[114] Z. Izri, *Experimental study of swimming droplets Physico-chemical and hydrodynamic mechanisms*. PhD thesis, ESPCI Paris, 2014.

[115] S. Herminghaus, C. C. Maass, C. Krüger, S. Thutupalli, L. Goehring, and C. Bahr, "Interfacial mechanisms in active emulsions," *Soft Matter*, vol. 10, no. 36, pp. 7008–7022, 2014.

[116] M. Li, M. Brinkmann, I. Pagonabarraga, R. Seemann, and J.-B. Fleury, "Spatiotemporal control of cargo delivery performed by programmable self-propelled Janus droplets," *Communications Physics*, 2018.

[117] M. J. Comuñas, X. Paredes, F. M. Gaciño, J. Fernández, J. P. Bazile, C. Boned, J. L. Daridon, G. Galliero, J. Pauly, K. R. Harris, M. J. Assael, and S. K. Mylona, "Reference Correlation of the Viscosity of Squalane from 273 to 373 K at 0.1 MPa," *Journal of Physical and Chemical Reference Data*, 2013.

[118] S. M. Greenberg, D. S. Rosenthal, T. A. Greeley, R. Tantravahi, and R. I. Handin, "Characterization of a new megakaryocytic cell line: The Dami cell," *Blood*, 1988.

[119] D. Bartolo, G. Degré, P. Nghe, and V. Studer, "Microfluidic stickers," *Lab on a Chip*, 2008.

[120] P. Zhu and L. Wang, "Passive and active droplet generation with microfluidics: a review," *Lab on a Chip*, 2016.

[121] R. Dangla, E. Fradet, Y. Lopez, and C. N. Baroud, "The physical mechanisms of step emulsification," *Journal of Physics D: Applied Physics*, 2013.

[122] Y. Xia and G. M. Whitesides, "SOFT LITHOGRAPHY," *Annual Review of Materials Science*, 1998.

[123] S. Lopera and R. D. Mansano, "Plasma-Based Surface Modification of Polydimethylsiloxane for PDMS-PDMS Molding," *ISRN Polymer Science*, 2012.

[124] W. Thielicke and E. J. Stamhuis, "PIVlab – Towards User-friendly, Affordable and Accurate Digital Particle Image Velocimetry in MATLAB," *Journal of Open Research Software*, 2014.

[125] R. Lindken, M. Rossi, S. Große, and J. Westerweel, "Micro-Particle Image Velocimetry (PIV): Recent developments, applications, and guidelines," 2009.

[126] K. Drescher, R. E. Goldstein, N. Michel, M. Polin, and I. Tuval, "Direct measurement of the flow field around swimming microorganisms," *Physical Review Letters*, 2010.

[127] A. I. Campbell, S. J. Ebbens, P. Illien, and R. Golestanian, "Experimental observation of flow fields around active Janus spheres," *Nature Communications*, pp. 1–10, 2019.

[128] S. Ketzetzi, J. de Graaf, R. P. Doherty, and D. J. Kraft, "Slip length dependent propulsion speed of catalytic colloidal swimmers near walls," *Phys. Rev. Lett.*, vol. 124, no. 4, p. 048002, 2020.

[129] D. M. Huang, C. Sendner, D. Horinek, R. R. Netz, and L. Bocquet, "Water slippage versus contact angle: A quasiuniversal relationship," *Physical Review Letters*, 2008.

[130] J. R. Blake and A. T. Chwang, "Fundamental singularities of viscous flow," *J. Eng. Math.*, vol. 8, no. 1, pp. 23–29, 1974.

[131] S. Michelin and E. Lauga, "Autophoretic locomotion from geometric asymmetry," *European Physical Journal E*, vol. 38, pp. 7–22, 2015.

[132] E. Yariv, "Wall-induced self-diffusiophoresis of active isotropic colloids," *Physical Review Fluids*, vol. 1, p. 32101, 2016.

[133] N. Liron and S. Mochon, "Stokes flow for a stokeslet between two parallel flat plates," *Journal of Engineering Mathematics*, vol. 10, pp. 287–303, oct 1976.

[134] C. Jin, C. Kru-ger, and C. C. Maass, "Chemotaxis and autochemotaxis of self-propelling droplet swimmers," *Proceedings of the National Academy of Sciences of the United States of America*, 2017.

[135] A. Zöttl and H. Stark, "Nonlinear dynamics of a microswimmer in Poiseuille flow," *Physical Review Letters*, 2012.

[136] L. Zhu, E. Lauga, and L. Brandt, "Low-Reynolds-number swimming in a capillary tube," *Journal of Fluid Mechanics*, 2013.

[137] N. Oyama, J. J. Molina, and R. Yamamoto, "Hydrodynamic alignment of microswimmers in pipes," *arxiv*, pp. 1–11, 2016.

[138] J. Plateau, *Statique experimentale et theorique des liquids soumis aux seules forces moleculaires*. Gauthier-Villars, 1873.

[139] J. W. Strutt, "On the instability of a cylinder of viscous liquid under capillary force.," *PHILOS. MAG.*, vol. 34, pp. 145–154, 1892.

[140] K. Piroird, C. Clanet, and D. Queźreź, "Capillary extraction," *Langmuir*, vol. 27, no. 15, pp. 9396–9402, 2011.

[141] S. Howison, "Practical Applied Mathematics," in *Practical Applied Mathematics*, ch. Chp 16, Cambridge University Press, 2005.

[142] A. Mazouchi and G. M. Homsy, "Thermocapillary migration of long bubbles in cylindrical capillary tubes," *Physics of Fluids*, 2000.

[143] G. I. Barenblatt, *Scaling, self-similarity, and intermediate asymptotics*. Cambridge University Press, 2014.

[144] J. Gratton, *Similarity and self similarity in fluid dynamics*. Fundamentals of Cosmic Physics V15, 1991.

[145] R. Bird, W. Stewart, and E. Lightfoot, *Transport Phenonena*. John Wiley & Sons, 1924.

[146] M. Benzaquen, T. Salez, and E. Raphaël, "Intermediate asymptotics of the capillary-driven thin-film equation," *European Physical Journal E*, 2013.

[147] J. U. Klamser, *Phase trensition at low dimension, at equilibrium and out of equilibrium*. PhD thesis, Sorbonne university, 2018.

[148] M. C. Marchetti, J. F. Joanny, S. Ramaswamy, T. B. Liverpool, J. Prost, M. Rao, and R. A. Simha, "Hydrodynamics of soft active matter," *Reviews of Modern Physics*, 2013.

[149] T. Vicsek and A. Zafeiris, "Collective motion," *Physics Reports*, vol. 517, pp. 71–140, 2012.

[150] S. Ramaswamy, "The Mechanics and Statistics of Active Matter," *Annual Review of Condensed Matter Physics*, 2010.

[151] M. E. Cates and J. Tailleur, "Motility-Induced Phase Separation," *Annual Review of Condensed Matter Physics*, 2015.

[152] P. Gács, "Reliable computation with cellular automata," *Journal of Computer and System Sciences*, 1986.

[153] R. Soto and R. Golestanian, "Run-and-tumble dynamics in a crowded environment: Persistent exclusion process for swimmers," *Physical Review E - Statistical, Nonlinear, and Soft Matter Physics*, 2014.

[154] A. P. Solon and J. Tailleur, "Revisiting the flocking transition using active Spins," *Physical Review Letters*, 2013.

[155] B. Derrida, "An exactly soluble non-equilibrium system: The asymmetric simple exclusion process," *Physics Report*, 1998.

[156] U. Nagel and H. Machemer, "Physical and physiological components of the graviresponses of wild-type and mutant Paramecium tetraurelia," *Journal of Experimental Biology*, 2000.

[157] D. P. Häder, P. R. Richter, M. Schuster, V. Daiker, and M. Lebert, "Molecular analysis of the graviperception signal transduction in the flagellate Euglena gracilis: Involvement of a transient receptor potential-like channel and a calmodulin," *Advances in Space Research*, 2009.

[158] A. M. Roberts, "The mechanics of gravitaxis in Paramecium," *Journal of Experimental Biology*, 2010.

[159] C. Streb, P. Richter, M. Ntefidou, M. Lebert, and D. P. Häder, "Sensory transduction of gravitaxis in Euglena gracilis," *Journal of Plant Physiology*, 2002.

[160] A. M. Roberts and F. M. Deacon, "Gravitaxis in motile micro-organisms: The role of fore-aft body asymmetry," *Journal of Fluid Mechanics*, 2002.

[161] A. M. Roberts, "Mechanisms of gravitaxis in Chlamydomonas," *Biological Bulletin*, 2006.

[162] B. Ten Hagen, F. Kümmel, R. Wittkowski, D. Takagi, H. Löwen, and C. Bechinger, "Gravitaxis of asymmetric self-propelled colloidal particles," *Nature Communications*, 2014.

[163] D. Loi, S. Mossa, and L. F. Cugliandolo, "Effective temperature of active matter," *Physical Review E - Statistical, Nonlinear, and Soft Matter Physics*, 2008.

[164] J. Tailleur and M. E. Cates, "Statistical mechanics of interacting run-and-tumble bacteria," *Physical Review Letters*, 2008.

[165] R. W. Nash, R. Adhikari, J. Tailleur, and M. E. Cates, "Run-and-tumble particles with hydrodynamics: Sedimentation, trapping, and upstream swimming," *Physical Review Letters*, 2010.

[166] F. Rühle, J. Blaschke, J. T. Kuhr, and H. Stark, "Gravity-induced dynamics of a squirmer microswimmer in wall proximity," *New Journal of Physics*, 2018.

Résumé en Français

7.3 Introduction générale

Ce document est un court résumé en français de mon travail de thèse "Swimming water droplets in complex environments, Confinement, gravity and collective effects.", et en présente les principaux résultats. Il est construit de la même manière que le manuscrit de thèse, en deux parties constituées respectivement de trois et quatre chapitres. La première partie se veut pédagogique et présente les bases théoriques et expérimentale de ce travail. La deuxième partie rassemble les résultats obtenus tout au long de la thèse sur les axes de recherche suivants: la nage en 2D, la nage en 1D, les effets collectifs en 1D et la nage sous gravité.

7.4 Contextes experimental et théorique

Ces chapitres introductifs ont pour but de présenter les enjeux de ce travail, mais aussi le système étudié et les mécanismes physiques principaux qui vont nous intéresser.

7.4.1 Nager, un enjeux biologique et physique

Les systèmes vivants présentent un certain nombre de points communs, qui sont jugés être les ingrédients indispensables à la vie: la compartimentation, grandir et se diviser, traiter des informations, transformer de l'énergie et pouvoir s'adapter (bouger).

Un des enjeux de la création de cellules artificielles est de regrouper tous ces ingrédients dans un seul système. L'une des techniques utilisée est la technique "de bas en haut", qui consiste à partir de systèmes physiques ou chimiques simples et à les complexifier. En particulier, des systèmes de gouttes, trivialement compartimentées, ont été utilisés pour reproduire chacune des caractéristiques citées plus haut, bien que jamais toutes en même temps.

Le système auquel nous nous intéressons dans ce travail est une goutte active, qui va puiser de l'énergie dans son environnement pour produire des flux à son interface et se propulser. Ce système présente donc trois des caractéristiques du vivant (compartimentation, transformation d'énergie et adaptation), ce qui font d'elles un système modèle simple particulièrement intéressant pour étudier certaines caractéristiques des

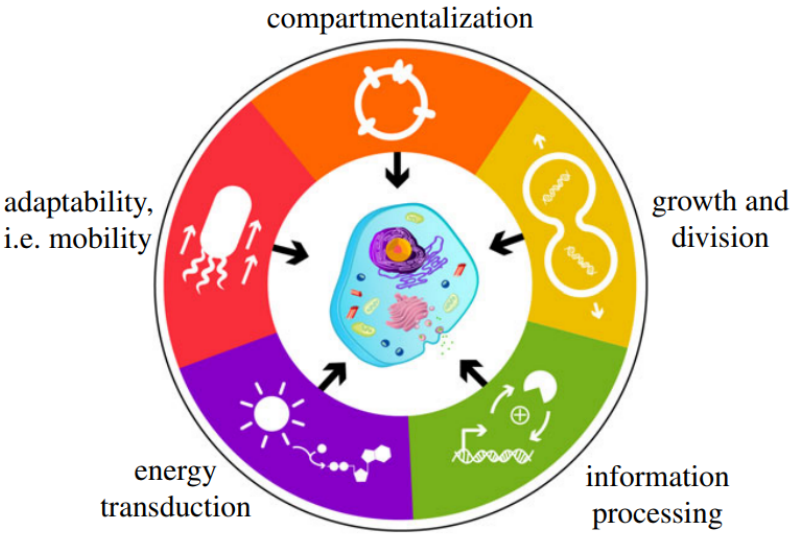

Figure 7.12: **Figure 1 de [3], les signatures du vivant:** un résumé des cinq caractéristiques requises pour qu'un système vive.

micro-organismes, et en particulier, ce sur quoi nous allons nous concentrer, la motilité.

7.4.2 Théorie générale

Nous introduisons tout d'abord les notions théoriques nécessaires à la compréhension du phénomène de nage. Pour se déplacer, le micro-nageur déplace le fluide extérieur. Le problème hydrodynamique est régi par l'équation de Stokes. Dans le cas d'un problème axisymétrique loin de tout bord, la résolution du problème hydrodynamique autour d'un objet sphérique montre que le champ de vitesse est la superposition d'une infinité de symétries azimutales (monopole, dipole, quadripole, etc). L'amplitude de ces symétries est déterminée par les conditions aux limites à l'interface entre l'objet et le fluide extérieur. Seule la symétrie dipolaire (symétrie avant-arrière) conduit à un déplacement net de l'objet.

Les conditions aux limites à l'interface de l'objet, dans le cas d'une goutte, sont une vitesse de glissement, un saut de contrainte, ainsi que le bilan des forces sur la goutte. La vitesse de la goutte est alors la combinaison de la moyenne des vitesses de glissements et des sauts de contraintes à l'interface, et d'une éventuelle force extérieur, le tout donné par la formule dite de Lamb.

Le modèle le plus communément utilisé pour des nageurs est le modèle du squirmer, dont les conditions aux limites sont fixées. Ce modèle limite aussi souvent la description du champ hydrodynamique aux seules symétries dipolaire (responsable de la nage) et quadripolaire (responsable des interactions à longue portée).

Dans le cas d'un nageur physique, la vitesse de glissement et le saut de contrainte peuvent avoir pour origine une action physique (ex: des flagelles) ou une interaction physico-chimique, à l'échelle de l'interface entre l'objet et le liquide extérieur. Cette interaction a lieu dans une couche interfaciale d'épaisseur finie, mais petite par rapport à l'objet, dans laquelle, par exemple, des gradients de concentration mettent en mouvement le fluide (effets phorétiques ou Marangoni).

Un nageur est un objet qui induit lui-même ces conditions aux limites pour produire un mouvement. Le nageur doit alors briser la symétrie isotrope pour partir dans une direction privilégiée. Cette brisure de symétrie peut être géométrique (cas des particules de Janus), ou résulter d'une instabilité (cas des gouttes nageuses). Il est important de noter que dans ce dernier cas, les conditions aux limites sont couplées à l'hydrodynamique.

Une influence extérieure peut aussi briser la symétrie (ex: un mur, la gravité...). Dans le cas d'une goutte nageuse, à cause du couplage entre l'hydrodynamique et les conditions aux limites, cette influence a de grandes chances d'influer sur l'activité du nageur, et donc de modifier effectivement sa nage.

7.4.3 Goutte d'eau nageuses

7.4.3.1 Présentation des gouttes d'eau pure nageuses

Le système étudié a été découvert durant la thèse de Ziane Izri [87]. Il s'agit de gouttes d'eau pure dans une solution de 25mM de mono-oleine (un tensioactif) dans du squalane (une phase huile). Ces gouttes se mettent à nager dès leur production. La Fig. 7.13 présente le comportement typique de ces gouttes. La nage de ces gouttes est

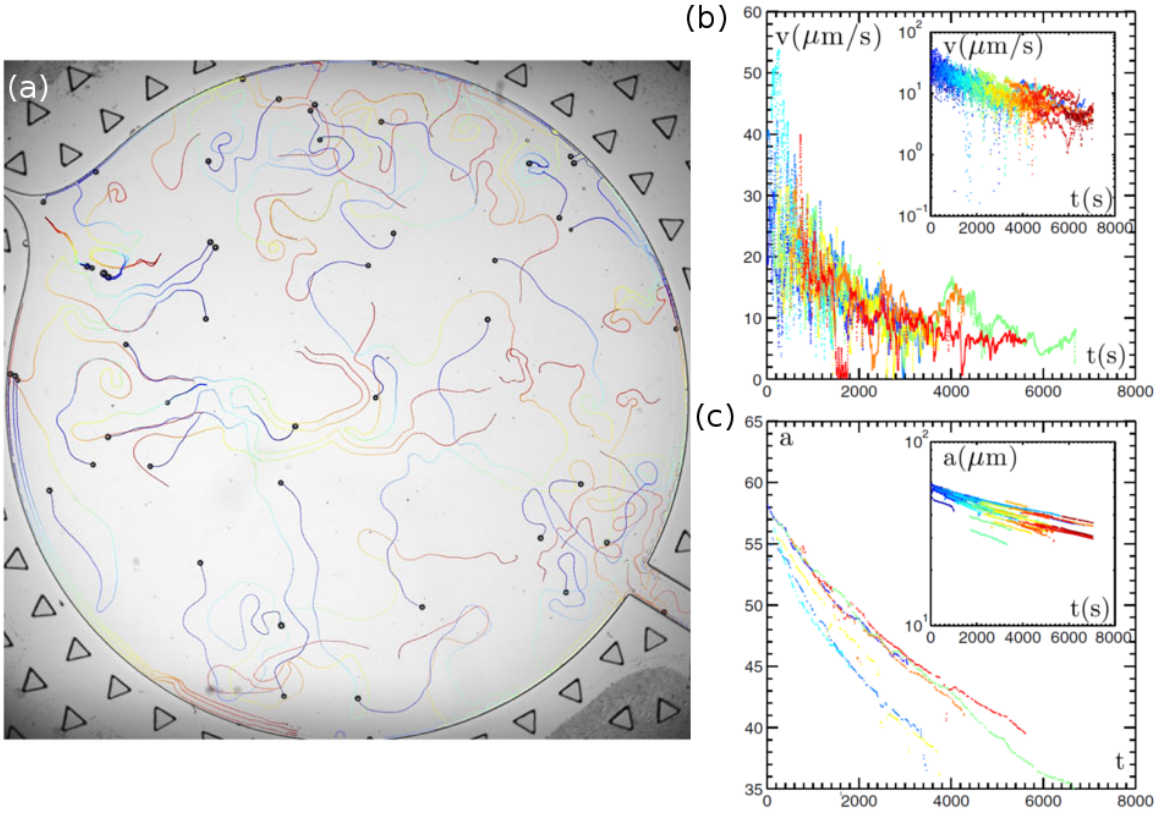

Figure 7.13: **Figures de [87] Nage de gouttes d'eau pure:** (a) trajectoires d'une cinquantaine de gouttes d'eau de rayon ~ 50 μm dans une chambre d'observation de 1 cm remplie d'une solution de 25mM de mono-oleine dans du squalane, d'une durée de 500 s. Le code couleur représente le temps. (b) Vitesse et (c) diamètre des gouttes au cours du temps pour une sélection de huit trajectoires. En insert: courbe linéaire-log pour une sélection de 35 trajectoires.

due à trois phénomènes:

(i) Une relaxation thermodynamique: dans la phase huile (squalane), le surfactant (mono-oleine) est présent en grande concentration, ($\sim$ 5 CMC), et va former des micelles. Le système goutte d'eau + micelles n'est pas à l'équilibre: un flux d'eau s'établit spontanément entre la goutte et les micelles proches de l'interface, ce qui produit des micelles gonflées en eau.

(ii) Des flux phorétiques: ces micelles gonflées interagissent avec l'interface. Leur gradients produisent des flux, principalement phorétiques, et mettent le fluide en mouvement.

(iii) Une instabilité: le couplage entre les champs de concentration et l'hydrodynamique donne lieu à une instabilité qui met en mouvement la goutte.

En conséquence, les gouttes nagent et se vident lentement (en quelques heures).

7.4.3.2 Réalisation expérimentale

En fonction des besoins, nous utilisons deux méthodes de production des gouttes:

- Pour générer des gouttes uniques, nous utilisons un femtojet qui permet de former par contrôle de pression une goutte à l'embout d'une aiguille, directement dans la chambre d'observation remplie de la phase d'huile.

- Pour générer de nombreuses gouttes, nous utilisons des circuits microfluidiques. La combinaison d'une jonction en T, et d'un saut de hauteur permet de créer des gouttes qui sont ensuite amenées dans la zone d'observation.

Nous disposons aussi de deux méthodes d'observations:

- Pour observer des zones larges (1 cm^2), nous utilisons un macroscope en lumière blanche, ce qui nous permet d'observer les longues trajectoires des gouttes.

- Pour visualiser des champs de vitesse, nous utilisons la microscopie confocale en fluorescence, ce qui nous permet de suivre des traceurs dans un plan précis près de la goutte.

Enfin, un des enjeux de ce travail est de regarder l'influence de la géométrie sur la nage des gouttes, nous avons donc fabriqué des chambres d'observation très variées;

- en 2D: des grandes chambres de natures du mur du fond différentes (verre, verre silanizé, PDMS, NOA).

- en 1D: dans des capillaires carrés ou circulaires, ou encore des géométries plus exotiques telles que des constrictions.

7.5 Travaux expérimentaux et théoriques

Nous présentons dans ces chapitres une sélection des expériences menées au cours de ce travail, ainsi que des outils théoriques permettant d'appréhender les phénomènes physiques en jeu.

7.5.1 Nage en 2D

Que ce soit dans un environnement naturel, ou dans un circuit microfluidique, les micro-nageurs évoluent souvent dans des milieux bornés, constitués d'obstacles et de parois, et de nombreuses observations ont montré l'importance critique de ce confinement sur la dynamique des nageurs.

Nos gouttes sont plus denses que le milieu environnant, et nagent donc naturellement près du mur du fond de la chambre. Nous nous intéressons dans ce chapitre au comportement d'une goutte nageuse unique en chambre microfluidique, en particulier à l'effet du mur du fond et du confinement.

7.5.1.1 Cinétique en présence d'un mur

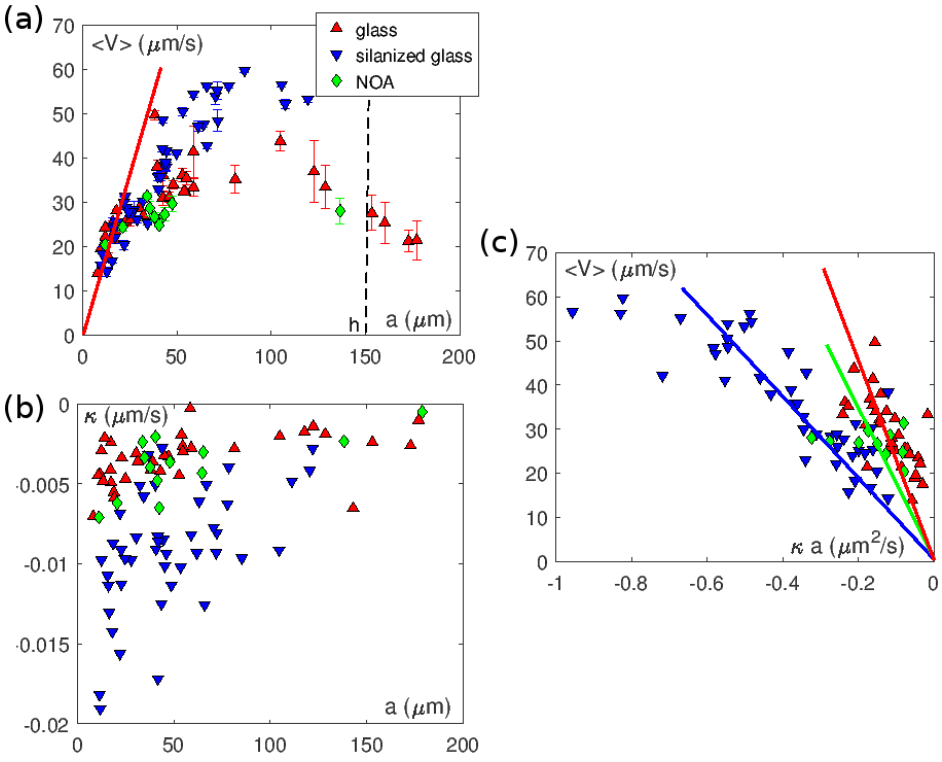

Figure 7.14: Étude de la nage stationnaire, pour différentes natures de mur de fond: lame de verre (triangles droits rouges), lame de verre silanizée (triangles inverses bleus), couche de NOA (losanges verts). (a) Vitesse stationnaire en fonction du rayon des gouttes a. La ligne rouge continue représente la pente aux petits rayons. La ligne verticale pointillée noir représente la hauteur de la chambre. (b) vitesse de dégonflement de la goutte $\kappa = \frac{da}{dt}$ en fonction de son rayon. (c) Vitesse de la goutte en fonction de la quantité $a\kappa$.

Nous plaçons une goutte d'eau unique dans une chambre de typiquement 1 cm de rayon remplie de la solution huile+micelles. Dès qu'elle est formée, la goutte se met à nager, et atteint une vitesse constante après quelques centaines de secondes. Un certain nombre de phénomènes peuvent venir perturber l'état stationnaire de la goutte; en particulier (i) la rencontre avec la paroi de la chambre, la goutte ralentit alors et rebondit ou s'aligne avec le mur, et (ii) la rencontre avec sa trace, qu'elle évite - la goutte remplissant les micelles sur son passage, elle laisse derrière elle une trace de micelles gonflées, qui constitue une zone répulsive pour la goutte. La goutte peut aussi s'auto-empoisonner: rester bloquée par sa propre trace pendant plusieurs minutes.

En dehors ces événements, la goutte de taille a a un comportement stationnaire, et nous mesurons dans ce régime la vitesse moyenne de la goutte $\langle V \rangle$, et sa vitesse de dégonflement $\kappa = \frac{da}{dt}$, pour différentes natures de mur du fond. Les résultats sont présentés Fig. 7.14. Nous faisons quelques observations: la vitesse des petites gouttes ($a < 50$ μm) augmente avec leur taille, quelque soit le mur du fond, ce qui va dans le même sens que la prédiction théorique pour des gouttes évoluant en 3D loin de tout mur. La vitesse des gouttes de tailles intermédiaires ($50 < a < 100$ μm) augmente avec leur taille, mais dépend de la nature du mur du fond: la goutte est plus rapide lorsque le fond est hydrophobe. Cela montre que ces gouttes interagissent avec le mur du fond. La vitesse des grosses gouttes ($a > 100$ μm) diminue avec leur taille, cela montre que le confinement a un effet sur le comportement des gouttes.

7.5.1.2 Visualisation du champ de vitesse autour de la goutte

Les résultats de cette partie ont été l'objet d'un article [1]. Ici, nous profitons de la taille relativement grosse de nos nageurs (~ 100 μm), pour effectuer les premières mesures tri-dimensionnelles du champ de vitesse autour d'un micro-nageur.

Pour visualiser le champ de vitesse, nous ensemençons le fluide extérieur de colloides fluorescents de taille 0.6 μm; puis nous visualisons leur déplacement dans un plan précis parallèle au mur du fond par imagerie confocale. La Fig. 7.15 montre la reconstitution en 3D de ce champ de vitesse autour de la goutte. Une première observation est que contrairement au cas 3D, le champ de vitesse n'est pas axisymmetrique: les champs sont modifiés par la présence du mur.

Représentation des champs expérimentaux

Les champs de vitesse gardent dans chaque plan une symétrie axiale, et présentent certaines symétries azimutale. Nous avons donc choisi de décomposer ce champ de vitesse en ses symétries azimutales principales, la symétrie monopolaire, la symétrie dipolaire et la symétrie quadripolaire. Le haut de la Fig. 7.16 montre cette décomposition dans le cas du plan médian de la goutte, ainsi que la somme des symétries principales, qui est en effet très semblable au champ total (on peut se restreindre à ces trois symétries pour décrire le champ de vitesse). Chacune de ces symétries est le produit d'une dépendance azimutale, appelée les polynômes de Legendre $L_n(\cos\theta)$[1] et qui caractérise la symétrie, ainsi que d'une dépendance radiale, que l'on appelle l'amplitude de la symétrie $\phi_n(\rho, z)$. Nous extrayons ces amplitudes dans chaque plan, et nous les représentons en bas de la Fig. 7.16.

[1] n est l'ordre de la symétrie, n=0 pour le monopole, n=1 pour le dipôle et n=2 pour le quadrupole

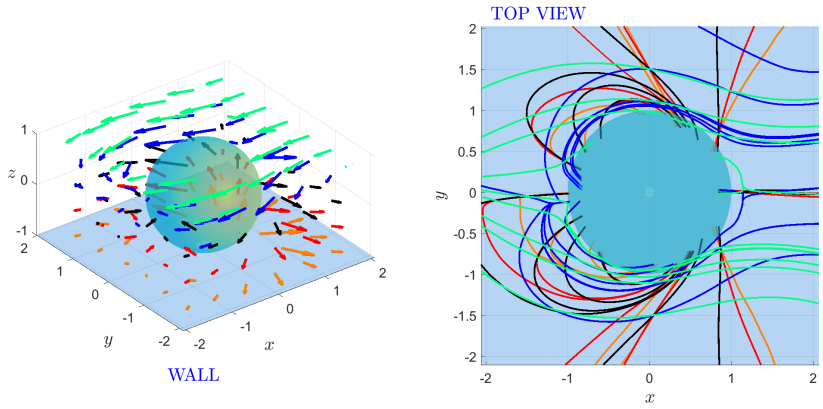

Figure 7.15: Champ de vitesse expérimental autour d'une goutte nageant proche et parallèle au mur du fond. **A gauche**: reconstruction 3D de la PIV dans les plans parallèles au mur (plan bleu). **A droite**: Vue de haut des lignes de courant du champ de vitesse. Les couleurs codent la distance du plan au mur; par souci de clarté, seuls certains plans sont représentés.

Ces amplitudes présentent un certain nombre de particularités, des extrémas locaux qui évoluent en fonction de ρ et de z, et vont caractériser entièrement le champ de vitesse. Comprendre l'origine de ces particularités va donc permettre de comprendre ce qui contribue au champ de vitesse.

Comparaison avec le modèle du squirmer

Nous développons dans un second temps un modèle théorique, dont le but est de retrouver les caractéristiques observées expérimentalement.

Le modèle étudié est celui du squirmer, qui loin de tout mur produit un champ de vitesse qui est la somme d'une symétrie dipolaire et d'une symétrie quadripolaire. Nous prenons en compte la présence du mur en utilisant la méthode des images. Cette méthode consiste à calculer l'image du champ hydrodynamique de chaque symétrie à travers le mur, de telle sorte que la vitesse au mur soit nulle. Cette méthode est une approximation, puisque les conditions aux limites à l'interface du nageur ne sont alors plus vérifiées. Il est intéressant de noter que l'image d'une certaine symétrie peut conduire à des champs de vitesses aux symétries plus complexes. Nous calculons le champ de vitesse théorique totale, puis le décomposons de la même manière que pour le champ expérimental, en haut de la Fig. 7.17., puis nous extrayons leurs amplitude, en bas de cette même figure.

Les amplitudes ainsi obtenues pour les symétries dipolaire et quadripolaire se comportent quantitativement comme celles mesurées expérimentalement. Il est intéressant de noter que ce modèle produit aussi une symétrie monopolaire qui n'existait pas à priori en l'absence de mur. Cependant cette l'amplitude du monopole est très faible comparé à l'amplitude expérimentale.

Influence de la gravité

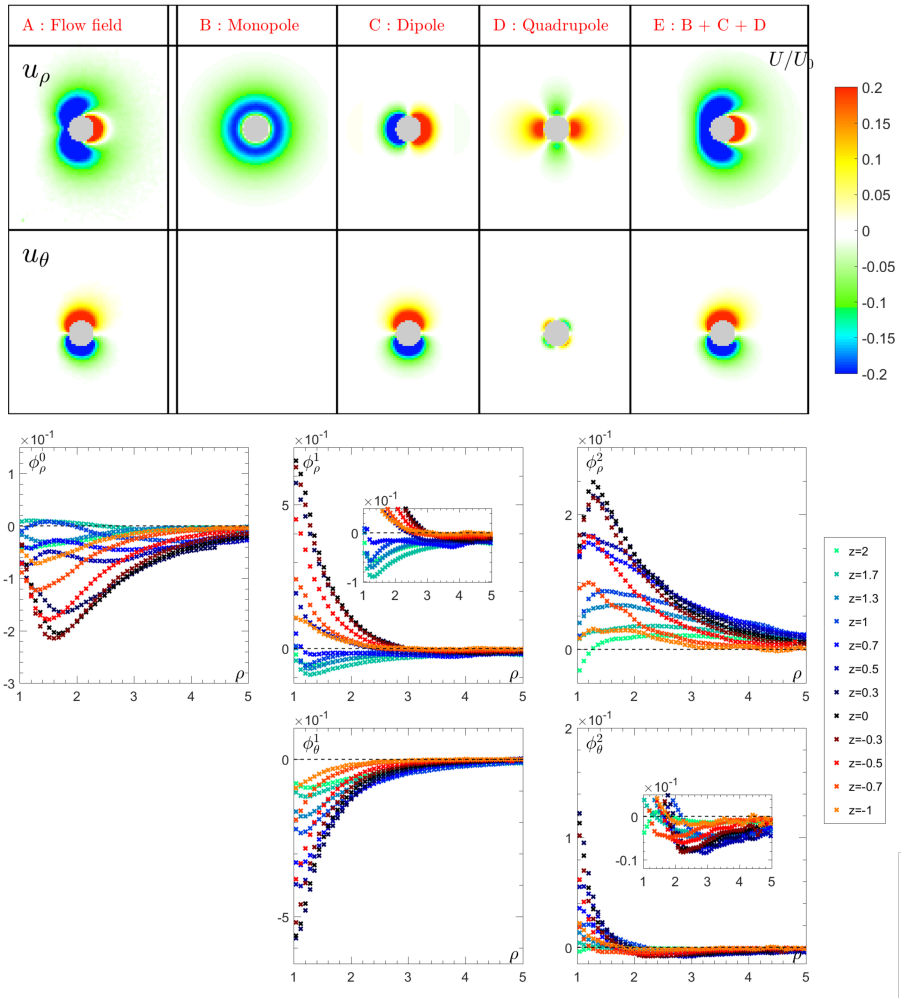

Figure 7.16: Représentation des champs expérimentaux: **En haut**: u_ρ et u_θ dans le plan médian ($z = 0$). Nous montrons le champ de vitesse complet (A) ainsi que sa décomposition en symétries azimutales: (B) la composante monopolaire, (C) la composante dipolaire et (D) la composante quadipolaire, et enfin la somme des symétries (B), (C) et (D) est montrée en (E). **En bas:** les amplitudes $\phi_\rho(\rho, z)$ et $\phi_\theta(\rho, z)$ pour chacune des symétries azimutales, en fonction de la distance à la goutte ρ, et pour différents plans en z (code couleur).

Pour comprendre d'où vient le monopole expérimental, il faut se rappeler que les champs de vitesses sont générés par les gradients de concentration en micelle gonflée à l'interface de la goutte. Donc le mur va avoir un effet non seulement sur les champs de vitesses, ce qui a été pris en compte précédemment, mais aussi sur les champs de concentrations. Qualitativement, la présence du mur va créer une accumulation de micelles gonflées près du mur, et donc un gradient vertical de concentration. Ce gradient vertical devrait soulever la goutte. Cependant, notre goutte est pesante, et donc maintenue près du mur par la gravité. Ces deux effets vont se compenser à l'interface de la goutte: nous n'observons pas de mouvement verticale des gouttes, sauf pour les très petites gouttes. Par contre, ils vont créer des flux autour de la goutte, que l'on peut calculer, et le champ de vitesse ainsi généré a une symétrie purement monopolaire (dans les plans parallèles au mur). La Fig. 7.18 compare l'amplitude du monopole expérimental à l'amplitude du monopole théorique, qui prend en compte les

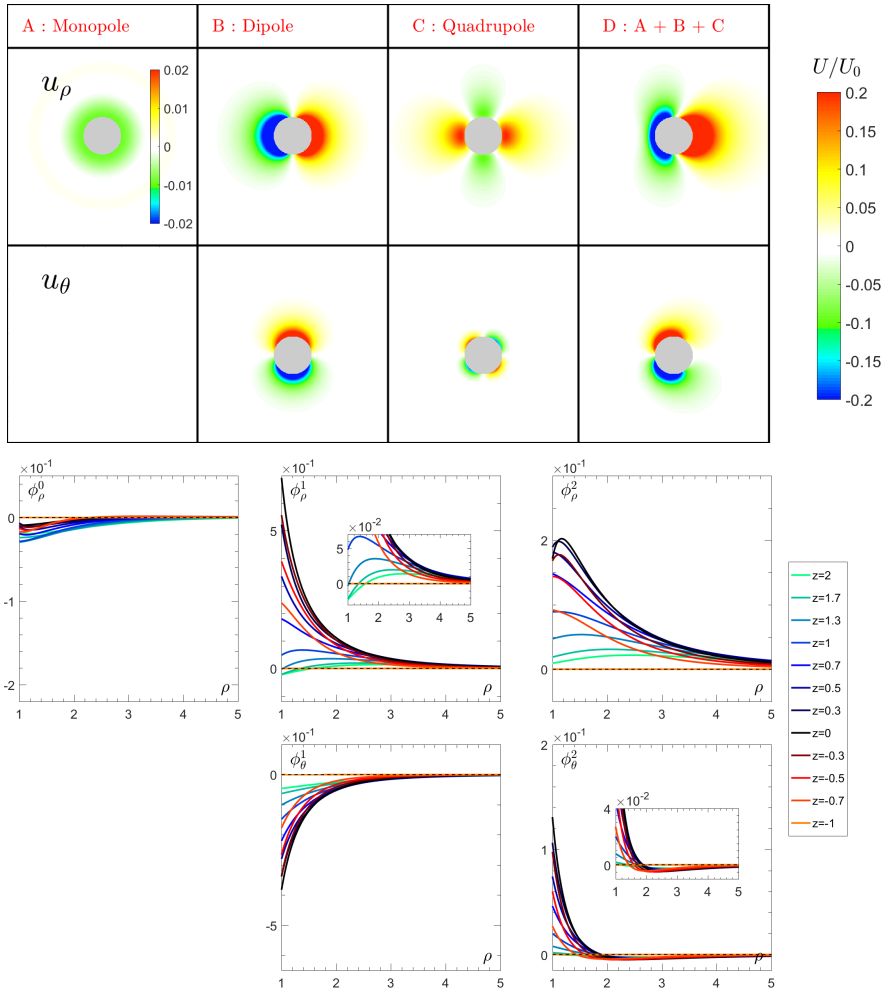

Figure 7.17: Représentation des champs théoriques: **En haut**: u_ρ et u_θ dans le plan médian ($z = 0$). Nous montrons (A) la composante monopolaire, (B) la composante dipolaire et (C) la composante quadipolaire, et enfin la somme des symétries (A), (B) et (C) est montrée en (D). **En bas:** les amplitudes $\phi_\rho(\rho, z)$ et $\phi_\theta(\rho, z)$ pour chacune des symétries azimutales, en fonction de la distance à la goutte ρ, et pour différents plans en z (code couleur).

effets d'un flux phorétique vertical compensé par la gravité. Ces amplitudes ont des comportements très similaires.

7.5.1.3 Conclusion

Nous avons présenté brièvement la cinétique de gouttes nageant près d'un mur. Nous avons aussi caractérisé le champ de vitesse généré autour de ces gouttes, mettant en évidence l'influence du mur sur le champ de vitesse, ainsi qu'un effet inattendu, la conjugaison de l'effet du mur sur le champ de concentration et de la gravité. Ces derniers n'ont pas d'influence directe sur la trajectoire de la goutte, mais créent un monopole fort qui domine à longue distance, et donc va être déterminant pour l'étude des interactions entre nageurs.

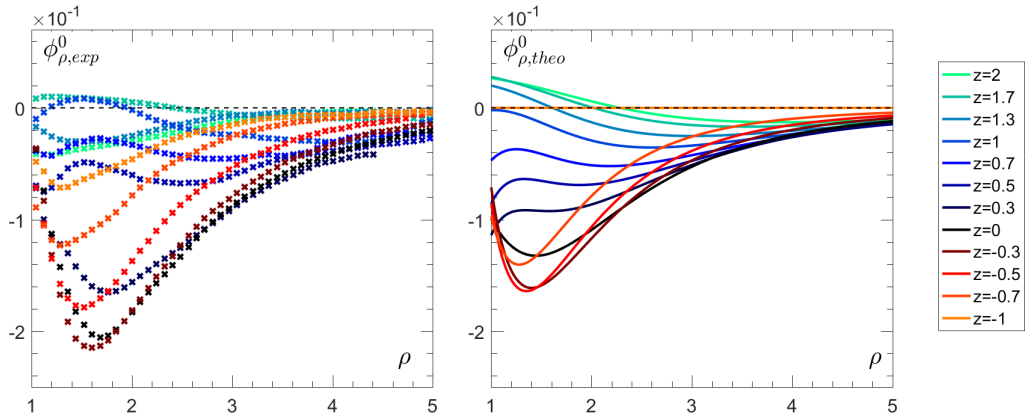

Figure 7.18: Amplitude de la symétrie monopolaire: **A gauche:** amplitude de la composante monopolaire du champ expérimental, et **à droite**: amplitude de la composante monopolaire du champ théorique autour d'un squirmer axisymétrique pour lequel des flux phorétiques perpendiculaires au mur se développent, tandis que le nageur est maintenu au mur par la gravité.

7.5.2 Nage en 1D

Les gouttes nageuses pourraient être utilisées en microfluidique pour une multitude de taches (transport, mélange...). De plus, la géométrie 1D est un moyen de diriger des gouttes nageuses. D'un autre coté, un trop grand confinement risque de limiter la place nécessaire à l'induction de flux; et donc de rendre plus difficile la nage. L'étude de nageur en géométrie 1D présente donc un intérêt certain.

Nous présentons ici une série d'études expérimentales complétées de considérations théoriques sur le comportement d'une goutte nageuse dans diverses géométries 1D.

7.5.2.1 Capillaire carré

Les canaux microfluidiques ayant généralement une section carrée, nous nous intéressons tout d'abord au comportement de gouttes nageuses en capillaire carré. Dans un capillaire carré de demi-hauteur h variant de 40 à 200 μm, et rempli de la solution huile+micelle, nous observons une goutte d'eau unique de taille L variant entre $0.1h$ (goutte sphérique) et $16h$ (goutte allongée). Des images de telles gouttes sont données Fig. 7.19(a). Toutes les gouttes ainsi produites nagent. Nous mesurons la vitesse de nage V représentée en fonction du confinement que subi la goutte $\frac{L}{2h}$, dans la Fig. 7.19(b).

Nous observons que les données forment une seule courbe (la vitesse ne dépend que du confinement). Globalement, la vitesse diminue avec le confinement. Nous distinguons trois comportements en fonction du confinement: (i) les petites gouttes ($\mathbf{\frac{L}{2h} < 1}$) ont une trajectoire 2D, elles oscillent périodiquement entre les deux parois du capillaire. La vitesse des gouttes varie beaucoup pendant une période d'oscillation, ce qui explique la disparité des vitesses lorsque le confinement est faible. (ii) Les gouttes qui ont typiquement la taille du capillaire ($\mathbf{1 < \frac{L}{2h} < 2}$) ont une trajectoire droite dans une direction fixée. La vitesse diminue beaucoup quand le confinement augmente. La goutte se déforme et s'allonge. (iii) Les longues gouttes ($\mathbf{2 < \frac{L}{2h}}$) ont une trajectoire droite dans une direction fixée. Même les très longues gouttes nagent. La vitesse des

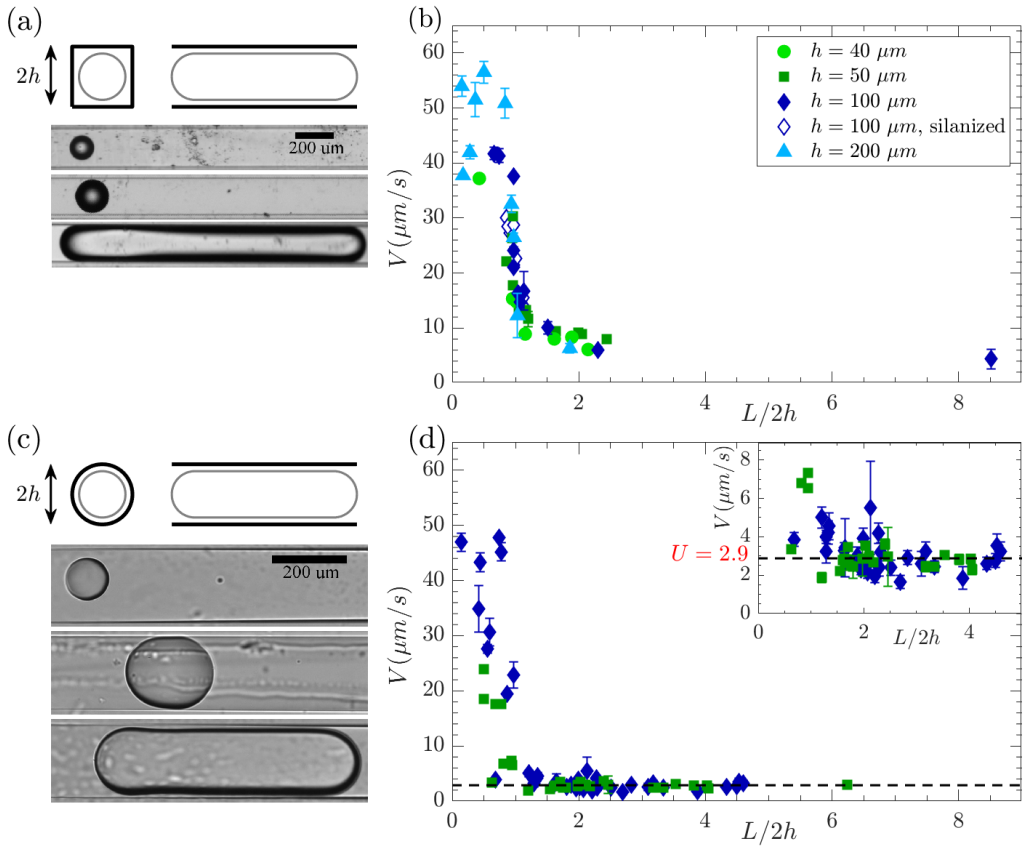

Figure 7.19: Schéma et images de gouttes de différentes tailles (a) en capillaire carré, et (c) en capillaire circulaire, et images de gouttes de différentes longueurs. Vitesse V de gouttes nageant (b) en capillaire carré et (d) en capillaire circulaire en fonction du confinement des gouttes $\frac{L}{2h}$, pour différentes demi-hauteurs de capillaires h. Les bars d'erreur représentent l'écart type à la moyenne temporelle sur la durée d'une expérience.

gouttes converge vers une valeur finie $V_{lim} \sim 5$ μm/s lorsque le confinement augmente.

Nous avons aussi réalisé de la PIV pour visualiser le champ de vitesse autour des gouttes. Sans entrer dans les détails, les principaux résultats sont que la goutte modifie le fluide extérieur sur une distance typique de quelques diamètres de goutte, avec un comportement longue porté répulsif.

7.5.2.2 Capillaire circulaire

D'un point de vue analytique, la géométrie circulaire est bien plus facile à considérer. Nous nous intéressons maintenant à de telles géométries. Dans un capillaire circulaire silanizés de rayon h variant de 50 à 100 μm, et rempli de la solution huile+micelle, nous observons une goutte d'eau unique de taille L variant entre $0.1h$ (goutte sphérique) et $12h$ (goutte allongée). Des images de telles gouttes sont données Fig. 7.19(c). Toutes les gouttes ainsi produites nagent. Nous mesurons la vitesse de nage V représentée en fonction du confinement que subi la goutte $\frac{L}{2h}$, dans la Fig. 7.19(d).

Le résultat est très similaire à celui observé en capillaire carré. Les données forment

une seule courbe (la vitesse ne dépend que du confinement). Globalement, la vitesse diminue avec le confinement. Nous distinguons deux comportements en fonction du confinement: (i) les petites gouttes ($\frac{\mathbf{L}}{\mathbf{2h}} < \mathbf{1}$) ont une trajectoire 3D, elles oscillent sur les parois du capillaire. La vitesse des goutte varie beaucoup pendant une période d'oscillation, ce qui explique la disparité des vitesses lorsque le confinement est faible. (ii) Les longues gouttes ($\frac{\mathbf{L}}{\mathbf{2h}} > \mathbf{1}$) ont une trajectoire droite dans une direction fixée. Même les très longues gouttes nagent. La vitesse des gouttes converge vers une valeur finie $V_{lim} \sim 2.5$ μm/s lorsque le confinement augmente.

Les longues gouttes présentent une forme particulière, Fig. 7.20(c): contrairement à ce qui était observé dans les capillaires carrés, le long de la goutte (exceptées les extrémités) n'a pas la forme d'un cylindre droit, mais est de courbure variable, et en particulier on observe à l'arrière de la goutte une zone de rétrécissement local de l'épaisseur la goutte, que l'on appelle le cou.

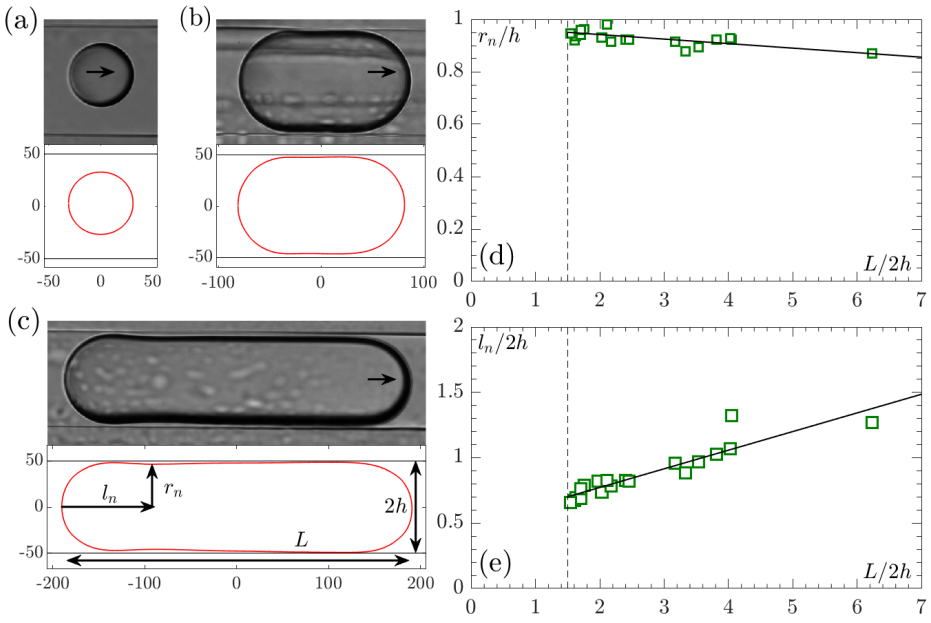

Figure 7.20: Caractérisation de la forme de gouttes en capillaires circulaires. (a), (b) et (c) image et détection du contour de gouttes de différentes tailles $\frac{L}{2h} = 0.5$ (a), $\frac{L}{2h} = 2$ (b), $\frac{L}{2h} = 6$ (c). Évolution (d) du rayon du cou r_n et (e) de sa position l_n avec le confinement pour les longues gouttes.

Nous mesurons l'évolution de cette forme particulière en fonction du confinement; plus particulièrement, nous mesurons le rayon du cou r_n (Fig. 7.19(d)), et sa position par rapport à l'arrière de la goutte l_n (Fig. 7.19(e)). Nous observons en particulier que le cou se creuse lorsque le confinement augmente, et que sa position évolue.

7.5.2.3 Capillaire étiré

Pour étudier plus précisément l'évolution de la forme des gouttes en fonction du confinement, nous utilisons des capillaires étirés, dont le rayon varie continument entre $h = 50\mu$m et une valeur minimum h_{min} (canal convergent), puis de h_{min} à 50μm (canal divergent).

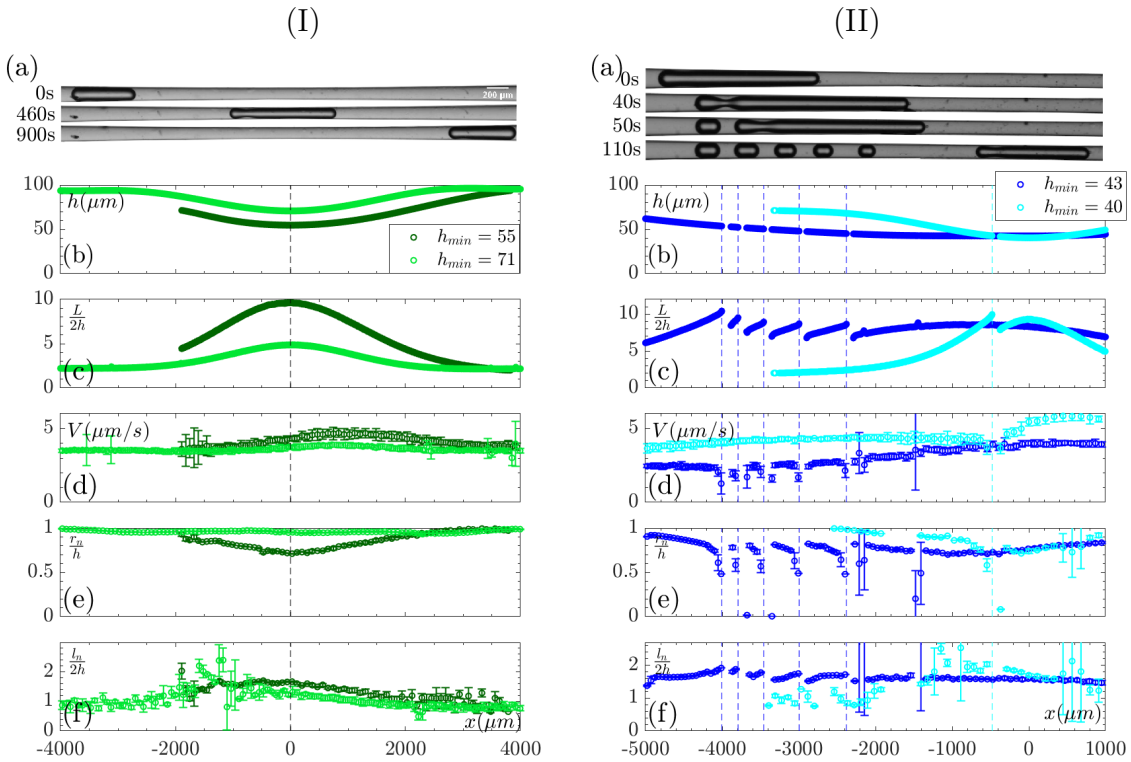

Figure 7.21: **Comportement de gouttes nageant dans des capillaires étirés:** les deux capillaires ont un gradient $\frac{dh}{dx} = 0.02$. **I** - Élongation - la goutte s'allonge puis rétréci le long du capillaire. **II** - Division: La goutte se divise spontanément, elle se divise au niveau du cou, ce qui forme derrière elle des gouttes "filles" qui ne nagent pas. (a) Images de la goutte au cours du temps. Évolution (b) du rayon du capillaire, (c) de la longueur de la goutte, (d) de la vitesse de la goutte, (e) du rayon du cou et (f) de la position du cou en fonction de la position de la goutte dans le capillaire étiré.

En fonction de l'étroitesse du capillaire, deux cas de figure se présentent. (i) Quand le capillaire n'est pas trop étroit (Fig. 7.21(I)), par conservation de volume, la goutte s'allonge dans la partie convergente du canal, puis rétréci dans la partie divergente. (ii) Quand le capillaire est étroit (Fig. 7.21(II)), la goutte commence à s'allonger dans la partie convergente, puis se divise spontanément au niveau du cou, laissant derrière elle une goutte "fille" qui ne nage pas, la goutte "mère" continue à nager et à s'allonger, et peut subir plusieurs divisions successives; jusqu'à ce qu'elle parvienne à la partie divergente, où elle rétrécit.

Étude d'une simple élongation

Intéressons nous plus précisément à la forme de la goutte. En l'absence de division, le cou de la goutte se creuse continument dans la partie convergente du canal, puis s'épaissit de nouveau dans la partie divergente (7.21(I,e)). Cela signifie que la présence de ce cou est due à un phénomène stable et réversible. Si l'on regarde plus précisément l'évolution de ce cou avec le confinement, on s'aperçoit que l'épaisseur du cou varie de manière non triviale avec le confinement.

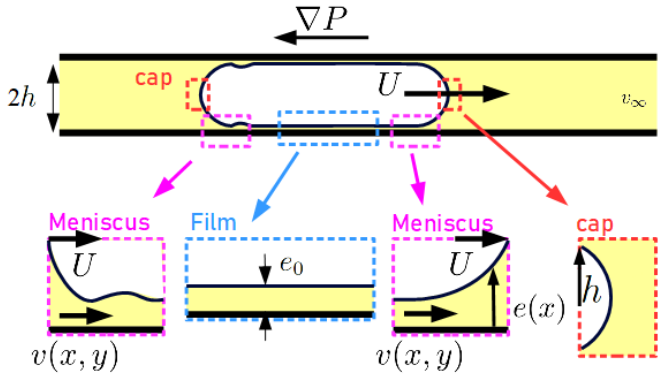

Figure 7.22: L'approche de Bretherton consiste à séparer la goutte en cinq zones, deux calottes sphériques (pointillés rouges), un film de lubrification (pointillés bleus), et deux ménisques dynamiques (pointillés violets).

Pour mieux comprendre les phénomènes physiques en jeu, nous pouvons avancer quelques considérations théoriques. Une approche classique de l'étude de gouttes mobiles (historiquement poussées par un gradient de pression) peu visqueuses en tube circulaire est la méthode de Bretherton, illustrée Fig. 7.22.

La goutte est divisée en cinq zones, deux calottes sphériques, un film de lubrification d'épaisseur constante, et deux ménisques dynamiques qui raccordent les zones précédentes. La courbure de la goutte varie le long des ménisques dynamiques, ce qui génère des gradients de pression, et donc des flux. Résoudre ces flux permet d'obtenir l'équation qui gouverne la forme des ménisques $E''' = \frac{1-E}{E^3}$. Après résolution et ajustement asymptotique avec les hémisphères et le film de lubrification, on trouve en particulier que le ménisque arrière présente une oscillation très semblable à ce que nous avons appelé le cou dans nos expériences; mais contrairement aux expériences, cette forme ne dépend pas du confinement de la goutte.

Dans le cas des gouttes nageuses, la source de motilité n'est pas un gradient de pression global, mais des gradients de concentrations locaux qui génèrent des flux phorétiques. Nous utilisons la même approche que Bretherton en prenant en compte l'activité de la goutte. Les résultats obtenus présentent deux différences majeurs avec le cas classique.

(i) L'équation qui gouverne la forme des ménisques dynamiques est $E''' = \frac{1-E^2}{E^3}$. Après résolution et ajustement asymptotique avec les hémisphères et le film de lubrification, on trouve que les formes des ménisques sont différentes, mais qualitativement similaires au cas classique de Bretherton (le ménisque arrière présente une oscillation).

(ii) A cause de l'advection-diffusion des micelles dans le film de lubrification, les gradients de micelles diminuent le long de la goutte. Les champs de vitesse vont donc diminuer le long de la goutte, provoquant, par conservation du flux, un épaississement du film de lubrification. Ce phénomène a pour conséquence que plus la goutte est longue, plus elle est fine au niveau du ménisque dynamique arrière, et donc plus le cou est prononcé; c'est ce qui est observé expérimentalement.

Étude de la division

La division de la goutte se fait toujours à hauteur du cou, et est précédée par son rétrécissement rapide et irréversible (Fig. (7.21)(II,e)). Il est probable que si le cou est trop prononcé, la forme de la goutte devienne instable, et que donc la goutte entre dans un régime dynamique d'amincissement du cou qui conduit à la division.

7.5.2.4 Constriction carrée

Nous avons regardé précédemment des gouttes dans un capillaire dont le rayon variait continument et lentement. Il est intéressant de se demander ce qu'il se passerait si on variait abruptement la taille du capillaire. Nous étudions ici la nage de goutte dans une constriction carrée, composée d'un canal d'entrée de demi-hauteur $w_{in} = 50$ μm, et de canal de sortie de hauteur variable w_{out} plus petite.

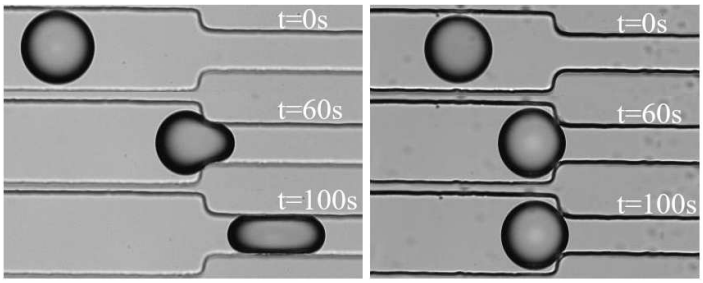

Figure 7.23: **Images de gouttes à une constriction:** A gauche: goutte qui passe à travers une constriction $w_{out} = 50$ μm et (b) goutte stoppée à une constriction $w_{out} = 40$ μm.

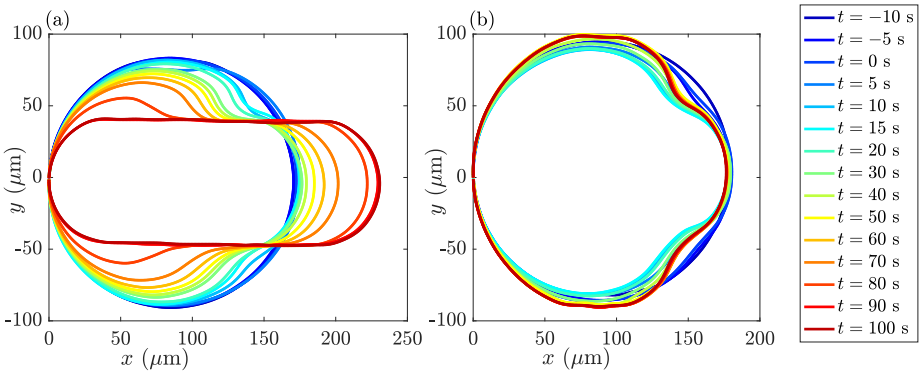

Figure 7.24: **Forme de gouttes à la constriction:** (a) Forme d'une goutte passant à travers la constriction, $w_{out} = 45$ μm. (b) Forme d'une goutte stoppée à la constriction $w_{out} = 40$ μm. La couleur code le temps, bleu foncé = juste avant d'atteindre la constriction; rouge vif = longtemps après avoir atteint la constriction.

Nous observons globalement que lorsque le canal est assez grand ($w_{out} > 0.5w_{in}$), les gouttes sont capables de se déformer pour passer dans le canal de sortie, comme illustré Fig. 7.23, à gauche. Lorsque le canal est trop petit cependant ($w_{out} < 0.5w_{in}$), les gouttes sont stoppées à la constriction, comme illustré Fig. 7.23, à droite. Une mesure précise de la forme de la goutte, Fig. 7.24, montre que même lorsque la goutte n'est pas capable de passer (à droite), elle reste active et se déforme à l'entrée de la constriction.

7.5.2.5 Conclusion

Dans ce chapitre, nous avons observé le comportement de goutte nageuses dans des géométries simples ou plus exotiques. L'un des résultats les plus étonnants, pourtant conceptuellement simple, est que les gouttes sont toujours capable de nager en 1D, pour tous les confinements considérés. La seule "limitation" à ce confinement est le phénomène de division spontanée lorsque les gouttes sont trop longues en capillaire circulaire. Ce phénomène de division est en lui même particulièrement attractif, puisque la capacité à se diviser fait partie des points communs des systèmes vivants.

7.5.3 Nager ensemble en 1D

L'argument de Landau-Peierls prédit qu'il ne peut pas y avoir à l'équilibre de transition de phase pour les systèmes passifs 1D, homogènes et avec interaction courte portée. Un moyen de contourner cet argument est de considérer des systèmes hors équilibre. Expérimentalement, le moyen le plus simple d'étudier un système actif 1D est de confiner les particules, la difficulté étant que le confinement risque alors de gêner l'activité. D'un point de vue théorique, des difficultés surgissent aussi des contraintes géométriques (les particules ne peuvent se dépasser).

Nous avons vu précédemment que nos gouttes nageuses continuaient d'être actives sous confinement, ce qui font d'elles de bons candidats pour explorer le comportement d'un système actif 1D.

7.5.3.1 Réalisation expérimentale

Expérimentalement, nous utilisons un circuit microfluidique pour produire puis placer avec un flux extérieur nos gouttes dans un serpentin dont la largeur fait typiquement la taille de la goutte. Une fois les flux coupés, les gouttes se mettent à nager dans une direction aléatoire, et nous observons leur comportement. La Fig. 7.25 montre les résultats de quelques expériences typiques à diverses densités de goutte, les diagrammes spatio-temporelles (à gauche), la distribution des vitesses (au milieu) et les vitesses moyennes (à droite).

En regardant le diagramme spatio-temporelle, nous observons une riche variété de comportements; des collisions binaires entre les gouttes, pendant lesquelles les gouttes changent de direction, mais aussi à l'échelle de l'expérience, l'émergence de structures denses dans lesquelles les gouttes sont alignées, et que nous appellerons les "trains". Ces trains interagissent avec les autres gouttes, mais aussi avec les autres trains. Nous souhaitons savoir quelle est le phénomène à l'origine de la création des trains. Un dernier phénomène observé est la création de "bouchons" dans lesquels les gouttes sont pratiquement immobiles, dans les zones très denses, typiquement lorsque deux trains se rencontrent.

Pour ce faire, nous nous intéressons à l'événement le plus simple ayant lieu dans notre système: la collision binaire entre deux gouttes. La Fig. 7.26 répertorie les différents types de collisions observées dans notre système. Si nous mettons de coté les collisions persistantes, qui sont rares, les autres collisions (a-d) peuvent toutes être décrites par des collisions inélastiques, qui conservent la quantité de mouvement (vitesse du centre de masse constant), mais perdent de l'énergie cinétique après la collision. Notablement,

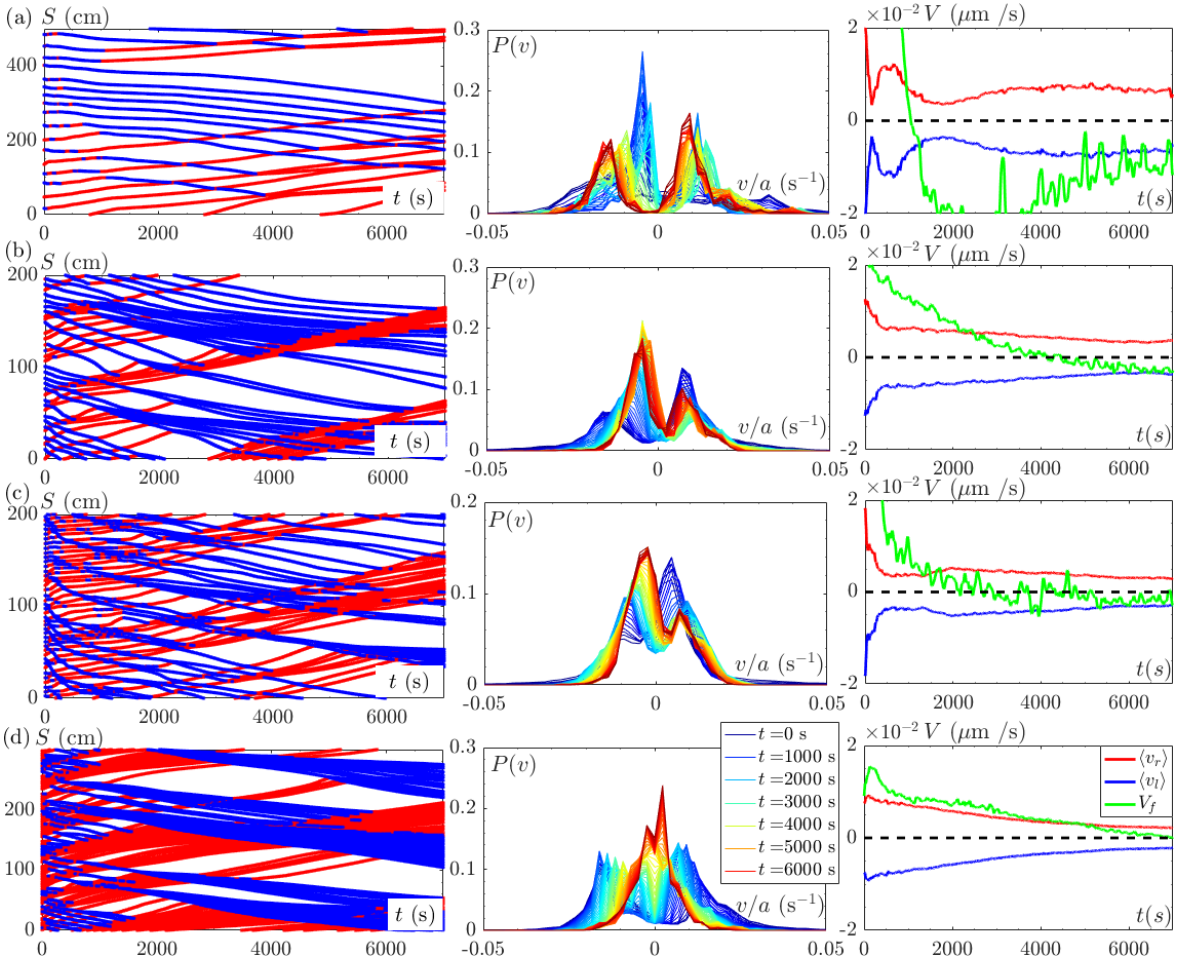

Figure 7.25: Expériences typique pour diverses densités de goutte. De haut en bas: (a) $d = 0.05$, (b) $d = 0.25$, (c) $d = 0.35$, (d) $d = 0.4$. **A droite**: diagramme spatio-temporelle de la position des gouttes. La couleur code pour la direction des gouttes (rouge vers le haut, bleu vers le bas). **Au milieu**: histogramme de la vitesse des gouttes, la couleur code pour le temps (bleu=début, rouge=fin). **A gauche**: Moyenne des vitesses "positives" (en rouge), "négatives" (en bleu), et flux résiduel (en vert).

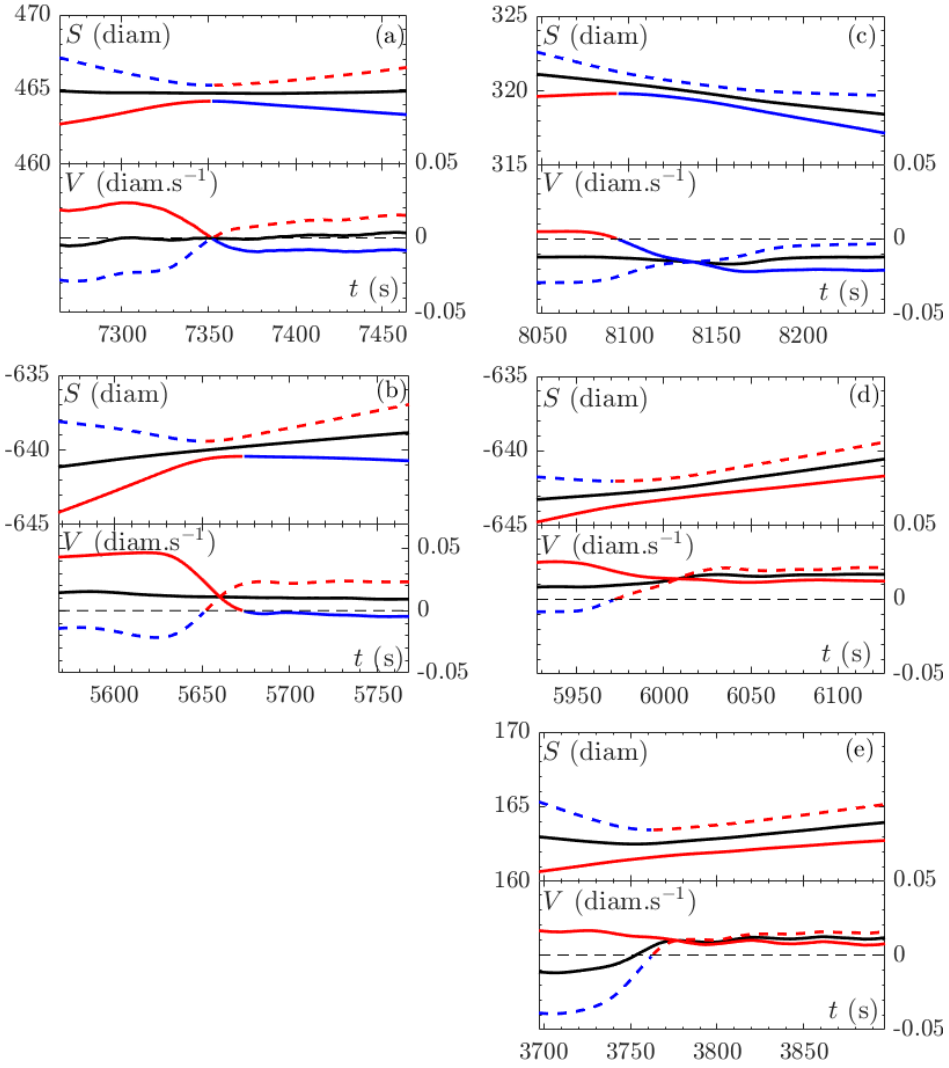

Figure 7.26: Toutes les sortes de collisions observées en expériences diluées. La goutte allant vers le haut avant la collision est en ligne continue, tandis que celle allant alors vers le bas est en ligne pointillée. La couleur correspond à l'orientation de la goutte; rouge = vers le haut et bleu = vers le bas. Le centre de masse est en noir. **A gauche**: collisions entre gouttes qui échangent leurs directions, (a) collision inélastique symétrique ($U_g = 0$), (b) collision inélastique asymétrique ($U_g \neq 0$). **A droite**: collisions entre gouttes qui s'alignent, (c) et (d) collision inélastique asymétrique conduisant à un alignement ($U_g \neq 0$), (e) collision persistante (Une goutte persiste dans sa direction avec une vitesse pratiquement inchangée).

lorsque deux gouttes de vitesses très différente se heurtent (c-d), la goutte la plus rapide peut ne pas se retourner, et les deux gouttes repartent dans la même direction: le système a gagné en alignement. Nous appelons $\alpha \sim 0.6$ le coefficient inélastique typique des gouttes.

D'autre part, les gouttes étant actives, après une perturbation de leur vitesse (typiquement après une collision inélastique au cours de laquelle la vitesse des gouttes décroit fortement), et en l'absence d'autres perturbations, la vitesse de la goutte va relaxer vers sa vitesse active. Nous appelons $\lambda \sim 10^{-3}\mathrm{s}^{-1}$ le taux typique de relaxation des gouttes.

7.5.3.2 Développement d'un modèle simple

Nous souhaiterions savoir si ces deux caractéristiques à l'échelle de la goutte: la relaxation vers l'activité et la nature inélastique de la collision, peuvent à elles seules expliquer l'émergence des phénomènes à l'échelle de l'expérience observée précédemment (trains, bouchons).

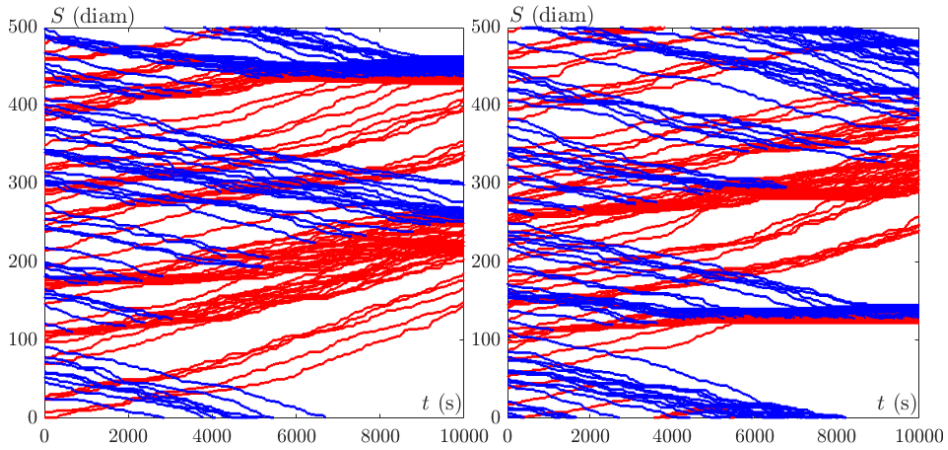

Figure 7.27: Diagramme spatio-temporel pour deux simulations de paramètres proches des paramètres expérimentaux.

Pour cela, nous avons développé un modèle numérique simple de particules actives en 1D, qui suivent les caractéristiques précédentes. Deux diagrammes spatio-temporels typiques pour les mêmes paramètres α et λ que l'expérience sont donnés Fig. 7.27. Nous observons l'émergence de trains et de bouchons. Donc les deux seuls ingrédients qui caractérisent l'activité de la goutte (la relaxation), et son interaction binaire avec une autre goutte (la collision inélastique) suffisent à l'établissement de structures collectives dans notre système.

Nous pouvons ensuite utiliser notre modèle numérique pour explorer des temps plus longs, et faire varier les paramètres α et λ. Les régimes observés à l'échelle de l'expérience ne sont en fait que des régimes transitoires, qui relaxent vers trois états possibles en fonction des paramètres: lorsque les collisions sont peu inélastiques (α proche de 1), et que les gouttes regagnent rapidement leur vitesse active (λ proche de 1), alors les gouttes sont en régime quasi-élastique, et continuent à se heurter. Lorsque les collisions sont très inélastique (α proche de 0), les gouttes s'alignent globalement. Enfin si le taux de relaxation est trop petit, les gouttes perdent de leur vitesse à chaque

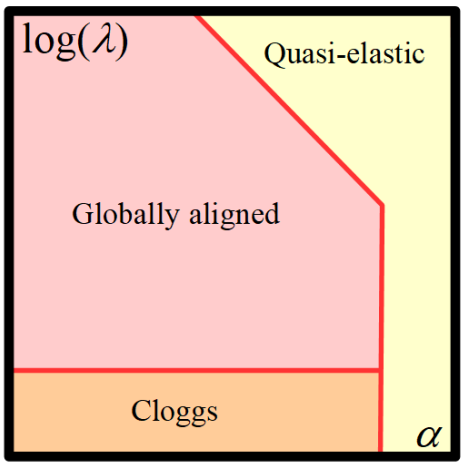

Figure 7.28: Diagramme de phase schématique.

collision, et forment des bouchons de gouttes immobiles. Le diagramme des phases de ces régimes en fonction des paramètres α et λ est donné Fig. 7.28

7.5.3.3 Conclusion

Nous avons réalisé un système expérimental de gouttes nageuses en 1D. Nous observons l'émergence de phénomènes collectifs macroscopiques, telles que les trains ou les bouchons. Un modèle simple montre que de telles structures peuvent être expliquées par des observations à l'échelle des gouttes, la relaxation vers l'activité et l'inélasticité des collisions. En fonction de l'importance des ces deux phénomènes, le système converge vers un état globalement aligné, ou un état qui reste désordonné. Il y a donc dans notre système une transition de phase.

7.5.4 En cours : Nage sous gravité

Cette dernière partie présente un travail en cours, et pour lequel nous allons simplement présenter les enjeux et les résultats préliminaires.

Dans le monde du vivant, de nombreux micro-organismes sont capable de gravitotaxie: d'adapter leur motilité en présence de gravité. La machinerie cellulaire nécessaire à cette adaptation n'est pas parfaitement comprise; certaines études suggèrent que l'activité des micro-organismes pourrait à elle seule être suffisante pour l'expliquer.

Dans notre système, le comportement de nos gouttes nageuses dépend d'un couplage entre le déplacement de la goutte, et la production d'un champ de concentration. Les gouttes étant pesantes, la gravité modifie nécessairement le déplacement de la goutte; et donc pourrait potentiellement avoir une influence sur le champ de concentration, et donc sur l'activité. C'est ce que nous souhaiterions étudier dans ce projet. Quelques expériences préliminaires montrent des résultats prometteurs. Nous avons mesuré la vitesse de gouttes de différentes tailles sur des plans inclinés, en faisant varier l'angle α du plan, et donc la force de gravité ressentie par la goutte dans ce plan. Les résultats sont présentés Fig. 7.29

Si la gravité n'affectait pas l'activité de la goutte, alors la vitesse de la goutte serait la somme de deux contributions indépendantes: la vitesse active $V_a(\alpha = 0)$, qui ne dépend

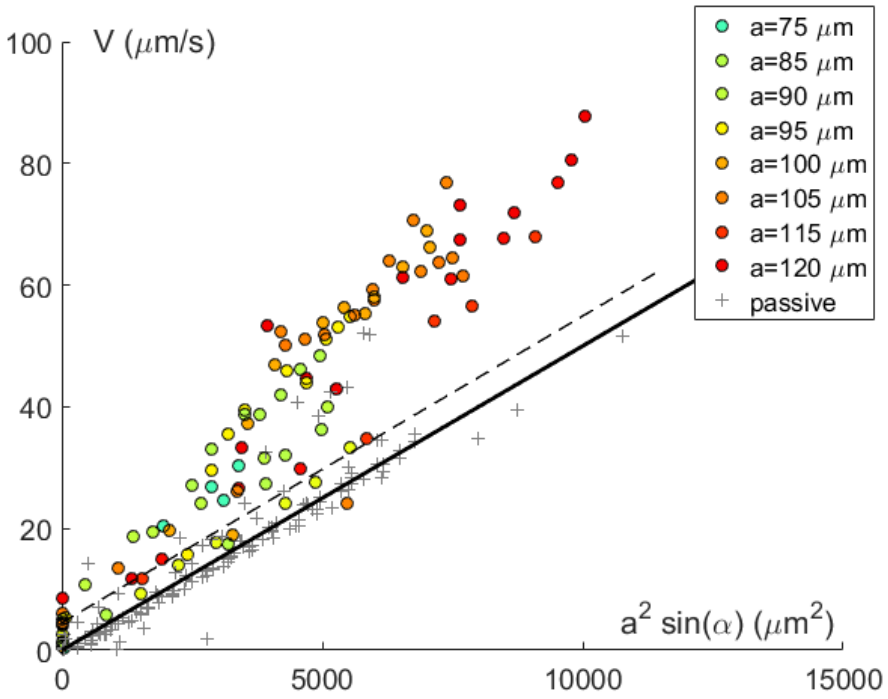

Figure 7.29: Composante de la vitesse parallèle à la gravité de gouttes nageuses de différentes tailles (cercles de couleurs), et de gouttes passives (croix grises), sur un plan incliné avec un angle α variable. La ligne noire continue représente la régression linéaire de la vitesse des gouttes passives; et la ligne noire pointillée représente la vitesse attendue des gouttes nageuses en présence de gravité, si la gravité n'avait pas d'influence sur la nage.

pas de l'angle du plan; et la vitesse de chute, $V_g \propto a^2 \sin\alpha$, qui est la même que pour des gouttes passives de même taille. Des expériences témoins, faites avec des gouttes passives, sont représentées par des croix grises: leur vitesse est bien proportionnelle à $a^2 \sin\alpha$, et nous représentons par une ligne continue la régression linéaire de la vitesse des gouttes passives. Lorsque l'angle est nul; la vitesses des gouttes actives est la vitesse de nage. Nous représentons par un trait pointillé la courbe $V(\alpha = 0) + V_g(\alpha)$. Si les effets de la gravité et de l'activité ne sont pas couplés, alors la vitesse des gouttes actives devrait suivre cette courbe. Nous observons que ce n'est pas le cas; en particulier aux grands angles, la vitesse des gouttes actives est bien au dessus de la courbe pointillée; cela montre que la gravité a bien un effet sur l'activité de la goutte.

7.6 Conclusion générale

Ce travail, qui est essentiellement de nature fondamentale, explore expérimentalement au travers d'un nageur modèle, l'influence de facteurs extérieurs sur le comportement des micro-nageurs. La goutte d'eau nageuse se déplace en induisant elle même un gradient de micelles gonflées à son interface. Nous l'observons dans de nombreuses situations: en présence de murs, confinée en 1D, avec de nombreuses autres gouttes ou encore sous gravité. Ces facteurs extérieurs influencent le champ de vitesse autour de la goutte, mais aussi, au travers du couplage entre l'hydrodynamique et les

champs de concentration, modifient le nageur lui même. Chapitre 7.5.1, nous avons vu que la présence d'un mur changeait le comportement longue portée des gouttes. Chapitre 7.5.2 a montré que le fort confinement n'empêchait pas les gouttes de nager, mais modifie leurs formes ce qui mène à des phénomènes complexes tels que des divisions spontanées. Chapitre 7.5.3, les interactions entre nageurs provoquent l'émergence d'effets collectifs tels que les trains ou les bouchons. Dans tous ces cas, ces contraintes extérieures qui n'auraient pu avoir comme effet que de gêner la nage, enrichissent grandement la phénoménologie du système. Au delà de la simple compréhension de toutes ces situations particulières, ces études donnent des clés de compréhension sur de nombreux phénomènes à l'interface entre l'hydrodynamique, la physico-chimie et l'étude des systèmes actifs.

RÉSUMÉ

La vie est d'une extraordinaire diversité. Peut-être plus merveilleux encore, les systèmes vivants partagent des caractéristiques communes : la compartimentalisation, la croissance et la division, le traitement d'informations, la transduction d'énergie et la capacité à s'adapter. La capacité à se mouvoir, en particulier, joue un rôle crucial dans la compétition entre espèces. La physique à l'échelle micrométrique étant différente de celle à notre échelle macroscopique, les micro-nageurs ont des stratégies spécifiques pour se déplacer. Comprendre ces stratégies est capital au niveau fondamental pour appréhender le comportement des micro-nageurs biologiques, mais aussi pour développer des applications techniques et médicales, où des nageurs artificiels permettent d'effectuer de nombreuses tâches (transport, mélange). Dans ce contexte, les micronageurs biologiques et artificiels ont été abondamment étudiés, et nous plaçons notre étude dans le cadre d'un environnement réaliste, et donc complexe, où la nage est influencée par des facteurs extérieurs (la géométrie, une force extérieure, d'autres nageurs). Tout au long de cette étude, nous utilisons la microfluidique pour créer, mettre en situation complexe et observer un nageur modèle : une goutte d'eau nageuse dans une solution d'huile et de micelles. Il a été montré que la nage de la goutte est due au couplage non linéaire entre l'hydrodynamique et l'advection-diffusion de micelles remplies d'eau. Nous étudions d'abord l'effet du confinement en utilisant une technique de micro-PIV en 3D. La présence d'un mur brise l'axisymétrie naturelle du problème. Nous proposons une formulation analytique simplifiée qui prend en compte la présence du mur et la densité de la goutte. Ce modèle décrit l'hydrodynamique longue distance en présence d'un mur, qui diffère de celle en l'absence de mur. Nous regardons ensuite des géométries plus confinées : des capillaires en verre. Nous observons que la vitesse des gouttes décroît quand le confinement augmente, mais sature à une valeur faible mais finie quand la goutte devient plus longue que la hauteur du capillaire. Dans des géométries plus complexes, telles que des capillaires étirés, nous observons un étonnant phénomène de divisions spontanées successives de la goutte pour les grands confinements. Nous montrons que ce cela vient d'une saturation en micelle gonflée le long de l'interface de la goutte. La présence d'une force extérieure a aussi une influence sur le comportement de la goutte. En 2D, nous observons pour une goutte sur un plan incliné que la gravité oriente la dynamique et que pour une forte gravité, la vitesse de la goutte est plus que la simple composition des vitesses due à la gravité et à l'activité. Nous confrontons ces résultats à une étude théorique du mécanisme d'instabilité en présence de gravité. En 1D, la goutte a un comportement similaire, mais nage aussi contre la gravité. Nous finissons en étudiant la dynamique collective des gouttes en canal 1D. Le système expérimental présente une phénoménologie riche : des gouttes voisines s'alignent et forment de larges trains. Nous observons que l'interaction entre deux gouttes qui se ≪ collisionnent ≫ est le résultat d'un effet combiné des fluctuations de vitesses et de l'absence d'invariance galiléenne. Nous construisons un modèle simple de particules actives, et à l'aide d'outils analytiques et numériques, nous montrons qu'il existe une transition vers une dynamique collective. En conclusion, la goutte nageuse partage de nombreuses similarités avec les systèmes vivants : la compartimentalisation (une goutte), la division (quand elle est confinée), la transduction d'énergie (par relaxation thermodynamique), et la capacité à s'adapter à son environnement (par la nage). Au-delà de la simple étude de notre système particulier, ces études donnent de nombreuses clés de compréhension sur des phénomènes à l'interface de l'hydrodynamique, de la physico-chimie et de la matière active.

MOTS CLÉS

Matière active, Goutte nageuse, Micro-fluidique, Dynamique de Stokes, Confinement, Sédimentation.

ABSTRACT

One may simply be amazed in front of the diversity and complexity of life. Yet, and maybe even more bewildering, living systems all share common hallmarks: compartmentalization, growth and division, information processing, energy transduction and adaptability. In particular, the mobility plays a crucial role in the competitiveness between different species. Physics at microscales is different from the one we are used to at our macroscopic scale. This is why, micro-swimmers have developed specific strategies to induce motion. The understanding of such strategies is crucial at the fundamental level to apprehend the behavior of biological micro-swimmer, but also to achieve artificial locomotion in a surrounding fluid at the micron-scale, in order to perform a multitude of tasks in technical and medical applications (transport, mixing), which has become a central goal of nanoscience. In this context, biological and artificial micro-swimmers have been intensively studied, and we place our study in the framework of swimming in a realistic and complex environment, in the case where external factors (confinement, external force, other swimmers) may influence the swimming properties. In this work, using microfluidic, we create, put into complex situation and observe a model swimmer: a pure water swimming droplet in an outer oil-micelle solution. It was shown that the droplet motion emerges from the nonlinear coupling of hydrodynamics and advection-diffusion of micelles filled with water. We first study the effect of confinement on such geometries using confocal PIV in 3D. The presence of one wall breaks the natural axisymmetry of the flow field. We propose a simplified analytical formulation taking into account the presence of the wall and the effect of buoyancy. This model accounts for the far field hydrodynamic of the droplet close to a wall that differs from the no-wall case. We then look at more confined geometries using glass capillary microfluidic. The velocity of the droplet decreases with increasing confinement; but surprisingly; it saturates at a non-zero value for droplets bigger than the channel height: even very long droplets swim. In more complex geometries, such as stretched capillaries; the droplet elongates while swimming, and amazingly, may undergo successive spontaneous splitting events for high enough confinement. We show that this behavior comes from a saturation in the swollen micelles concentration along the droplet length. External force - such as gravity – also influence the droplet behavior. In 2D, by observing a swimming droplet on an inclined plane, we show that gravity orients the droplet, and that under strong gravity, the droplet's velocity is more than the simple additivity of the gravity and activity. This is discussed in the light of a theoretical study of the instability mechanism under an external force. The droplet in 1D exhibit a similar behavior, but is also able to swim against gravity. Finally, we investigate their collective dynamics in a 1D micro-fluidic channel. We observe experimentally a rich phenomenology: neighboring droplets align and form large trains. Exanimating the interactions between two "colliding" droplets shows that alignment rises from the interplay between velocity fluctuations and the absence of Galilean invariance. Taking these observations as the basis for a minimalistic 1D model of active particles and combining analytical and numerical arguments, we show that the system exhibits a transition to collective motion. Altogether, the swimming droplet shares numerous similarities with living system: compartmentalization (a droplet), division (under confinement), energy transduction (by thermodynamic relaxation) and adaptability (through the swimming). Beyond the simple understanding of our peculiar system, these studies give insight on various phenomena at the interface of hydrodynamics, physico-chemical engineering and active matter.

KEYWORDS

Swimming droplets, Active matter, Microfluidics, Stokes dynamics, Confinement, Sedimentation.